BEAM DYNAMICS CHARACTERIZATION AND UNCERTAINTIES IN THE MUON g-2 EXPERIMENT AT FERMILAB

By

David Alberto Tarazona

A DISSERTATION

Submitted to
Michigan State University
in partial fulfillment of the requirements
for the degree of

Physics — Doctor of Philosophy

2021

ABSTRACT

BEAM DYNAMICS CHARACTERIZATION AND UNCERTAINTIES IN THE MUON g-2 EXPERIMENT AT FERMILAB

By

David Alberto Tarazona

The most recent measurement of the muon magnetic anomaly, $a_\mu = (g-2)/2$, from the Muon g-2 Experiment at Fermilab (E989) yielded an experimental relative uncertainty of 0.46 ppm, which differs from current Standard Model (SM) predictions by about 3.3σ and agrees with the previous result from the Brookhaven National Laboratory (BNL) Muon g-2 Experiment (E821). In contrast to E821, the goal of the experiment at Fermilab is to deliver a measurement of the anomaly to a precision of 0.14 ppm or less in order to reach more than 5σ discrepancy with the SM and, therefore, strongly establish evidence for new physics. In view of this stringent determination, a thorough description of the delivery, storage, and dynamics of the detected muon beam sets the stage for constraining beam-dynamics driven effects to the muon magnetic anomaly at the ppb level. To that extent, this dissertation introduces the background, principles, and beam requirements of E989; elaborates data-driven numerical models of the Beam Delivery System and Muon g-2 Storage Ring at Fermilab; characterizes the linear and nonlinear dynamics of the muon beam in the storage ring; and describes the contributions to the largest beam-dynamics systematic corrections and their uncertainties in the experiment derived from this work.

To Father and Mother.

ACKNOWLEDGMENTS

This section is currently being written. It is hard to find the right words and express all my gratitude to many persons that have contributed so greatly to this document and to my life. Martin Berz, Mike Syphers, Bill Morse, James Mott, David Hertzog, Kyoko Makino, Remco Zegers, Kim Crosslan, the Muon g-2 Collaboration, my MSU fellows Adrian Weisskopf and Eremey Valetov, among others. And most importantly my Family and girlfriend; without them, everything is not as worth as it is. And lastly, to the Universe for enriching and entertaining our lives with so many beautiful and interesting problems to be understood.

TABLE OF CONTENTS

LIST OF TABLES

LIST OF FIGURES

Chapter 1

Introduction

Our current understanding of elementary particles from which the physical Universe is made of and the interactions among them has led to the Standard Model of particle physics (SM). Nearly all the constituent parts of this theory and its implications have been validated experimentally over the course of the last five decades, being the observation of the Higgs boson at CERN's Large Hadron Collider (LHC) a contemporaneous example. In spite of its remarkable success, the numerous evidence of physics beyond the frontiers of the Standard Model (e.g., the hierarchy problem and dark matter) demands for high-precision completeness tests. In particular, the muon's g-factor, or equivalently the anomalous magnetic moment $a \equiv (g-2)/2$, has served as a sensitive physical quantity for this purpose. A well-established discrepancy between experiment and the Standard Model prediction of the muon's anomalous magnetic moment "a_μ" would serve as unambiguous evidence of as yet undiscovered particles beyond the Standard Model, and perhaps validate or disprove other theoretical models beyond the SM.

The Muon g-2 Experiment at Fermilab (E989) is directed toward measuring the anomalous magnetic moment of muons with total statistical and systematic fractional errors of 140 ppb or less. This experiment is the consummation of a series of experiments initiated in 1957 [17], in which longitudinally-polarized muons from the $\pi \to \mu \to e$ weak-decay channel offer a path to determine the anomalous magnetic moment. Over this period of

time, several machines—i.e., cyclotrons, a synchrocylotron, and storage rings—have been employed for this purpose. The objects of study of this dissertation are the beam dynamics at the Muon g-2 Storage Ring and, additionally, the Beam Delivery System (BDS) that produces the highly-polarized muon beam at Fermilab. Specifically, the combination of high-fidelity numerical models, mathematical methods, measurements, and data analysis detailed throughout the Chapters 2-4 allowed for a detailed beam performance analysis during the commissioning stages of the BDS and beam measurements' understanding, operational characterization of the g-2 storage ring, and quantifications of systematic corrections.

The following sections of this chapter introduce the main concepts in relation to the muon's anomalous magnetic moment, as well as the experimental technique implemented at Fermilab's g-2 experiment for the determination of a_μ; at the end, the beam-dynamics requirements to achieve the goals of the g-2 experiment are discussed.

1.1 The Anomalous Magnetic Moment

In classical electrodynamics [18], the magnetic field associated to localized and steady current distributions $\boldsymbol{j}$ at an observation point r far outside from the source can be expressed as a Taylor expansion, where the non-zero leading term yields[1]

$$\boldsymbol{B}(\boldsymbol{r}) = \nabla \times \left(\frac{\mu_0}{4\pi} \frac{\boldsymbol{m} \times \boldsymbol{r}}{r^3} \right). \tag{1.1}$$

[1] SI units are used throughout this document, unless otherwise specified.

μ_0 corresponds to the magnetic permeability, whereas the vector $\boldsymbol{m}$ is the *magnetic dipole moment* (or *magnetic moment* within this context)

$$\boldsymbol{m} = \frac{1}{2}\int d^3r\, \boldsymbol{r} \times \boldsymbol{j}(\boldsymbol{r}). \tag{1.2}$$

A particle with charge q, mass m, and located at $\boldsymbol{r'}$ has an associated current density of

$$\boldsymbol{j}(\boldsymbol{r}) = q\boldsymbol{v}\delta(\boldsymbol{r} - \boldsymbol{r'}). \tag{1.3}$$

Thus, its orbital magnetic moment in terms of the orbital angular momentum $\boldsymbol{L'} = m\boldsymbol{r'} \times \boldsymbol{v}$ can be defined as

$$\boldsymbol{m}_L = \frac{q}{2m}\boldsymbol{L'}. \tag{1.4}$$

Naturally, this proportionality between the dipole moment and angular momentum remains in quantum mechanics. From the union between special relativity and quantum mechanics, Dirac's equation of a "$\boldsymbol{S}$" spin-1/2 elementary particle (e.g., electrons, muons, and taus) under the influence of an external electromagnetic field [19] predicts a spin magnetic moment equal to

$$\boldsymbol{m}_S = g\frac{q}{2m}\boldsymbol{S}. \tag{1.5}$$

Within the realm of Dirac's equation the g-factor in Eq. (1.5) is exactly equal to 2. This theoretical achievement successfully explained early spin measurements such as the Stern-Gerlach experiments [20], from which in spin terms—first proposed by Compton [21] and Uhlenbeck-Goudsmit [22]— the electron's g-factor was found to be $g \approx 2$ [23].

However, as the precision g-factor measurements increased over the years, deviations of

fractions of a percent away from Dirac's prediction $g = 2$ were clearly observed in hyperfine-structure and subsequent experiments [3,24]. Table 4.1 shows recent experimental g-2 values of charged leptons.

Table 1.1: Recent g-2 values of charged leptons, taken from Refs. [1] and [2]. Tensions between g-2 values from experiments and theory have been the main motivation of g-2 experiments.

	***g*-2**	**Relative uncertainty**
e	0.002 319 304 361 82(52)	2.6×10^{-13}
μ	0.002 331 841 8(13)	6.3×10^{-10}
τ	-0.036(34)	1.8×10^{-2}

With g-factors being initially contrasted with Dirac's equation, it became customary since then to refer to the relative deviation from the $g = 2$ expectation back then as the *anomalous magnetic moment*, namely:

$$a \equiv \frac{g-2}{2}. \tag{1.6}$$

Nowadays, the origins of the "anomalous" magnetic moment are explained to a more detailed extent by accounting for radiative corrections within the framework of the Standard Model of particle physics, as presented in Subsec. 1.1.1 where, in particular, the SM prediction of the muon's anomalous magnetic moment relevant for the goals of the Muon g-2 Experiment at Fermilab is summarized.

1.1.1 Muon g-2 from the Standard Model

In essence, the Standard Model encompasses *all* known contributions to a_μ from quantum fluctuations in the form of intermediate elementary particles, i.e., radiative corrections. As the muon's spin-1/2 field interconnects with the external electromagnetic field as theorized

by quantum electrodynamics (QED), perturbation theory allows for a serial loop-by-loop description of the corresponding muon-photon interaction in the SM. Each of these loops can be represented via Feynman diagrams as shown in Fig. 1.1, where intermediate (or virtual) particles contribute to the muon-photon interaction, also known as the QED vertex.

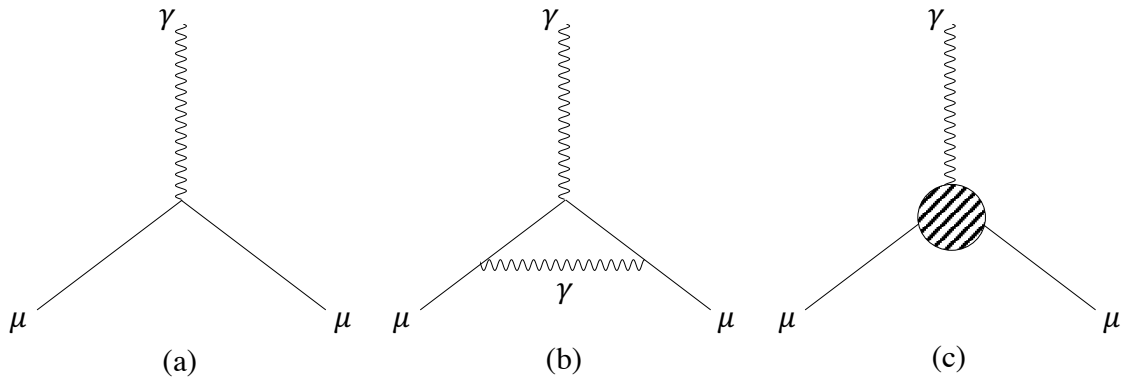

Figure 1.1: QED vertex perturbative loops represented with Feynman diagrams. The interaction described by Dirac's equation is represented in the 0th-order loop order diagram shown in (a). In (b), the 1st-order loop contribute $\alpha/2\pi$ to a_μ [3]. The diagram in (c) represents all the other higher-order contributions to a_μ of virtual particles coupling to leptons or photons.

The anomalous magnetic moment can be calculated from the Standard Model from the matrix element describing the physical process within the loop. In general, it contains two independent form factors that specify the parameters of the interaction (see Fig. 1.1(c)). Specifically, for higher-order loops the SM predicts that in the limit of the photon's momentum being zero in the QED vertex, one of these form factors directly defines the anomalous magnetic moment. Thus, by renormalizing the QED vertex with the perturbative higher order terms, a precise calculation of a_μ is established from the theory side. It is worth to mention that the higher-order loops contribute to a_μ in proportion to the virtual particle and muon masses, m_V and m_μ respectively, as $(m_\mu/m_V)^2$. Even though electrons are more

accessible in the laboratory than muons, the latter are preferred since—given the muon-to-electron ratio $(m_\mu/m_e)^2 \approx 4.3 \times 10^4$—they are four orders of magnitude more sensitive to interactions with heavier virtual particles.

The theoretical contributions to a_μ from the Standard Model are typically characterized as follows:

$$a_\mu^{SM} = a_\mu^{QED} + a_\mu^{EW} + a_\mu^{HVP} + a_\mu^{HLbL}, \tag{1.7}$$

where a_μ^{QED} and a_μ^{EW} result from quantum electrodynamics and electroweak interactions, respectively. The other two terms,a_μ^{HVP} and a_μ^{HLbL}, are the hadronic vacuum polarization and hadronic light-by-light contributions which make up the contribution from hadronic interactions. Next, each of these components is discussed.

The QED contribution: a_μ^{QED}

Quantum electrodynamics encapsulates about 99.994 % of the a_μ^{SM} prediction and results from lepton and photon interactions. Schwinger calculated the 1st-order loop [3] (see Fig. 1.1b) contribution $a_\mu^{QED,1}$ in terms of the fine structure constant $\alpha = e^2/4\pi$:

$$a_\mu^{QED,1} = \frac{\alpha}{2\pi} \approx 0.00116. \tag{1.8}$$

The other non-dominant higher-order terms are further calculated with higher powers of α, comprising contributions from more involved loops where numerous virtual lepton-photon interactions take place. Expressed as a perturbation expansion,

$$a_\mu^{QED} = a_\mu^{QED,1} + \sum_{n=2}^{\infty} a_\mu^{(2n)} \left(\frac{\alpha}{\pi}\right)^n. \tag{1.9}$$

Since $|\alpha| \ll 1$, the contribution to a_μ^{QED} vanishes for higher n orders.

Kinoshita *et al.* undertook the exceptional effort of computing up-to-tenth order QED contributions [25], where over 12,000 Feynman diagrams containing up to 5 loops were involved:

$$a_\mu^{QED} = 116584718.931(104) \times 10^{-11}. \tag{1.10}$$

The result in Eq. (1.10)—limited by the measurement of α—has been verified independently and is well established, contributing to the associated δa_μ^{SM} error the smallest amount.

The contribution from electroweak interactions: a_μ^{EW}

Contributions to a_μ^{SM} from electroweak interactions account for the smallest value among the other forces. Being mediated by the exchange of charged W, Z, and H neutral bosons as shown in Fig. 1.2, the relatively large masses lead to terms suppression (i.e., 0.0001 % of a_μ^{QED}). In Fig. 1.2, leading order (LO) EW processes are shown; Feynman's diagram

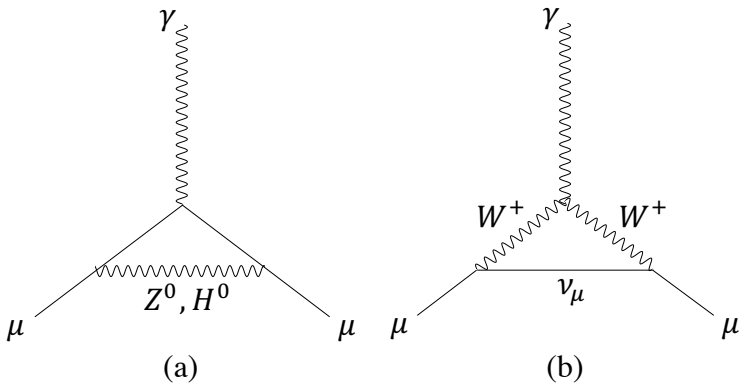

Figure 1.2: Lowest order (a) and (b) largest EW contributions to a_μ^{SM}.

(a) illustrates the exchange of a virtual Z^0 or H^0 boson, closely resembling the LO QED interaction. On the other hand, the interaction depicted in Fig. 1.2b corresponds to the emission and recapture of a positively-charged W boson and a muon neutrino, being the

largest contribution to a_μ^{EW}. The LO contributions from W and Z bosons result to be:

$$a_\mu^{EW(LO)} \approx \frac{G_F m_\mu^2}{8\sqrt{2}\pi^2}\frac{1}{3}\left[2+\left(\frac{m_W}{m_Z}\right)^2\right], \tag{1.11}$$

where G_F is Fermi coupling constant. Processes with Higgs-boson exchange are negligible due to its relatively large mass. Second-order EW processes make up a small component part of a_μ^{EW}, of about -40×10^{-11} [26]. In total [27],

$$a_\mu^{EW} = 153.6(1.0)\times10^{-11}. \tag{1.12}$$

The contribution from hadronic interactions: $a_\mu^{HVP} + a_\mu^{HLbL}$

In QED, the Standard Model is remarkably powerful in calculating processes to energy scales of interest and, largely, the perturbation expansions converge. Nevertheless, when the interaction involves quantum chromodynamics (QCD) interactions via quarks, a power expansion in terms of the strong coupling constant, α_s, alone does not lead to convergence at low energies. Consequently, hadronic contributions to a_μ^{SM} dominate its uncertainty. Hadronic processes relevant in this context are typically broken into two components, namely, the hadronic vacuum polarization (HVP) and light-by-light (HLbL) terms (a_μ^{HVP} and a_μ^{HLbL}, respectively).

The lowest-order HVP diagram shown in Fig. 1.3 dominates the hadronic contribution and its associated error. Virtual hadron energies in these processes are below the perturbative region of QCD (pQCD). For this reason, dispersion relations (R) from experimental data are

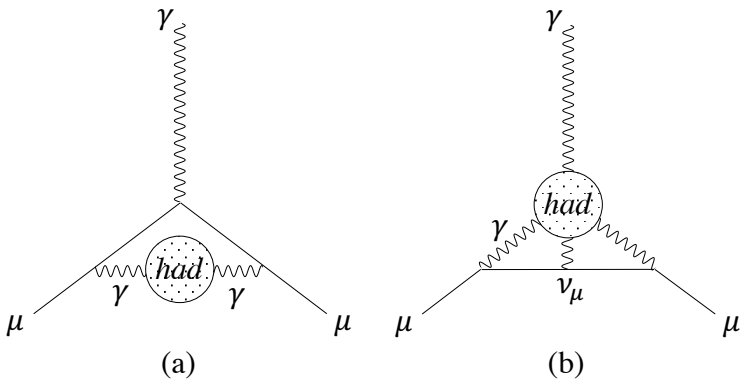

Figure 1.3: Feynman diagrams of the LO hadronic vacuum polarization (HVP) and light-by-light scattering (HLbL).

required in addition to pQCD in order to calculate the LO hadronic contribution to a_μ^{SM}:

$$a_\mu^{HVP,LO} = \Big(\frac{\alpha m_\mu}{3\pi}\Big)^2 \int_{m_\pi^2}^{\infty} K(s)R(s) \quad \text{for} \quad R \equiv \frac{\sigma_{tot}(e^+e^- \to \text{hadrons})}{\sigma(e^+e^- \to \mu^+\mu^-)}, \tag{1.13}$$

where s is the energy ($E = \sqrt{s}$), $K(s)$ a known function, and σ's are cross sections. In Eq. (1.13), perturbative QCD can be used at larger energies instead of data-driven input. A number of experiments—BaBar, BELLE, KLOE, VEPP, and BES— provide the experimental data to calculate the cross sections for all final states [28, 29]. The leading HVP contribution comes from the $\pi^+\pi^-$ channel, and yields in total [5]:

$$a_\mu^{HVP} = 6845(40) \times 10^{-11}. \tag{1.14}$$

In the light-by-light hadronic contribution to a_μ^{SM}, processes involving four virtual photons coupled to a hadronic state as shown in Fig. 1.3b are computed. Since no aid from data-driven dispersion relations as for the HVP contributions can be applied to HLbL interactions, low-energy hadronic models with relatively large associated errors are needed [26]. HLbL terms represent around 2% of the overall hadronic a_μ-contribution; however, it ac-

counts for about 40% of its error. A contemporaneous value for HLbL contributions to a_μ^{SM} was established by a collaboration of theorists under the name "Glasgow consensus" [30]. In it, several alternative and model-dependent approaches were accounted for and a detailed discussion of the consensus can be found in Ref. 26. The accepted value from HLbL processes is [31]:

$$a_\mu^{HLbL} = 92(18) \times 10^{-11}. \tag{1.15}$$

Another strategy for quantifying hadronic effects is lattice QCD [5]; an established method for first principle calculations of certain simple hadronic observables. HVP is a multi-scale quantity and hence not as simple as other quantities for which lattice calculations have been performed with sub-percent precision. The SM contributions aforementioned follow the guidance from the Muon g-2 Theory Initiative [5] of a reliable theory prediction.

The above component parts of a_μ^{SM} are added together to encapsulate from the theory side

$$a_\mu^{SM} = 116591810(43) \times 10^{-11}. \tag{1.16}$$

With this prediction determined to a relative precision of 369 ppb, the search for tensions between a_μ^{SM} and the experimental muon's anomalous magnetic moment embodies the spirit of Fermilab's muon g-2 experiment. Next, previous comparisons between theoretical and experimental anomalous magnetic moments of the muon that have traced the path to E989 are presented.

1.1.2 Muon g-2: Theory versus experiment

The symbiosis between theoretical formulations posterior to Dirac's $g = 2$ prediction and experimental measurements of g-factors has been the main driver of muon g-2 experiments

during the last decades [17], culminating in the Muon g-2 experiment at Fermilab. When Schwinger formulated the first radiative correction of the g-factor beyond Dirac's equation—and motivated by observations of an unexpectedly large hydrogen's hyperfine structure [3]—, the posterior work from Lee and Yang on parity violation from decays mediated by the weak force [32] paved the way to go beyond $g = 2$ with muons from the experimental front. Since then, a consecutive series of both experimental and theoretical improvements have led to the tension between the world average measurement and the prediction shown in Eq. (1.16) that Fermilab's g-2 experiment aims to settle down.

Figure 1.4 shows the tension between recent SM predictions of a_μ together with the measurement performed at Brookhaven National Laboratory (BNL) from years 1997 to 2001 [33] and the latest measurement at E989 from 2018 [4]. Fermilab result is the most precise mea-

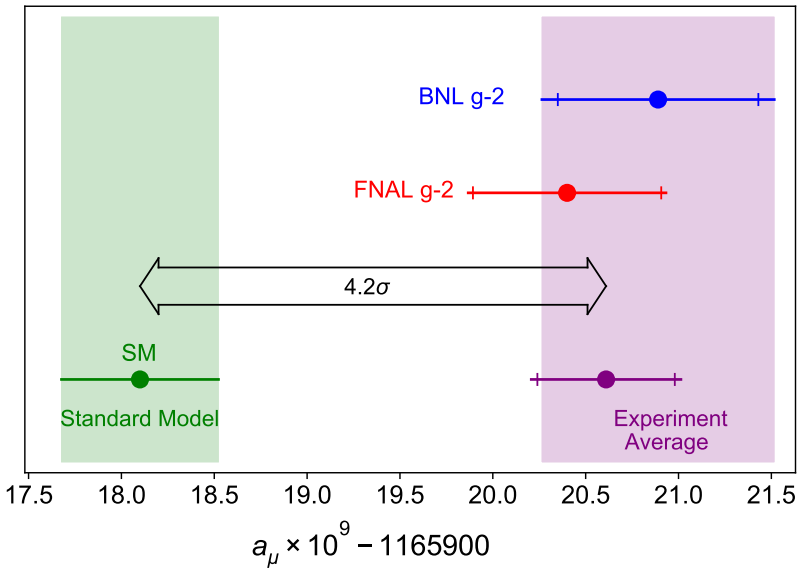

Figure 1.4: Difference between the theoretical (green) and most recent measurements of a_μ [4]. The inner tick marks indicate the statistical contribution to the total uncertainties. The theoretical value follows the recommendation from the Muon g-2 Theory Initiative [5]. The $\times 4$ smaller experimental error goal at FNAL requires twenty times more statistics and systematic uncertainties reduced by a factor of $\simeq 3$.

surement of the anomalous magnetic anomaly of the muon. The experimental technique employed during this experiment, which are presented in Sec. 1.2, followed the same principles as in the g-2 experiment at BNL. With a combined precision of 350 ppb from E821 and E989 measurements:

$$a_\mu^{Exp} = 116592061(41) \times 10^{-11}. \tag{1.17}$$

The experimental result deviates from the current theoretical by a significance of 4.2σ, being σ the fractional error associated to the difference [5]

$$\Delta a_\mu = a_\mu^{Exp} - a_\mu^{SM} = (251 \pm 59) \times 10^{-11}. \tag{1.18}$$

Consequently, the result prompts numerous formulations beyond the Standard Model and further experiments toward explaining and validating the discrepancy.

From the theoretical side, a first lattice result at sub-percent precision ($\sim 0.7\,\%$) was reported by the BMW collaboration [34] at the time of this dissertation. Their result is in 2σ tension with the data-driven evaluation, but with a systematics-dominated uncertainty. Given the complexity of the computations, independent results from different lattice groups with comparable errors are required to test and validate the lattice calculations. These calculations are a high priority for the Theory Initiative, thus are expected to take place in the near future [5].

From the experimental side, the muon g-2 experiment at Fermilab was proposed to reduce BNL's experimental error by a factor of about 4 (see Fig. 1.4), allowing for a significance larger than 5σ—if the central theory and experiment values remain unchanged—that could lead to fundamental breakthroughs. This amount of data is expected to be collected and analyzed by fiscal year 2023.

1.2 The Muon g-2 Experiment at Fermilab: Experimental Method

Searching for evidence of new physics, muon g-2 experiments have made use of longitudinally-polarized muons to measure their anomalous magnetic moment. Fermilab's muon g-2 experiment (E989) aims at extracting this quantity experimentally by counting the number of high-energy positrons over time from the $\mu^+ \to e^+\nu_e\bar{\nu}_\mu$ weak-decay channel. With the same– and significantly upgraded–machine and concept employed at the muon g-2 experiment at Brookhaven National Laboratory (BNL) [33], a highly-polarized muon beam produced along the Muon Campus as part of Fermilab's accelerator complex (see Ch. 2) is injected into a storage ring [35] (see Ch. 3). The muon beam circulates the storage ring for hundredths of microseconds until all of them have decayed, while specialized detection systems measure positrons from muon decay and characterize the injected beam and magnetic guide field for systematic error assessment.

In this section, the experimental technique to measure the anomalous magnetic moment of the muon is presented. A brief overview of the systems directly involved in the experimental technique and beam dynamics measurements is also included. The other component parts of the g-2 storage ring are presented in Ch. 3 altogether with corresponding numerical models of them for beam dynamics studies and beam tracking simulations.

1.2.1 The anomalous muon precession frequency ω_a

Ideally, muons with "magic" momentum $p_0 = m_\mu c/\sqrt{a_\mu}$ perfectly injected into the g-2 storage ring would circulate around centered orbits of radius $r_0 \approx 7.112\,\mathrm{m}$, perpendicular to a perfectly-uniform vertical magnetic field $\vec{B}_0 = p_0/er_0\hat{y}$. Under such circumstances, the

spin and cyclotron frequencies [35], $\vec{\omega}_s$ and $\vec{\omega}_c$ respectively, at which the muon's spin and momentum rotate in the laboratory frame would be equal to

$$\vec{\omega}_s = -g\frac{e\vec{B}_0}{2m_\mu} - (1-\gamma_0)\frac{e\vec{B}_0}{\gamma_0 m_\mu} \quad \text{and} \quad \vec{\omega}_c = -\frac{e\vec{B}_0}{\gamma_0 m_\mu}. \tag{1.19}$$

In Eq. (1.19), g, e, γ_0, and m_μ are the g-factor, electric charge, ideal Lorentz factor, and mass of the muon, respectively.

For this case, a frequency of the spin relative to the muon's direction of motion, known as the *anomalous precession frequency*, can be well defined:

$$\vec{\omega}_a \equiv \vec{\omega}_s - \vec{\omega}_c = -a_\mu \frac{e\vec{B}_0}{m_\mu}. \tag{1.20}$$

This direct relation between $\vec{\omega}_a$ and a_μ in Eq. (1.20) is the foundation of Fermilab's muon g-2 experiment; a careful measurement of $\vec{\omega}_a$ is tantamount to a precise measurement of the muon's anomalous magnetic moment.

Without any radiative corrections, a_μ would be equal to zero and the relative angle between momentum and spin in the storage ring would not change. However, as this is not the case, the anomalous magnetic moment introduces a frequency of $\omega_a \approx 4.37\,\mu$s (i.e., about one revolution every 29.33 turns around the storage ring).

The anomalous precession frequency is measured by exploiting parity violation in the $\mu^+ \to e^+\nu_e\bar{\nu}_\mu$ weak-decay channel. In the muon's rest frame, positrons with the highest energy (i.e., with momentum $p'^*_{e\,max} \approx 53\,\text{MeV}/c$) are produced when the two neutrinos are parallel to each other. On the other hand, parity violation constraints the spin and momentum directions of the emitted neutrino(anti-neutrino) to be anti-aligned(aligned) (i.e.,

± 1 helicity). Consequently, conservation of angular momentum implies that highest-energy positrons are emitted parallel to the muon spin. From V-A theory [36], the differential decay distribution of positrons from $\mu^+ \to e^+ \nu_e \bar{\nu}_\mu$ in the muon's rest frame (given the positron's energy much larger than its rest mass) is equal to:

$$dP(y', \theta') \propto n'(y') \left[1 + \mathcal{A}(y') \cos\theta'\right] dy' d\Omega'. \tag{1.21}$$

Here, $d\Omega'$, y', and θ' are the solid angle, fractional momentum of the positron $p'_e / p'_{e\,max}$, and angle between the positron-momentum and muon-spin directions, respectively. The quantities $n'(y')$ and $\mathcal{A}(y')$ are given by:

$$n(y') = 2y'^2(3 - 2y') \quad \text{and} \quad \mathcal{A}(y') = \frac{2y' - 1}{3 - 2y'}. \tag{1.22}$$

Both $n'(y')$ and $\mathcal{A}(y')$ increase for higher y' values, which translates into decay positrons emitted along the muon's spin direction being a more probable process, especially for $y' \geq 0.5$.

In the laboratory frame, a Lorentzian boost of Eq. (1.21) yields a time-dependent number of decay positrons from a muon beam proportional to:

$$N_e(t, E) \propto e^{-t/\gamma\tau} N_{e0}(E) \left[1 + A_e(E) \cos(\omega_a t + \varphi_0(E))\right], \tag{1.23}$$

where

$$N_{e0}(E) \propto (y - 1)(4y^2 - 5y - 5) \quad , \quad A_e(E) = \mathcal{P} \frac{-8y^2 + y + 1}{4y^2 - 5y - 5} \quad , \quad y = \frac{E}{E_{max}}, \tag{1.24}$$

E is the positron energy in this frame and $\mathcal{P}$ is the muon beam polarization. $\gamma\tau \approx 64.44 \mu s$

is the dilated muon lifetime and $E_{max} \approx 3.1\,\text{GeV}$ the maximum positrons' energy in the laboratory frame for magic-momentum muons. Ignoring the exponential term, Fig. 1.5 illustrates the oscillation of $N_e(E)$ for a highly-polarized muon beam.

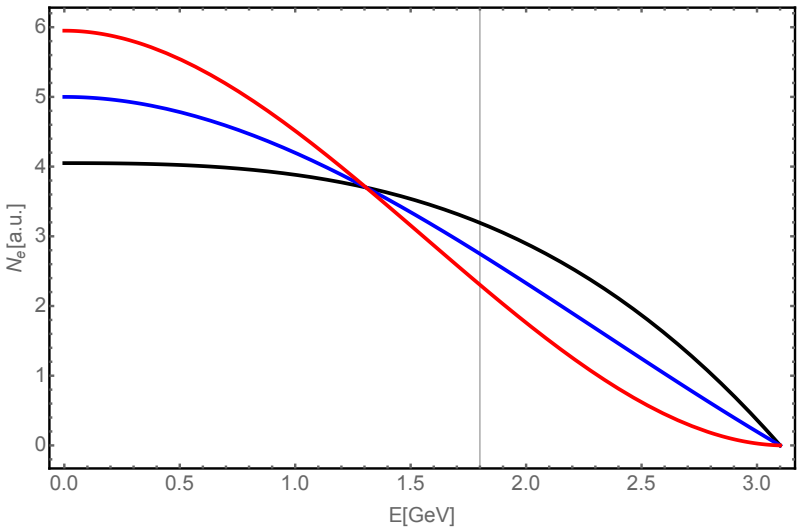

Figure 1.5: Number of positrons from a highly polarized muon beam ($\mathcal{P} = 0.95$) decaying via $\mu^+ \to e^+\nu_e\bar{\nu}_\mu$, subject to the positron energy E in the laboratory frame and ignoring the exponential term $e^{-t/\gamma\tau}$. The energy distribution oscillates as the muon beam polarization rotates relative to the beam's direction of motion with an angular frequency ω_a independent of time. The black curve corresponds to the polarization parallel to momentum, whereas the blue and red curves show the energy distribution when these two directions are perpendicular and anti-parallel to momentum, respectively. The oscillation is statistically maximized when integrating above $\sim 1.8\,\text{GeV}$.

In the experiment, positrons above a threshold energy E_{th} are selected to maximize the statistical power of the detected number-of-positrons signal:

$$N(t, E_{th}) = N_0(E_{th})e^{-t/\gamma\tau}\left[1 + A(E_{th})\cos(\omega_a t + \varphi_0(E_{th}))\right], \tag{1.25}$$

where

$$N_0(E_{th}) \propto (y_{th} - 1)^2(-y_{th}^2 + y_{th} + 3) \quad , \quad A(E_{th}) = \mathcal{P}\frac{y_{th}(2y_{th} + 1)}{-y_{th}^2 + y_{th} + 3}, \tag{1.26}$$

and $y_{th} = E_{th}/E_{max}$. When a fitting of the form of Eq. (1.25) is performed to data collected as shown in Fig. 1.6, the threshold energy that minimizes the statistical fractional error, inversely proportional to $\sqrt{NA^2}$, is $E_{th} \approx 1.8$GeV, where detectors acceptance and energy resolution play a role. Additional effects from detection acceptance must be included in Eq. (1.25) to obtain a reasonable χ^2-value when fitting collected data for a clean extraction of ω_a [37]

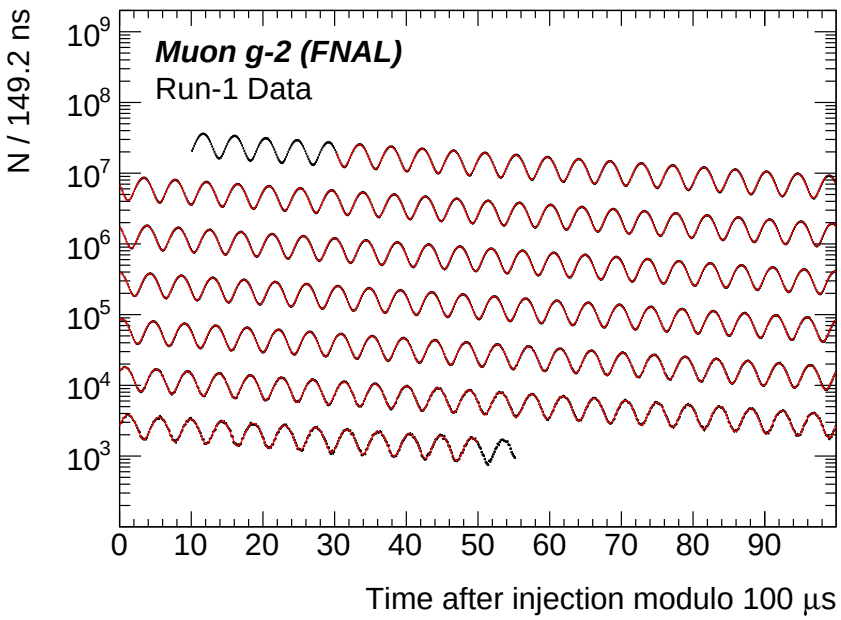

Figure 1.6: Number of positrons above energy threshold detected at Fermilab's g-2 experiment, Run-1.

1.2.2 Muon g-2 detection systems

A set of 24 calorimeter detectors are equidistantly distributed along the inner part of the storage ring, being their main purpose to measure ω_a. By measuring the energy and arrival time of positrons, calorimeters count the number of positrons over time produced by the muon beam as it decays while circulating the storage ring. This way, the modulated signal

as shown in Fig. 1.6 is obtained for the subsequent extraction of the anomalous precession frequency.

Each calorimeter station is composed of 25 mm × 25 mm × 140 mm crystals made of PbF_2 and arrayed in a 9(wide) : 6(tall) grid [38]. The depth of the crystals (140 mm) equals about 13 radiation lengths, allowing for stopping positrons effectively. The energy deposited by the positrons into the crystal lead-fluoride material excites e^+e^- production, from which short-pulsed Cherenkov light is emitted. The total amount of light bounces toward Silicon PhotoMultipliers (SiPMs), where photons hit electrons in pixels that then cascade into a measurable current (and posteriorly amplified multiple times). The emanated digitized pulses are fitted to get a peak time and pulse integral, proportional to the positrons arrival time and energy, respectively.

In order to fulfill the precision goals of the ω_a measurement, calorimeters have to distinguish light showers separated by 5 ns or more with 100% efficiency, as well as support a time resolution smaller than 100 ps of the short-pulsed signals. The systematic uncertainty associated to the pileup of two low-energy positrons entering a PbF_2 crystal with similar impact times and being recorded as one single signal is reduced with such requirements. Since the time-arrival measurement is taken from positrons above a specific energy threshold, an energy resolution of 5% at 2 GeV is sufficient. Furthermore, a laser calibration system guarantees residual gain stability while correcting gain drifts during the measurement time window.

In addition to the calorimeter detectors aimed to measure the anomalous precession frequency, the muon g-2 experiment at Fermilab possesses supplementary detection systems to characterize the spatial and temporal distributions of the injected muon beam. On the one hand, the beam profile (altogether with its intensity and relative arrival time) is measured

upstream the entrance to the storage ring with a SiPM and photomultiplier tubes (PMTs) attached to a scintillator [39]. On the other hand, an inflector beam monitoring system (IBMS) of three scintillating-fiber retractable detectors —placed nearby the hole in the ring's magnet yoke through which the beam enters the ring— provides transverse beam profile measurements during beam injection for beam-tuning purposes [40]. Furthermore, a set of two "fiber harp" detectors made of seven parallel scintillating fibers each measure the transverse profiles (horizontal and vertical) of the beam when inserted into the ring's storage region [41].

Of particular importance in the context of the work presented in this thesis is the Muon g-2 Straw tracking detection system [42]. Its ability to measure the transverse beam profile non-destructively at two azimuthal locations of the ring[2] allows for a thorough determination of the muon beam dynamics along the entire ring and, moreover, the reconstruction of unmeasured guide fields under special conditions as described with detail in Ch. 3. Its main principle to resolve the transversal coordinates of a muon is to reconstruct its position prior to decay based on the detected trajectory of the corresponding decay positron.

A straw tracking station consists of eight detector modules in series (see Fig. 1.7), where four layers of 32 straws of 5 mm in diameter are grouped in pairs of two and oriented at $\pm 7.5^{\circ}$ away from the vertical to resolve vertical locations. The straws are coated with gold on their inner wall and grounded to act as a cathode, in conjunction with a 25 µm thick wire made of gold-plated tungsten and placed along the straw axis. A positive high voltage of 1.625 kV is applied across the wires to create a cylindrical electric field. As decay positrons cross the straws, argon gas trapped inside is ionised along their path. The released electrons form

[2] A third station is probable to be installed in fiscal year 2021 or afterwards for the remaining data-taking g-2 runs at Fermilab.

an avalanche which is strongly attracted by the electric field towards the wire in the center, inducing a detectable signal. A quench gas (i.e., ethane) is also added to a 1:1 ratio with the argon gas in the interior of the straws to avoid secondary avalanches originated beyond the positron trajectory, which would add false track signals to the main readouts. Additionally, a small amount of water is confined inside the straws to help reduce their aging. A fitting algorithm extrapolates the momentum and time back to the muon decay position.

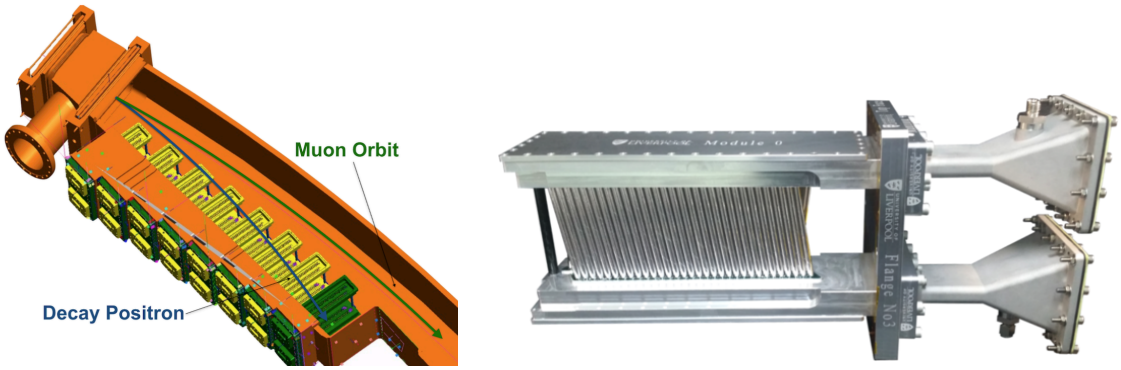

Figure 1.7: (a) Straw tracking station and (b) a detector module.

1.2.3 The muon g-2 magnetic field

In concert with the anomalous precession frequency measurement, the magnetic field utilized at E989 [43] to induce this precession must be known to a precision of 70 ppb or less in order to achieve the experimental goals.

A vertical magnetic field of $p_0/er_0 \approx 1.4513$ T is supplied by four circular superconducting coils operating at about 5200 A [35], exciting the g-2 Storage Ring magnet (See Fig. 1.8) which is built as one continuous superferric magnet made of mainly six layers of high quality magnet steel and two pole pieces as shown in Fig. 1.9. With the yoke steel manufactured

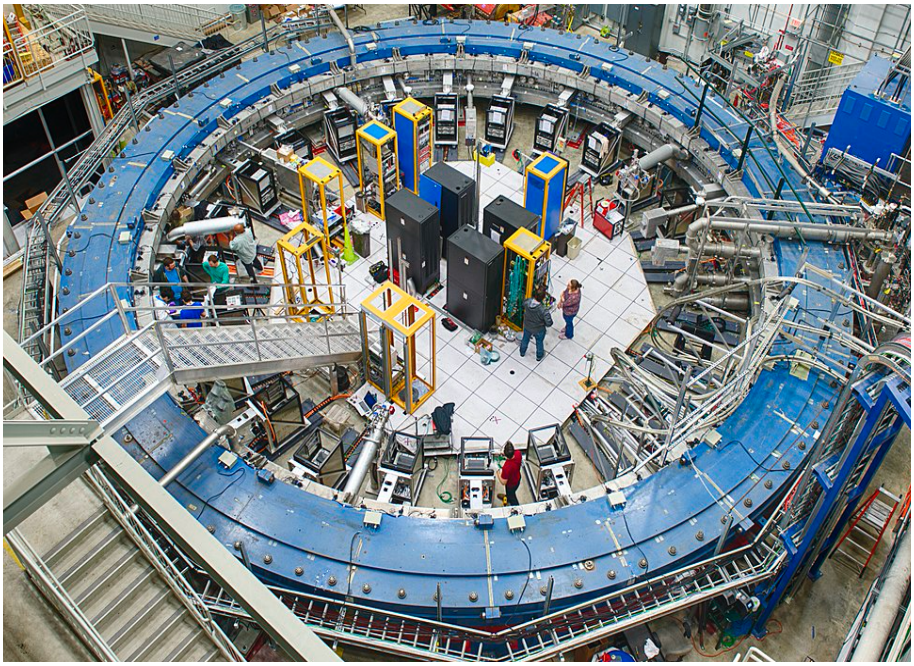

Figure 1.8: Muon g-2 storage ring housed at Fermilab. The steel yokes and superconductive coils crossed thousands of miles from BNL to Fermilab for an extended use. After the first data-taking period at Fermilab, the storage ring magnet was covered with thermal insulation to reduce temperature gradients that affect the uniformity of the magnetic field.

for the muon g-2 experiment at BNL being reused at E989, the physical parameters of the g-2 storage ring magnet are unchanged (see Table 1.2). Nevertheless, the magnetic field shimming at E989 for the first data-taking runs achieved a factor of two improvement in the uniformity of the magnetic field [44].

A network of pulsed nuclear magnetic resonance probes (pNMR) is used to measure the magnetic field in the muon storage region [6]. An RF magnetic field rotates the net magnetization of protons in petroleum jelly samples inside the pNMR probe by $\pi/2$ rad with respect to the mostly vertical magnetic field from the storage ring. By virtue of the Larmor precession of spins under the influence of an external magnetic field, the magnetization rotates around the storage ring's B-field with a Larmor frequency $\omega_L = geB/2m$ until relaxing back to equilibrium, parallel to the external field. The 'free induction decay' signal correspond-

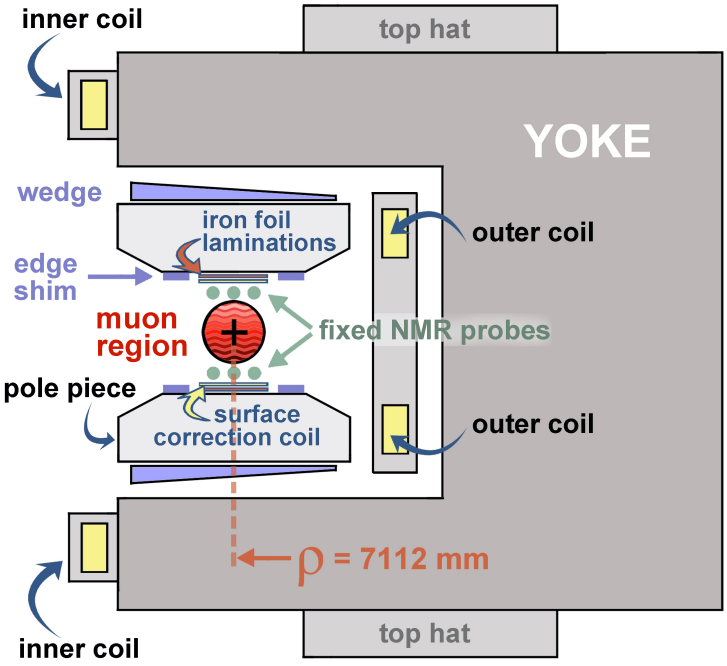

Figure 1.9: Cross section of the storage ring magnet. The yoke is made of six layers of magnet steel with an open side to allow for positrons from muon decay to reach the inner side of the ring. A total of twelve of these sections assembled together provide a continuous and ultra-uniform magnetic field within the poles gap, where the stored muon beam revolves for several thousands of turns. Passive and active shimming via surface currents, thousands of pieces and around the muon storage region, and other movable pieces of the storage-ring magnet allow to calibrate and further reduce inhomogeneities of the magnetic field in the storage region to ppb levels [6].

Table 1.2: Magnet parameters of the g-2 storage ring.

Parameter	Value
Design magnetic field	1.45 T
Design current	5200 A
Design orbit radius	7.112 m
Nominal gap between poles	18 cm
Iron mass	682 tons
Magnet self inductance	0.48 H
He-cooled lead resistance	6 μΩ
Warm lead resistance	0.1 mΩ
Yoke height	157 cm
Yoke width	139 cm
Pole Width	56 cm

ing to this relaxation is read out by pickup coils embedded inside the pNMR probes.These signals provide a 10 ppb-precision measurement of the Larmor precession frequency which in turn yields the magnetic field at the location of the material sample within the probe.

A set of 17 pNMR probes distributed across a trolley as shown in Fig. 1.10 periodically measures the magnetic field in the storage region of the ring. When the Muon Campus at Fermilab is not delivering beam to the g-2 experiment, rails around the storage ring guide the trolley around the storage region to capture local variations of the magnetic field. For the conversion from petroleum jelly to free proton Larmor frequencies and calibration of the trolley probes, a 'plunging' pNMR probe with water as the proton sample is used [45]. between Additionally, 378 fixed probes distributed along the ring's azimuth (see Fig. 1.9) are constantly taking data, even during muon beam storage, to interpolate data recorded by the trolley.

1.3 Beam Dynamics: Requirements

1.3.1 Polarization and beam production performance

It is essential for the muon g-2 experiment to control and minimize the statistical and systematic uncertainties of the anomalous magnetic moment measurement. The need of sufficient number of positrons that compose the ω_a histogram (Fig. 1.6) to deliver a ω_a measurement to a statistical precision of 100 ppb or less sets the statistical minimum limit. In a method with energy thresholds as in Eq. (1.25), such statistical error $\delta\epsilon$ [35] is subject

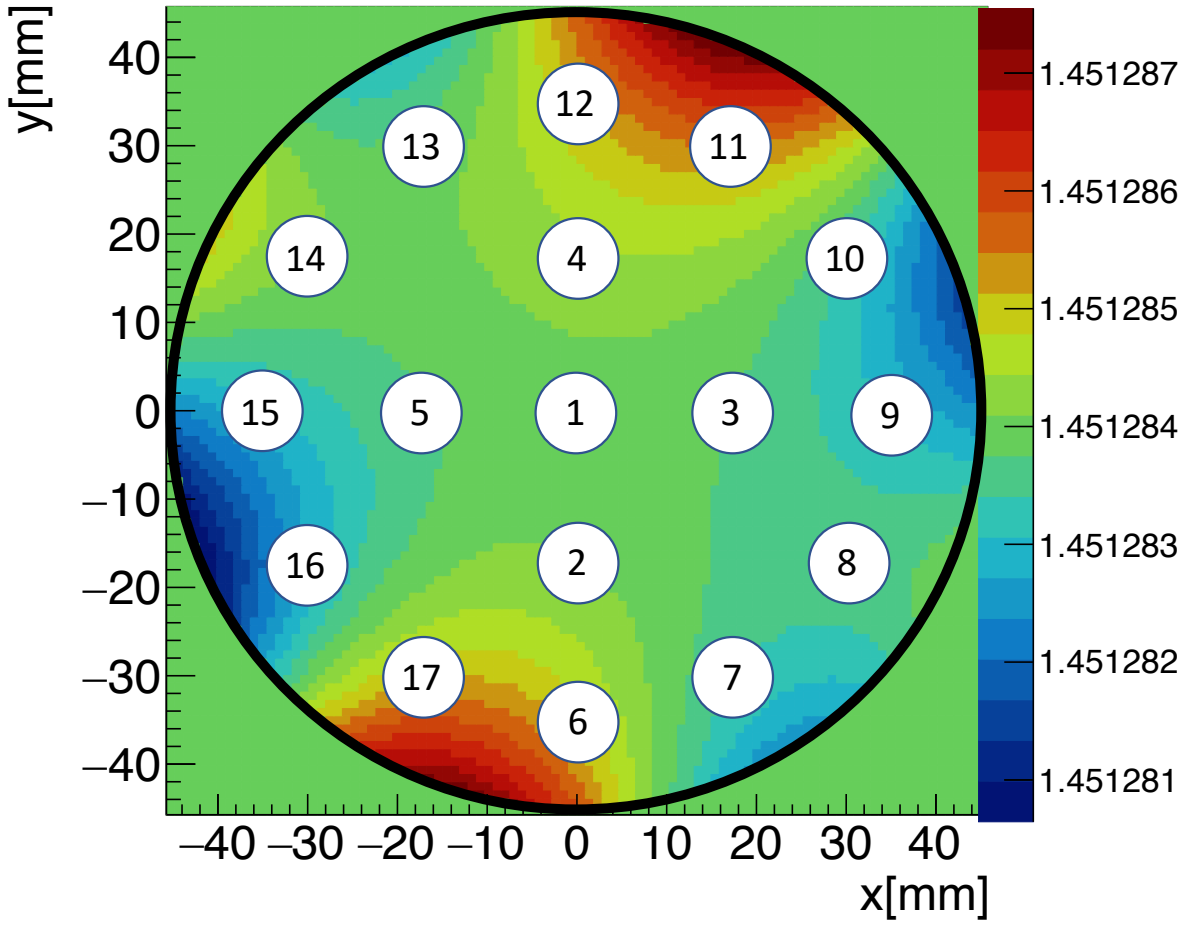

Figure 1.10: Array of pNMR probes installed in the trolley (white circles), used to periodically measure the magnetic field in the storage region. Fixed probes installed above and below the storage region (shown Fig. 1.9) are used to interpolate the magnetic field data between trolley runs. The heat map represents a typical sample of the magnetic field from trolley data fitted with a multipole expansion, within the storage region and averaged azimuthally along the ring. The color legend units are Tesla.

to the beam polarization $\mathcal{P}$ of the injected muon beam via the asymmetry (A in Eq. (1.26)):

$$\delta\epsilon = \frac{\sqrt{2}\omega_a}{\tau_\mu\sqrt{NA^2}}. \tag{1.27}$$

As explained in Subsec. 2.3.2, the muon beam production across the Muon Campus at Fermilab exploits parity violation in the $\pi \to \mu\nu_\mu$ decay which, constrained by the momentum acceptance, transports longitudinally polarized muons through the beamlines. A highly-polarized muon beam is therefore expected to be injected into the storage ring. However, while muons exponentially decay at different locations of the beam delivery system, the coupling between the muon production location and beamline elements distribution along the Muon Campus can potentially affect the resulting beam polarization. These latent imprints on $\mathcal{P}$ and other possible sources of de-polarization are presented in Ch. 2 as well as the beam production performance, to which the stored positrons rate in the storage ring is bounded.

From the systematic-errors front, correlations between beam polarization and other dynamic variables can lead to apparent ω_a shifts, caused by the so-called "g-2 Phase" φ_0 in the functional form "$f(t)$" used to extract the anomalous precession frequency from data (see Eq. (1.25)):

$$f(t) \propto \cos\left(\omega_a t + \varphi_0\right). \tag{1.28}$$

The g-2 phase represents the overall muon beam angle between spin and momentum at injection time. Besides positron detection effects, stored muons that do not contribute to an expected calorimeter signal—due to them being lost by hitting instrumentation during data collection—can potentially introduce a time-dependent g-2 phase. If the individual phases of these "lost muons" are not equal to each other and, additionally, are correlated with an

observable Z, the corresponding apparent ω_a can be quantified:

$$\Delta\omega_a(t) = \frac{d\varphi_0(t)}{dt} = \frac{d\varphi_0}{d\langle Z\rangle}\Big|_{t_0} \frac{d\langle Z(t)\rangle}{dt}. \tag{1.29}$$

Lost muons favoring specific values of Z yield a nonzero $\Delta\omega_a(t)$ if $d\varphi_0/d\langle Z\rangle \neq 0$. Section 4.2 presents the contribution to this systematic error by taking the muons momentum as the observable Z in data-driven simulations of the beam delivery system and storage ring.

1.3.2 Beam characterization along the entire storage ring

The g-2 straw tracker detectors permit to precisely determine several properties of the beam circulating the storage ring (see Subsec. 1.2.2). With the broad transverse acceptance at the tracker locations, small spatial resolution of a few milimeters, and a time resolution of less than 3.4 ns, it is possible to measure the beam widths, centroids, and longitudinal decoherence on a run-by-run basis. Nevertheless, such information is limited to the locations where the two trackers are placed, as shown in Fig. 1.11. For this reason, in order to characterize the beam behavior along the whole azimuthal extension of the ring for quantifying beam-dynamics-related systematic errors, a dedicated model of the storage ring is pertinent for this purpose.

The g-2 storage ring is a weak focusing system in which a mismatched muon beam is injected, occupying most of the 45 mm storage aperture. Moreover, in addition to coherent betatron oscillations due to beam-ring mismatch, the ppm-level inhomogeneities of the vertical magnetic field and sub-mm misalignments of electrode plates used for vertical beam focusing originate milimetric azimuth-dependent distortions of the closed orbit around which the beam revolves the ring. In principle, these features altogether with $\sim 2\%$ beam width

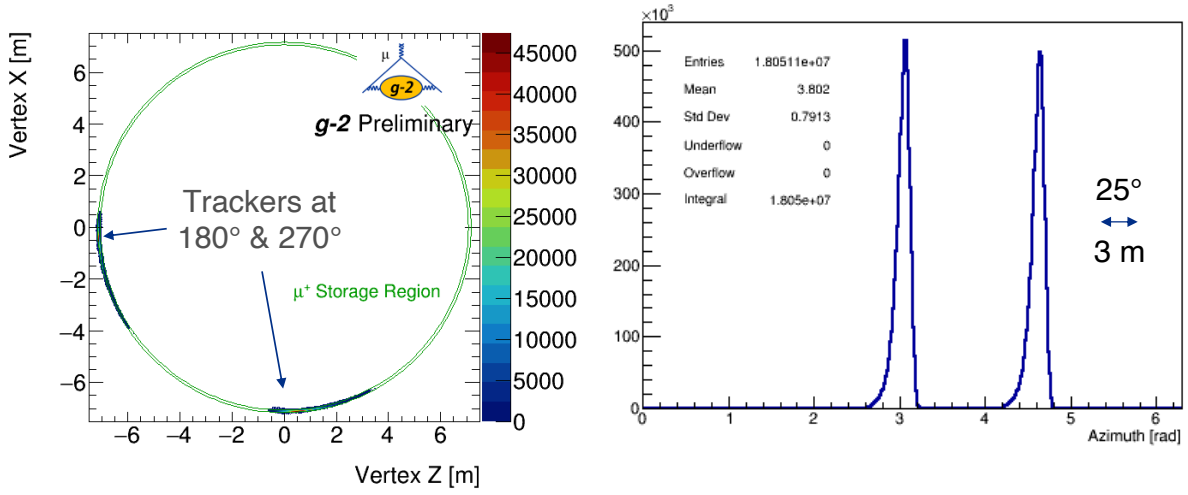

Figure 1.11: Horizontal (left) and longitudinal (right) acceptances of the two g-2 straw tracker detector stations (Ref. [7]). Each tracker station reads decay vertexes along azimuthal segments of $\approx$ 0.4 mrad, whose maximum acceptance peaks are positioned at about 1 m downstream the modules.

longitudinal variations of hundredths of microns across the ring do not significantly affect the g-2 measurement to first order. However, due to the tight systematic-errors budget of the experiment, the aforementioned transverse variations of the stored muon beam need to be accounted for.

In particular, the coupling between the g-2 phase and detection acceptance [16] introduces a phase dependence on time when the beam moments exhibit slow-trend behavior (specially the beam vertical width due to the calorimeter muon efficiency). During the first official run of the experiment, as a consequence of damaged instrumentation this was the case [46]. A method that takes the beam profile measured by the straw tracker and calorimeter detectors as input and provides a full reconstruction of the time-dependent electric guide fields during the first g-2 run is elaborated in Ch. 4. With the reconstructed fields and the storage ring model explained in Ch. 3, a full characterization of the muon beam is delivered, which is critical to the determination of the aforementioned largest systematic uncertainty for the

first g-2 official results.

Another relevant case is the magnetic field that plays a role in the anomalous magnetic moment (see Eq. (1.20)). In E821, it was calculated by convoluting the muon distribution moments with a representative multipole expansion of the magnetic field, azimuthally averaged and from representative NMR trolley runs [33]. Though this approach does not account for the entanglements between azimuthal variations of the muon distribution and the magnetic field, the associated systematic error is negligible compared to the statistical error from E821 [47]. But for the g-2 experiment at Fermilab, the target systematic uncertainty of the muon-weighted magnetic field is 10 ppb or less, demanding a different approach. In Ch. 4, a method to calculate the magnetic field experienced by muons at E989 is presented, altogether with related systematic-error studies.

1.3.3 Momentum spread and vertical motion

In terms of the magnetic ($\vec{B}$) and electric ($\vec{E}$) guide fields within the storage ring, the anomalous precession frequency ω_a is the precession frequency of the muon beam polarization relative to its momentum in the lab frame [48]:

$$\omega_a = |\langle \vec{\omega}_S - \vec{\omega}_C \rangle| = \left| -\frac{e}{m_\mu} a_\mu \langle \vec{B} \rangle + \frac{e}{m_\mu} a_\mu \left\langle \left(\frac{\gamma}{\gamma+1} \right) (\vec{\beta} \cdot \vec{B}) \vec{\beta} + \left(1 - \frac{1}{(1+\delta)^2} \right) \frac{\vec{\beta} \times \vec{E}}{c} \right\rangle \right|, \tag{1.30}$$

where $\vec{\omega}_S$ and $\vec{\omega}_C$ are the spin and cyclotron frequencies, respectively, γ the Lorentz factor, $\vec{\beta}$ the velocity in speed-of-light units, and δ the momentum offset relative to magic momentum $p_0 = m_\mu c/\sqrt{a_\mu}$. Under conventional g-2 storage ring settings, ω_a is treated as the first term on the right-hand side of Eq. (1.30)—aka (g-2) frequency—with the explicit addition of the so-called "E-field" (C_e) and "pitch" (C_p) corrections, whose standard expressions are derived

from Eq. (1.30) [35, 49] (see Fig. 1.12):

$$\omega_a = \omega_{a0}\left(1 + \left\langle \Delta\omega_a^E \right\rangle + \left\langle \Delta\omega_a^B \right\rangle\right) \approx \omega_{a0}\left(1 - C_e - C_p\right), \tag{1.31}$$

where $\omega_{a0} = -(e/m_\mu c)a_\mu\langle\vec{B}\rangle$ and $\vec{B}$ is the mainly-vertical magnetic field.[3] In Eqs. (1.30)

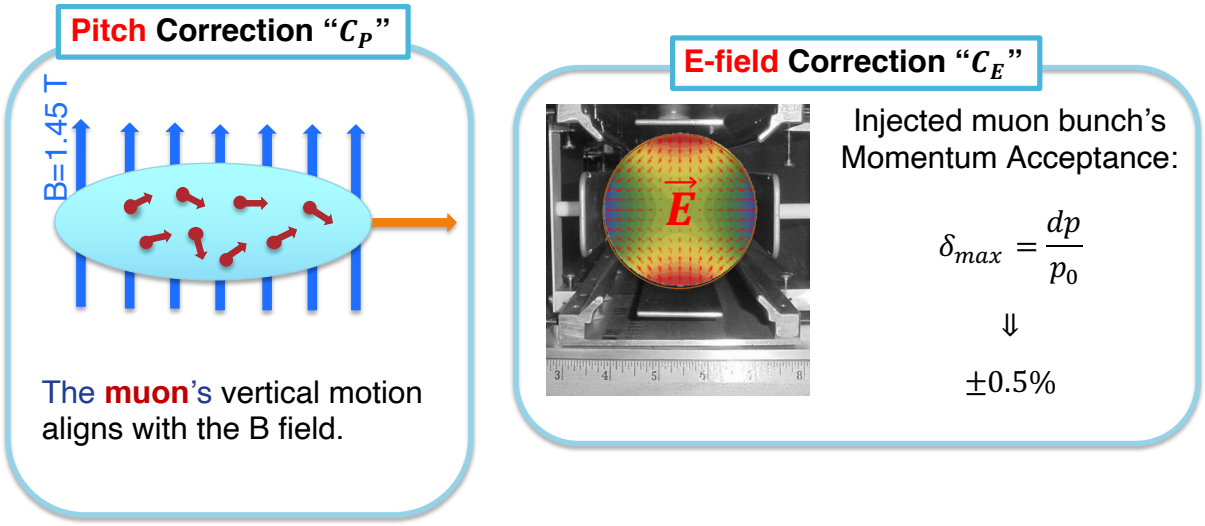

Figure 1.12: Illustrations of the pitch (left) and E-field (right) corrections. The pitch correction emerges mainly from the muon's motion partially parallel to the magnetic field in the lab frame; the standard pitch correction becomes non-negligible at E989 for the typical pitch-angle scales (i.e., ~ 2 mrad vertical oscillations relative to the horizontal mid-plane) that take place in the storage ring. In the E-field correction, the spin of muons away from the magic momentum $p_0 = m_\mu c/\sqrt{a_\mu}$ experiences rotations mostly contained in the transversal plane as expressed in the last term of Eq. (1.30). The momentum acceptance $\delta \sim 0.5\%$ and the electric field of $E_y \sim 6$ kV/cm, at 4 cm from the ideal orbit, provided by the Electrostatic Quadrupole stations (ESQ) contribute to an overall vertical precession frequency of about 400 ppb opposite to the nominal (g-2) frequency.

and (1.31), the delimiters $\langle\rangle$ denote quantities averaged over the stored muons.

At present, the amount e/m_μ in Eq. (1.31) contributes to an uncertainty of about 26 ppb [1], while the magnetic field experienced by muons at E989 is expected to be measured to a precision of 70 ppb or less. On the other hand, the E-field and pitch corrections lower the

[3] indirect ω_a biasing from the g-2 time dependencies—due to muon loss "C_{ml}" and phase-acceptance "C_{pa}" effects introduced in this section—can also be added to Eq. (1.31) similar to C_e and C_p.

nominal frequency ω_a by a non-negligible level of the order of tenths of ppm. The standard formulae of these corrections are given by [35, 49]

$$C_e = \frac{n_0 \beta_0^2}{1 - n_0} 2 \left\langle \delta^2 \right\rangle \tag{1.32}$$

and

$$C_p = \frac{n_0}{2\rho_0^2} \left\langle y^2 \right\rangle, \tag{1.33}$$

where the subscript 0 denotes the nominal case of a muon with magic momentum and no betatron amplitudes. The field index $n_0 = -(39/90)(\rho_0/vB_y)\partial E_y/\partial y$ is the effective field index commonly used in the muon g-2 collaboration [50], which is proportional to the nominal orbital radius $\rho_0 \approx 7.112\,\mathrm{m}$ and the axial focusing gradient $\partial E_y/\partial y$. Figures 1.13 and 1.14 illustrate typical relative-momentum and vertical beam spreads, which yield corrections in the order of $C_E \to \mathcal{O}(400\,\mathrm{ppb})$ and $C_p \to \mathcal{O}(200\,\mathrm{ppb})$. However, several assumptions are

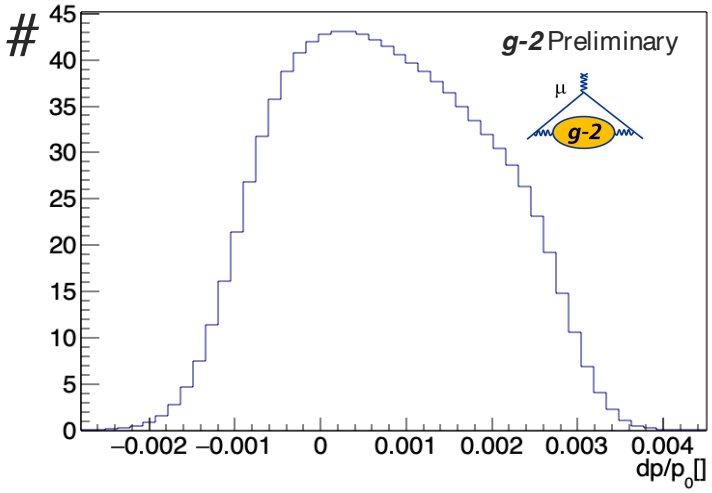

Figure 1.13: Sample of the muon spread distribution fro Fast-Rotation analysis.

needed to be imposed in order to get the standard equations (1.32) and (1.33), including

- continuous electrostatic quadrupole stations (and thus no fringe fields),

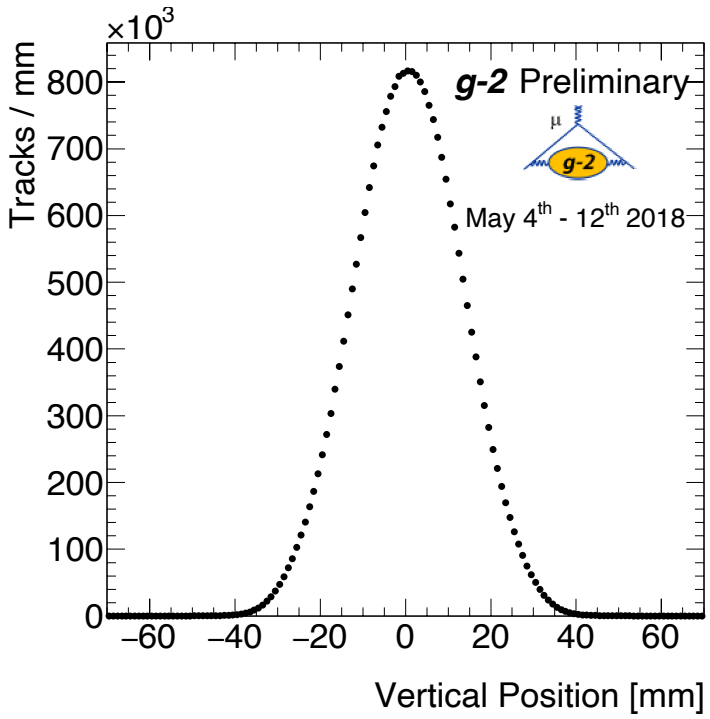

Figure 1.14: Vertical beam profile from the tracking detection system.

- linear guide fields,
- harmonic transverse motion, and
- orbital muon frequencies beyond the ballpark g-2 frequency.

For the purpose of validating the standard E-field/pitch corrections and assessing any associated systematic errors, direct calculations of $omega_a$ were carried out via nonlinear orbital and spin tracking (see Ch. 4). Several of the assumptions to derive C_e and C_p were also tested with simulated storage ring configurations.

Another effect from the beam-dynamics front that introduces a considerable systematic correction to C_e is the momentum-time correlation [51]. By construction, the overall momentum spread in Eq. (1.32) is obtained from the Fourier transform of the intensity signal (see Fig. 1.15) detected by calorimeters. When the relative time-of-flight and momentum

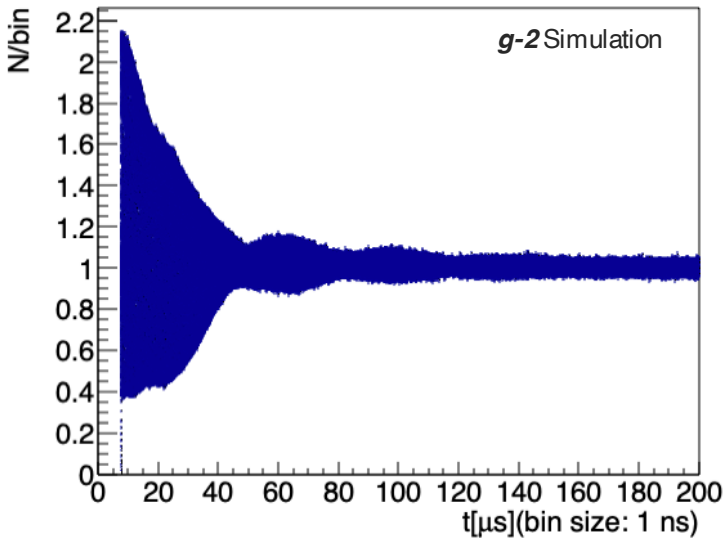

Figure 1.15: Beam transverse intensity from realistic storage ring simulations, referred as the fast-rotation signal. Due to momentum spread, the range of cyclotron frequencies causes high- and low- momentum muons to recombine as the beam decoheres in the longitudinal direction. The cyclotron frequencies distribution is recovered from a Fourier transform, which yield the momentum spread distribution (see sample in Fig. 1.13) for the E-field correction.

coordinates of the muon beam are uncorrelated at the start time of the Fourier analysis, all the cyclotron frequencies are equally weighted in the transformation as expected. Alas, a momentum-time correlation breaks the symmetry which potentially distorts the momentum spread reconstruction for C_e. Correlations between momentum and time-of-flights in the stored beam are a consequence of an imperfect injection kicker; the under-kicking of high-momentum muons out of sync with the kicker-strength peaks favors them to end up getting stored. The ringing of the kicking signal also dictates which muons are stored. With a detailed modeling of the Run-1 injection kicker as well as beam collimation and realistic parameters of the storage ring, the momentum-time distribution—currently unknown—is calculated (Subsec. 3.5.4) and allows for C_e systematic correction quantifications.

Chapter 2

The Beam Delivery System (BDS)

2.1 Introduction

The number of recorded high energy positrons from muon decay in the g-2 storage ring at E989 is required to increase by a factor of 20 with respect to E821. The Fermilab Muon Campus E989 beam delivery system (BDS), which is a set of 1 km-long beamlines between the pion production target and the entrance of the Muon g-2 Storage Ring (SR) downstream, is designed to meet the statistical goal and deliver $(0.5–1.0) \times 10^5$ muons to the storage ring per 10^{12} protons that arrive to the pion production target.

On the other hand, the relative statistical uncertainty in the experimental a_μ is inversely proportional to the muon beam polarization (see Eq. (16.6) in Ref. 35). Thus, it is worth to study the effect of nonlinearities and perform spin dynamics simulations. In addition, due to the momentum acceptance of about $\pm 0.5\%$ of the storage ring, it is of interest to numerically evaluate the dynamical properties of the muon beam as it is delivered to the storage ring.

Motivated by these reasons, a model of the E989 beamlines [52] was developed to reproduce numerical simulations of the muon beam's statistical performance and dynamical behavior including spin using COSY INFINITY [53]. In particular, the transport efficiency of secondary protons, pions, daughter muons from pion decay, and muons produced right at the entrance of the E989 beamlines downstream the pion production target is addressed

with these high statistical simulations. Nonlinear effects due to standard fringe fields, up to 4th-order beam dynamics, spin dynamics, beam collimation, and misalignments of the multiple BDS beamline elements are examined.

This chapter begins with a description of the Muon Campus E989 beam delivery system. Then, details of the beam dynamics simulations throughout the E989 beamlines from the production target to the storage ring entrance and beam performance results modeling nonlinear effects are described.

2.2 The E989 Beam Delivery System (BDS)

The main purpose of the E989 beamlines analyzed in simulations, depicted in Fig. 2.1, is to deliver a clean muon beam with "magic momentum" $p_0 \sim 3.094\,\mathrm{GeV}/c$ to the storage ring. Batches of four bunches made of 10^{12} protons each are directed to an Inconel-600 "pion production" target located at the AP0 target hall, from which positive secondary particles emerge. The main components and beamline sections of the Fermilab Muon Campus E989 beam delivery system (BDS) are the aforementioned target station, the M2/M3 beamlines, the Delivery Ring, and the M4/M5 beamlines, described next.

2.2.1 The pion production target station

The Pre-Accelerator, Linac, Booster, MI-8 line, and Recycler as part of the Fermilab Accelerator Complex deliver $8.9\,\mathrm{GeV}/c$ protons to the Pion production target station, which is the already existing target station that was in operation for antiproton production prior to the Tevatron Collider shutdown, but repurposed for pion production. Figure 2.2 illustrates the proton pulses per cycle. A magnetic quadrupole triplet focuses the proton pulses upstream

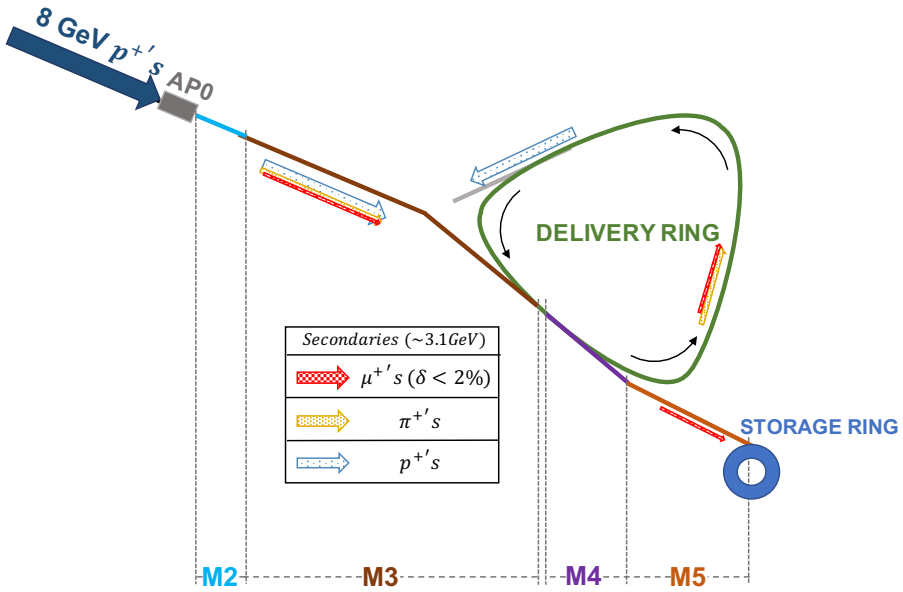

Figure 2.1: A schematic layout of the beam delivery system (BDS). Secondary particles (mostly pions, muons, and protons) downstream the target station at AP0 are canalized through the M2/M3 lines and injected to the Delivery Ring (DR) where protons are discarded and most of the remaining pions decay after four turns. A cleaner beam of mostly muons is extracted to the M4/M5 lines and ultimately delivered to the Muon g-2 Storage Ring (SR).

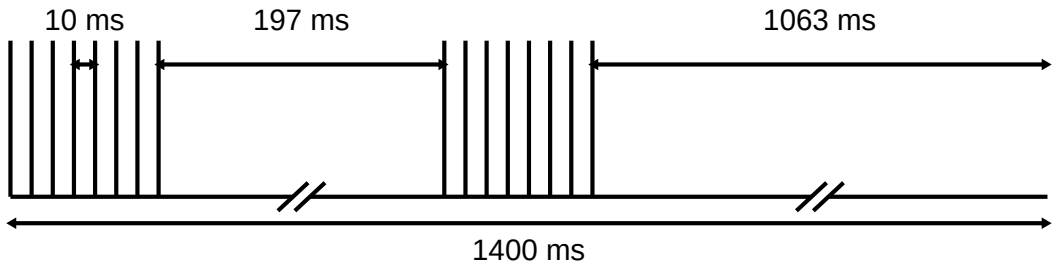

Figure 2.2: Time structure of the 10^{12}-, 120 ns-pulse train impinging the production target per cycle [8].

the production target to a transverse size of about 150 μm to minimize beam loss [54]. 30 cm downstream the "Inconel 600" production target –an alloy of iron, chromium, and nickel– a 160 kA current flowing through a lithium cylinder provides a 232 T/m strong magnetic gradient around the optical axis to transversely focus the secondary particles that emerge from the target. Thereafter, a pulsed magnet "PMAG" with a field of 0.53 T selects 3.115 GeV/c ±10% positive particles and bends them 3 ° up, towards the 50 m long M2 line.

2.2.2 M2/M3 beamlines

Encompassing a total of 50 m of beamlines, starting from the lithium lens and leading to the intersection with the M3 line further downstream, the M2 beamline collects the pions separated by the PMAG and is designed to transport magic-momentum muons with momentum and transverse acceptance of ±2% and 40 mm.mrad, respectively, from pion decay. The M3 beamline, a $\sim$ 230 m section of mainly focusing/defocusing quadrupole magnets and bending insertions, shares the same goal as the M2 line in order to deliver a beam composed of mostly pions, muons, protons that bypass the production target, and other secondary particles to the Delivery Ring. The optical lattice of the M2/M3 beamlines is shown in Fig. 2.3, which altogether with the beamline apertures and post-target beam conditions dictate the number of particles that enter the Delivery Ring (see Fig. 2.4). The beta, β, and dispersion, η, functions are calculated with COSY INFINITY [53] by transporting the Twiss parameters α_0, β_0, and γ_0 0.723 m upstream the PMAG as follows:

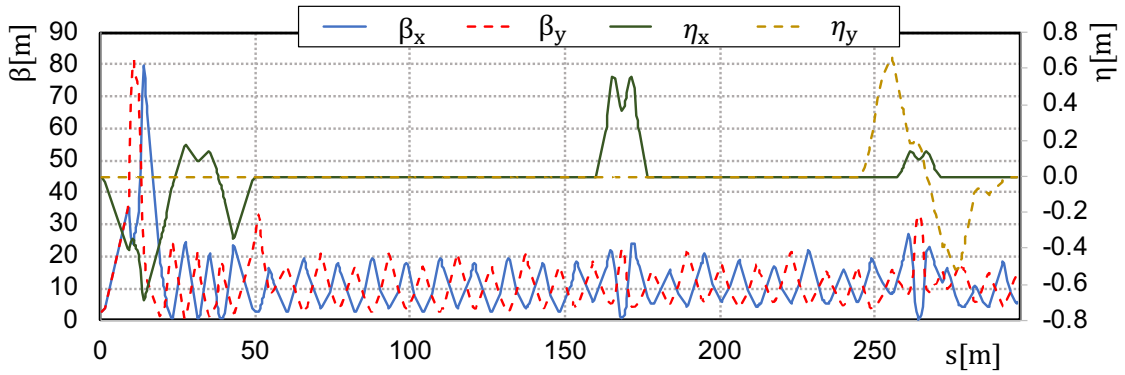

Figure 2.3: M2/M3 lattice functions. The horizontal dispersion (green solid line) originated by the pulsed magnet at the start of the M2 line is canceled out by a switch dipole 50 m downstream, whose large pole width accommodates the beam to enter the M3 line. At around 170 m, the 100 m FODO is interrupted by two horizontal bends (18.3 °) to align the optical axis with the AP3 line and a quadrupole triplet to cancel out horizontal dispersion. On the right-hand side of the plot, the optical functions reflect the geometric and optical matching section to transport the beam to the Delivery Ring, elevated 4 ft above from M3.

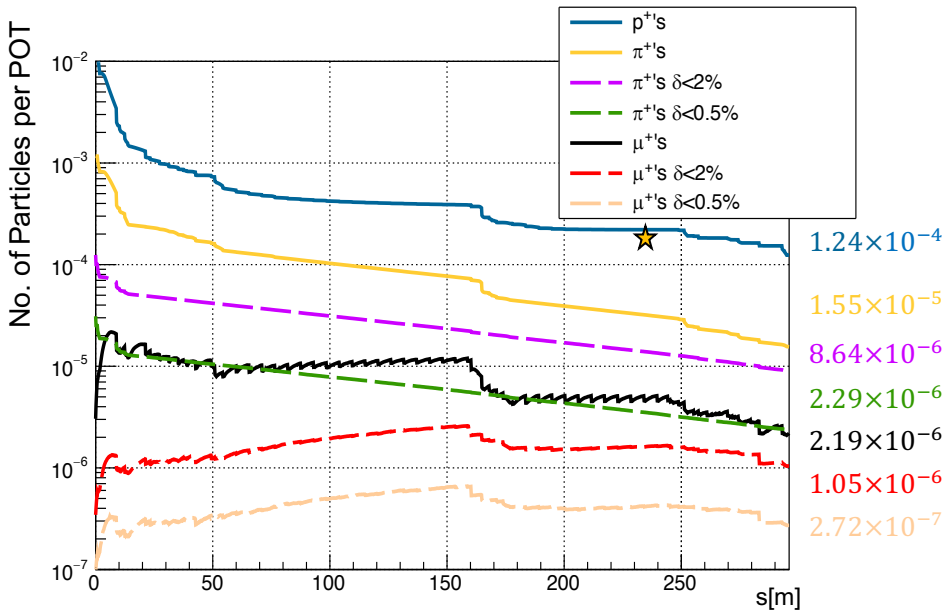

Figure 2.4: Number of muons, μ^+, pions, π^+, and protons, p^+, per proton on target (POT) along the M2/M3 beamlines. The horizontal axis represents the longitudinal distance of the optical axis. Main muon losses of about 11% and 20% take place at the 18.5 ° horizontal bend ($s \sim 160.0$ m) and along the vertical injection upstream the DR ($s \sim 280.0$ m), respectively. The star-shaped marker around $s \sim 235$ m depicts the number of total particles per POT from measurements (Ref. 9, Fig. 3).

$$\begin{pmatrix} \beta_x(s) \\ \alpha_x(s) \\ \gamma_x(s) \end{pmatrix} = \begin{pmatrix} (x|x)^2 & -2(x|x)(x|x') & (x|x')^2 \\ -(x|x)(x'|x) & (x|x)(x'|x') + (x'|x)(x|x') & -(x|x')(x'|x') \\ (x'|x)^2 & -2(x'|x)(x'|x') & (x'|x')^2 \end{pmatrix} \begin{pmatrix} \beta_{x0} \\ \alpha_{x0} \\ \gamma_{x0} \end{pmatrix} \tag{2.1}$$

The vertical Twiss parameters (denoted with subscript y) are transformed in a similar way as in Eq. (2.1) [55], where the variable s denotes the longitudinal distance along the optical axis relative to the coordinates of the initial Twiss parameters. The elements inside the transformation matrix are linear components of the transfer map (see Eqs. (2.2) and (2.3)), calculated from the beamline settings during Run-1 of the muon g-2 experiment.

$$\begin{pmatrix} x(s_2) \\ x'(s_2) \\ \delta \end{pmatrix} = \begin{pmatrix} (x|x) & (x|x') & (x|\delta) \\ (x'|x) & (x'|x') & (x'|\delta) \\ 0 & 0 & (\delta|\delta) \end{pmatrix} \begin{pmatrix} x(s_1) \\ x'(s_1) \\ \delta \end{pmatrix} \tag{2.2}$$

$$\begin{pmatrix} y(s_2) \\ y'(s_2) \\ \delta \end{pmatrix} = \begin{pmatrix} (y|y) & (y|y') & (y|\delta) \\ (y'|y) & (y'|y') & (y'|\delta) \\ 0 & 0 & (\delta|\delta) \end{pmatrix} \begin{pmatrix} y(s_1) \\ y'(s_1) \\ \delta \end{pmatrix} \tag{2.3}$$

In Eqs. (2.2) and (2.3), (x, x') and (y, y') are the horizontal and vertical canonically conjugated pairs in which the map is symplectic[1]. The variable $\delta = \Delta p/p_0$ symbolizes the momentum offset. Due to the dominant absence of electrostatic fields along the BDS, δ is a constant of motion. On the other hand, the correspondance between dispersion functions

[1] In COSY INFINITY notation, $x' \equiv a$ and $y' \equiv b$ [56].

and linear matrix components is as follows:

$$\eta_x = (x|\delta) \quad , \quad \eta_y = (y|\delta). \tag{2.4}$$

2.2.3 The Delivery Ring (DR)

At the end of the M3 line, a series of magnets involving a C-magnet, a pulsed magnetic septum dipole, and kicker modules inject the beam to the Delivery Ring (DR) after a vertically upward bend of about 5.7 °. Through the 505 m of circumference of the DR, previously used as a debuncher ring and now reconditioned for the muon g-2 experiment, the remaining pions have enough time to decay into mostly muons as they circulate four times before being extracted into the M4 line (see Fig. 2.5). The DR also allows protons to longitudinally separate from the other lighter particles by a rate of 75 ns per turn [54]; this feature lets a 180 ns rise-time kicker within the DR to safely remove the protons after the fourth turn. The optical functions β_x, β_y, η_x, and η_y of the DR using COSY INFINITY are shown in Fig. 2.6. An arrangement of FODO cells fills all the sections of the DR, interrupted by a series of 22 rectangular magnets at each of the three-fold symmetric sections from which horizontal dispersion and spin-momentum beam correlations are originated. The betatron tunes in the DR are approximately equal to 9.78 in both horizontal and vertical directions, whereas the associated chromaticity of the DR sections is balanced by sextupole magnets.

2.2.4 M4/M5 beamlines

After four turns around the Delivery Ring, a system of two kicker magnets at a bending-free section of the DR and parallel to the M3-line end extracts the beam radially outwards into the

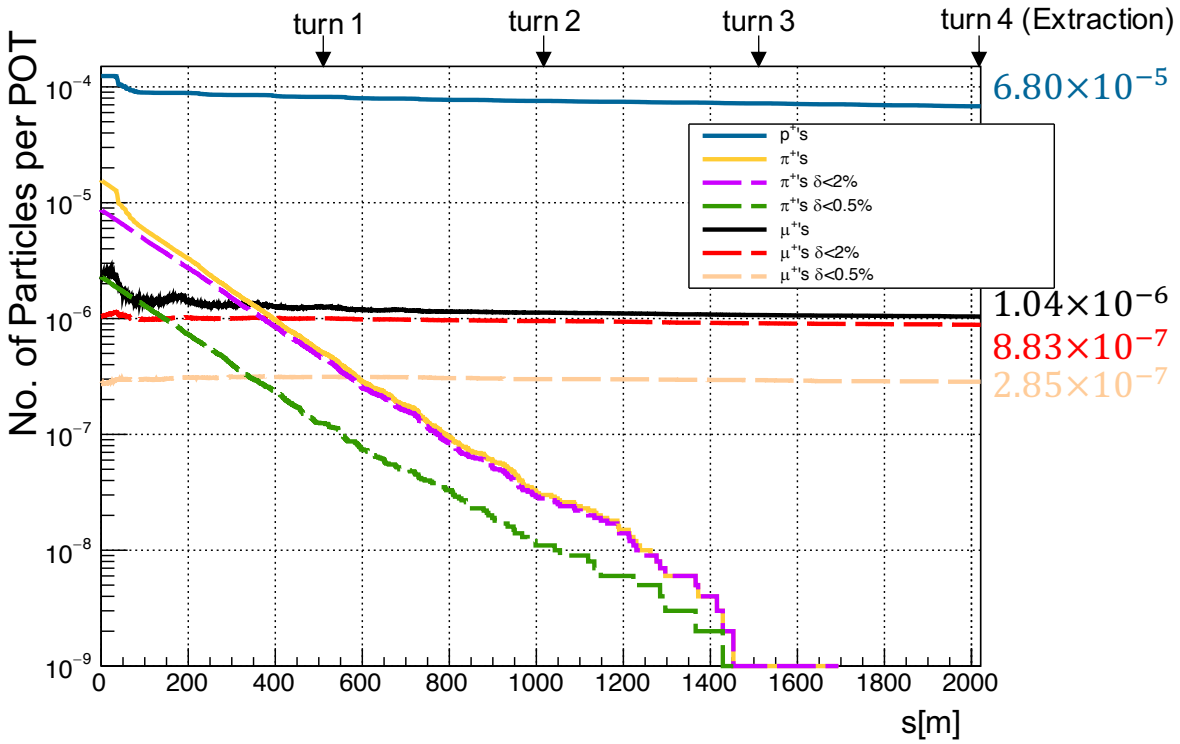

Figure 2.5: Number of muons, μ^+, pions, π^+, and protons, p^+, per proton on target (POT) along four turns around the Delivery Ring. The design momentum acceptance of 2% reveals naturally in beam tracking simulations when accounting for the beamline apertures present in the DR. All pions decay prior to the third turn along the DR.

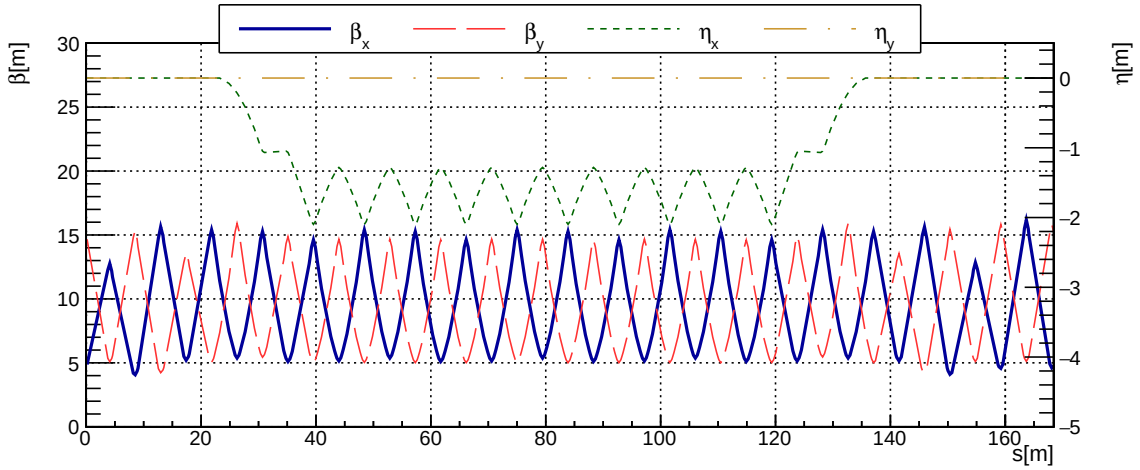

Figure 2.6: Optics functions at one three-fold symmetric section of the delivery ring (DR) where the longitudinal distance of the beamline is shown in the horizontal axis. Fringe fields modeled in simulations change the beta functions, β_x and β_y, by less than 3%.

M4 beamline. The beam is further bent upwards with a set of three vertical bending magnets to reach a final elevation of 0.81 m with respect to the Delivery Ring. 30 m downstream, a beam composed of mostly $|\delta| < 2\%$ muons (see Fig. 2.8) crosses the last 100 m of the BDS, i.e. the M5 beamline. Around $s \sim 70$ m in Fig. 2.8, the radial dispersion introduced by horizontal bending magnets (27.1 ° deflection) to align the beam towards the muon g-2 storage ring entrance is shown. At the end of the M5 beamline, four tunable section with four quadrupole magnets provides the right configuration to maximize the stored beam fraction [57].

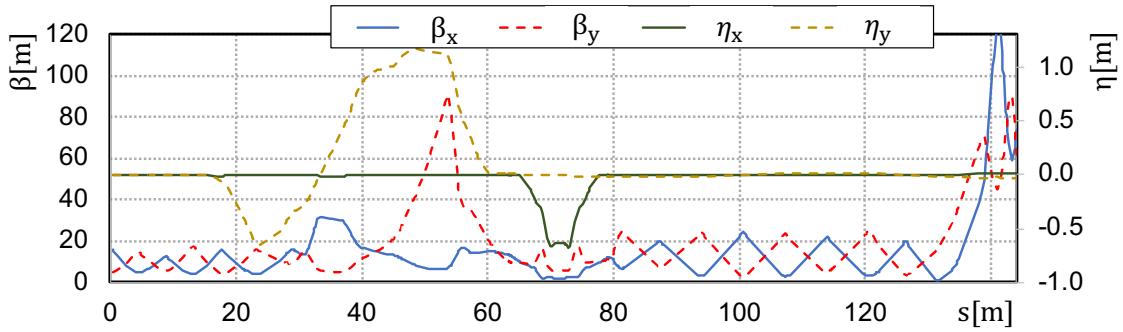

Figure 2.7: M4/M5 lattice functions calculated with COSY INFINITY. The design of the M4/M5 beamlines favors losses minimization.

2.3 Realistic Modeling of the BDS

With a package dedicated to the design and analysis of particle optical systems as part of COSY INFINITY [53], high-order transfer maps $\mathcal{M}$ calculated with an 8th order Runge-Kutta integrator and Differential-Algebraic (DA) methods to solve the beam optics Ordinary Differential Equations (ODEs) are prepared to recreate the beam dynamics along the BDS. By defining the secondary particles beam downstream the pion production target as an array

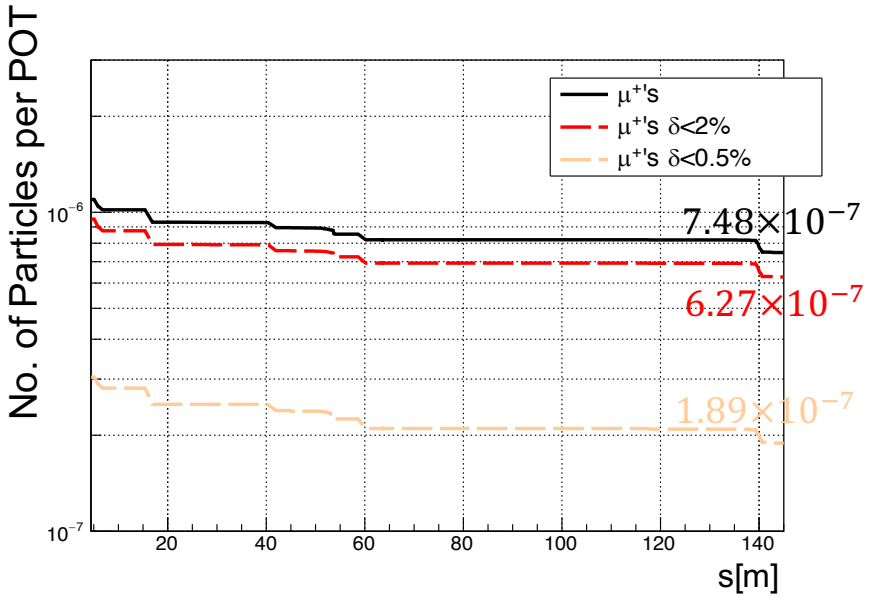

Figure 2.8: Number of muons, μ^+, per proton on target (POT) along the M4/M5 beamlines. The pale-rose dashed line depicts muons within the muon g-2 storage ring momentum acceptance. For g-2 runs posterior to Run 1, the insertion of passive wedge absorbers in the BDS maximized the muons population within $|\delta| < 0.5\%$ to increase the stored beam fraction [10].

of scaled coordinates

$$\vec{z} = (x, x', y, y', l, \vec{\delta}), \tag{2.5}$$

BDS beam tracking simulations are performed via

$$\vec{z_f} = \mathcal{M}(\vec{z_0}). \tag{2.6}$$

In Eq. (2.6), the transfer map can represent a beamline element (e.g. magnetic sextupole, drift), a segment, or a set of beamline elements of the BDS, which transforms the vector $\vec{z}$ from the longitudinal position s_0 to s_f. In Eq. (2.5), x and y are the horizontal and vertical positions relative to the optical axis; $x' = p_x/p_0$ and $y' = p_y/p_0$, where p_0 is the reference momentum (in this case the magic momentum) and p_x, p_y correspond to the momentum

perpendicular to the optical axis; and $l = -(t - t_0)v_0\gamma_0/(1 + \gamma_0)$.[2] For BDS beam tracking simulations using COSY INFINITY, the vector $\vec{\delta}$ contains the kinetic energy and rest-mass offsets (δ_K and δ_m, respectively) relative to the magic-momentum muon.

Tracking simulations of the E989 beamlines start with an initial distribution at the exit of the pion production target from a MARS [58] simulation of 10^9 protons on target [59]. Protons, positive pions, and positive muons from the target and pion decay (see 2.3.2) are tracked down and collimated by the BDS beamline physical apertures (see 2.3.1). Simulations of the BDS were carried out in parallel cumputing on clusters from the Department of Physics and Astronomy at Michigan State University.

2.3.1 Beamline elements

The transfer maps $\mathcal{M}$ contain the Taylor coefficients to track each of the z_i components of a ray $\vec{z}$ as follows:

$$z_{i,f} = \sum_{j_1 \cdots j_7} (z_i \,|\, x^{j_1}\, x'^{j_2}\, y^{j_3}\, y'^{j_4}\, l^{j_5}\, \delta_K^{j_6}\, \delta_m^{j_7}\,)\, x_0^{j_1}\, x_0'^{j_2}\, y_0^{j_3}\, y_0'^{j_4}\, l_0^{j_5}\, \delta_K^{j_6}\, \delta_m^{j_7}\,. \tag{2.7}$$

The summations go from $j_i = 0$ up to the chosen map order. As an example, Table 2.1 displays the Delivery Ring transfer map (without fringe fields accounted for).

To assess the statistical performance of the beam across the BDS, transfer maps representing $\sim 20\,\text{cm}$ segments of beamline elements are prepared. In between these sections, specific routines eliminate particles with spatial coordinates beyond the transverse apertures of the BDS beamline elements. Beamline apertures of the BDS take multiple shapes, e.g., circular,

[2] the subindex "0" corresponds to a reference ray with $\vec{z} = \vec{0}$, lab-frame speed v_0, time-of-flight t_0, and Lorentz factor γ_0.

Table 2.1: Second-order transfer map of the Delivery Ring. The first six columns correspond to $(x|$, $(x'|$, $(y|$, $(y'|$, $(l|$, whereas the last column indicates $(j_1, j_2, \ldots, j_7)$ in that order. For instance, in the ninth row, first column, the $(x|xx')$ coefficient is displayed.

$(x\|$	$(x'\|$	$(y\|$	$(y'\|$	$(l\|$	$j_1j_2j_3j_4j_5j_6j_7$
5.9525950E-01	2.6487970E-01	0.0000000E+00	0.0000000E+00	2.8760050E-05	1000000
-4.6900250E+00	-4.0703700E-01	0.0000000E+00	0.0000000E+00	-1.8329100E-04	0100000
0.0000000E+00	0.0000000E+00	-1.6020400E+00	2.8708540E-01	0.0000000E+00	0010000
0.0000000E+00	0.0000000E+00	-1.4857920E+01	2.0383330E+00	0.0000000E+00	0001000
0.0000000E+00	0.0000000E+00	0.0000000E+00	0.0000000E+00	1.0000000E+00	0000100
2.5779670E-05	-3.6843670E-05	0.0000000E+00	0.0000000E+00	-7.5443060E+00	0000010
8.7984830E-07	-1.2574580E-06	0.0000000E+00	0.0000000E+00	-8.2662620E-01	0000001
9.3642760E-02	-1.3390570E-01	0.0000000E+00	0.0000000E+00	9.4620480E-02	2000000
-1.1940090E+00	1.7068280E+00	0.0000000E+00	0.0000000E+00	-5.8103630E-01	1100000
3.8058830E+00	-5.4386960E+00	0.0000000E+00	0.0000000E+00	-7.5259510E-01	0200000
0.0000000E+00	0.0000000E+00	-5.3148190E-01	-4.6300560E-01	0.0000000E+00	1010000
0.0000000E+00	0.0000000E+00	-7.2282930E+00	3.1733130E+00	0.0000000E+00	0110000
-1.2017650E+00	2.1644980E-01	0.0000000E+00	0.0000000E+00	6.4741360E-02	0020000
0.0000000E+00	0.0000000E+00	-7.4658000E+00	-3.6324400E+00	0.0000000E+00	1001000
0.0000000E+00	0.0000000E+00	-7.5726850E+01	3.3803910E+01	0.0000000E+00	0101000
-1.8049540E+01	5.3450280E+00	0.0000000E+00	0.0000000E+00	3.2265500E+00	0011000
-5.8702240E+01	3.1994630E+01	0.0000000E+00	0.0000000E+00	1.8204650E+01	0002000
5.4167760E-01	-7.6876660E-12	0.0000000E+00	0.0000000E+00	-1.5090600E-01	1000010
-3.6210540E+00	-6.3519760E-01	0.0000000E+00	0.0000000E+00	9.6209290E-01	0100010
0.0000000E+00	0.0000000E+00	-3.2449130E+00	6.6236000E-01	0.0000000E+00	0010010
0.0000000E+00	0.0000000E+00	-1.0385800E+01	3.8754890E+00	0.0000000E+00	0001010
1.8487210E-02	-2.6237660E-03	0.0000000E+00	0.0000000E+00	-5.1503210E-03	1000001
-1.2358490E-01	-2.1679010E-02	0.0000000E+00	0.0000000E+00	3.2835580E-02	0100001
0.0000000E+00	0.0000000E+00	-1.1074740E-01	2.2606050E-02	0.0000000E+00	0010001
0.0000000E+00	0.0000000E+00	-3.5446260E-01	1.3226870E-01	0.0000000E+00	0001001
-6.7526670E-02	9.6723460E-02	0.0000000E+00	0.0000000E+00	-1.1706210E+00	0000020
-4.6092790E-03	6.6022130E-03	0.0000000E+00	0.0000000E+00	1.0019550E+00	0000011
-7.8671320E-05	1.1268670E-04	0.0000000E+00	0.0000000E+00	-2.4413610E-01	0000002

rectangular, elliptical, and more involved geometries to accommodate the large transverse acceptance for the muon g-2 experiment, as those present in most of the BDS magnetic quadrupoles (see Fig. 2.9).

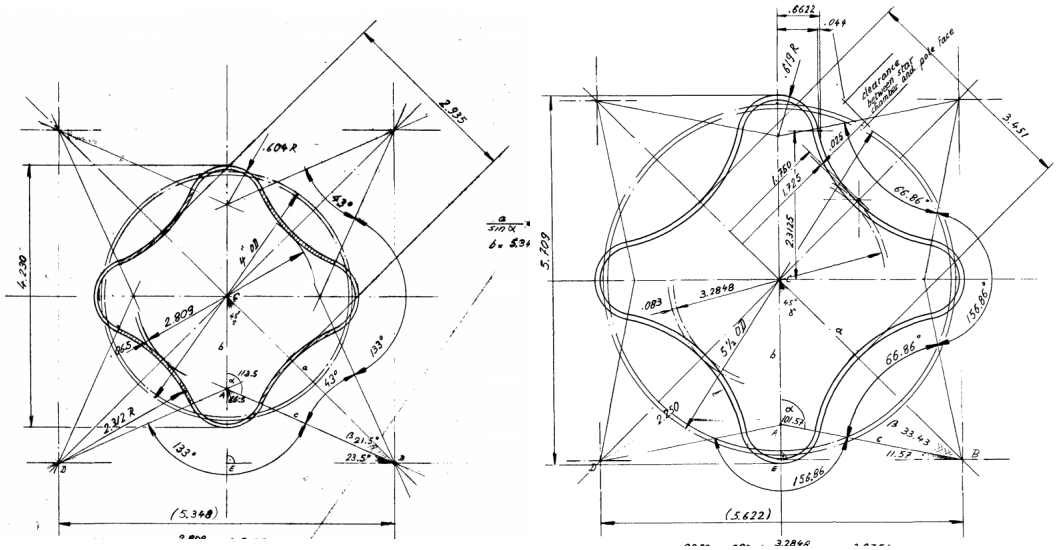

Figure 2.9: Typical transverse layouts of magnetic quadrupoles in the BDS.

2.3.2 Muon production from pion decay

COSY-based modules were implemented in the BDS tracking simulations to account for the following particle decays:

$$\mu^+ \rightarrow e^+ + \nu_e + \bar{\nu}_\mu \quad , \quad \pi^+ \rightarrow \mu^+ + \nu_\mu. \tag{2.8}$$

Even though the former case (muon decay) is the main channel through which ω_a is experimentally measured in the muon g-2 storage ring, its impact on the beam performance along the BDS is minimal; due to the relatively long muon lifetime in the rest frame, $\gamma_0 \tau_\mu \approx 64.5\,\mu s$, compared to the longitudinal extent of the BDS (about 2.4 km when the beam circulates the DR four times), most of muons born near the production target reach the end of M5 unless

they hit a beamline element. Furthermore, positrons from $\mu^+ \to e^+\nu_e\bar{\nu}_\mu$ do not survive for more than 4 μs after being injected into the muon g-2 storage ring [60]; thus, positrons are neglected in the studies presented here.

On the other hand, the $\pi^+ \to \mu^+\nu_\mu$ decay requires more attention as most of the muon beam emerges via this channel and its kinematics dictates the muon beam polarization [61]. Parity violation of the $\pi^+ \to \mu^+\nu_\mu$ weak decay constraints the spin and momentum directions in the pion rest frame of the emitted neutrino to be anti-aligned (i.e., -1 helicity). Therefore, conservation of angular momentum implies that the emitted muon is completely polarized in the pion rest frame.

From two-body kinematics, we have the decay-muon momentum p^*_μ and energy E^*_μ in the pion rest frame to be constant and well defined ($c = 1$):

$$p^*_\mu = \frac{(m^2_\pi - m^2_\mu)}{2m_\pi} \quad , \quad E^*_\mu = \frac{(m^2_\pi + m^2_\mu)}{2m_\pi} \tag{2.9}$$

where m_π and m_μ are the pion and muon rest masses, respectively.[3] In the laboratory frame where the longitudinal axis is parallel to the pion's momentum prior to decay, a Lorentz transformation yields the longitudinal p_L and transverse p_T components of the muon momentum in this frame as follows:

$$p_L = \gamma_\pi(\beta E^*_\mu + p^* \cos\theta^*) \quad , \quad p_T = p^* \sin\theta^* \tag{2.10}$$

where θ^* is a random number, γ_π corresponds to the pion's Lorentz factor and $\beta_\pi = v_\pi/c$ in the lab frame (v is the speed as observed in the lab frame). To express the decay-muon direction in terms of x' and y' for numerical simulations (see Eq. (2.7)), p_T is randomly

[3] The neutrino mass has been approximated to zero

decomposed into two orthogonal directions and, together with p_L, transformed to the optical axis frame:

$$x'_\mu = \frac{1}{p_0}\left[f\left(p_L\sqrt{1-\left(\frac{y'_\pi}{1+\delta_\pi}\right)^2} - p_T\cos\alpha\frac{y'_\pi}{1+\delta_\pi}\right) + p_T\sin\alpha\sqrt{1-f^2}\right] \tag{2.11}$$

$$y'_\mu = \frac{1}{p_0}\left[p_L\frac{y'_\pi}{1+\delta_\pi} + p_T\cos\alpha\sqrt{1-\left(\frac{y'_\pi}{1+\delta_\pi}\right)^2}\right] \tag{2.12}$$

In Eqs. (2.11) and (2.12), α is a unifromly-random angle and the subindex "π" denotes z_i coordinates of the pion in the optical frame. The factor f is equal to

$$f = \frac{y'_\pi}{\sqrt{(1+\delta_\pi)^2 - y'^2_\pi}}. \tag{2.13}$$

The new muon's momentum offset δ_μ is axiomatically defined from Eqs. (2.10):

$$\delta_\mu = \sqrt{p_L^2 + p_T^2}/p_0 - 1. \tag{2.14}$$

From the muon polarization side, the transverse component of the velocity four-vector is invariant under Lorentz transformation. Consequently, in the optical coordinates the muon polarization is given by

$$S_x = S_L x'_\mu - S_T\cos(\alpha)\, x'_\mu y'_\mu + S_T\sin(\alpha) \tag{2.15}$$

$$S_y = S_L y'_\mu + S_T\cos(\alpha) \tag{2.16}$$

$$S_z = S_L - S_T\cos(\alpha)\, y'_\mu - S_T\sin(\alpha)\, x'_\mu, \tag{2.17}$$

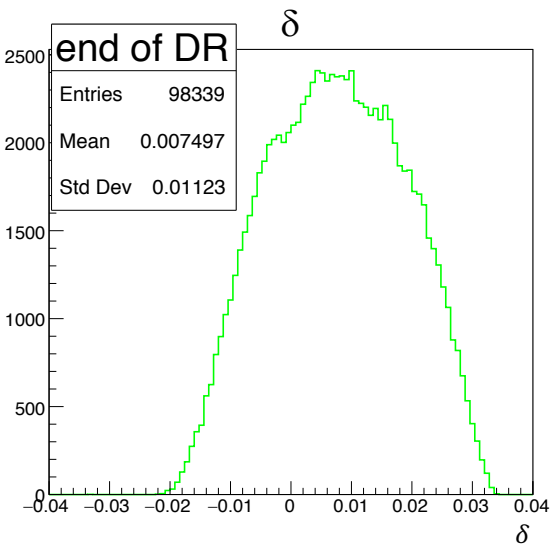

Figure 2.10: Momentum spread of the muon beam after four turns around the Delivery Ring. The momentum acceptance sustained at the BDS beamlines allows for the preparation of a highly polarized muon beam (P=0.969 from BDS simulations).

where

$$S_T = \frac{p_\pi m_\mu}{p_\mu m_\pi} \sin\theta^* \quad , \quad S_L = \sqrt{1 - S_T^2} \tag{2.18}$$

are the transversal, S_T, and longitudinal, S_L, muon polarizations relative to the pion's motion in the lab frame. From Eq. (2.10) and on the other hand the limited momentum acceptance throughout the Muon Campus (see Fig. 2.10), only decay muons with angles θ^* in the rest frame close to zero—i.e., forward muons—remain within the beamline channel, which further constraints the transversal muon beam polarization S_T yielding a highly polarized muon beam at the end of the M5 beamline as shown in Fig. 2.11.

2.3.3 Nonlinear effects on beam performance

In addition to the linear description of the beam dynamics, COSY INFINITY allows the computation of high-order effects of the beamline elements [56]. Specifically, particle coordinates are calculated as shown in Eq. (2.7). BDS tracking simulations were performed

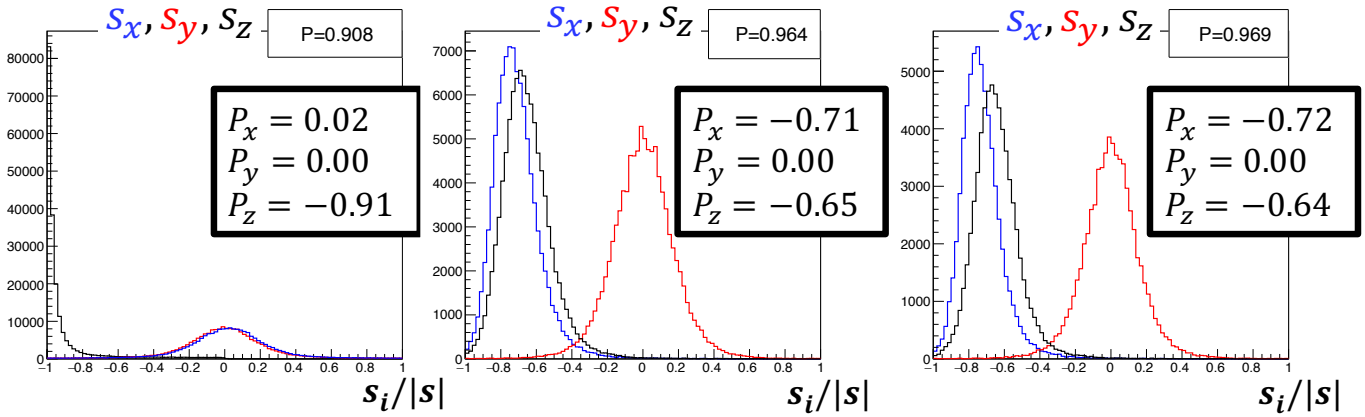

Figure 2.11: Histograms of the normalized muon beam spin components (in natural units) in optical coordinates at the end of M3 (left), Delivery Ring (center), and M5 (right) beamline sections. The high polarization, P, of the beam is centered with the horizontal plane. The spin components are expressed in terms of the coordinates that describe the relative dynamics around the reference orbit

up to fourth-order terms. High-order effects on the beam population were studied with the BDS model by computing the beam performance with and without high-order terms. In Table 2.2, the relative number of particles per species from the production target at the end of the M3, Delivery Ring, and M5 beamlines is shown.

Table 2.2: Number of protons (p), muons (μ), and pions (π) along the BDS (quantities per POT).

	M3 exit	**DR exit** ($n = 4$)	**SR entrance**
μ's	2.19×10^{-6}	1.04×10^{-6}	7.48×10^{-7}
μ's*	2.72×10^{-7}	2.85×10^{-7}	1.89×10^{-7}
π's	1.55×10^{-5}	0	0
p's**	1.24×10^{-4}	6.80×10^{-5}	5.86×10^{-5}

*Results for $\delta < 0.5\%$.
**Results for the case of proton removal at DR turned off.

Figure 2.12 shows the subtle effects of high-order terms (up to fourth) on the muons population as well as pions as they decay. Such nonlinearities tend to reduce the amount of muons/pions as they are transported throughout the BDS; nevertheless, the repeated beam

collimation, specially across bending elements, washes out the mitigation. Even though the combination of beamlines can accommodate at least 40π mm-mrad phase space, high-order effects do not have a considerable effect on the muon beam population (see Table 2.4).

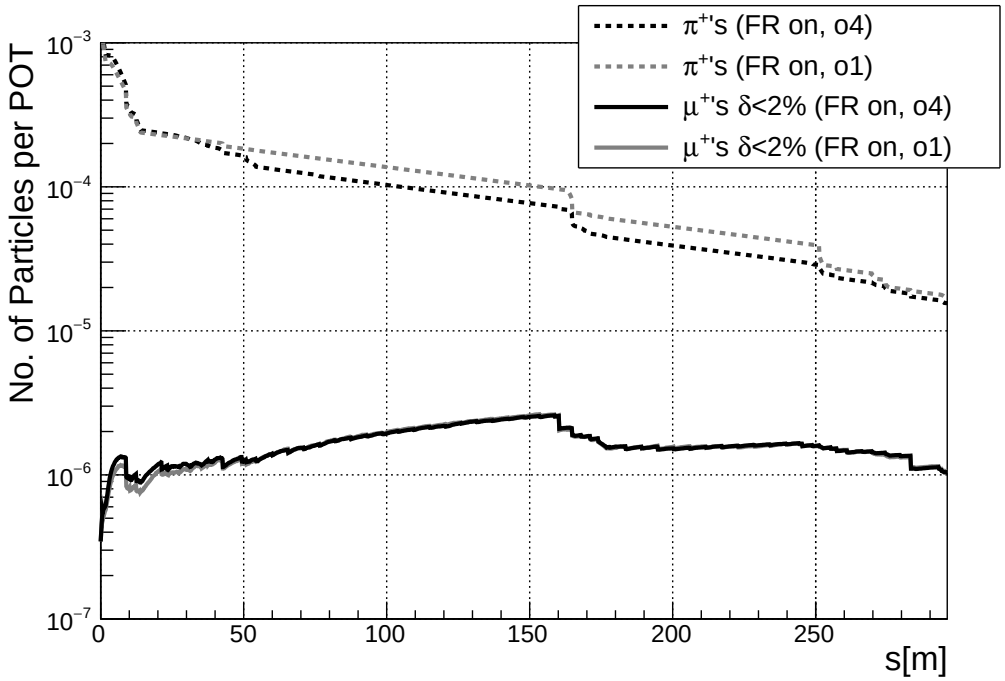

Figure 2.12: Simulation results of the number of pions and muons with $|\delta| < 2\%$ per POT under up to 4th order ($o4$) effects along the M2/M3 lines with fringe fields (FR) turned on. The longitudinal distance along the M2/M3 lines is shown in the horizontal axis. As depicted by the overlapping curves of the muons population for the two $o1/o4$ cases, linear simulations do not significantly differ from results when high-order terms in the computation of the particle dynamics are simulated.

Fringe fields map computations are performed at the edges of each beamline element. The longitudinal-dependent tapering of the multipole strengths is modeled by a six parameter Enge function (see Fig. 2.13):

$$F(z) = \frac{1}{1 + \exp\left(a_1 + a_2 \cdot (z/D) + \cdots + a_6 \cdot (z/D)^5\right)} \tag{2.19}$$

where z is the distance perpendicular to the effective field boundary and D is the full aperture

of the particle optical element. The a_i coefficients are taken by default based on measured data from PEP at SLAC [56]; for such cases, the integrated multipole strengths along the optical axis of each beamline element remain the same as for simulations with hard-edge modeling, guaranteeing this way reliability in the following comparisons between numerical results with fringe field effects turned on and off.

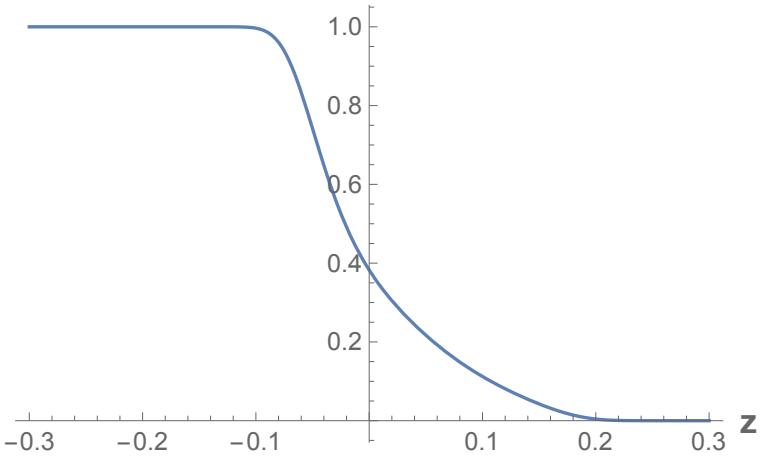

Figure 2.13: Enge function falloff of a typical dipole element in COSY INFINITY, used to represent fringe fields in the BDS simulations. The aperture for this case is equal to 10 cm.

Fourth-order numerical calculations with and without fringe fields were implemented. Figure 2.14 shows the differences between the two scenarios along the DR. After four turns in the DR, simulations suggest a favorable contribution due to fringe fields on the muons (i.e. 9.4% increment) and pions population. Fringe fields introduce fields longitudinal to the beam motion, which may be the essential contributor to keep more particles focused in a similar way to solenoids for low-energy experiments. However, such effect is not sufficiently large to compensate for losses at the beam bends along the beam delivery system in a significant way. Specifically, simulation results show an increment of 5.2% more muons at the entrance of the storage ring. Furthermore, fringe fields have a larger contribution in the number of surviving muons than in pions; i.e. at the end of the M3 line ($s = 290$ m)—where most of

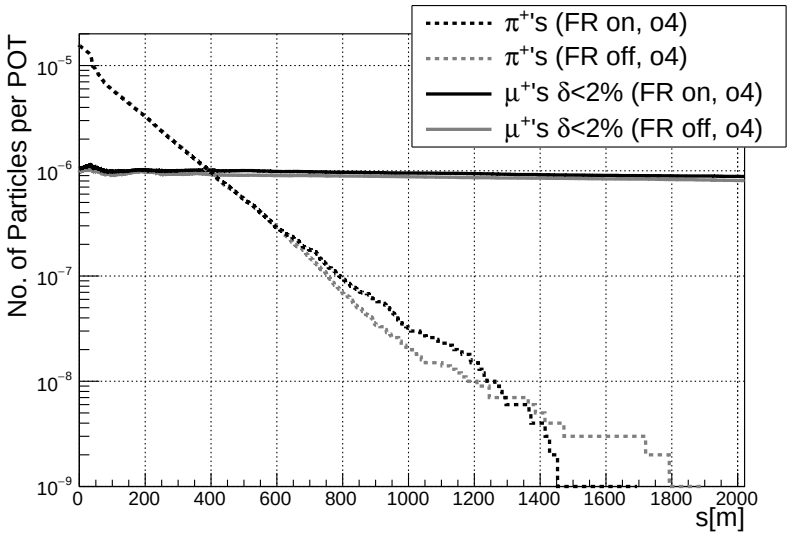

Figure 2.14: Fringe field effects on the population of pions and muons along the delivery ring (DR). The horizontal axis represents the longitudinal distance corresponding to four consecutive turns in the DR. From the *COSY*-based BDS model simulations, fringe fields (FR) contribute to maintaining more pions within the apertures of the DR which consequently increase the population of muons by 9.4% before being extracted to the M4 line. The "o4" abbreviation in the legend denotes the order of the computation (i.e. 4-th order).

pions still have not decayed—fringe fields maintained 8.9% more muons on track whereas pions population at that location increased by only 0.4%, which is within the ∼2% range of the simulations' statistical error. Fringe fields do not distort the optical lattice significantly, reflected in the modulated distortion in beta functions which from calculations does not exceed 4% [62].

Misalignments also studied in our *COSY*-based BDS simulations are introduced by transforming the transport maps that represent each beamline element. Transformations follow randomly Gaussian-distributed horizontal and vertical misplacements with standard deviations of 0.25 mm, introducing constant terms to the maps. A total of ten random misalignment configurations of the beam delivery system initialized with different random seeds were analyzed to procure statistical ranges within which the beam performance would be expected to occupy.

Figure 2.15 shows how the repercussions of misalignments under consideration could accumulate as muons travel along the BDS, decreasing the number of muons that make it to the end of M5. However, even though 0.25 mm is a small root mean square of the overall misplacements, the correctors along the beamlines are expected to mitigate such detrimental effect.

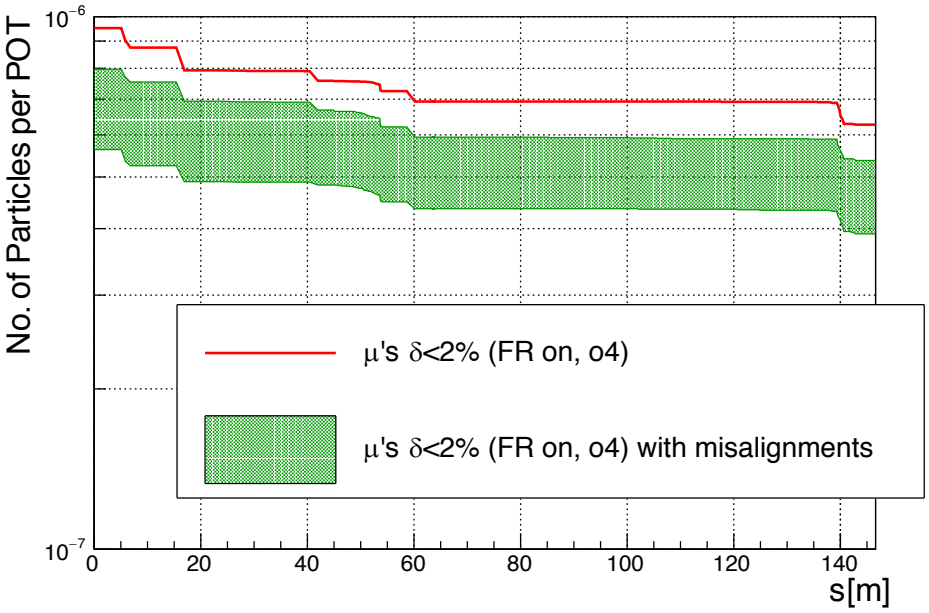

Figure 2.15: Simulation results of the muons population with $|\delta| < 2\%$ under the effects of beamline misalignments along the M4/M5 lines. The number of muons per proton on target (POT) is shown in the vertical axis as a function of the longitudinal distance along the M4/M5 lines. The red line depicts the number of muons for the ideal case of no misalignments present in the beam delivery system. The green band summarizes simulation results for several scenarios of beamline elements randomly misaligned in both vertical and horizontal directions.

Tables 2.3 and 2.4 summarize the impact of high-order terms, fringe fields, and realistic misalignments on the muon and pion population.

Table 2.3: Relative difference in pions population at the end of the M3 beamline from fringe field effects, up to 4th order nonlinear terms, and misalignments (horizontal and vertical misplacements with standard deviations of 0.25 mm). Statistical errors in the last row are calculated based on numerical simulations with ten different misplacement scenarios, initialized with independent random seeds.

	M3 exit
Fringe Fields	0.4%
Higher-order	-9.6%
Misalignments	-10.5±5.5%

Table 2.4: Relative difference in muons population at the end of the M3, Delivery Ring (after four turns), and M5 beamline sections from fringe field effects, up to 4th order nonlinear terms, and misalignments (horizontal and vertical misplacements with standard deviations of 0.25 mm). Statistical errors in the last row are calculated based on numerical simulations with ten different misplacement scenarios, initialized with independent random seeds.

	M3 exit	**DR exit**	**SR entrance**
Fringe Fields	8.9%	9.4%	5.2%
Up to 4th-order	-1.9%	-2.2%	-1.7%
Misalignments	-9.2±9.7%	-27.5±16.2%	-26.0±11.6%

2.3.4 Spin-orbit correlations

Fringe fields from the BDS beamline elements were also modeled in spin tracking simulations. For the pion decay channel, the resulting muon beam polarization is calculated based on the module explained in Subsec. 2.3.2, thereafter tracked with COSY INFINITY's DA mapping methods.

The resulting polarization, shown in Fig. 2.11, is P = 0.97, in agreement with *G4beamline* numerical simulations [54] which do not include fringe fields. Therefore, fringe fields do not interfere with the muon beam polarization. Another spin variable worth to analyze is the angle between the spin vector projection in the horizontal plane and the reference optical axis, φ_a, which resembles the phase that is indirectly measured in the storage ring (see Fig. 2.16). The muon beam average precession frequency of this phase, $\langle\omega_a\rangle$, plays an essential role in the final measurement of a_μ^{E989} which implies a deep understanding of its evolution as

the beam circulates through the storage ring. In particular, the correlation between φ_a and the Lorentz factor γ of a muon might result in a sub-ppm systematic effect of $\langle\omega_a\rangle$. High-momentum muons decay at a slower rate than low-momentum muons – which might be lost at higher rates, too, before they decay depending on the stored beam matching with the storage ring and nonlinear effects – and as a consequence $\langle\omega_a\rangle$ could shift as the muon beam decays [63].

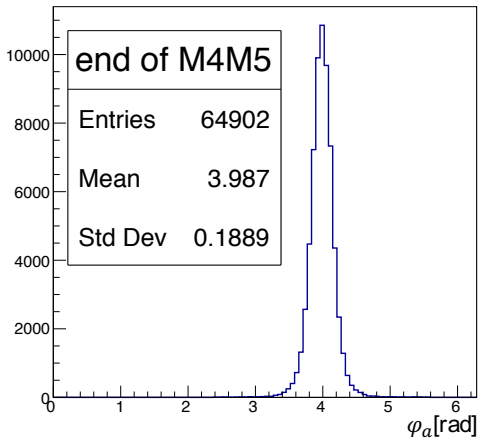

Figure 2.16: Histogram of the muons' spin projection angle in the horizontal plane with respect to the reference optical axis at the storage ring (SR) entrance from simulations. The beam delivery system (BDS) is designed to favor the capture of muons from pion decay that are longitudinally polarized. However, as the muon beam travels through the bending sections of the the BDS –especially along the Delivery Ring which houses multiple rectangular bending magnets– the polarization develops a transversal component before the beam is delivered to the g-2 storage ring.

Tracking simulations were performed with and without fringe fields to study the effect of fringe fields on the spin-momentum correlation $m_\gamma = d\langle\varphi_a\rangle/d\gamma$. For the case of fringe fields turned on, simulations show a correlation m_γ equal to 29.2 ± 9.4 mrad after four turns around the Delivery Ring as shown in Fig. 2.17. On the other hand, similar simulations without fringe fields—conventional hard-edge model—indicate a correlation $m_\gamma = 92.1 \pm 9.8$ mrad. This unexpected discrepancy on spin-momentum correlations apparently originated

from fringe field effects of the numerous magnetic beamline elements within the DR, specially the rectangular bending magnets, is worthy of more detailed studies. Specifically, the large error bars in Fig. 2.17 can be reduced by increasing the statistics in simulations. Moreover, higher computational orders of the fields that represent the beamline elements in the BDS *COSY*-based ring model could be implemented; in this way, the modeling of fringe fields would encompass higher nonlinear effects.

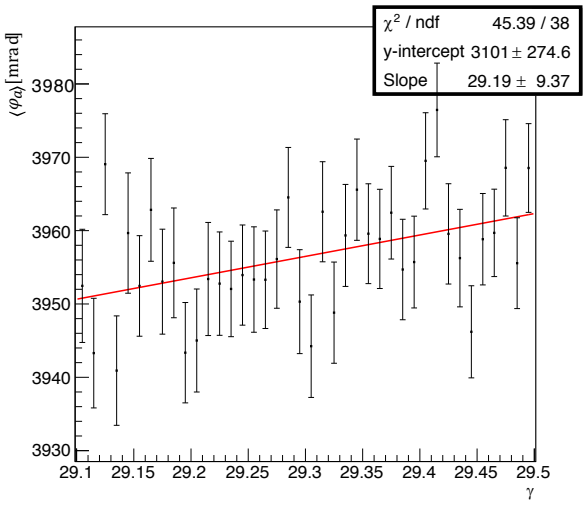

Figure 2.17: Beam average of the spin projection angle in the horizontal plane with respect to the reference optical axis, $\langle\varphi_a\rangle$, versus the Lorentz factor, γ, at the exit of the delivery ring after four turns. Simulation results presented in this figure correspond to our *COSY*-based BDS model with fringe fields turned on.

2.4 Conclusions

A detailed model of the beam delivery system at E989 has been developed. Realistic features based on DA methods such as fringe fields, high-order effects, and misalignments are included to describe the statistical and dynamical performance of the secondary beam produced at the pion production target. Simulation results suggest that fringe fields increase the number of

muons that are delivered to the storage ring by ∼5%, whereas the muon beam polarization is unaffected. However, spin-momentum correlations that could add systematic effects to the final measurement of E989 due to differential decays are significantly affected by the fringe fields from the rectangular dipole magnets of the delivery ring; further studies with higher statistics and computational orders in simulations are pertinent to confirm this effect. Regarding high-order effects, our numerical studies indicate that they do not affect the secondary beam performance along the BDS. In addition to the presented results, the *COSY*-based model served to validate numerical calculations prepared by other members of the Muon g-2 Collaboration and check the performance of the Fermilab Muon Campus E989 beam delivery system.

Chapter 3

Beam Dynamics at the Muon *g*-2 Storage Ring

3.1 Introduction

With a high-fidelity characterization of the muon beam that gets stored inside the g-2 storage ring, the ω_a corrections driven by beam dynamics effects and the magnetic field experienced by the stored beam can be assessed to the precision demanded by the experiment goals. To first order, the periodic functions of the storage ring (i.e., α, β, and γ) together with closed orbit distortions are used to describe the entire azimuthal behavior of the storage ring, beyond the tracker detectors longitudinal acceptance. To higher orders, nonlinear contributions of the storage ring guide fields drive betatron resonances, longitudinal beam decoherence, amplitude- and momentum-tune shifts, and betatron-amplitude modulations. Furthermore, a sensible modeling of the electric and magnetic fields in the ring storage volume allows to quantify the periodic ring functions, as well as the nonlinear effects aforementioned.

For this characterization purpose, a detailed particle optical model of the Muon g-2 Storage Ring [64] has been developed using a computational environment for various advanced concepts of modern scientific computing with specialized application packages in COSY INFINITY [53]. The package dedicated to the design and analysis of particle optical systems

is employed for the modeling of the storage ring. Differential-algebraic (DA) map methods in COSY INFINITY allow the preparation of transfer maps which describe the solutions of storage ring beam optics ordinary differential equations (ODEs) for arbitrarily complicated fields and to arbitrary order [56]. The manipulation of such transfer maps in COSY INFINITY facilitates the characterization of the leading-order and nonlinear properties of the storage ring, as well as their action on the dynamics of the injected beam through repetitive tracking. Map methods allow for the incorporation of all measured field effects for these purposes and, in conjunction with COSY INFINITY's parallel computation features, yield fast high-statistics particle tracking in contrast to conventional orbit-integration beam dynamics codes. Symplecticity is enforced in beam tracking with high-order transfer maps in COSY INFINITY to ensure energy conservation and control error propagation [65].

Each of the optical elements that constitute the storage ring is represented by a time-dependent transfer map, and their ordered multiplication via map methods result in the assembly of the COSY-based storage ring model. The following elements are the main components of the model (see Fig. 3.1):

1. *The Electro-Static Quadrupole system (ESQ).* The electrostatic fields generated by each of the eight sets of curved electrodes aligned with the design orbit are computed in COSY INFINITY from the field information in the midplane, which was calculated using conformal mapping methods [66]. The geometry of the ESQ is symmetric with respect to the horizontal midplane, allowing to recreate the 3D electrostatic field immersed in the vertical magnetic field as a Taylor expansion in transversal coordinates [67]. The coefficients of the expansion are automatically computed to satisfy the Laplacian in curvilinear coordinates. The fringe fields and the effective field boundary are modeled based on numerical calculations using *COULOMB* [66]. The map

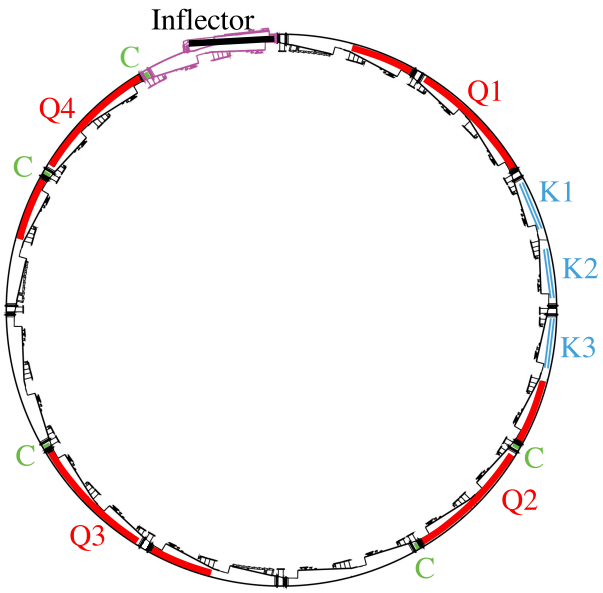

Figure 3.1: Layout of the Muon g-2 storage ring at Fermilab.The four locations of the ESQ are found next to labels "Q1-Q4" (each covering 39 degrees azimuthally) and labels "K1-K3" indicate the place of the injection kicker plates within the ring. "C" labels denote the beam collimators arrangement.

representation of the fringe fields is accurately computed with DA methods in COSY INFINITY [67]. The modeling during the scraping and time-dependent stages of the ESQ is handled with transfer maps of the mis-powered ESQ electrodes combined with the maps that describe the main guide fields.

2. *Injection kickers.* The transversal kicker action on the injected beam is represented via a symplectic kick map proportional to the longitudinal lengths and characteristic time-dependent strengths of the kickers. The kick is instantaneously applied to each particle within the beam and it is proportional to the strength at the azimuthal center of the kicker.

3. *Magnetic field data.* The ppm-level magnetic field inhomogeneities measured by the nuclear magnetic resonance (NMR) probes in the storage ring are fitted with transverse

multipole expansion functions to prepare segmented transfer maps of the magnetic field. Magnetic multipole elements encompassing $\sim$ 2 mrad azimuthal sections throughout the ring represented by such maps simulate the azimuthal dependence of the magnetic field. These representations, together with symplectic kicks that recreate the lowest-order fits to magnetic field measurements, are superimposed over the uniform portion of the guide fields automatically computed in 3D from the midplane information.

Aperture cuts are applied during repetitive tracking employing special commands of COSY INFINITY's beam physics package, and particles with transverse coordinates beyond the circular apertures of the collimators inserted at specific locations of the storage ring are flagged as lost. High-statistics numerical studies of muon loss rates of the stored muon beam due to betatron resonances are computed with a short turnaround time based on the tools described above. Numerous studies concerning the lowest-order and nonlinear dynamics of the muon beam and lattice properties of the storage ring have been performed, such as muon capture efficiency, amplitude-dependent betatron tune shifts, muon beam characterization (spin dynamics, distribution correlations, beam decoherence, etc.), closed orbit distortions, ring lattice parameterization, and systematic studies and correction calculations of the precession frequency ω_a. The contributions to ω_a where the output of the COSY-based storage ring model played a direct role are presented in Ch. 4. In terms of the Beam Dynamics framework, the main deliverables—and some of them intermediate in view of beam-dynamics-driven ω_a and $\langle B \rangle$ corrections— of the model are presented in Sec. 3.3 and 3.4 from both the linear and nonlinear front. A nominal characterization (i.e., under nominal operational settings) of the stored muon beam is delineated in Sec. 3.5, whereas the peculiar behavior of the beam during the first official run of the g-2 storage ring (i.e., "Run-1") is described in Sec. 3.6.

3.2 The COSY-based Muon Storage Ring Model

Figure 3.2 illustrates the components, interrelations, and input of the COSY-based Muon Storage Ring Model (or "COSY-based model" for short) as part of the muon g-2 experiment. The main purpose of this model is to express the physics that dictates the dynamics of the

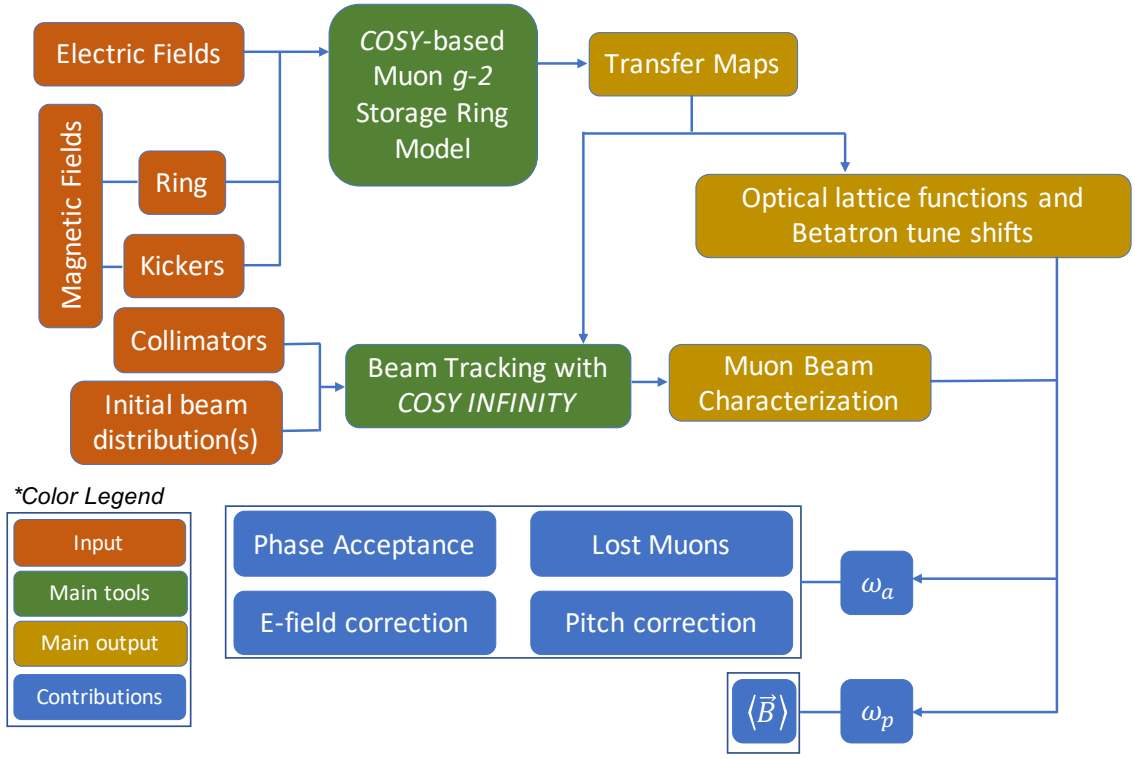

Figure 3.2: Work flow of the COSY-based Muon Storage Ring Model. Experimental measurements constitute the guide fields as defined in the model, whose main output is nonlinear transfer maps for the calculation of optical lattice functions and beam orbital (and spin) symplectic tracking. With special methods explained along this chapter, guide fields are reconstructed and initial beam distributions recreated for a detailed characterization of the muon beam in the g-2 storage ring. The characterization is further used for quantifications of beam-dynamics systematic corrections in the g-2 final measurement.

muon beam in practical terms, in order to use it for beam characterization (see Sec. 3.3-3.6) and accurate calculations of beam-driven uncertainties (see Ch. 4) in the E989 main measurement. To achieve a trustworthy beam-physics representation of the storage ring, the COSY-based model heavily relies on precise measurements of its guide fields (or data-driven

reconstructions of them when not available) and realistic initial beam distributions.

Two initial beam distributions are prepared with different methods. The features of these two inputs are described in Subsec. 3.2.5 and 3.6.3.

The physics emerged from the implemented guide fields (see Subsec. 3.2.1-3.2.3) is captured as high-order transfer maps. For the preparation of these maps, the beam physics code of COSY INFINITY integrates the ordinary differential equations of motion (ODEs) in particle optical coordinates with an 8th-order Runge-Kutta integrator [68] over a differential algebra (DA) ${}_nD_v$, where n is the computation order and v is the number of phase space coordinates [67]. The result is a transfer map $\mathcal{M}$ used to obtain the z_f coordinates of any particle based on its initial conditions:

$$\vec{z}_f = \mathcal{M}(\vec{z}_i). \tag{3.1}$$

Besides performing long-term beam tracking, the resulting maps are further used and manipulated for tracking-independent formulations of the storage ring optical lattice (e.g., beta functions, dispersion functions, and closed orbits, and betatron tunes) as well as amplitude- and momentum-dependent tune shifts (see Ssec. 3.3-3.6).

3.2.1 The Electro-Static Quadrupole system (ESQ)

The ESQ is a four-fold azimuthally symmetric system (see Fig. 3.1) with four plates centered around the ideal orbit [69] (see Fig. 3.3) meant to supply vertical beam focusing, but at the cost of horizontal defocusing and nonlinear beam dynamics effects due to the specific geometry of the plates. Each ESQ station consists of a short and long section separated by 4°, and extended by azimuthal lengths of 13° and 26° respectively. Together with the vacuum

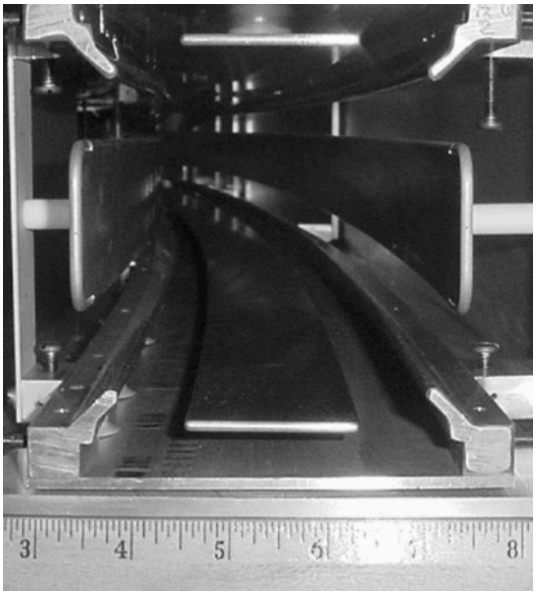

Figure 3.3: Cross section of an ESQ station. For vertical confinement of (positive) muons, the top and bottom plates are positively charged whereas the lateral plates are charged with negative voltage. The vertical magnetic field in the storage ring largely contributes to stable motion in the horizontal direction, in spite of the defocusing radial gradient form the ESQ inner and outer plates.

chambers, all the ESQ was adopted from the previous E821 experiment at BNL. The plates are made with aluminum graded such that their low magnetic susceptibility and thicknesses do not interfere neither with the overall magnetic field quality nor the calorimeters energy resolution (as decay positrons trajectories often cross the lateral plates). The four-fold symmetry, inherited from E821, was chosen so to accommodate instrumentation in-between the stations and, simultaneously, minimize beam variations (i.e., less than 3%) around the ring.

The ESQ plates play the role of electrodes while being charged by power supplies via high-voltage resistors; the circuitry involved to carry the voltage to the plates is configured to deliver charge to them every 700 μs in one or two steps. To generate closed orbit distortions (see Subsec. 3.3.3) for beam scraping purposes, a specific set of plates (i.e., all bottom plates, inner plates at Q2, and outer plates at Q4) is connected to the 2-step pulsers which

rise initially from 0 to about 6 kV below the nominal High-Voltage (HV) set point (see Fig. 3.4). The rising times are such that these mis-powered plates reach a steady HV for

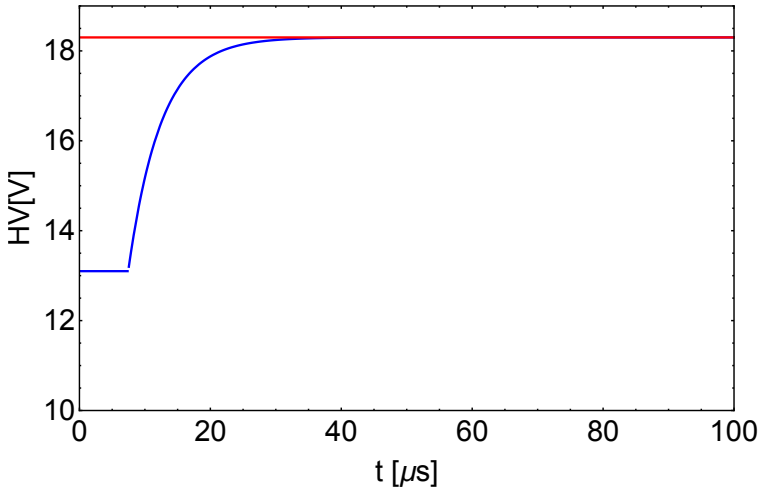

Figure 3.4: Illustration of the HV traces from plates connected to the 1-pulse (red line) and 2-pulse (blue curve) HV supplies.The mis-powered ESQ plates (blue) during the initial $\sim 7\,\mu$s after injection shift the beam towards the limiting apertures of the storage volume, in order to scrape the beam in preparation for the data taking period at $t > 30\,\mu$s.

when the beam is injected into the storage ring for about 7 μs, at which point the second pulse takes place to charge them up to the nominal HV value. The transitions from mis-powered to nominal HVs are adiabatic, where the resistors connected to the plates are chosen to yield transition times of $\tau_C = RC \approx 5\,\mu$s. The total to-ground capacitance of the plates, on the order of $100 - 300\,$pF [70], are not easily malleable since they surge from several properties on the grounding, intervened by HV leads, feedthroughs, plates geometry, etc. Since $\tau_C \gg T_C$—where $T_C \approx 0.1492\,\mu$s is the cyclotron period—beam tracking simulations are reliably performed with one-turn transfer maps prepared per cyclotron period. After commissioning, the typical HV set points of the first g-2 runs (HV$\sim 18\,$kV) were chosen so that the ESQ can stably run without discharging sparks and, other hand, to try to avoid betatron resonances. The resulting focusing/defocusing electric fields reach values on the order of 6 kV/cm.

Due to the longitudinal curvature and overall geometry of the ESQ electrodes, the generated electric fields exhibit nonlinear features whose effect is perceived more noticeably near the limits of the storage volume, as shown in Fig. 3.5. To reproduce a realistic representa-

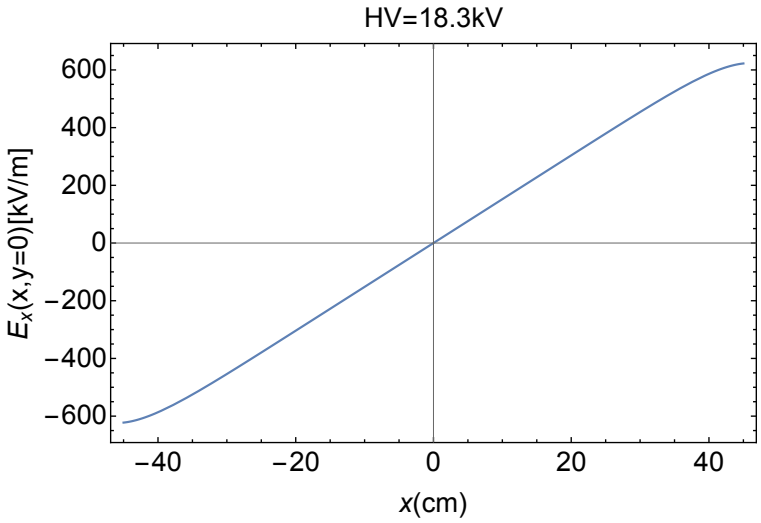

Figure 3.5: Radial electric field along the midplane (HV= 18.3 kV). Near the aperture limits at $x = 45$ mm, nonlinearities from the ESQ electric fields distort the otherwise linear radial field.

tion of the ESQ electric fields, the transverse electrostatic potential is defined as a transverse Taylor expansion in the radial-vertical (or, equivalently, x-y) plane at a longitudinal location s:

$$V = V(x, y, s) = \sum_{k=0}^{\infty} \sum_{l=0}^{\infty} a_{k,l}(s) \frac{x^k y^l}{k!l!}. \tag{3.2}$$

By exploiting the horizontal-plane symmetry of the ESQ station's cross section, all the $a_{k,l}(s)$ coefficients are uniquely determined out of the midplane coefficients $a_{k,0}(s)$ as follows [71]:

$$\begin{aligned} a_{k,l+2} = &- a''_{k,l} - kha''_{k-1,l} + kh'a'_{k-1,l} - a_{k+2,l} - (3k+1)ha_{k+1,l} \\ &- 3khka_{k-1,l+2} - k(3k-1)h^2 a_{k,l} - 3k(k-1)h^2 a_{k-2,l+2} \\ &- k(k-1)^2 h^3 a_{k-1,l} - k(k-1)(k-2)h^3 a_{k-3,l+2}, \end{aligned} \tag{3.3}$$

where h is the inverse of the station curvature radius (7.112 m) and $a'_{k,l} = da_{k,l}/ds$. The resulting set of coefficients satisfies Laplace's equation in curvilinear coordinates to ensure a Fully-Maxwellian field.The $a_{k,0}$ coefficients at the main ESQ field region are calculated with conformal mapping methods [66] and specified in COSY INFINITY, which recursively calculates all the other $a_{k,l}$ terms via Eq. (3.3) and DA methods [67] for the transfer maps preparation.

Table 3.1 shows the $a_{k,l}$ terms specific to a nominal ESQ station charged at HV= 18.3 kV.

Table 3.1: $a_{k,0}$ coefficients at the main ESQ field region (see Eq. (3.3)) for HV= 18.3 kV. x and y are in meters and electrostatic potential in Volts. Due to the ESQ midplane symmetry, coefficients with odd l values are zero.

k	$l=0$	$l=2$	$l=4$	$l=6$	$l=8$	$l=10$
0	0	1.520E+07	-3.605E+06	-2.210E+12	2.569E+13	-2.712E+22
1	0	-6.410E+06	3.549E+06	8.389E+12	-8.251E+13	2.860E+23
2	-1.520E+07	3.605E+06	2.210E+12	-2.569E+13	2.712E+22	-2.059E+24
3	0	-2.028E+06	-7.457E+12	7.167E+13	-2.745E+23	1.246E+25
4	0	-2.210E+12	1.887E+13	-2.712E+22	1.821E+24	7.217E+30
5	0	4.660E+12	-4.219E+13	2.402E+23	-9.955E+24	-1.370E+32
6	2.210E+12	-7.863E+12	2.712E+22	-1.377E+24	-7.217E+30	1.575E+33
7	0	1.135E+13	-1.830E+23	6.442E+24	1.218E+32	-1.419E+34
8	0	-2.712E+22	8.170E+23	7.217E+30	-1.241E+33	-1.425E+41
9	0	1.029E+23	-2.978E+24	-1.005E+32	9.880E+33	3.907E+42
10	2.712E+22	-2.895E+23	-7.217E+30	8.544E+32	1.425E+41	-6.221E+43
11	0	6.634E+23	7.306E+31	-5.689E+33	-3.366E+42	7.515E+44
12	0	7.217E+30	-4.691E+32	-1.425E+41	4.649E+43	-7.654E+45
13	0	-3.957E+31	2.382E+33	2.705E+42	-4.884E+44	6.947E+46
14	-7.217E+30	1.558E+32	1.425E+41	-3.056E+43	4.336E+45	-5.815E+47
15	0	-4.887E+32	-1.924E+42	2.647E+44	-3.440E+46	4.593E+48
16	0	-1.425E+41	1.613E+43	-1.951E+45	2.525E+47	-3.478E+49
17	0	1.022E+42	-1.051E+44	1.295E+46	-1.756E+48	2.556E+50
18	1.425E+41	-5.173E+42	5.933E+44	-8.016E+46	1.176E+49	-1.840E+51

The four-fold symmetric geometry of the plates around the station center favors the presence of the leading quadrupole (k=2), 12-pole (k=6), 20-pole (k=10), and further $4(2i-1)$-pole midplane-symmetric (l=0) terms, being the quadrupole term—which largely defines the betatron tunes of the ring—about 3.4% higher than the voltage applied to the plates [72]. Of special interest is the 20-pole, whose larger relative magnitude manifests itself in betatron

resonance and tune shifts, as elaborated in the next chapter. Figure 3.6 shows the overall and nonlinear structures of the electrostatic potential from a charged ESQ station implemented in the COSY-based model.

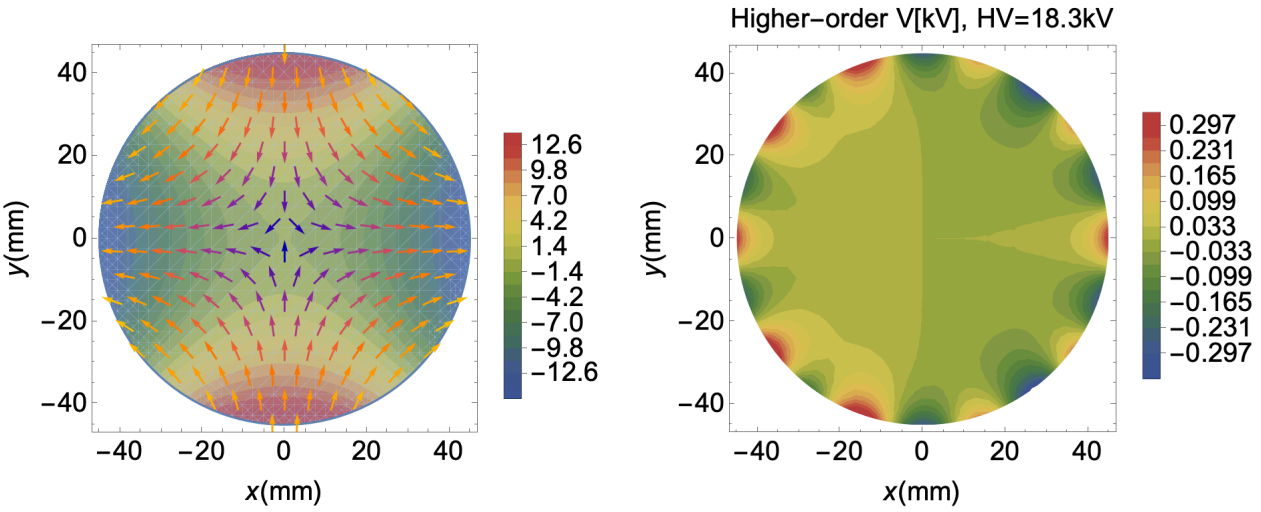

Figure 3.6: Main electrostatic potential $[kV]$ from an ESQ station on the left side, overlaid with electric vector field represented with arrows. On the right, electrostatic potential from higher-order terms in the Taylor expansion; the curvature of the plates and the presence of the 20-pole are manifested.

The effective field boundary ($z_{EFB} = 1.2195\,\text{cm}$) and fringe fields of the ESQ are calculated using COULOMB's [50, 66] boundary-element method field solver. Figure 3.7 shows the resulting fringe field falloff, which is implemented in the COSY-model ESQ transfer maps via an Enge-function fit:

$$F(z) = \frac{1}{1 + \exp\left(a_1 + a_2 \cdot (z/D) + \ldots + a_6 \cdot (z/D)^5\right)}, \tag{3.4}$$

where D is the full aperture of the ESQ ($D = 10\,\text{cm}$) and the Enge coefficients are

$$\begin{aligned} a_1 &= 0.14389529, \quad a_2 = 6.85939851, \quad a_3 = -1.87096936 \\ a_4 &= 0.80158053, \quad a_5 = -0.40704326, \quad a_6 = 0.06588881. \end{aligned} \tag{3.5}$$

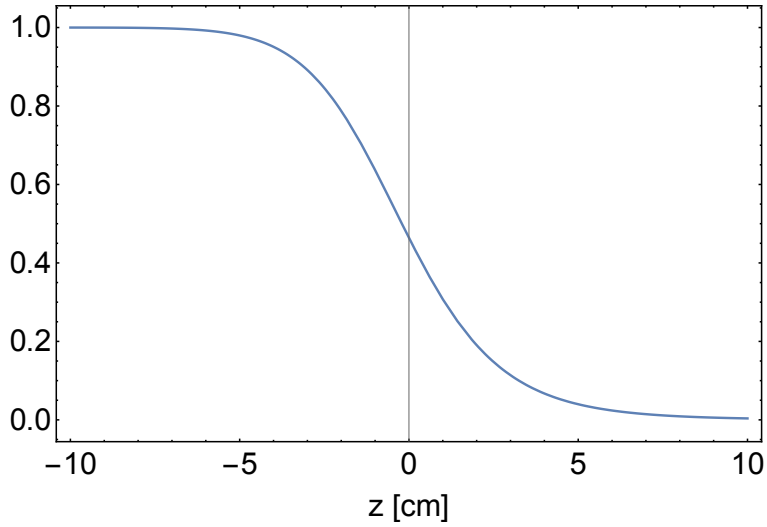

Figure 3.7: Longitudinal fringe field at an ESQ station edge. The effective field boundary extends the occupancy of the electric fields in the hard-edge view by $\sim 0.436\%$.

With the fringe fields falloff, the leading electric multipole coefficient strengths are scaled accordingly and the longitudinal dependencies are captured recursively in COSY INFINITY for the ESQ modeling. The effective field boundary for this specific case elongates the field extension of each station, reducing radial tunes by $\sim 0.07\%$ and increasing the vertical ones by $\sim 0.05\%$ with respect to a hard-edge case.

Two of the 32 HV resistors connected to the ESQ plates were damaged during the first data-taking run ("Run-1") of the g-2 experiment. Consequently, the resulting electric fields exhibited special behaviors that affected the transverse stability of the stored beam, as described in Sec. 3.6.

For the transfer maps preparation in the COSY-based model, the ODEs subject to the ESQ electric fields described above also account for the embedding magnetic field in the storage ring. The implementation and features of the magnetic fields in the COSY-based model are described next.

3.2.2 Magnetic field data

The subtle imperfections of the magnetic field within the storage region of the ring drive closed orbit distortions and betatron resonances at specific high voltage settings of the ESQ. In our model, such inhomogeneities are included based on fits of nuclear magnetic resonance (NMR) trolley run measurements from the g-2 Field Team. The azimuth-independent fits provide the extraction of 2D magnetic normal and skew multipole coefficients (up to the decapole term) by attributing the scalar measurements to the predominant vertical magnetic field.

By considering Laplace's equation in cylindrical coordinates and assuming no longitudinal z variations of the magnetic potential V,

$$\nabla V(r,\theta,z) = \frac{1}{r}\frac{\partial}{\partial r}\left(r\frac{\partial V}{\partial r}\right) + \frac{1}{r}\frac{\partial}{\partial \theta}\left(\frac{1}{r}\frac{\partial V}{\partial \theta}\right) = 0, \tag{3.6}$$

the vertical magnetic field is expressed as a summation of magnetic multipole coefficients:

$$B_y(r,\theta) = b_0 + \sum_{n=1}^{\infty} r^n \left[b_n \cos n\theta + a_n \sin n\theta\right]. \tag{3.7}$$

Since the NMR measurements of the scalar magnetic field are insensitive to its direction—which is known *a priori* to be dominantly vertical—the sensible approximation of taking B_y as the scalar field itself yields

$$B(r,\theta) \approx B_y(r,\theta) = B_0\left(b_0 + \sum_{n=1}\left(\frac{r}{r_0}\right)^n \left[b_n \cos(n\theta) + a_n \sin(n\theta)\right]\right). \tag{3.8}$$

Due to the ppm-level radial and longitudinal components of the magnetic field in the storage

ring [6], this approach adds a small error of only $\approx 10\,\text{ppb}$ to NMR measurements [73]. The relative strengths of the magnetic multiple components implemented in the COSY-based model are shown in Fig. 3.8 and follow the notation in Ref. 74:

$$\Delta B_y + i\Delta B_x = B_0 \sum_n (b_n + ia_n)\,(x + iy)^n. \tag{3.9}$$

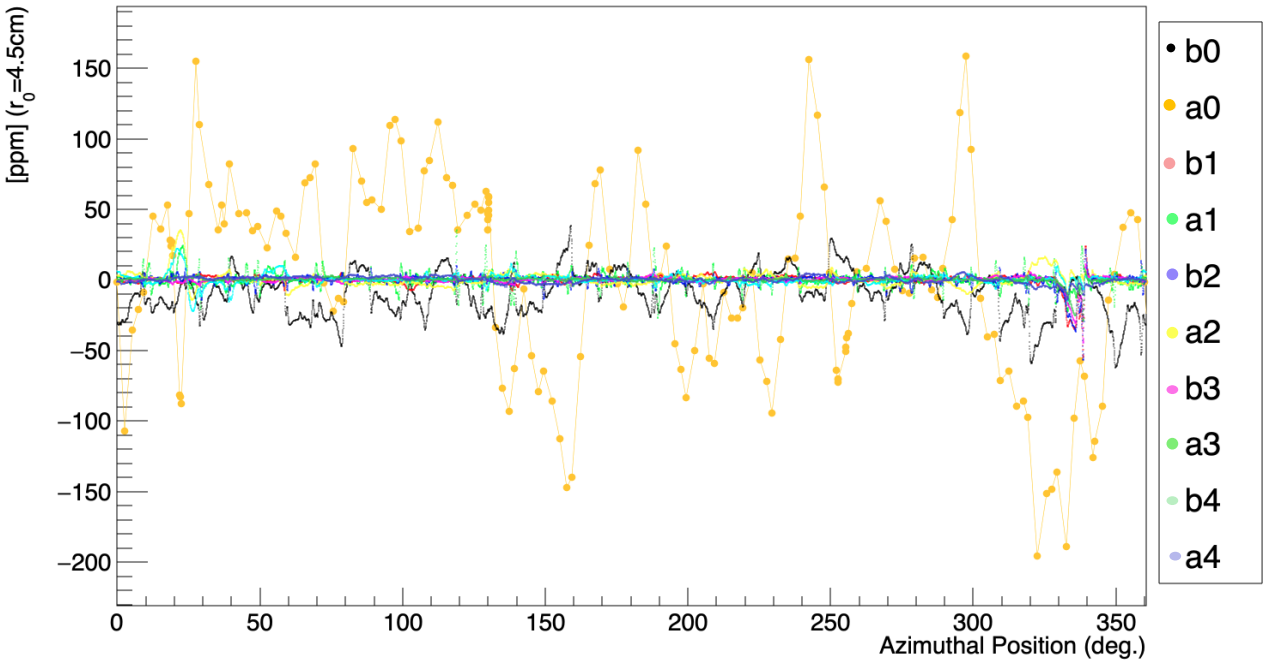

Figure 3.8: Magnetic field multipoles from Trolley Run 3956. All the multipole terms are expressed relative to the ideal vertical magnetic field B_0 that sustains magic muons in the ideal orbit. The skew dipole term (also called radial field) was measured with a Hall probe in 2016 [6] and averaged out to recreate the expected effect of the surface correction coils (SCC).

In the model, the transfer map of a ESQ station of azimuthal length L with magnetic field inhomogeneities within ($\mathcal{M}_{E,B}$) is prepared as a sequence of adjacent optical elements

as follows:

$$\mathcal{M}_{E,B}(L) = \left(\mathcal{M}_E(L_i/2)\cdot\mathcal{M}_L(-l)\cdot\mathcal{M}_B(\phi,l)\cdot\mathcal{M}_E(L_i/2)+\mathcal{C}_x(L_i,\phi)+\mathcal{C}_y(L_i,\phi)\right)^n. \tag{3.10}$$

The map $\mathcal{M}_E(L_i)$ encapsulates the Fully-Maxwellian ESQ electric fields (see Subsec. 3.2.1) embedded in the ideal vertical magnetic field $B_0 = p_\mu/e\rho_0$ where p_0 is the magic momentum, e the elementary charge, and the design radius is $\rho_0 \approx 7.112\,\mathrm{m}$. The azimuthal length L_i (typically about 0.1°) is chosen so that the final map length corresponds to L and the azimuthal variation of the magnetic multipoles is captured. By virtue of the thin lens approximation—and the significantly small sizes of the magnetic field inhomogeneities relative to the main vertical field—, an element $\mathcal{M}_B(\phi,l)$ with a superposition of the azimuthally dependent normal and skew magnetic multipoles at the azimuth ϕ acts on the map to cover the effects of the magnetic field errors; the length l is equal to $1\,\mu\mathrm{m}$ and the multipoles are properly scaled. A multi-Gaussian function is implemented to calculate the magnitudes of the measured magnetic multipoles at any azimuth. A drift element $\mathcal{M}_L(-l)$ of negative length is accounted for counteracting the nonzero length of $\mathcal{M}_B(\phi,l)$. The low-order skew and normal magnetic coefficients, a_0 and b_0, are modeled as symplectic kicks and act on the constant part (written explicitly as $\mathcal{C}_x$ and $\mathcal{C}_y$ in Eq. (3.10)) of the transfer map so that

$$\Delta a = -B_0 b_0 L_i/\chi_m \quad , \quad \Delta b = B_0 a_0 L_i/\chi_m, \tag{3.11}$$

where $\chi_m = B_0\rho_0$ is the magnetic rigidity. Δa and Δb are the radial and vertical direction offsets in particle optical coordinates. To preserve the Hamiltonian (via phase-space preservation) during beam tracking simulations with this detailed implementation of the subtle

magnetic field errors, the symplectic condition is enforced in COSY INFINITY.

3.2.3 Injection kicker magnets

Three kicker stations (see Fig. 3.10) 1.27 m long and about 1/4 of radial betatron wavelength downstream from the inflector exit, where the beam enters the ring, are installed in the storage ring (see Fig. 3.1) for beam injection. The muon beam emerges ~ 77 mm tangentially

Figure 3.9: Transverse vie of a kicker station. The plate geometry is designed to maximize current-to-field conversion in the storage region.

shifted from the ideal orbit. In order for the injected muons to end up within the ring storage volume, the kicker stations are required to steer them about 10.5 mrad radially outward. For this end, the kicker plates supply an integrated magnetic field of 1.1 kG.m oppositely directed to the vertical field of the storage ring. The kicker stations need to pulse at 100 Hz in synchrony with the 120 ns pulse train from the beamlines (see Fig. 2.2), and shut off before the pulse revolves the 149 ns-long storage ring [75]. In view of these timing specifications, a

robust pulser and low-impedance kicker stations are desired to meet the required rise and decay times.

Due to impedance mismatch, the temporal shape of the kicker strengths exhibit a ringing structure as the signal is reflected after the main transient field is induced. Figure 3.10 shows a typical sample during the first run of the g-2 experiment [76].

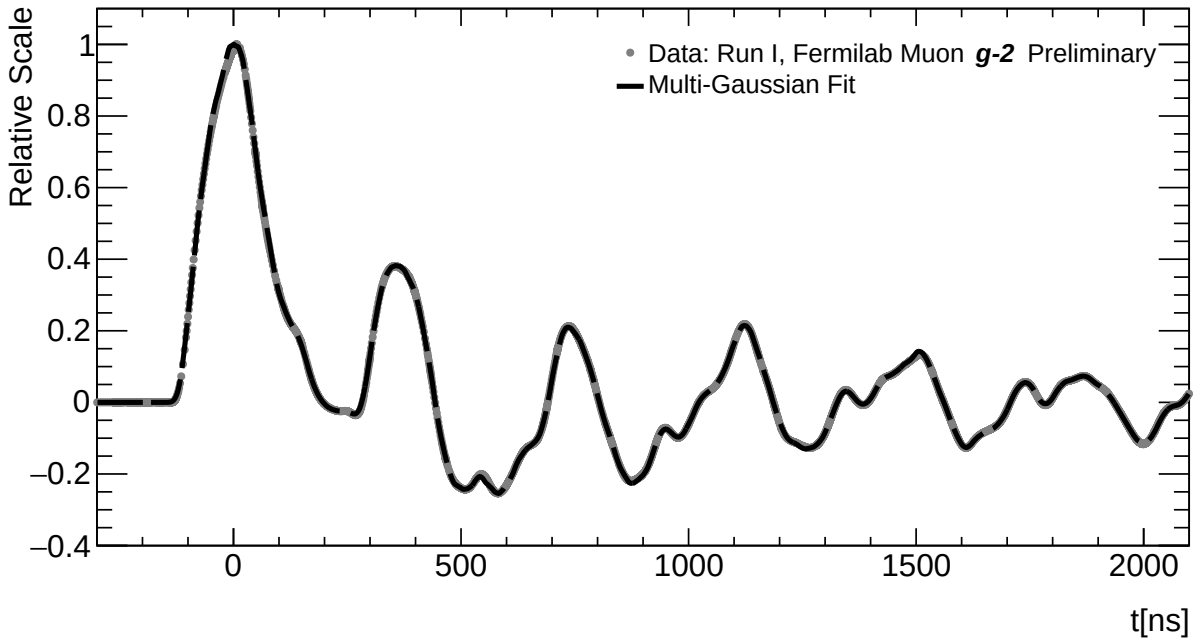

Figure 3.10: Representative kicker strength pulse during the first run of the muon g-2 experiment, measured with a magnetometer.

In the COSY-based model, each injected muon is deflected at each longitudinal center of the three kicker stations per turn. The steering is applied as symplectic kicks in both radial and vertical directions:

$$\Delta a(x,y,t) \approx -\frac{e\Delta L}{p_0} B_y^k(x,y,t) \quad , \quad \Delta b(x,y,t) \approx \frac{e\Delta L}{p_0} B_x^k(x,y,t), \tag{3.12}$$

where ΔL is the design kicker length. The transverse structure of the transient field $\vec{B}^k$ is based on available *OPERA* simulations of the $x-y$ kickers geometry enclosed by the storage

ring vacuum chamber [77]; Fig. 3.11 shows the vector field. The time dependence of $\vec{B}^k$ is

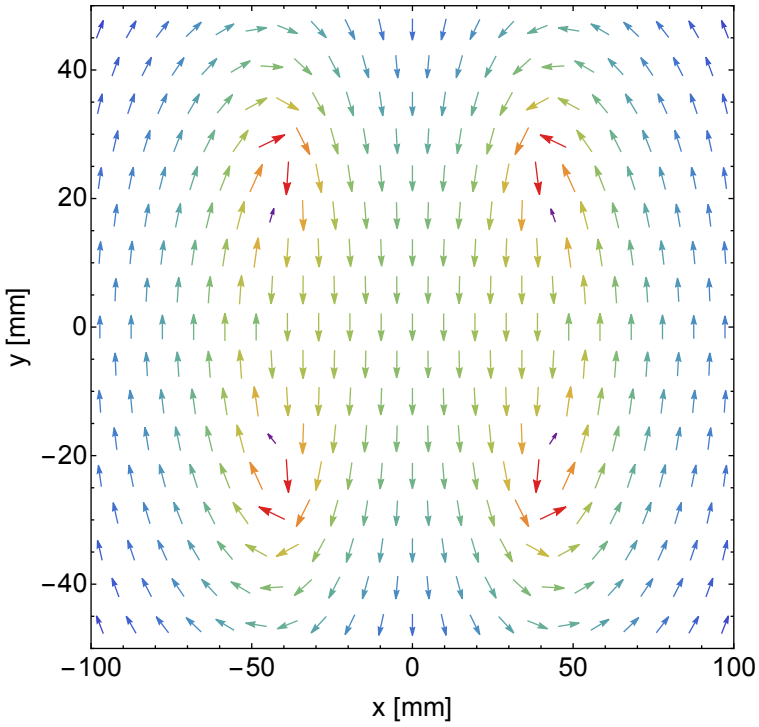

Figure 3.11: Cross section of the magnetic field implemented in the COSY-based model for tracking. The field is stronger near the plate edges and uniform around the center, to deflect muons radially outward.

captured based on magnetometer measurements of the kicker strength (see Fig. 3.10), scaled according to the specific kicker settings of the g-2 data period being analyzed; typical summed kicker strengths during the first production runs were around 130 kV. Further improvements can be made on the implementation of Eqs. (3.12), namely multiple scaled kicks along each kicker station and the addition of momentum-offset dependence.

For spin tracking, a 3×3 rotation matrix $R(\vec{z}_i)$ (due to electric $\vec{E}'$ and magnetic $\vec{B}'$ fields) to act on the initial $\vec{s}_i = (s_x, s_y, s_z)$ spin coordinates of muons in optical coordinates $\vec{z}_i = (x_i, a_i, y_i, b_i, l_i, \delta)$ (see Sec. 3.3 for a definition of the coordinates) is prepared from the

T-BMT equation [48]

$$\vec{\omega}'_S = -\frac{e}{m}\left\{\left(\frac{1}{\gamma}+a_\mu\right)\vec{B}' - a_\mu\frac{\gamma}{1+\gamma}\left(\vec{\beta}\cdot\vec{B}'\right)\vec{\beta} - \left(a_\mu+\frac{1}{1+\gamma}\right)\frac{1}{c}\vec{\beta}\times\vec{E}'\right\} \tag{3.13}$$

where $\vec{\omega}'_S$ is the spin precession frequency in the laboratory frame. The $\vec{z}$ variable δ is the particle momentum offset relative to p_0 and l is proportional to the time of flight relative to the maximum beam's time profile maximum peak, which coincides in turn with the maximum kicker strength at station K2 in COSY-based tracking injection studies. The timing between these two profiles is not easily determined, though no offset between them is a good proxy for storage fraction optimization.

The spin-rotation matrix axis of rotation direction $\vec{u}$—defined in the Frenet-Serret frame relative to the reference particle—is defined from Eq. (3.13). Further expressing the instantaneous precession angle θ' in terms of a differential arc-length advance, the matrix is defined as

$$R(x,a,y,b,\delta) = \begin{pmatrix} \cos\theta' + u_x^2\left(1-\cos\theta'\right) & u_x u_y\left(1-\cos\theta'\right) - u_z\sin\theta' & u_x u_z\left(1-\cos\theta'\right) + u_y\sin\theta' \\ u_y u_x\left(1-\cos\theta'\right) + u_z\sin\theta' & \cos\theta' + u_y^2\left(1-\cos\theta'\right) & u_y u_z\left(1-\cos\theta'\right) - u_x\sin\theta' \\ u_z u_x\left(1-\cos\theta'\right) - u_y\sin\theta' & u_z u_y\left(1-\cos\theta'\right) + u_x\sin\theta' & \cos\theta' + u_z^2\left(1-\cos\theta'\right) \end{pmatrix} \tag{3.14}$$

where

$$u_x = \frac{\omega'_{Sx}}{\omega'_S} \quad , \quad u_y = \frac{\omega'_{Sy}}{\omega'_S} \quad , \quad u_z = \frac{\omega'_{Sz}}{\omega'_S} \tag{3.15}$$

and

$$dt = \frac{dL}{v} = \left(1+\frac{x}{\rho_0}\right)\frac{ds_0}{v} \quad \Rightarrow \quad \theta' = \omega'_S dt = \omega'_S\left(1+\frac{x}{\rho_0}\right)\frac{ds_0}{v}. \tag{3.16}$$

ds_0 is the nominal arc length advance in a time interval dt; ρ_0 is the deflection radius, v the particle speed, and x the radial offset relative to the design orbit. In terms of optical

particle coordinates, momenta p_i and $\beta_i = v_i/c$ in the Frenet-Serret frame can be defined in terms of $\vec{z}_i$ coordinates:

$$\begin{aligned} p_x = \gamma mc\beta_x = p_0 a \quad &\Longrightarrow \quad \beta_x = \tfrac{p_0}{\gamma mc} a = \tfrac{\gamma_0\beta_0}{\gamma} a \\ p_y = \gamma mc\beta_y = p_0 b \quad &\Longrightarrow \quad \beta_y = \tfrac{p_0}{\gamma mc} b = \tfrac{\gamma_0\beta_0}{\gamma} b \\ p_z = \gamma mc\beta_z = p_0\sqrt{(1+\delta)^2 - a^2 - b^2} &\Longrightarrow \beta_z = \tfrac{\gamma_0\beta_0}{\gamma}\sqrt{(1+\delta)^2 - a^2 - b^2}, \end{aligned} \tag{3.17}$$

we get

$$\begin{aligned} \omega'_{Sx} &= -\frac{\gamma_0 v_0}{B_0\rho_0}\left\{\left(\frac{1}{\gamma} + a_\mu\right) B'_x - a_\mu \frac{\gamma}{1+\gamma}\left(\vec{\beta}\cdot\vec{B}'\right)\beta_x - \left(a_\mu + \frac{1}{1+\gamma}\right)\frac{1}{c}\left[\vec{\beta}\times\vec{E}'\right]_x\right\} \\ &= -\frac{\gamma_0 v_0}{B_0\rho_0}\left\{\left(\frac{1}{\gamma} + a_\mu\right) B'_x - a_\mu \frac{(\gamma_0\beta_0)^2}{\gamma(1+\gamma)}\left(aB'_x + bB'_y\right) a\right. \\ &\quad \left. + \frac{E'_y}{c}\frac{\gamma_0\beta_0}{\gamma}\left(a_\mu + \frac{1}{1+\gamma}\right)\sqrt{(1+\delta)^2 - a^2 - b^2}\right\}, \end{aligned} \tag{3.18}$$

$$\begin{aligned} \omega'_{Sy} &= -\frac{\gamma_0 v_0}{B_0\rho_0}\left\{\left(\frac{1}{\gamma} + a_\mu\right) B'_y - a_\mu \frac{\gamma}{1+\gamma}\left(\vec{\beta}\cdot\vec{B}'\right)\beta_y - \left(a_\mu + \frac{1}{1+\gamma}\right)\frac{1}{c}\left[\vec{\beta}\times\vec{E}'\right]_y\right\} \\ &= -\frac{\gamma_0 v_0}{B_0\rho_0}\left\{\left(\frac{1}{\gamma} + a_\mu\right) B'_y - a_\mu \frac{(\gamma_0\beta_0)^2}{\gamma(1+\gamma)}\left(aB'_x + bB'_y\right) b\right. \\ &\quad \left. - \frac{E'_x}{c}\frac{\gamma_0\beta_0}{\gamma}\left(a_\mu + \frac{1}{1+\gamma}\right)\sqrt{(1+\delta)^2 - a^2 - b^2}\right\}, \end{aligned} \tag{3.19}$$

and

$$\begin{aligned} \omega'_{Sz} &= -\frac{\gamma_0 v_0}{B_0\rho_0}\left\{-a_\mu \frac{\gamma}{1+\gamma}\left(\vec{\beta}\cdot\vec{B}'\right)\beta_z - \left(a_\mu + \frac{1}{1+\gamma}\right)\frac{1}{c}\left[\vec{\beta}\times\vec{E}'\right]_z\right\} \\ &= -\frac{\gamma_0 v_0}{B_0\rho_0}\left\{-a_\mu \frac{(\gamma_0\beta_0)^2}{\gamma(1+\gamma)}\left(aB'_x + bB'_y\right)\sqrt{(1+\delta)^2 - a^2 - b^2}\right. \\ &\quad \left. - \frac{\gamma_0\beta_0}{\gamma}\left(a_\mu + \frac{1}{1+\gamma}\right)\left(a\frac{E'_y}{c} - b\frac{E'_x}{c}\right)\right\}, \end{aligned} \tag{3.20}$$

where $\vec{E}' = E'_x\hat{x} + E'_y\hat{y}$ and $\vec{B}' = B'_x\hat{x} + B'_y\hat{y}$. For the injection kickers case, $\vec{B}' = \vec{B}^k$ and

$\vec{E}' = 0$.

3.2.4 Beam collimation

The components that define the bounds of the storage volume in the ring are the so-called collimators; see Fig. 3.12. These rings are made of copper, with inner and outer radii of

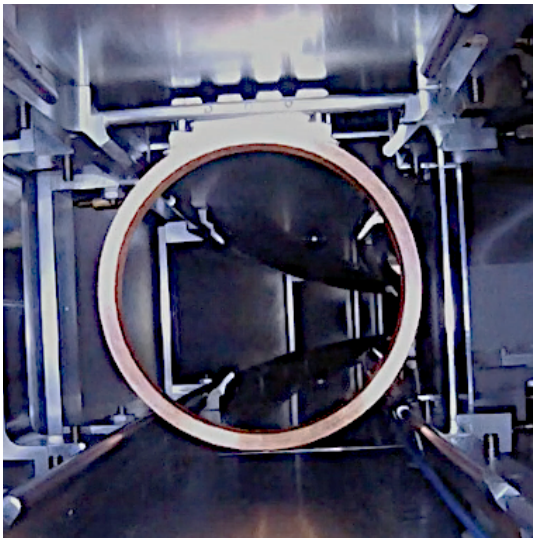

Figure 3.12: Picture of a collimator inserted around the design orbit.

45 mm and 50 mm respectively. Due to their low magnetic susceptibility of -9.63×10^{-6}, the effect on the surrounding magnetic field when they are inserted or retracted is equally negligible [78].

The main purposes of the collimators are to scrape the muons with largest transverse excursions during the first ~ 50 turns after beam injection—while the application of asymmetric voltage along the ESQ stations distort the closed orbits to enhance scraping—and to minimize muon losses while data is taken by excluding significantly the nonlinear electric fields from the ESQ beyond the collimator apertures. For the former intent, muons hitting collimators lose rigidity by transferring energy to the collimators, made of copper. Moreover, once these muons start diverging from the storage volume towards the inner side of the ring,

they do so quick enough so that their corresponding emitted positrons do not enter into the ω_a histogram.

There are five collimator stations along the storage ring, as shown in Fig. 3.1. During the first run of Fermilab's muon g-2 experiment only two collimators were inserted around the ideal orbit to compensate for the initially lower-than-nominal kickers injection scheme. Afterwards, all the 5 collimators were inserted.

With intrinsic procedures in COSY INFINITY, the muon beam is treated as an array of vectors which allows for efficiently collimate muons beyond well-defined apertures during tracking.

3.2.5 Initial beam distribution

As explained in Ch. 2, the accelerator complex at Fermilab delivers highly polarized muon bunches to the g-2 storage ring at 100 Hz. A handful of numerical studies with different programs recreated the beam delivery system during the commissioning of the muon g-2 experiment [52, 54, 79], whose coordinated effort allowed to benchmark each package. For betatron resonance scans and momentum-time correlation studies, an external distribution [80] was taken for subsequent beam analysis with the COSY-based storage ring model. This distribution results from transferring *G4beamline* numerical simulations [54] at the end of the M5 line through fringe fields to the entrance of the ring backleg iron [81]. The maps of these fields are superimposed with the field through the material-free yoke volume where a superconducting inflector is placed to cancel out the field, accounting for the parameters (e.g., inflector angle and field) that maximize the stored fraction. At this point, the mismatched beam is centered ~ 77 mm radially outward from the ideal orbit. Figure 3.13 illustrates the beam distributions in phase space and momentum-time spread. The beam initial time profile

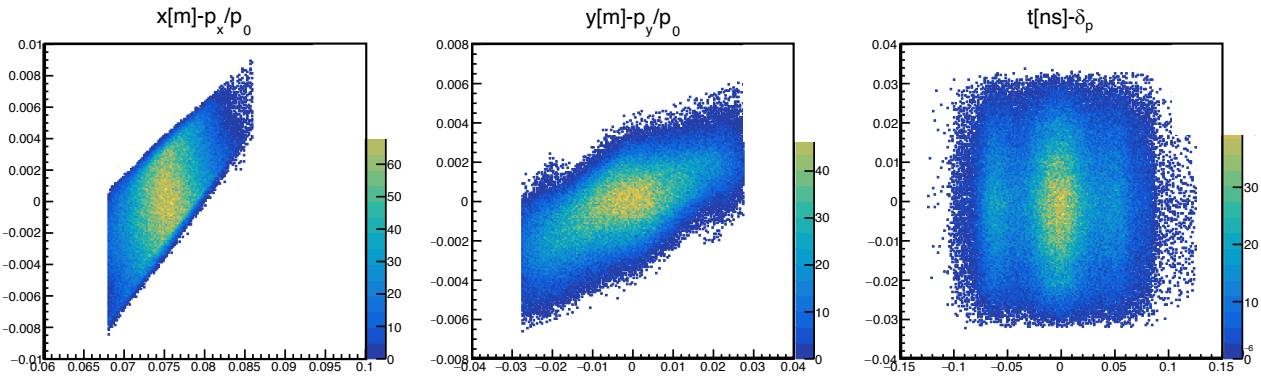

Figure 3.13: Simulated beam distribution at the exit of the inflector, after the final focus to pass the beam through the hole in the backleg iron. The beam is mostly tangential to the design orbit and about 77 mm radially outward at injection.

is set based on measurements from scintillating detectors [39]. Two photomultiplier tubes (PMTs) on the vertical sides of a scintillator read out the resulting light, which is adjusted with density filters to ensure an operational range. Prior to entering the storage ring, the incoming beam crosses the "T0" detector which measures its intensity and longitudinal profile. For beam tracking simulations, an interpolation to T0 data—from the average of a representative train of eight pulses during the first runs of the experiment—replaced the original time profile from the transferred *G4beamline* distribution transferred through the inflector (see Fig. 3.14). The maximum peak of the T0 signal is aligned with the rays originally with no time-of-flight and its relative timing with the central kicker maximum strength is set to zero; this proxy relation is in line with the experimental tuning to maximize muon storage via this parameter. The time profile coupled with the injection kicker ringing signals determine the correlation between time-of-flight and momentum of the stored muon beam.

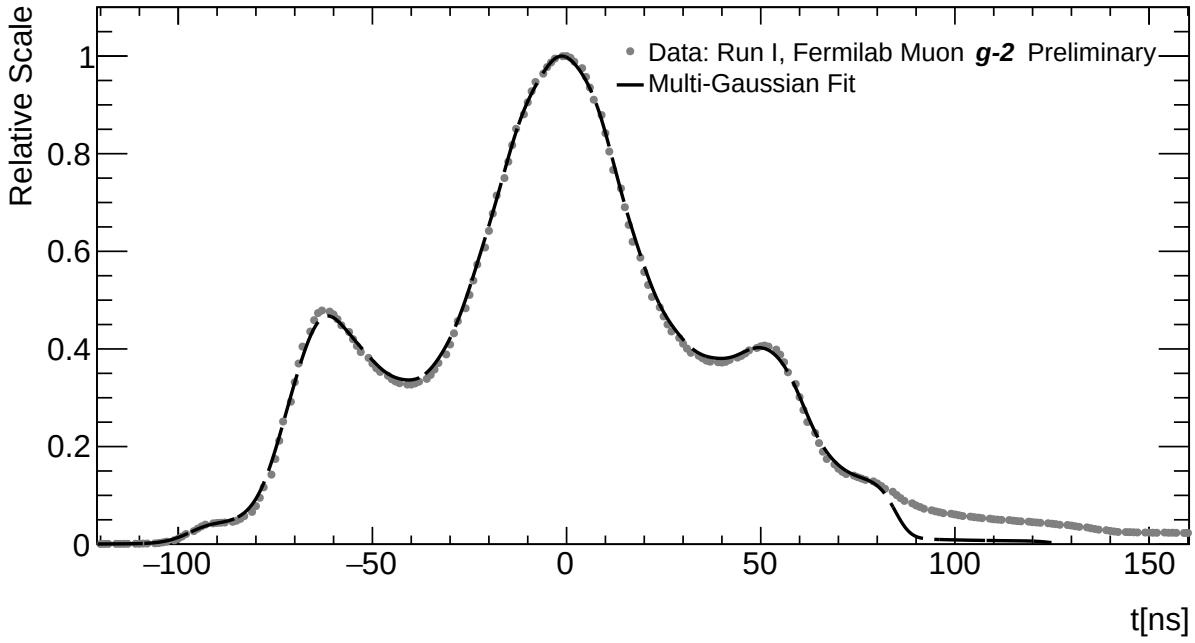

Figure 3.14: Representative longitudinal profile of the muon beam as measured by the T0 detector. Its length is desired to be contained within the main peak of the kicker pulse to maximize beam storage.

3.3 Linear Beam Dynamics

By treating the g-2 storage ring as an optical system, the beam dynamics framework lays out practical conceptual tools for a thorough characterization of the stored beam. To achieve a full extent of such characterization for further a_μ systematic error analysis to the ppb-level, the action of nonlinear guide fields on the muon beam needs to be accounted for (see Sec. 3.4). Nevertheless, the consideration of electric and magnetic fields in the storage ring up to first order (i.e., dipole and quadrupole components in a Taylor-expansion description of the fields, in terms of the optical particle coordinates) encompasses most of the effects that define the beam orbital motion along the ring. Even though the difficult injection process for the muons to get into the storage ring yields the storage volume (i.e., a mostly circular toroid with sectional radius $r_0 \approx 45\,\text{mm}$ and overall radius $\rho_0 \approx 7.112\,\text{mm}$) almost full of

muons, the small admittance limited by the inserted collimators and weak focusing allows to satisfy the paraxial approximation and, this way, the following linear matrix formalism.

In this regime, the equations of motion are linearized so that the optical coordinates of an individual muon $\vec{z}(\theta_2) = \{x_2, a_2, y_2, b_2, l_2, \delta\}$ are defined by its initial state $\vec{z}(\theta_1) = \{x_1, a_1, y_1, b_1, l_1, \delta\}$, where θ_1 and θ_2 are two azimuthal locations in the ring:

$$z_i(\theta_2) = \sum_{j=1}^{6} \left(z_i|z_j\right) z_j(\theta_1) + C_i. \tag{3.21}$$

In Eq. (3.21), z_i is the ith coordinate of the vector $\vec{z}$ where x and y are the horizontal and vertical spatial deviations from the reference orbit[1]; $a = p_x/p_0$ and $b = p_y/p_0$ are the momentum deviations in x and y relative to the reference momentum p_0 (in this case the magic momentum $m_\mu c/\sqrt{a_\mu} \approx 3.094\,\mathrm{GeV/c}$);[2] $l = -(t - t_0)v_0\gamma_0/(1 + \gamma_0)$ a parameter proportional to the time-of-flight $t - t_0$ relative to a reference particle with $t = t_0$, speed v_0 and Lorentz factor γ_0; and $\delta = (p - p_0)/p_0$ the momentum deviation. The $\left(z_i|z_j\right)$ and C_i terms are coefficients derived from the equations of motion and it is customary to arrange them algebraically in a linear matrix $M(1 \to 2)$ such that

$$\vec{z}(\theta_2) = M(1 \to 2)\vec{z}(\theta_1), \tag{3.22}$$

[1] Reference orbit (also known as ideal orbit) refers to the circular trajectory with radius ρ_0, fully horizontal, aligned with the storage ring center, and in the vertical center of the ESQ stations.

[2] Throughout Chs. 3 and 4, coordinates a and b are interchangeable with $x' = dx/ds$ and $y' = dy/ds$, respectively, under paraxial approximation ("s" is the arc length tangential to the reference orbit). That is the case of the storage ring, where $x' \lesssim 6\,\mathrm{mrad}$ and $y' \lesssim 2\,\mathrm{mrad}$.

or in extended form:

$$\begin{pmatrix} x \\ a \\ y \\ b \\ l \\ \delta \end{pmatrix}_2 = \begin{pmatrix} (x|x) & (x|a) & (x|y) & (x|b) & (x|l) & (x|\delta) \\ (a|x) & (a|a) & (a|y) & (a|b) & (a|l) & (a|\delta) \\ (y|x) & (y|a) & (y|y) & (y|b) & (y|l) & (y|\delta) \\ (b|x) & (b|a) & (b|y) & (b|b) & (b|l) & (b|\delta) \\ (l|x) & (l|a) & (l|y) & (l|b) & (l|l) & (l|\delta) \\ (\delta|x) & (\delta|a) & (\delta|y) & (\delta|b) & (\delta|l) & (\delta|\delta) \end{pmatrix} \begin{pmatrix} x \\ a \\ y \\ b \\ l \\ \delta \end{pmatrix}_1 + \begin{pmatrix} C_x \\ C_a \\ C_y \\ C_b \\ C_l \\ C_\delta \end{pmatrix}. \tag{3.23}$$

This formalism permits to treat the g-2 storage ring as an optical lattice made of a sequence of optical elements, where each of these elements is represented with a corresponding matrix defined by the guide fields along its azimuthal span. In the storage ring, there are four types of optical elements in the absence of magnetic field errors or ESQ plate misalignments (see Fig. 3.1 for visualization):

- "*DIEQS*": Short ESQ station ($\theta_{DIEQS} = 13^\circ + 2\theta_{EFB}$ long).
- "*DIS*": Short magnetic section between a short ESQ station (upstream) and a long ESQ station (downstream) ($\theta_{DIS} = 4^\circ - 2\theta_{EFB}$ long).
- "*DIEQL*": Long ESQ station ($\theta_{DIEQL} = 26^\circ + 2\theta_{EFB}$ long).
- "*DIL*": Long magnetic section between a long ESQ station (upstream) and a short ESQ station (downstream) ($\theta_{DIL} = 47^\circ - 2\theta_{EFB}$ long).

As explained in Subsec. 3.2.1, the angle $\theta_{EFB} = z_{EFB}/\rho_0$ accounts for the effective field boundary at the edges of ESQ stations. In this simplified but representative approach, *DIL* and *DIS* are homogeneous sector magnets described [71] by

$$M_{DI}(\theta) = \begin{pmatrix} \cos\theta & \rho_0 \sin\theta & 0 & 0 & 0 & \rho_0(1-\cos\theta) \\ -\sin\theta/\rho_0 & \cos\theta & 0 & 0 & 0 & \sin\theta \\ 0 & 0 & 1 & \rho_0\theta & 0 & 0 \\ 0 & 0 & 0 & 1 & 0 & 0 \\ -\frac{\gamma_0}{\gamma_0+1}\sin\theta & -\frac{\gamma_0}{\gamma_0+1}\rho_0(1-\cos\theta) & 0 & 0 & 1 & -\rho_0\left[\frac{\gamma_0-1}{\gamma_0}\theta - \left(\frac{\gamma_0}{\gamma_0+1}\right)\sin\theta\right] \\ 0 & 0 & 0 & 0 & 0 & 1 \end{pmatrix}, \tag{3.24}$$

where θ is the azimuthal length of the sector and $\rho_0 = 7.112\,\mathrm{m}$ the nominal bending radius. In a similar manner, the *DIEQ* elements correspond to inhomogeneous sector magnets [50] where the inhomogeneity index n_e—which introduces a linear dependence to the effective bending field $B_y(x)$—emerges from the ESQ electric quadrupole gradient:

$$B_y(x) = B_0\left(1 - n_e\frac{x}{\rho_0}\right) \tag{3.25}$$

$$= B_0\left(1 - \left[\frac{\rho_0}{v_0 B_0}\frac{\partial E_x}{\partial x}\right]\frac{x}{\rho_0}\right). \tag{3.26}$$

$B_0 = p_0/e\rho_0 \approx 1.4513\,\mathrm{T}$ is the vertical nominal field and the radial electric field gradient $\partial E_x/\partial x$ horizontally defocuses the positively charged muon beam. The solution of the

linearized equations of motion for such optical element produce the following result:

$$M_{DIEQ}(\theta) = \begin{pmatrix} \cos(\sqrt{1-n_e}\theta) & \frac{\rho_0}{\sqrt{1-n_e}}\sin(\sqrt{1-n_e}\theta) & 0 & 0 & 0 & (x|\delta) \\ -\frac{\sqrt{1-n_e}}{\rho_0}\sin(\sqrt{1-n_e}\theta) & \cos(\sqrt{1-n_e}\theta) & 0 & 0 & 0 & (a|\delta) \\ 0 & 0 & \cos(\sqrt{n_e}\theta) & \frac{\rho_0}{\sqrt{n_e}}\sin(\sqrt{n_e}\theta) & 0 & 0 \\ 0 & 0 & -\frac{\sqrt{n_e}}{\rho_0}\sin(\sqrt{n_e}\theta) & \cos(\sqrt{n_e}\theta) & 0 & 0 \\ (l|x) & (l|a) & 0 & 0 & 1 & (l|\delta) \\ 0 & 0 & 0 & 0 & 0 & 1 \end{pmatrix}, \quad (3.27)$$

where

$$(x|\delta) = \frac{\rho_0}{1-n_e}[1-\cos(\sqrt{1-n_e}\theta)], \quad (3.28)$$

$$(a|\delta) = \frac{1}{\sqrt{1-n_e}}\sin(\sqrt{1-n_e}\theta), \quad (3.29)$$

$$(l|x) = -\frac{\gamma_0}{\gamma_0+1}\frac{1}{\sqrt{1-n_e}}\sin(\sqrt{1-n_e}\theta), \quad (3.30)$$

$$(l|a) = -\frac{\gamma_0}{\gamma_0+1}\frac{\rho_0}{1-n_e}[1-\cos(\sqrt{1-n_e}\theta)], \text{and} \quad (3.31)$$

$$(l|\delta) = -\rho_0\frac{\gamma_0}{\gamma_0+1}\left\{\left[\frac{1}{1-n_e}-\frac{1}{(1+\eta_0)^2}\right]\theta - \frac{1}{(1-n_e)^{3/2}}\sin(\sqrt{1-n_e}\theta)\right\}. \quad (3.32)$$

With these transfer matrices, the coordinates vector $\vec{z}$ of a muon can be transferred through the ring. For instance, the coordinates $\vec{z}_i$ of a muon upstream of a short ESQ station after n full revolutions evolve according to the repeated action of each ring element as follows:

$$\vec{z}_n = M_n^0\vec{z}_i = \left(M_{DI}(\theta_{DIL})\cdot M_{DIEQ}(\theta_{DIEQL})\cdot M_{DI}(\theta_{DIS})\cdot M_{DIEQ}(\theta_{DIEQS})\right)^{4n}\vec{z}_i \quad (3.33)$$

At $HV = 18.3\,\text{kV}$ (a typical ESQ high voltage during Run-1 of the muon g-2 experiment),

the one-turn matrix M_1^0 is[3]

$$M_1^0 = \begin{pmatrix} 0.92045E+00 & -0.25743E+01 & 0.00000E+00 & 0.00000E+00 & 0.00000E+00 & 0.48687E+00 \\ 0.45556E-01 & 0.95902E+00 & 0.00000E+00 & 0.00000E+00 & 0.00000E+00 & -0.35324E+00 \\ 0.00000E+00 & 0.00000E+00 & -0.60304E+00 & 0.18795E+02 & 0.00000E+00 & 0.00000E+00 \\ 0.00000E+00 & 0.00000E+00 & -0.41356E-01 & -0.36936E+00 & 0.00000E+00 & 0.00000E+00 \\ 0.34732E+00 & -0.44242E+00 & 0.00000E+00 & 0.00000E+00 & 0.10000E+01 & -0.49502E+02 \\ 0.00000E+00 & 0.00000E+00 & 0.00000E+00 & 0.00000E+00 & 0.00000E+00 & 0.10000E+01 \end{pmatrix} . \quad (3.34)$$

As shown in M_1^0, the radial and vertical motion in the ring is linearly decoupled (e.g., $(x|y) = (x|b) = (y|x) = (y|a) = 0$). Expectedly, the momentum deviation δ is not influenced by the other orbital coordinates (and $C_\delta = 0$) being the storage ring a time independent Hamiltonian system. Furthermore, one can demonstrate that the transverse coordinates x and y do not diverge since

$$|(x|x) + (a|a)| < 2 \quad , \quad |(y|y) + (b|b)| < 2. \quad (3.35)$$

The map M_1^0 does not account for the ppm-level magnetic field inhomogeneities. When these are introduced in the calculation of the map as explained in Subsec. 3.2.2 based on NMR-probe measurements, constant terms (i.e., C_i terms in Eq. (3.23)) due to the magnetic dipole terms emerge. The nonzero terms in M_1^0 slightly change by less than 0.1 % as a consequence of the normal quadrupole terms from magnetic field imperfections. And moreover, magnetic skew quadrupole terms add weak coupling between the radial and vertical motion via nonzero $(x|y)$, $(x|b)$, $(a|y)$, $(a|b)$, etc. terms. Such new map M_1' relative to

[3] In the following discussion, δ-related components are sometimes expressed in terms of $\delta_k = (K - K_0)/K_0$ instead, where K is the kinetic energy for compatibility with COSY INFINITY's set of particle coordinates. For the momentum acceptance and reference value in the g-2 storage ring, δ and δ_k do not differ by more than $(\gamma_0 + 1)/\gamma_0 - 1 \approx 3.41\%$.

the ideal orbit in the storage ring can be re-expanded around the closed orbit originated by the magnetic field imperfections. Each of the $\vec{z}_0(\theta;\delta) = \{x_0(\delta), a_0(\delta), y_0(\delta), b_0(\delta), 0, \delta\}(\theta)$ momentum-dependent fixed points at any azimuth θ that compose this new closed orbit can be found with the following operation:

$$\vec{z}_0(\theta;\delta) = (M'(\theta) - I)^{-1}\vec{0}, \tag{3.36}$$

where I is the identity map, M' is the original map around the reference orbit at θ, and $\vec{0}$ contains the $\vec{z}$ coordinates of the reference orbit $\vec{0} = \{0, 0, 0, 0, 0, \delta\}$.

In order to extract the field index, Twiss parameters and dispersion functions (See Subsec. 3.3.2), as well as to perform symplectic beam tracking and nonlinear calculations, maps such as M_1' are re-expanded around their corresponding fixed points. This way, the resulting map is origin-preserving (i.e., $M\vec{0} = \vec{0}$). For this purpose, and taking M_1' as an example, the map around the fixed point M_1 is found as follows:

$$M_1(\theta) = M_1'(\theta)\,(\vec{z}_0(\theta;\delta) + I) - \vec{z}_0(\theta;\delta). \tag{3.37}$$

In the linear regime, $M_1 = M_1'$. However, under the presence of nonlinear terms, that is not the case; nonlinear terms leak inside the linear terms of M_1 when $\vec{z}_0$ is nonzero (refer to Sec. 3.4 for the discussion of nonlinear beam dynamics in the muon g-2 experiment). The

resulting one-turn map M_1 for NMR-probe data during the last Run-1 dataset is

$$M_1 = \begin{pmatrix} 0.92089E+00 & -0.25742E+01 & -0.43513E-03 & -0.23697E-03 & 0.00000E+00 & 0.48210E+00 \\ 0.45431E-01 & 0.95891E+00 & 0.26600E-04 & 0.73226E-04 & 0.00000E+00 & -0.35194E+00 \\ 0.88037E-03 & 0.65890E-02 & -0.60221E+00 & 0.18825E+02 & 0.00000E+00 & 0.90815E-02 \\ -0.13050E-04 & -0.12671E-03 & -0.41352E-01 & -0.36789E+00 & 0.00000E+00 & 0.26431E-03 \\ 0.34600E+00 & -0.44366E+00 & -0.35668E-03 & -0.83647E-02 & 0.10000E+01 & -0.49482E+02 \\ 0.00000E+00 & 0.00000E+00 & 0.00000E+00 & 0.00000E+00 & 0.00000E+00 & 0.10000E+01 \end{pmatrix}. \quad (3.38)$$

With these linear maps, beam tracking simulations are plausible with the limitations of not reproducing realistically neither betatron oscillations decoherence (i.e., nonlinear amplitude- and momentum-dependent tune shifts) nor betatron resonance effects (presented in the subsections below). Moreover, the information contained in the $(z_i|z_j)$ terms allow for the characterization of several beam parameters as shown next.

3.3.1 Betatron tunes

It is customary in the g-2 Collaboration to parametrize some dynamical properties of the beam by visualizing the storage ring as a single inhomogeneous sector magnet $M_{DIEQ}(360^\circ)$ (refer to Eq. (3.27)). In this perspective, which is possible thanks for the weak focusing in the ring, the field index n_e is scaled by the ESQ stations occupancy in the ring's azimuth to obtain:

$$n = \frac{4(\theta_{DIEQS} + \theta_{DIEQL})}{4(\theta_{DIEQS} + \theta_{DIS} + \theta_{DIEQL} + \theta_{DIL})} n_e = 0.4376998 n_e. \quad (3.39)$$

During the four Run-1 datasets, the two nominal ESQ voltages were HV = 18.3 kV and HV = 20.4 kV which correspond to the following g-2 field indices:

$$n = 0.108790931 \quad \text{and} \quad 0.121275137. \quad (3.40)$$

For comparison purposes with M_1^0 (Eq. (3.34)), at HV = 18.3 kV the representative linear map is

$$M_{DIEQ}(360^\circ) = \begin{pmatrix} 0.93882E+00 & -0.45717E-01 & 0.00000E+00 & 0.00000E+00 & 0.00000E+00 & 0.47213E+00 \\ 0.45717E-01 & 0.93882E+00 & 0.00000E+00 & 0.00000E+00 & 0.00000E+00 & -0.35279E+00 \\ 0.00000E+00 & 0.00000E+00 & -0.48084E+00 & 0.18906E+02 & 0.00000E+00 & 0.00000E+00 \\ 0.00000E+00 & 0.00000E+00 & -0.40664E-01 & -0.48084E+00 & 0.00000E+00 & 0.00000E+00 \\ 0.35279E+00 & -0.47213E+00 & 0.00000E+00 & 0.00000E+00 & 0.10000E+01 & -0.49560E+02 \\ 0.00000E+00 & 0.00000E+00 & 0.00000E+00 & 0.00000E+00 & 0.00000E+00 & 0.10000E+01 \end{pmatrix}. \quad (3.41)$$

A set of betatron tunes (ν_x, ν_y)—defined as the average number of transverse oscillations per turn—can be calculated from the traces of $M_{DIEQ}(360^\circ)$:

$$\nu_x = \frac{1}{2\pi}\cos^{-1}\left(\frac{(x|x)+(a|a)}{2}\right) = \sqrt{1-n} \quad (3.42)$$

$$\nu_y = \frac{1}{2\pi}\cos^{-1}\left(\frac{(y|y)+(b|b)}{2}\right) = \sqrt{n}, \quad (3.43)$$

where for HV = 18.3 kV:

$$\nu_x = 0.944038701 \quad \text{and} \quad \nu_y = 0.329834703. \quad (3.44)$$

In Table 3.2, relative comparisons with measurements [82] are shown (i.e., $(\nu_x - \nu_x^{data})/\nu_x^{data}$).

Table 3.2: Relative comparisons of computed horizontal tunes with measurements.

HV [kV]	M_{DIEQ}	M_1^0	M_1
18.3	-0.0557%	-0.0108%	-0.0053%
20.4	-0.0701%	-0.0137%	-0.0034%

Radial tunes from the approximated model $M_{DIEQ}(360^\circ)$, from the ideal ring matrix M_1^0 and from a ring with magnetic field inhomogeneities based on measurements present M_1

differ by less than 0.08% relative to tunes extracted from tracker data during Run-1, being M_1 the most accurate case; accounting for the ± 30 ppm background of the normal magnetic quadrupole component yields the superior description of the tunes. As explained in Subsec. 3.6, failures in the instrumentation of the ESQ led to time-dependent tunes which evolved by about 0.5 % during the measurement period. Thus, for the relative differences in Table 3.2 the stable tunes were extracted from the observed frequencies f_{CBO} of the beam radial betatron oscillation at late times of the fills, where

$$f_{CBO} = f_c(1 - \nu_x) \tag{3.45}$$

and the cyclotron frequency f_c is taken as

$$f_c = \frac{p_0}{2\pi m_\mu \gamma_0 \rho_0} = 6.704958\,\text{MHz}. \tag{3.46}$$

As explained in [50], fringe fields at the ESQ edges distort the tunes by less than 0.0008%. Other effects such as ESQ plate misalignments which are not considered in the presented models could be the reason of the small deviation from experimental data. By varying the voltage on the ESQ stations, the set point to control the set of betatron tunes is adjusted. Figure 3.15 shows several computations of the tunes for several ESQ voltages. It is desired to avoid $l\nu_x + m\nu_y = N$ conditions where l, m, and N are integers, which under the presence of the high-order components of the ring's main magnetic field and ESQ electric fields could drive betatron resonances as explained in Sec. 3.4.

Of particular interest for beam de-coherence and betatron resonance analyses are the

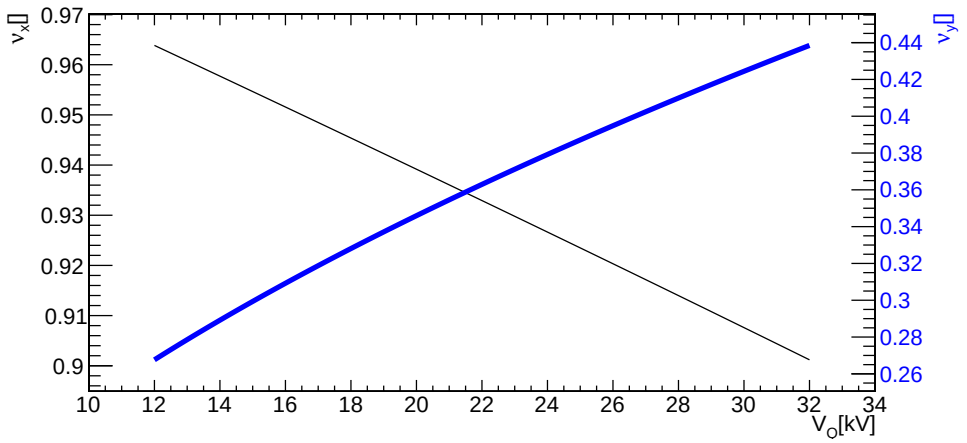

Figure 3.15: Radial (black) and vertical (blue) betatron tunes as a function of ESQ voltage.

linear chromaticities $\xi_{x,y}$, defined as

$$\xi_{x,y} \equiv \frac{\Delta\nu_{x,y}}{\delta} \tag{3.47}$$

where $\Delta\nu_{x,y}$ are tune shifts due to a momentum offset δ. To find them, momentum-dependent fixed points $\vec{z}_0(\theta;\delta)$ are computed and the diagonal terms of the map relative to the fixed points are used to calculate the momentum-dependent tunes:

$$\nu_x(\delta) = \frac{1}{2\pi}\cos^{-1}\left(\frac{(x|x)(\delta)+(a|a)(\delta)}{2}\right) = \nu_x^0 + \xi_x\delta + \cdots, \tag{3.48}$$

$$\nu_y(\delta) = \frac{1}{2\pi}\cos^{-1}\left(\frac{(y|y)(\delta)+(b|b)(\delta)}{2}\right) = \nu_y^0 + \xi_y\delta + \cdots. \tag{3.49}$$

In this way, linear chromaticities for several ESQ voltages are calculated; see Fig. 3.16 for the results.

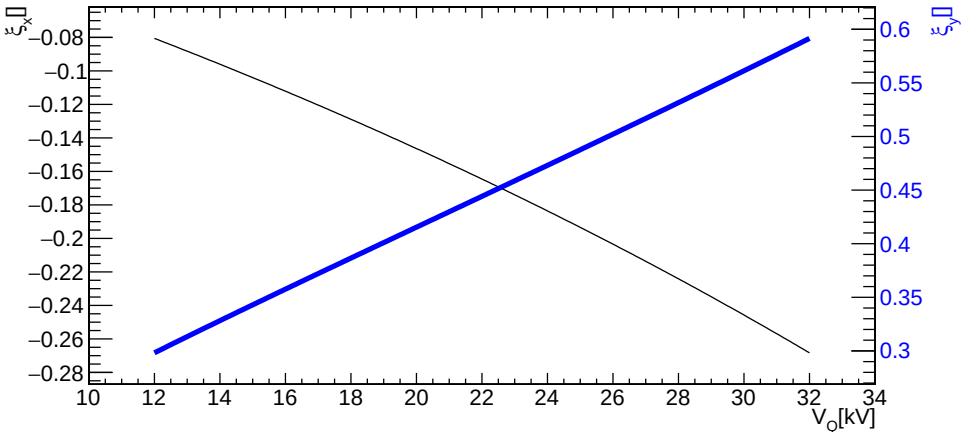

Figure 3.16: Radial (black) and vertical (blue) linear chromaticities as a function of ESQ voltage.

3.3.2 Optical lattice functions

With the origin-preserving linear transfer maps in hand, periodic functions that define the beam structure at equilibrium can be defined [83]. This parametrization results from the guide fields in the storage ring, which in more general terms is an optical lattice that acts on the muons treated as rays. There are three of such functions commonly used:

$$\alpha_x(\theta) = \frac{(x|x)(\theta) - (a|a)(\theta)}{2\sin 2\pi\nu_x}, \quad \beta_x(\theta) = \frac{(x|a)(\theta)}{\sin 2\pi\nu_x}, \quad \gamma_x(\theta) = -\frac{(a|x)(\theta)}{\sin 2\pi\nu_x}. \tag{3.50}$$

The angle θ indicates the azimuthal location in the ring, and the numerator components on the right hand side are extracted from one-turn maps at θ. The situation is analogous for the vertical case. With the guide fields implementation, the one-turn maps are prepared along the ring azimuth and then rotated around their fixed points for the extraction of the optical lattice functions. $\alpha(\theta)$, $\beta(\theta)$, and $\gamma(\theta)$ can also be transferred with the origin-preserving map components between to azimuths, though the former case was chosen for computational efficiency. Figures 3.17 and 3.18 show these lattice functions along the g-2

storage ring for ring configurations during Run-1.

Due to the momentum spread of the stored muon beam, the dispersion function $D_{x,y}(\theta)$ is also necessary to describe the beam. The following periodic condition is satisfied by the dispersion function:

$$\begin{pmatrix} D \\ D' \\ 1 \end{pmatrix} = \begin{pmatrix} (x|x) & (x|a) & (x|\delta) \\ (a|x) & (a|a) & (a|\delta) \\ 0 & 0 & 1 \end{pmatrix} \begin{pmatrix} D \\ D' \\ 1 \end{pmatrix}, \tag{3.51}$$

which implies

$$D_x(\theta) = \frac{(1-(a|a)(\theta))(x|\delta)(\theta) + (x|a)(\theta)(a|\delta)(\theta)}{2-(x|x)(\theta)-(a|a)(\theta)}. \tag{3.52}$$

In Figs. 3.19 and 3.20 dispersion functions for several storage ring settings are presented. The longitudinal derivative of the dispersion function, D', relates to the effect of momentum offsets on a and b and is not relevant for the characterization intended in this dissertation.

For the beam extrapolation around the ring based on beam diagnosis at two azimuthal locations, the following relations between beam widths (interpreted as RMSs and symbolized with σ) and lattice functions are used:

$$\sigma_x^2(\theta,t) = \varepsilon_x(t)\beta_x(\theta,t) + D_x^2(\theta,t)\sigma_\delta^2, \tag{3.53}$$

where the time dependence of the width, β and dispersion functions emerge from evolving guide fields, such as Run-1 during production period (see Sec. 3.6). The momentum distribution spread σ_δ is obtained from Fast Rotation analysis [84]. From realistic simulations with the COSY-based model, in worst-case scenarios accounting for muon scraping, σ_δ varies

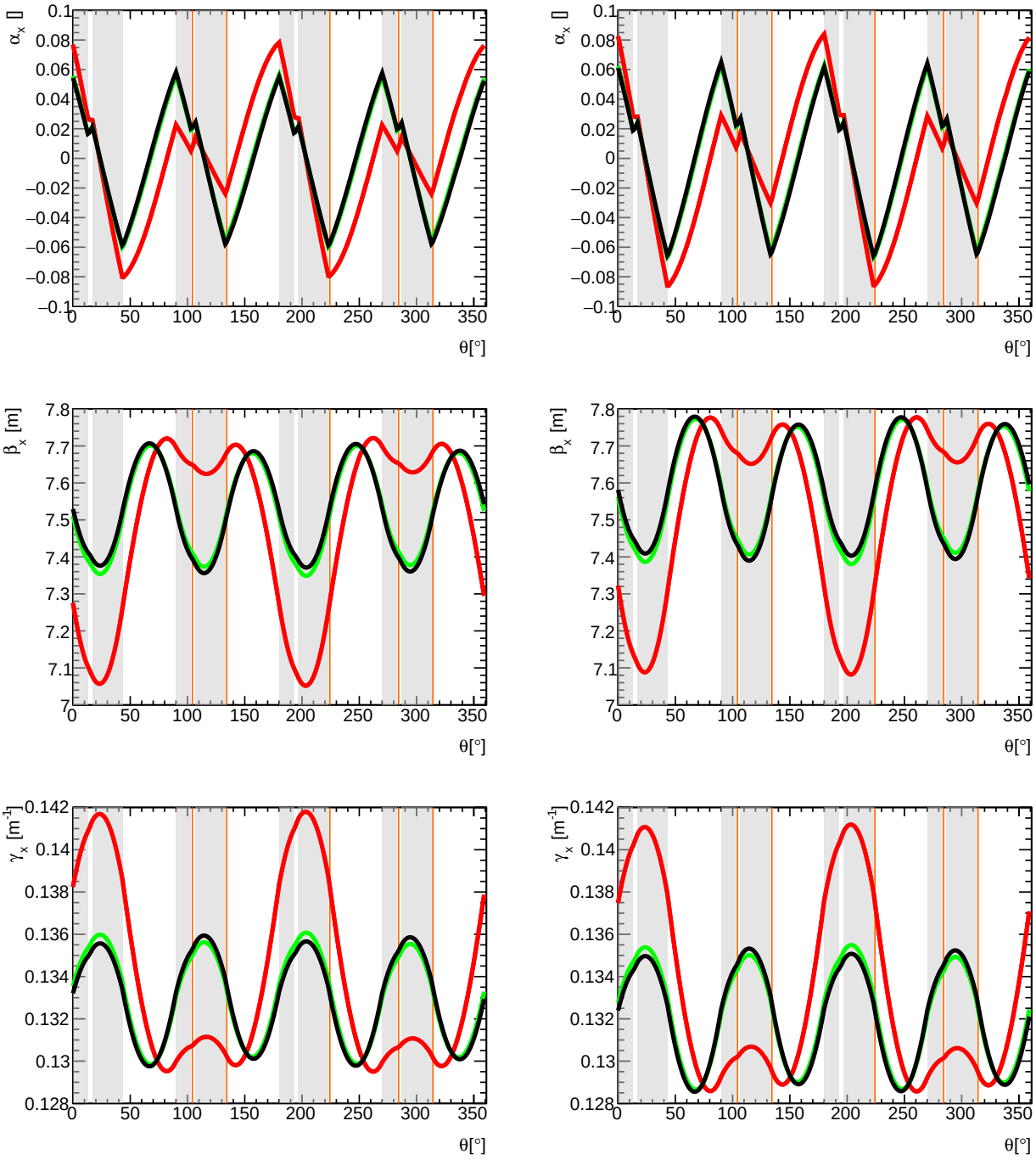

Figure 3.17: Radial α, β, and γ functions at 5 µs (red curves), 20 µs (green curves), and 1000 µs (black curves). On the left-side plots, the HV voltage is 18.3 kV whereas the ESQ set point is 20.4 kV for plots on the right side. Gray shadows depict ESQ stations along the azimuth, where the Q1S upstream edge is at $\theta = 0$. Orange lines indicate collimator locations. Red curves are subject to the effects of the ESQ scraping configuration and the green curves have almost reached the equilibrium values.

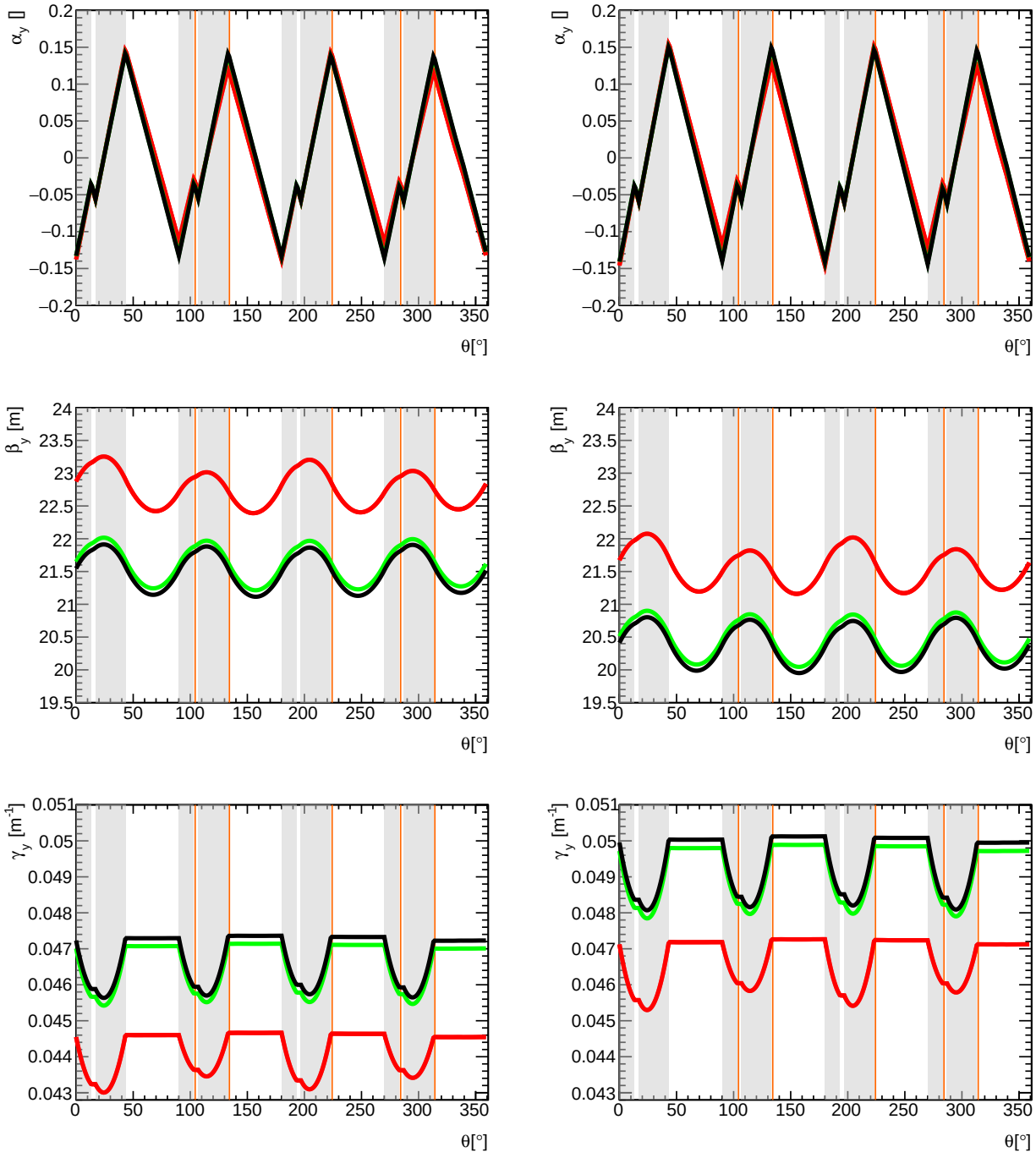

Figure 3.18: Vertical α, β, and γ functions at 5 µs (red curves), 20 µs (green curves), and 1000 µs (black curves). On the left-side plots, the HV voltage is 18.3 kV whereas the ESQ set point is 20.4 kV for plots on the right side. Gray shadows depict ESQ stations along the azimuth, where the Q1S upstream edge is at $\theta = 0$. Orange lines indicate collimator locations. Red curves are subject to the effects of the ESQ scraping configuration and the green curves have almost reached the equilibrium values.

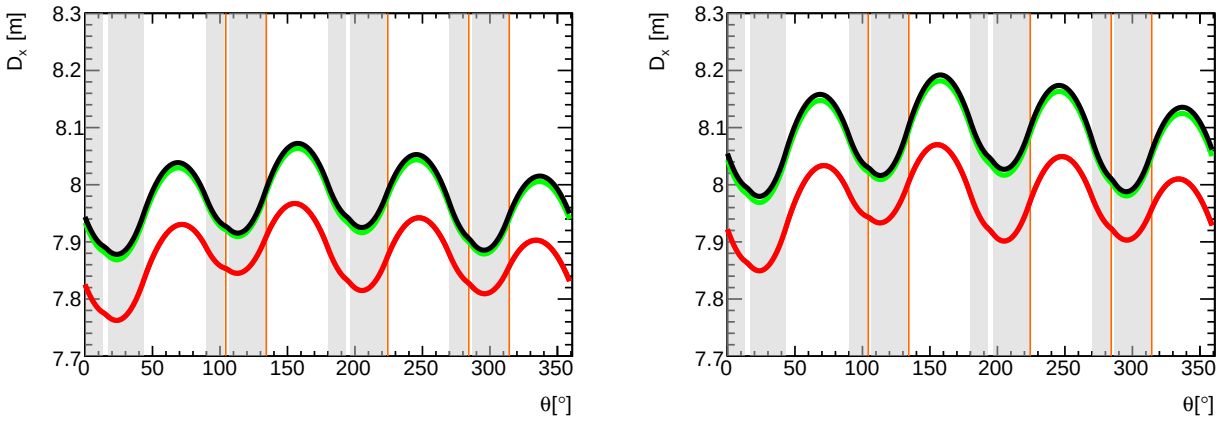

Figure 3.19: Radial dispersion function at 5 µs (red curves), 20 µs (green curves), and 1000 µs (black curves). On the left-side plot, the HV voltage is 18.3 kV whereas the ESQ set point is 20.4 kV for the plot on the right side. Inhomogeneities in the normal quadrupole term of the magnetic field break the four-fold symmetry.

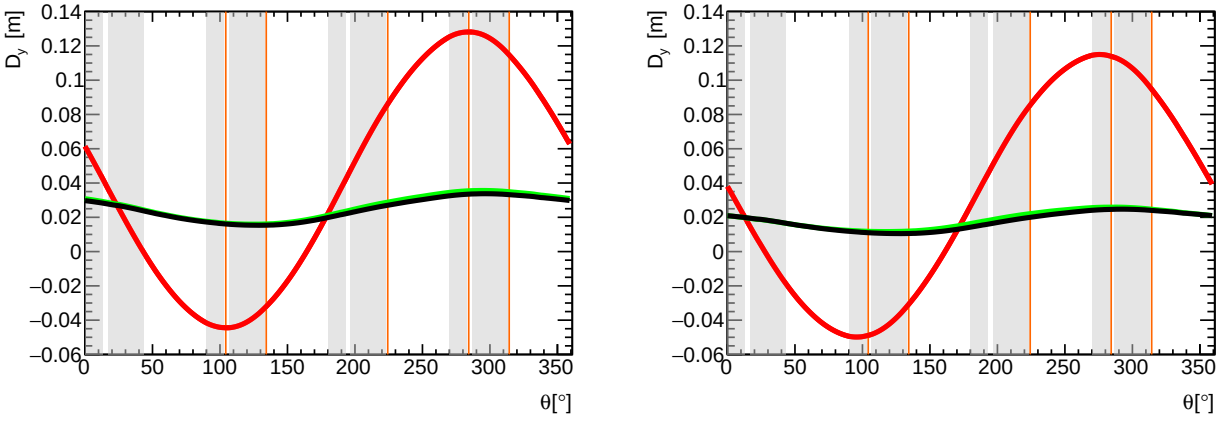

Figure 3.20: Vertical dispersion function at 5 µs (red curves), 20 µs (green curves), and 1000 µs (black curves). On the left-side plot, the HV voltage is 18.3 kV whereas the ESQ set point is 20.4 kV for the plot on the right side. As the magnetic field is mostly oriented vertically, vertical dispersions are negligible.

by less than 0.8% during the muon fill; the sensitivity level of radial widths to this scale of momentum spread variations is small compared to the overall azimuthal width modulations, i.e., on the order of 0.03 mm. For the analogous vertical case, the dispersion from measured magnetic gradients is negligible (see Fig. 3.20) for the beam characterization. The transverse emittance ε_x is the RMS of the beam distribution in phase space:

$$\varepsilon_x = \sqrt{\langle x^2 \rangle \langle a^2 \rangle - \langle xa \rangle^2}. \tag{3.54}$$

With the two straw tracking detectors data of the beam transverse coordinates over time together with Eq. (3.53), the emittance is quantified, allowing to project the beam widths in this way. For vertical width projections, tracker data at only one location is sufficient since $D_y \approx 0$.

The main modulations of the lattice functions are produced by the ESQ electric field and the vertical magnetic field. Magnetic field imperfections mostly from the normal quadrupole component contribute to additional modulations in the optical functions, of about 0.5% or less in relation to the case of a perfect magnetic field (see Figs. 3.21 and 3.22). Since the extracted multipole coefficients from trolley data (except dipole terms) changed by less than 100 ppb relative to B_0, the extra distortions from magnetic field imperfections are not expected to change on a run-by-run basis. On the other hand, ESQ plate misalignments can add gradient errors as well. An external analysis based on alignment survey data [85] have determined them to be similar in size as distortions from magnetic field errors. For Run-1 analysis, the implementation of (and effects from) magnetic field inhomogeneities are necessary for the beam means and widths calculation around the ring; the effects from ESQ plate misalignments are treated as errors.

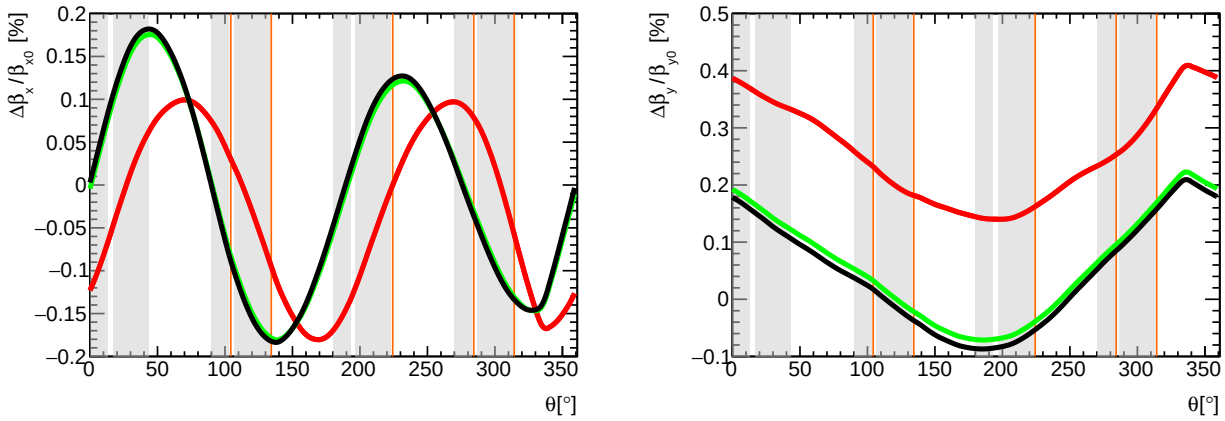

Figure 3.21: Beta function distortions from magnetic field inhomogeneities at 5 µs (red curves), 20 µs (green curves), and 1000 µs (black curves). On the left-side plot, the HV voltage is 18.3 kV whereas the ESQ set point is 20.4 kV for the plot on the right side.

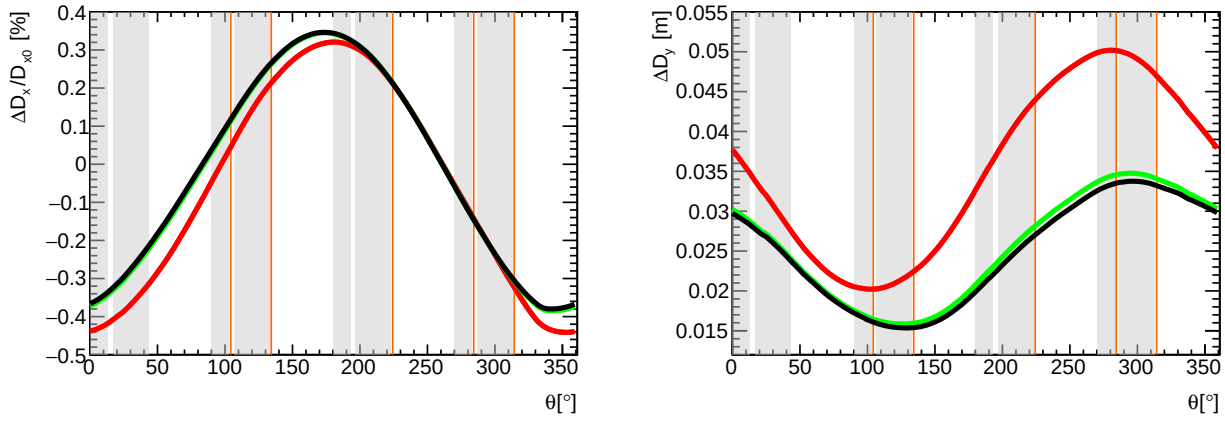

Figure 3.22: Dispersion function distortions from magnetic field inhomogeneities at 5 µs (red curves), 20 µs (green curves), and 1000 µs (black curves). On the left-side plot, the HV voltage is 18.3 kV whereas the ESQ set point is 20.4 kV for the plot on the right side.

The framework provided by the β and dispersion functions as used in Eq. (3.53) is well consolidated for beams with elliptical distributions in phase space and matched—i.e., aligned—with the invariant ellipse of the machine (in this case the storage ring) around the fixed point, defined by:

$$\gamma_x(x - D_x\delta)^2 + 2\alpha_x(x - D_x\delta)(a - D'_x\delta) + \beta_x(x - D_x\delta)^2 = A, \tag{3.55}$$

where A is a constant. Due to the challenging beam injection, the stored beam is mismatched to the invariant ellipse. As a result, coherent betatron oscillations—which mostly vanish at late times of the measurement-period cycles—produce temporal beating around the lattice functions. In spite of the mismatching, the lattice functions recreate the beam modulations around the ring for ω_a systematic corrections and the muon weighting, as explained in Sec. 3.5. The other ingredients for a full description of the muon beam along the azimuth are closed orbit distortions, presented next.

3.3.3 Closed orbits

As defined in this section, closed orbits are—within the framework of transfer maps—the set of fixed points $\vec{z}_0(\theta;\delta)$ for $0 \leq \theta < 2\pi$ that remain unchanged after being transferred around one full revolution ($M'(\theta)\vec{z}_0(\theta;\delta) = \vec{z}_0(\theta;\delta)$). These are obtained via $\vec{z}_0(\theta;\delta) = (M'(\theta) - I)^{-1}\vec{0}$ for $(M'(\theta) - I)$ invertible, as in the g-2 ring case. When the muon coordinates coincide with those of a fixed point, it follows the trajectory defined by the closed orbit in the absence of external perturbations. Furthermore, for a stable system (see Eq. (3.35)), muons within the dynamic aperture and apart from the closed orbit oscillate around it by virtue of the guide field restoring forces. In the linear case, the matched muon beam can be

statistically averaged to a centroid $\bar{z}(\theta, \delta)$ and its spatial coordinates will obey

$$\begin{aligned} \bar{x}(\theta, \delta) &= x_0(\theta, \delta), \\ \bar{y}(\theta, \delta) &= y_0(\theta, \delta). \end{aligned} \tag{3.56}$$

Due to the small momentum acceptance in the g-2 case, an explicit distinction from the momentum-dependent fixed point can be made with sufficient precision, by accounting for the linear momentum dependence of the fixed point:

$$\begin{aligned} \bar{x}(\theta) &= x_0(\theta) + D_x(\theta)\bar{\delta}, \\ \bar{y}(\theta) &= y_0(\theta). \end{aligned} \tag{3.57}$$

Similar to the beam widths case, a mismatched beam exhibits transverse oscillations of its centroids around the closed orbit. In this case, the individual betatron (i.e., transverse) amplitudes $A_{x,y}\sqrt{\beta_{x,y}}$ of the stored muons move coherently per turn N:

$$\begin{aligned} x(\theta, N) &= x_0(\theta) + D_x(\theta)\delta + A_x\sqrt{\beta_x(\theta)}\cos(2\pi\nu_x N + \phi_x), \\ y(\theta, N) &= y_0(\theta) + A_y\sqrt{\beta_y(\theta)}\cos(2\pi\nu_y N + \phi_y). \end{aligned} \tag{3.58}$$

From the harmonic transverse motion in Eq. (3.58), which results from the linear ODEs with the form of Hill's equations[4], oscillations of the mismatched beam centroids and widths emerge. As explained in Sec. 3.4, the coherent modulations tend to de-cohere after beam injection where nonlinear amplitude- and momentum-dependent tune shifts play a significant role.

There are two mechanisms that drive closed orbit distortions relative to the ideal orbit,

[4]As explained in Subsec. 3.4.3, nonlinearities drive betatron amplitude modulations for which cases Eq. (3.58) does not apply.

namely, the asymmetric ESQ voltage application during the first turns after beam injection (see Subsec. 3.2.1) for intentional collimation is one of them, and the presence of magnetic and electric steering errors.

In the former case, the imbalance between voltages from top/bottom and inner/outer ESQ plates induce an electric skew and normal dipole component, respectively. The effect is implemented as constant symplectic terms that act on the transfer map as (see Eq. (3.21))

$$C_{a,b} = -\frac{\Delta V}{D_e} b_0 \frac{e\Delta l}{p_0 v_0}, \tag{3.59}$$

where $\Delta V = V_0 - V'$ is the difference between nominal and mis-powered voltages (e.g., $V_0 = 18.3\,\mathrm{kV}$ and $V' = 13.3\,\mathrm{kV}$ for several Run-1 datasets), $D_e = 5\,\mathrm{cm}$ is the ESQ aperture, and $b_0 = 0.34428$ is the normal dipole term for one top/bottom ESQ plate at 1 V and the others at 0 V [86]. The Δl term is the ESQ segment length over which the additional dipole term is applied ($\sim 1\,\mathrm{cm}$ in the implementation). Once the regular one-turn map is prepared in this manner at several azimuthal locations, their x_0 and y_0 fixed points are calculated with Eq. (3.36) which all together compose the radial and vertical closed orbits. Figures 3.23 and 3.24 displays closed orbits during collimation in red color. The other mechanism through which the ideal orbit is distorted, steering field errors, are driven mostly by the electric and magnetic normal/skew terms (see Subsec. 3.2.2). Figure 3.25 shows closed orbit distortions during Run-1, where the magnetic multipole coefficients were taken from four trolley runs at each Run-1 dataset, named—and ordered in chronological order—as *60h* (1a), *HK* (1b), *9d* (1c), and *EG* (1d). The radial closed orbit evolved due to temperature-induced instabilities in the normal magnetic field, and similarly for the vertical case, whose effect on the overall vertical shift is determined from positrons vertical data as recorded by

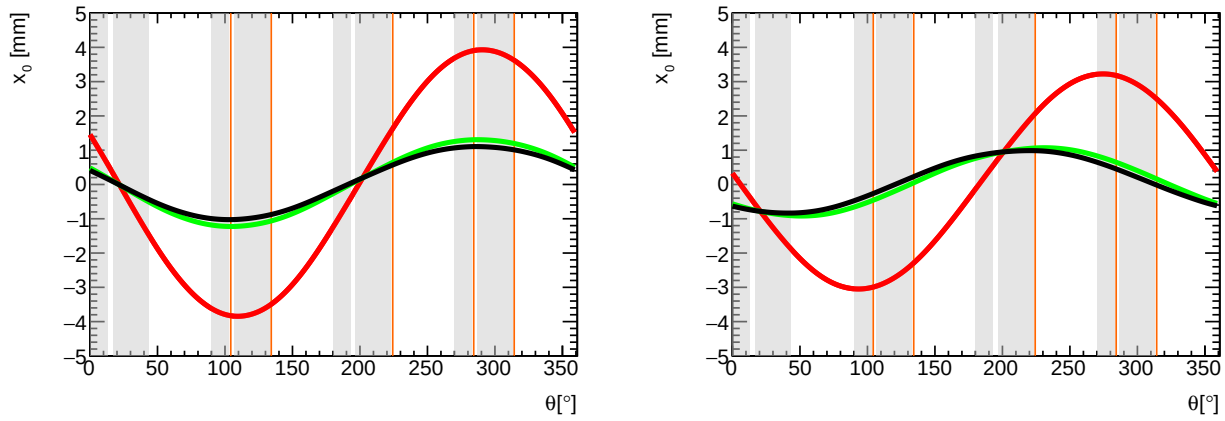

Figure 3.23: Radial closed orbits ($\delta = 0$) at 5 µs (red curves), 20 µs (green curves), and 1000 µs (black curves). On the left-side plot, the HV voltage is 18.3 kV whereas the ESQ set point is 20.4 kV for the plot on the right side. The intentional stretching of the orbit during scraping increases the probability of outermost muons to hit a collimator and, in this way, minimize muon loss rates.

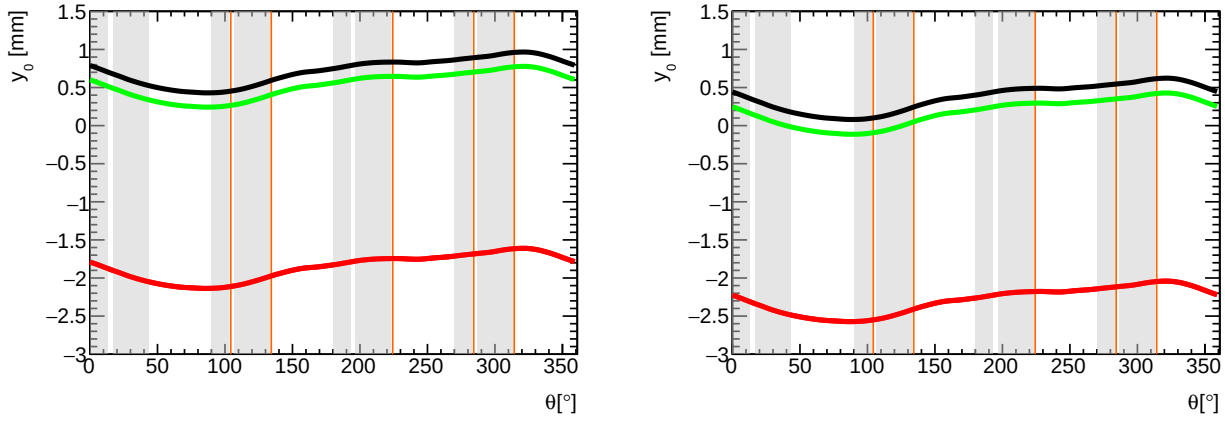

Figure 3.24: Vertical closed orbits at 5 µs (red curves), 20 µs (green curves), and 1000 µs (black curves). On the left-side plot, the HV voltage is 18.3 kV whereas the ESQ set point is 20.4 kV for the plot on the right side. The induced skew dipole ESQ field created from the HV imbalance between the top/bottom plates shifts the vertical closed orbit for beam scraping.

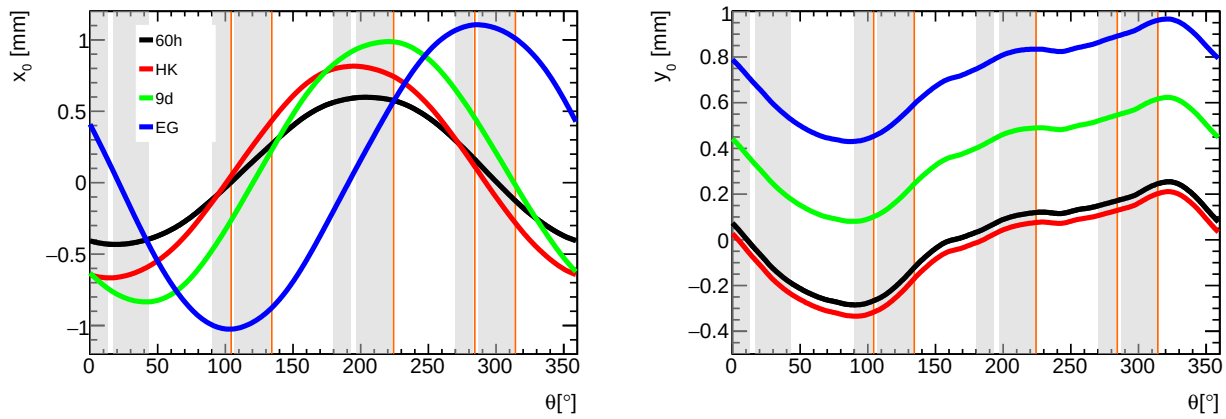

Figure 3.25: Representative closed orbits during the datasets of the first run (Run-1) of the experiment (60h (1a), HK (1b), 9d (1c), and EG (1d)). Fluctuations in temperature affected the dipole terms of the magnetic field, which led to different closed orbits per Run-1 dataset.

calorimeters; the azimuthal average of the implemented skew dipole field $\langle B_0 a_0 \rangle$ is tuned to match these measurements, where a vertical offset of 1 mm corresponds to $\langle a_0 \rangle \approx 19.5\,\text{ppm}$. It is assumed in these calculations that for the first Run-1 dataset $\langle a_0 \rangle \approx 0$, in line with the expected effect of the surface correction coils (SCC) on the radial field.

3.4 Nonlinear Beam Dynamics

Similar to the linear map components described to this point, nonlinear map terms are also calculated by integration of the ODEs where higher-order relations are considered [67]. The nonlinear map $\mathcal{M}$, computed to order n, transfers the initial particle coordinates $\vec{z}(\theta_1)$ at θ_1 to its final state $\vec{z}(\theta_2)$:

$$\vec{z}(\theta_2) = \mathcal{M}(1 \to 2)\vec{z}(\theta_1). \tag{3.60}$$

In this extended regime, the transfer map $\mathcal{M} = \{\mathcal{M}_x, \mathcal{M}_a, \mathcal{M}_y, \mathcal{M}_b, \dots\}$ is treated as a collection of DA vectors in COSY INFINITY and equivalent to the following Taylor polynomial

expansion:

$$
\begin{aligned}
z_i(\theta_2) &= \sum_{j_1 \cdots j_6 = 0} \left(z_i \mid x^{j_1} a^{j_2} y^{j_3} b^{j_4} l^{j_5} \delta^{j_6} \right) (x^{j_1} a^{j_2} y^{j_3} b^{j_4} l^{j_5} \delta^{j_6})(\theta_1). \\
&= C_i + \sum_{j=1}^{6} \left(z_i \mid z_j \right) z_j \, (\theta_1) \\
&\quad + \sum_{j_1 \cdots j_6 = 2} \left(z_i \mid x^{j_1} a^{j_2} y^{j_3} b^{j_4} l^{j_5} \delta^{j_6} \right) (x^{j_1} a^{j_2} y^{j_3} b^{j_4} l^{j_5} \delta^{j_6})(\theta_1).
\end{aligned}
\tag{3.61}
$$

The six summations $j_1, j_2, \ldots, j_6$ start at zero (constant terms) and go up to the order $n = 10$ (i.e., $\sum_{i=1}^{6} j_i \leq 10$) in the presented analysis, which is found to be sufficient to capture all the relevant high-order contributions for nonlinear effects, such as the 20-pole from the ESQ electrostatic field.[5] Nonlinear contributions $\mathcal{O}(2)$ are captured in the terms on the last row of Eq. (3.61); due to their relatively smaller effect on the muons motion when sufficiently away from betatron resonances, they can be treated as aberrations or corrections to the linear system of the g-2 storage ring. Nevertheless, the understanding of experimental observations and the high level of precision demanded for the E989 measurement requires the characterization of the nonlinear motion. In particular, nonlinear detuning, betatron resonances, and nonlinear-driven muon losses are elaborated next.

3.4.1 Momentum- and amplitude-dependent tune shifts

From design, the further muons move away from the closed orbit and the more they deviate from the nominal momentum, the stronger the influence of guide field nonlinear components on their dynamics becomes. This can be seen in Eq. (3.61); as $z_i \to \infty$, the nonlinear polynomial coefficients gain an increasing weight in the transformation of $\vec{z}(\theta_1)$. Thus, betatron

[5] In Eq. (3.37)—and for any re-expansion of maps around fixed points—nonlinear terms are also included.

tunes are no longer subject to only the usual effects from linear forces. The COSY-based environment, COSY INFINITY, allows to capture the effects of nonlinearities on betatron tunes via its differential algebra normal form (NF) algorithm; for a thorough explanation of the algorithm see Ref. [67]. In essence, the algorithm yields a set of NF coordinates for which the transformed map is greatly simplified and leads to rotational invariance up to the calculation order in the NF space. From this order-by-order transformation, the NF coordinates $\{x, a, y, b\} \rightarrow \{s_1, t_1, s_2, t_2\}$ exhibit circular behaviors that depend only on amplitudes and parameters such as δ:

$$\begin{pmatrix} s_1 \\ t_1 \end{pmatrix}_2 = \begin{pmatrix} \cos\left(\nu_x(r_1, r_2; \delta)\right) & -\sin\left(\nu_x(r_1, r_2; \delta)\right) \\ \sin\left(\nu_x(r_1, r_2; \delta)\right) & \cos\left(\nu_x(r_1, r_2; \delta)\right) \end{pmatrix} \begin{pmatrix} s_1 \\ t_1 \end{pmatrix}_1 , \tag{3.62}$$

where $r_1^2 = s_1^2 + t_1^2$ and $r_2^2 = s_2^2 + t_2^2$ are the squared amplitudes in normal form. Thus, with the NF map and a straightforward computation of, say, the arc cosine within the DA framework, the full tunes are expressed as Taylor expansions up to the order of the original map:

$$\begin{aligned} \nu_x &= \sum_{i,j,k=0} \left(\nu_x | r_1^i r_2^j \delta^k\right) r_1^i r_2^j \delta^k, \\ \nu_y &= \sum_{i,j,k=0} \left(\nu_x | r_1^i r_2^j \delta^k\right) r_1^i r_2^j \delta^k. \end{aligned} \tag{3.63}$$

For example, nominal tunes from the linear, origin-preserving maps correspond to the $\left(\nu_{x,y}|1\right)$ terms and linear chromaticities are naturally calculated from $\xi_{x,y} = \left(\nu_{x,y}|\delta\right)$.

A caveat of the rotational invariance in Eq. (3.62) emerges for systems near the effects of resonances. For these cases, the NF algorithm cannot remove some nonlinear map components—otherwise the map would not represent the original transfer—and a direct computation of amplitude-dependent tune shifts is not possible. As such, amplitudes of

rays under the effects of the resonance-driven terms are not constant and thus tunes can evolve over the motion in phase space, losing their physical meaning; however, their limiting average would correspond to the formal definition of a tune as in regular phase space. An important consequence is amplitude modulations that increase muon loss rates in the muon g-2 experiment, as described in Subsec. 3.4.2 and 3.4.3.

A thorough investigation of momentum- and amplitude-dependent tune shifts for the muon g-2 storage ring is reported in Ref. 87. Of special importance on nonlinear detuning is the 20-pole from the ESQ electrostatic potential. Its presence in the storage region is manifested in the amplitude-dependent tune shifts as shown in Figs. 3.26 and 3.27 (for $\delta = 0$) . The shift scaling grows in an 8th-power fashion from the closed orbit toward the

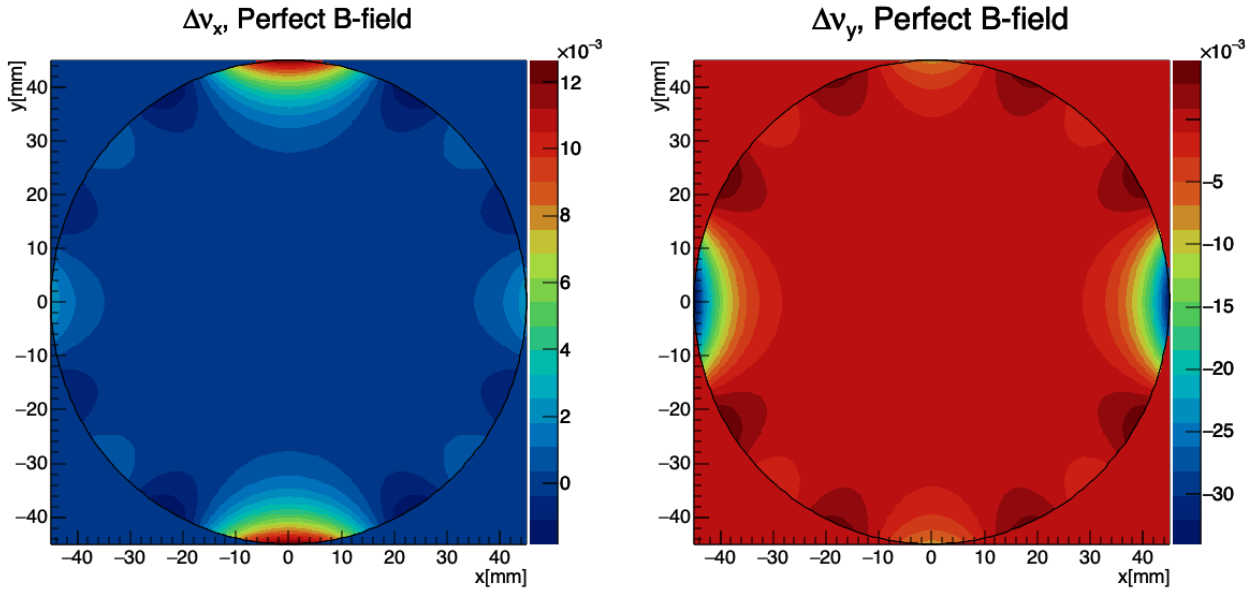

Figure 3.26: Amplitude-dependent tune shifts ($\delta = 0$) within the storage region without magnetic field imperfections (HV= 18.3 kV). The horizontal axis corresponds to radial betatron amplitudes and the vertical axis represents vertical amplitudes.

limiting apertures, as a consequence of the electric 20-pole [87]. On the other hand, magnetic field imperfections do not contribute noticeably to tune shifts as indicated in the figures.

In the momentum-dependent case ($r_{1,2} = 0$), tune shifts are mostly proportional to

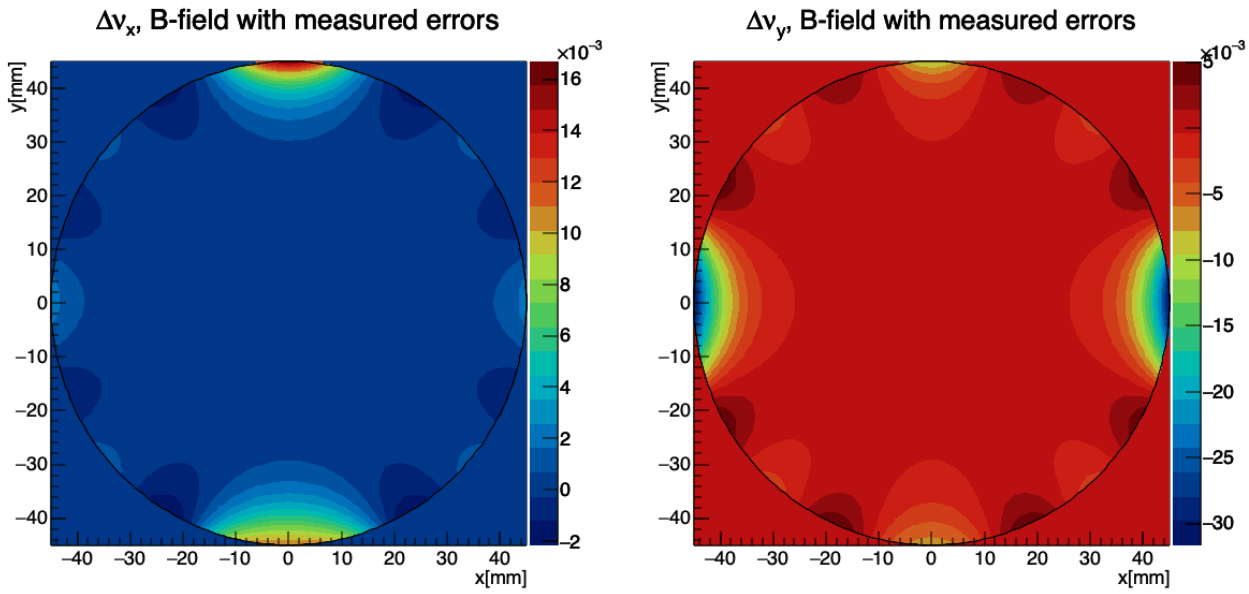

Figure 3.27: Amplitude-dependent tune shifts ($\delta = 0$) within the storage region with magnetic field imperfections (HV= 18.3 kV). The horizontal axis corresponds to radial betatron amplitudes and the vertical axis represents vertical amplitudes.

the linear chromaticities for $|\delta| < 0.2\%$ (see Fig. 3.28). Beyond that region and within the momentum acceptance, tunes experience shifts of $\sim 4 \times 10^{-3}$, being negative in the vertical case. The ppm-level magnetic field errors do not contribute noticeably to momentum-dependent tune shifts.

In reality, muons with the same betatron amplitudes but separated in momentum (see Eq. (3.58) for a good approximation) scan different regions of the storage volume and, consequently, different field nonlinearities. Thus, momentum- and amplitude-dependent have to be treated simultaneously as indicated by $\delta - r_i$ crossed terms in Table 3.3.

Particle-by-particle tune spreading in accelerator machines can lead to beam de-coherence [88]. The g-2 ring is not an exception. Beam tracking simulations with the COSY-based model indicate a strong influence of nonlinearities on the beam de-coherence of the coherent betatron oscillation (CBO). Furthermore, toy Monte Carlo simulations [89, 90] with only COSY-based tune shifts are capable of reproducing the observed beam decoherence. As an

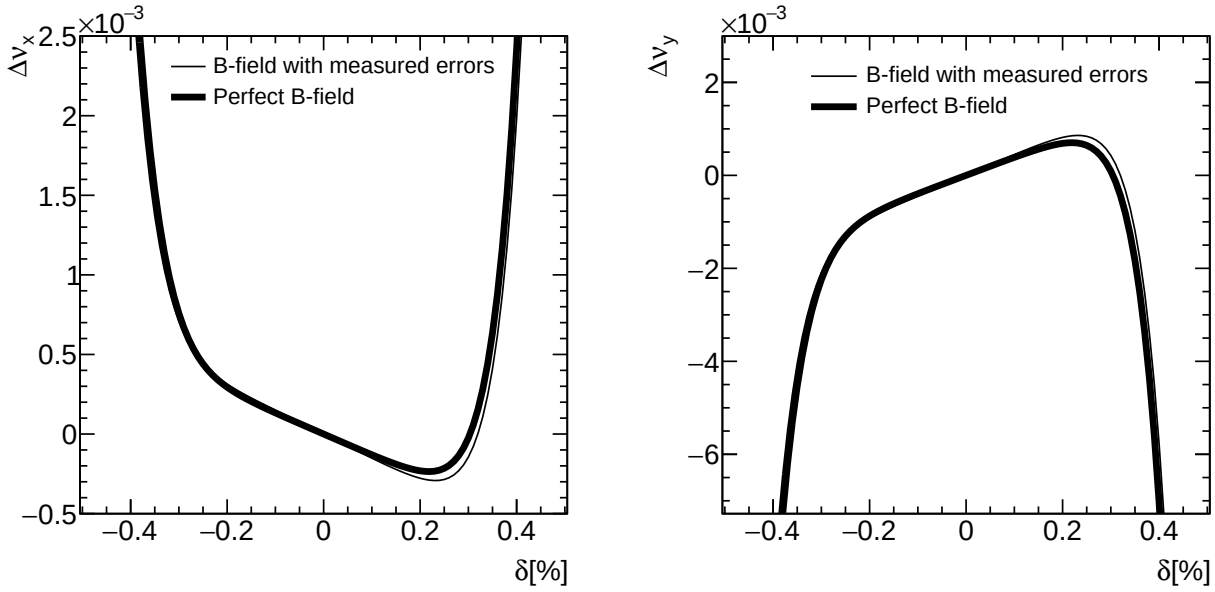

Figure 3.28: Momentum-dependent tune shifts (no betatron amplitudes) with and without magnetic field imperfections (HV= 18.3 kV).Nonlinear shifts take place for $|\delta| > 0.2\%$, inside the momentum acceptance.

example, by taking momentum- and amplitude-dependent tunes in Table 3.3 (up to order 10) with momentum and amplitude $\delta\nu$'s independently and scaled, and reproducing a simulated linear motion as in Eq. (3.58), the radial de-coherence recorded by the g-2 straw tracking detectors is closely recreated (see Fig. 3.29). Without tune shifts, the beam still reduces its initial CBO due to the longitudinal recombination between high- and low-momentum muons as shown in Fig. 3.47. However, without the nonlinear detuning, observations are not reproduced. At the end of the measurement period ($\sim 700\mu s$ after beam injection) a CBO amplitude remanent of about 1 mm might survive as suggested by these simulations extended in time (see Fig. 3.47). Also, Fig. 3.47 suggests small re-coherence pulsations might manifest but to a low extent.

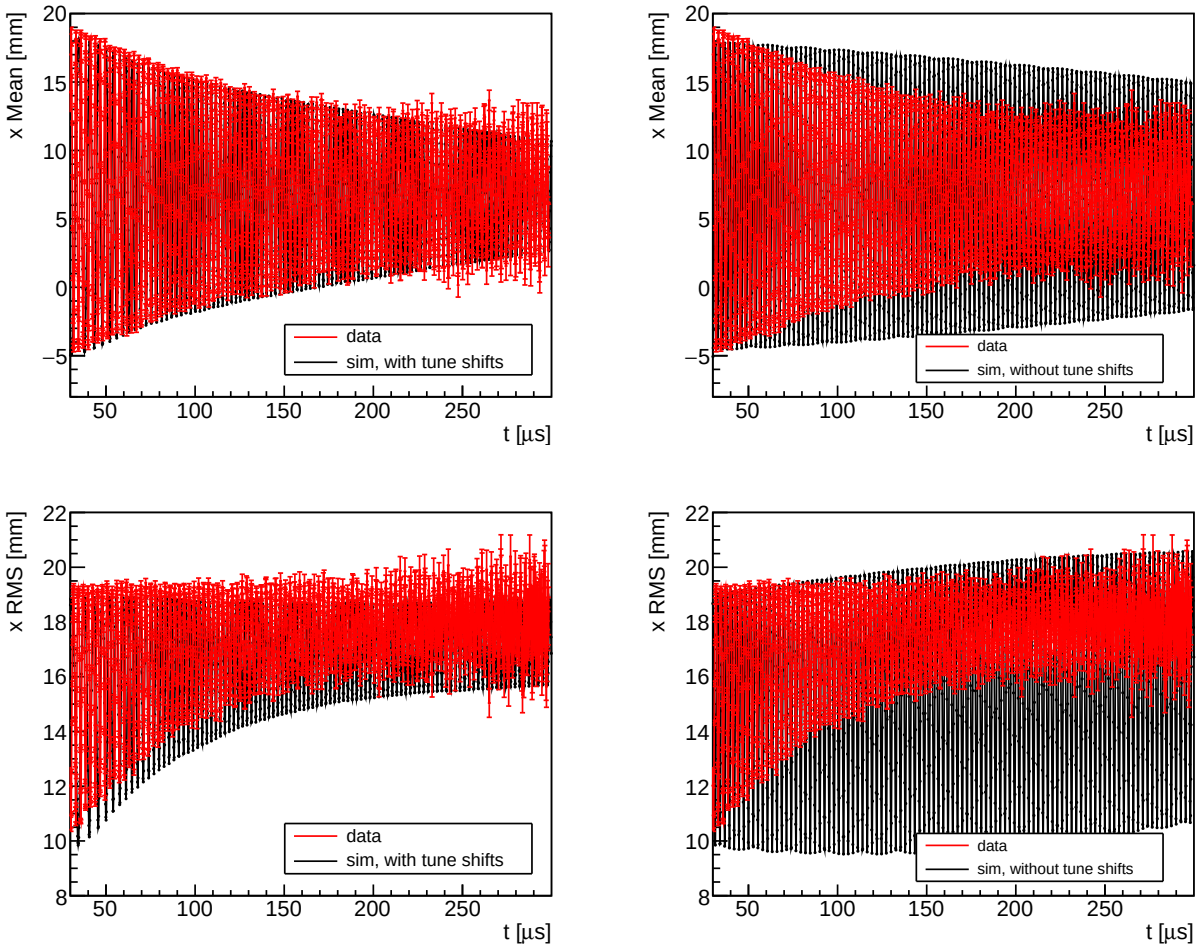

Figure 3.29: Beam radial de-coherence with and without tune shifts at the readout location of the straw tracking detector (station 12). As a reference, data from the tracker is shown in red.

Table 3.3: Tune coefficients at HV= 18.3 kV up to 5th order. Units: $1E\{2(i+j+k)\}$.

Table 3.4: Radial tune

$\left(\nu_x \vert r_1^i r_2^j \delta^k\right)$	order	i	j	k
9.4446263E-01	0	0	0	0
-1.3199935E-03	1	0	0	1
-1.3028752E-06	2	2	0	0
4.2332676E-06	2	0	2	0
-3.9055732E-05	2	0	0	2
6.9991197E-05	3	2	0	1
-4.2045086E-04	3	0	2	1
7.5544892E-04	3	0	0	3
2.3798658E-05	4	4	0	0
-4.1727784E-04	4	2	2	0
6.0854702E-04	4	0	4	0
2.2570512E-03	4	2	0	2
-1.3199217E-02	4	0	2	2
1.1914645E-02	4	0	0	4
1.9657417E-06	5	4	0	1
-3.3974259E-05	5	2	2	1
4.7589424E-05	5	0	4	1
7.9046305E-05	5	2	0	3
-2.8914099E-04	5	0	2	3
3.0339641E-04	5	0	0	5

Table 3.5: Vertical tune

$\left(\nu_y \vert r_1^i r_2^j \delta^k\right)$	order	i	j	k
3.3081444E-01	0	0	0	0
3.8975399E-03	1	0	0	1
4.2332682E-06	2	2	0	0
5.0651491E-06	2	0	2	0
4.3361598E-05	2	0	0	2
-4.2045082E-04	3	2	0	1
6.3490582E-04	3	0	2	1
-2.2468635E-03	3	0	0	3
-2.0863889E-04	4	4	0	0
1.2170941E-03	4	2	2	0
-5.9016314E-04	4	0	4	0
-1.3199216E-02	4	2	0	2
1.9295418E-02	4	0	2	2
-3.4840049E-02	4	0	0	4
-1.6986818E-05	5	4	0	1
9.5177294E-05	5	2	2	1
-5.3892581E-05	5	0	4	1
-2.8913252E-04	5	2	0	3
4.1910614E-04	5	0	2	3
-4.7759203E-04	5	0	0	5

3.4.2 Betatron resonances

When the transverse motion of muons couples with the periodicity of local forces in the storage ring, their betatron oscillation amplitudes may rapidly diverge from the storage volume defined by the collimators, or more commonly experience turn by turn amplitude modulations in a way that they end up hitting the collimators during data taking [64]. Such muons, commonly known as *lost muons* within the g-2 collaboration, give up energy to the material they interact with (see Subsec. 3.2.4), moving inward and whose daughter positrons escape from detection—in Subsec. 3.4.3 the impact of such muons on the ω_a measurement is explained. The electrostatic scraping right after beam injection is crucial for removing

muons with large betatron amplitudes. However, even muons with initially small betatron amplitudes around unstable motion regions and nonlinear fixed points in phase-space could become lost at later times under the modulation effects near resonant conditions.

High-statistical numerical studies of muon loss rates were performed with the COSY-based model to unveil the set of ESQ operating points where significant betatron resonances occur. In Fig. 3.30, simulation results for several high-voltage values applied to the ESQ are presented. The figure shows the fraction of lost muons during the time interval $121 - 186\,\mu$s

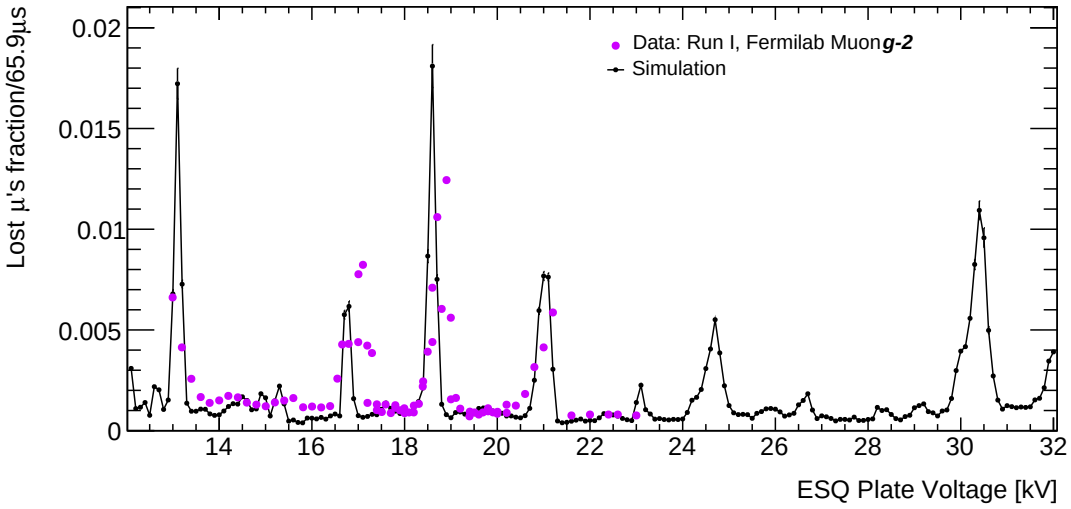

Figure 3.30: Fraction of muon losses between $121 - 186$ μs after beam injection with the COSY-based model for several ESQ configurations. Measurements [11]—shown in arbitrary units—result from detections of minimum ionizing particles that deposit $\sim$ 170 MeV of energy in two adjacent calorimeters within the ring while two collimators were inserted to the storage region.

after beam injection. Vertical error bars correspond to the standard error of the multiple simulations executed in parallel that were necessary to surpass the resolution required and clearly distinguish resonance peaks (i.e., $\sim 6.8 \times 10^6$ muons at beam injection).

Due to the sensitivity of E989, even the relatively small effects of high-order resonance conditions are avoided. To describe the interplay between the field imperfections in the storage ring and the resonant conditions, the ring is idealized as a superposition of a uniform

vertical magnetic field and electric quadrupole fields coming from the ESQ, where all the extra field from the ESQ design and magnetic field imperfections are treated as perturbations to the linear case. In particular, for simplicity this model assumes a smooth behavior of the unperturbed betatron oscillations that does resemble the real case [91]:

$$x(\theta) \approx H\cos(2\pi\nu_x\theta + \phi_x)\,, \quad y(\theta) \approx V\cos(2\pi\nu_y\theta + \phi_y) \tag{3.64}$$

where θ is the azimuth and H and V are constant radial and vertical betatron amplitudes (a good approximation in the weakly focused g-2 stored muon beam), respectively. Considering both magnetic and electric potentials in the form

$$\Phi(x, y, \theta) = \sum_{l=0}^{\infty}\sum_{m=0}^{\infty}\sum_{N=0}^{\infty} {}^{N}C_{l,m}x^l y^m \cos(N\theta + \phi_{lmN})\,, \tag{3.65}$$

we can combine Eq. (3.64) and Eq. (3.65) to estimate the transversal forces in terms of 2k-pole terms ($k = l + m$) and Nth azimuthal harmonics. The leading terms from Fourier analysis of the perturbations yield the following conditions that resonate with the betatron motion:

$$(l-1)\nu_x \pm m\nu_y \pm N = \Lambda\,, \quad l\nu_x \pm (m-1)\nu_y \pm N = \Lambda \tag{3.66}$$

where $\Lambda = \pm\nu_{x,y}$ depending on the field that drives the resonance. In general, vertical forces induce more muon losses than horizontal forces due to the relatively smaller vertical admittance of the ring (about 3 times smaller). The storage ring fields are mostly four-fold symmetric, thus favoring $N = 0, 4, 8, \ldots$. Figure 3.31 depicts resonance lines as well as the operating set points of the storage ring. Resonant tune lines up to $k = 10$ are shown, which are sufficient for our purposes of covering all the main multipole terms that are implemented

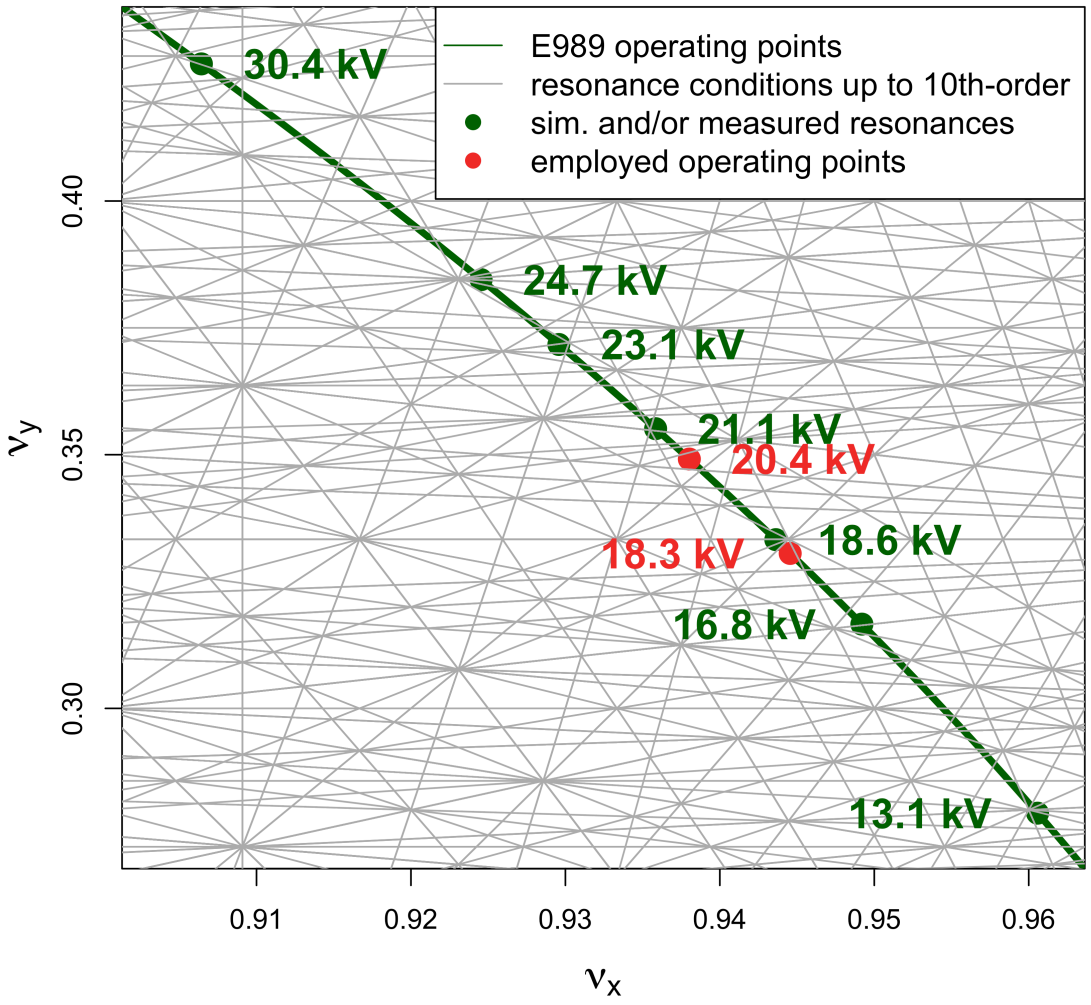

Figure 3.31: An illustration of resonant tune lines and operating points of the g-2 storage ring. The high-voltage applied to the ESQ plates to set operating points are shown next to resonances predicted by numerical studies with the COSY-based ring model. Measurements of lost muons have revealed resonance peaks at $\sim 13.1, 16.8, 18.6,$ and 21.1 kV as well (see Fig. 3.30). Lost muons measurements have not been performed for higher ESQ voltages. Triangular markers show the operating points used in Run-1.

in the COSY-based ring model, including the ESQ 20-pole.

Along with the resonance conditions shown in Fig. 3.31, the observed resonances in the storage ring depend on the angle advancement spread in phase-space, betatron amplitudes, momentum, and initial phase of muons revolving the storage ring. The combination of these properties dictates how frequently a muon traverses unstable conditions in phase-space to experience resonant effects or not. For instance, the continual growth of resonance peak widths for increasing HV observed in Fig. 3.30 relates to the vertical angle advancement spread. This angle, which can be defined as the turn-by-turn angular evolution of the muon coordinates in vertical phase-space at an arbitrary azimuth location, advances in a more periodic manner as the vertical betatron function of the storage ring, β_y, significantly decreases on average for higher voltages within the explored HV range. Regarding betatron amplitudes and momenta, these properties—unique to each muon within the stored beam—also indirectly define the attributes of the peaks presented in Fig. 3.30 in that resonance conditions in Eq. (3.66) are not uniquely satisfied by all the stored muons due to nonlinear tune shifts in the g-2 storage ring. The tune footprint for HV= 18.3 kV (used in Runs 1a and 1d) in Figure 3.32 illustrates this effect. Even though the operational set point is not at resonance, it is close enough to the $3\nu_y = 1$ resonant condition so that momentum- and amplitude-dependent tune shifts push muons to the resonance region.

To minimize systematic errors due to muon losses, the storage ring must run at operating points sufficiently away from betatron resonances. As shown in Fig. 3.31, the system falls into resonance around specific set points and not at every intersection with resonant tune lines. This is mostly due to the rather specific set of nonlinear electrostatic multipoles provided by the ESQ, where the 20-pole has the largest strength, and its fixed 4-fold symmetric longitudinal distribution. In addition, the reinforcement of multiple resonant conditions is

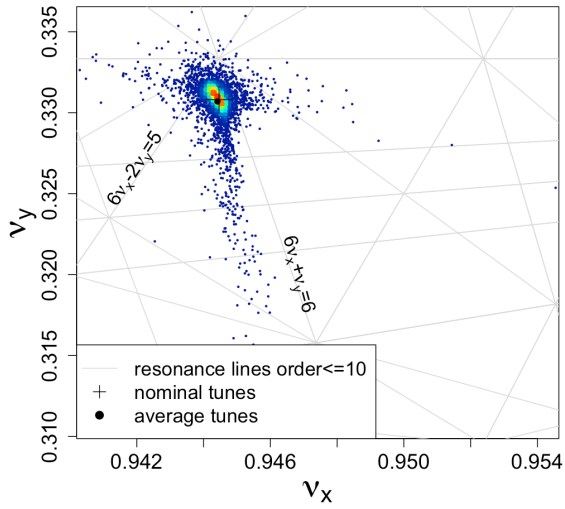

Figure 3.32: With the tune shifts readily available from the COSY-model, momentum and normal form radii of stored muons from a realistic initial distribution as described in Subsec. 3.2.5 are used for the calculation of the tune foorprint. The ESQ set point is 18.3 kV. Due to nonlinear amplitude- and momentum-tune shifts, a considerable fraction of the stored muons are affected by the resonance around in tune space, specially the $3\nu_y = 1$ resonant condition driven by the skew magnetic sextupole term.

also a main determinant of the observed and measured betatron resonances, which can be noticed in their proximity to the points where several resonance conditions converge. Nevertheless, even though the multipoles that describe the measured magnetic field imperfections do not favor particular azimuthal harmonics due to their somewhat random distribution along the ring azimuth, they still have an important effect on betatron resonances as shown next.

Resonance Driving Terms

A deep understanding of the forces that drive betatron resonances is tantamount to a detailed characterization of the conditions in the storage ring that excite muon loss rates. By identifying all the resonances that emerge from the imperfections of the ring already known (i.e., nonlinear electric perturbations contributed by the ESQ and magnetic field inhomo-

geneities from NMR probes measurements), it is possible to address the origin of resonant peaks from lost muons measurements not accounted for in the COSY-based model. Extra peaks could be generated by mis-powering or misalignments of the ESQ plates, transient magnetic fields outside the bandwidth of the NMR probes, and other factors not included in the symplectic tracking simulations that otherwise would be difficult to evaluate and would also directly affect the evolution of ω_a under momentum-spin correlations.

In addition, modifications to the default settings of the simulated ring model permit determining the driving terms that generate each betatron resonance peak. In Fig. 3.33, simulation results are shown for the following modifications to the original ring model configuration (see markers' legend in Fig. 3.33 for each case):

(i) All E-multipoles, B-field inhomogeneities ON (original case, red)

(ii) Only 4th E-multipole, B-field inhomogeneities ON (gold)

(iii) No 20th E-multipole, B-field inhomogeneities ON (magenta)

(iv) All E-multipoles, B-field inhomogeneities OFF (blue)

(v) Only 4th and 20th E-multipoles, B-field inhomogeneities OFF (green)

(vi) No 20th E-multipole, B-field inhomogeneities OFF (orange).

The 2D multipole fits to the magnetic field NMR measurements (abbreviated as "B-field inhomogeneities" in the list above) introduce lost muon fractions of $\sim 6 \times 10^{-4}/\gamma\tau_\mu$ even at operating points away from the main betatron excitations. Betatron resonance peaks observed from measurements and/or simulations can be explained from resonance conditions (Eq. (3.66)) which can be independently driven by one or several electric and magnetic high order multipoles in the storage ring model (see Table 3.6).

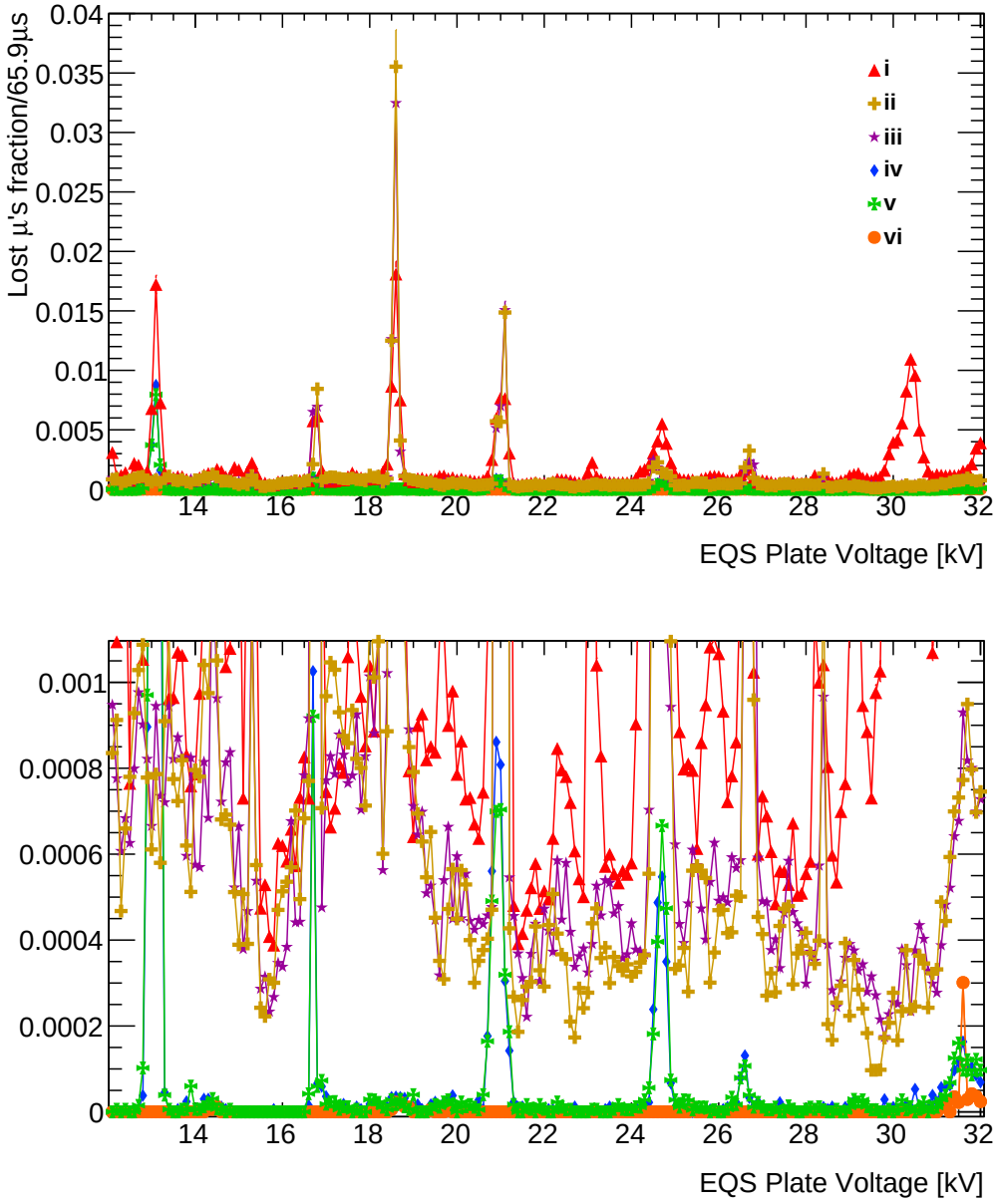

Figure 3.33: Fraction of muon losses from simulations during the time interval $121 - 186\mu$s after beam injection. Configuration details are listed in 3.4.2. The bottom figure depicts lost muon fractions with a reduced vertical range to discern losses when magnetic field imperfections are not accounted for.

Table 3.6: Resonant conditions related to betatron excitations.

HV[kV]	$a\nu_x + b\nu_y = c$
13.1	$3\nu_x + 4\nu_y = 4$
16.8	$\nu_x - 3\nu_y = 0$
18.6	$3\nu_y = 1$
21.1	$2\nu_x + 6\nu_y = 4$
24.7	$\nu_x + 8\nu_y = 4$
30.4	$3\nu_x + 3\nu_y = 4$

Nevertheless, Fig. 3.33 shows the interplay between magnetic(electric) nonlinearities and electric(magnetic) resonances. For instance, for a ring with $HV \sim 13.1$ kV the resonance driven by the electric 20-pole terms derived from the plates curvature is boosted by lower order nonlinearities from the imperfect magnetic field; several resonant tune lines near such an operating point reinforce the resonance. However, by analyzing the high order terms of the storage ring transfer map in Normal Form (NF) it is possible to understand with more detail the role of nonlinearities in relation to resonances.

For $HV \sim 16.8$ kV, either the magnetic or electric guide fields can drive the resonance condition $\nu_x - 3\nu_y = 0$. The magnetic forces build up a larger resonance than the electric case, as found in simulations. In the electric case, electrostatic potential coefficients from the 20-pole are needed to see a resonance. On the other hand, the magnetic octupole can drive the resonance through vertical forces from horizontal magnetic fields proportional to $B_x \propto xy^2$. Azimuthal independence of the electric/magnetic potential (i.e., $N = 0$) is favored for this resonance.

The $HV \sim 18.6$ kV resonance deserves particular attention [92–94] as it is near enough the ESQ operational set points during Runs 1a and 1d (i.e., 18.3 kV). Simulations with the COSY-based model indicate that the resonance is purely driven by magnetic field inhomogeneities, though a reciprocity between resonances and nonlinearities from different

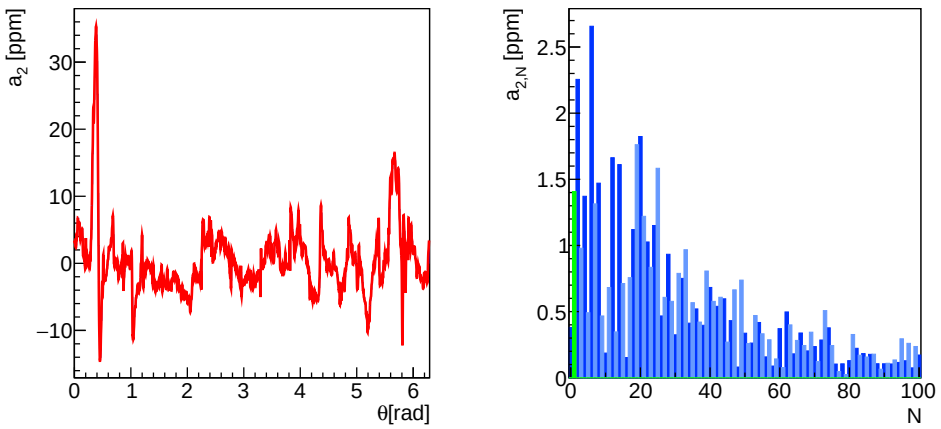

Figure 3.34: On the left, magnetic skew sextupole coefficient a_2 as measured by NMR probes. On the right plot, Fourier decomposition of a_2 in azimuthal harmonics $a_2 = \sum_{N=0}^{n} a_{2,N} \cos(N\theta + \phi_N)$. The $N = 1$ term, which is the main driver of the resonant condition $3\nu_y = 1$, is depicted in green color.

origin—electric or magnetic—exists. The driving force behind this vertical resonance is the radial magnetic field

$$\Delta B_x(x, y, \theta) = -B_0 a_{2,N=1} \cos(\theta + \theta_1) y^2, \tag{3.67}$$

The coefficient $a_{2,N=1}$ is the first azimuthal harmonic of the magnetic skew sextupole; a fast Fourier transformation (FFT) of the measured a_2 in Fig. 3.34 (right plot) shows a non-zero $N = 1$ component, sufficiently large to drive a nonlinear betatron resonance as depicted in Fig. 3.35.

The effect of the $3\nu_y = 1$ resonance extends all the way to the Run-1 ESQ set point $HV = 18.3\,\mathrm{kV}$ thanks to amplitude- and momentum-dependent tune shifts. By turning on and off the skew sextupole component of the magnetic field implementation in the COSY-based model [94], it was demonstrated that in the absence of a_2 the betatron resonance peak at $HV \approx 18.6\,\mathrm{kV}$ does not build up. Moreover, it was also found that by reducing the most prominent peak of the skew sextupole component around the azimuth noticeably reduces $a_{2,N=1}$ and, consequently, the resonance effect. However, it might be more practical

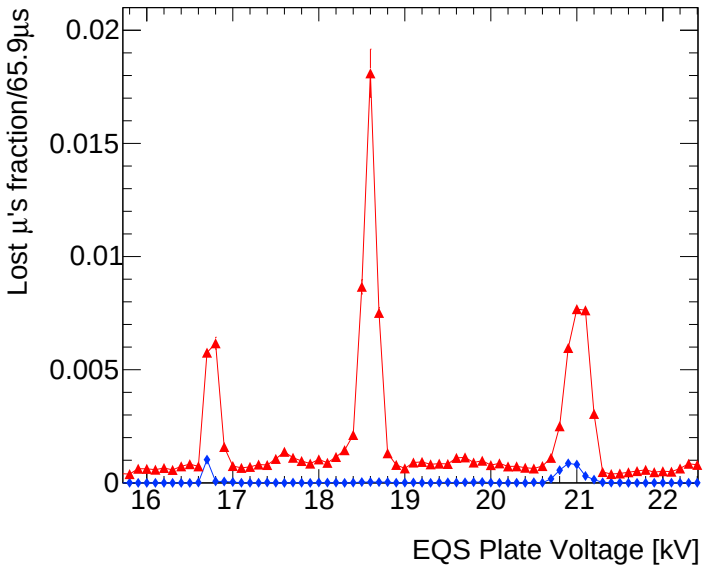

Figure 3.35: Lost muons fraction over a muon lifetime after the scraping stage is completed. In red (triangular markers), all the magnetic multipole terms are turned on during the beam-tracking simulation, whereas in blue (diamond markers), these are turned off. In subsequent simulations, it was found that only the magnetic skew sextupole term from measured field inhomogeneities was sufficient to drive the betatron-resonance peak at $HV \approx 18.6\,\mathrm{kV}$.

to configure the ESQ set point away from $HV \approx 18.6\,\mathrm{kV}$ rather than smoothing out the skew sextupole magnetic field inhomogeneities with active shimming, but it depends on the specific operational circumstances. The impact of equivalent electric skew sextupole coefficients from ESQ plate misalignments was also analyzed. Qualitatively, the sharpness of the observed muon loss rate resonance at $HV \approx 18.6\,\mathrm{kV}$ was not reproduced in this scenario. And quantitatively, the misalignment configuration necessary to recreate a discernible resonance peak was unrealistic based on subsequent misalignment surveys [95]. Thus, it was concluded that the magnetic skew sextupole was the main driving force of the $3\nu_y = 1$ resonance.

3.4.3 Lost muon mechanisms

For a stored beam with momentum-phase correlations at injection time, muons that permanently escape from the storage volume during data taking—and whose decay positrons are

not detected by the calorimeters—can potentially bias the measured ω_a by inducing slow drifts in the phase in Eq. (1.25). Since the BDS delivers a muon beam with a correlation of about 10 mrad per $\Delta\delta = 0.01$ (Subsec. 2.3.4) in the g-2 phase, a reduction of these so-called *lost muons* is tantamount to a mitigation in ω_a systematic errors.

By tracking symplectically the muon beam with the COSY-based model for $n = 1$ and $n = 10$ order transfer maps, a detailed picture of the mechanisms that drive muons to be lost can be developed. Externally to the work presented in this document, several mechanisms that potentially drive muon loss have been studied (for details, see Ref. 96), among them muon scattering with the residual vacuum in the storage region, transient electromagnetic fields, and nonlinear fields away from resonances. In the analysis, it was also determined that the main reason there are lost muons during production measurements in the linear regime is the scraping method implemented after beam injection; a small fraction of muons beyond the limiting apertures of the storage region (i.e., $\sqrt{x^2 + y^2} > 45$ mm at collimator locations) can revolve the ring for thousands of turns before a direct collision with a collimator. Linear simulations reproduce the baseline of muon loss rates shown in Fig. 3.30 [96].

At HV= 18.3 kV (the set point used in Runs 1a and 2d, and next to the ESQ voltage HV= 18.2 kV used in posterior g-2 runs), nonlinear resonances driven by the $3\nu_y = 1$ condition play a significant role in muon loss rates. As shown next, under the Run-1 injection settings nonlinear loss rates contribute to considerably higher muon loss rates than linearly driven losses.

It is helpful to start with a muon that does not get lost in the linear regime and take its motion as a reference, where HV= 18.3 kV. In the stroboscopic view (i.e., at one azimuthal location), such muon follows well-defined elliptical motion in radial/vertical phase space as indicated by Eq. (3.58) and expected from Liouville's theorem. Also, its radii in normal form

coordinates are invariant. Figure 3.36 illustrates the motion in this case. Consequently, the

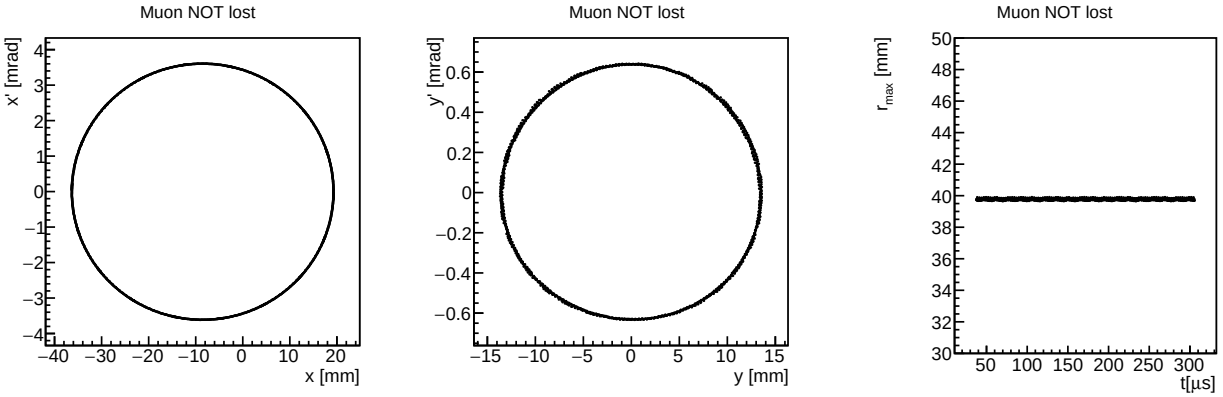

Figure 3.36: Phase space coordinates and maximum excursion of a muon not lost (reference case).

maximum transverse excursion r_0 relative to the ideal orbit can be described as

$$r_{max} = \sqrt{(A_x + |D_x\delta + x_0|)^2 + \left(A_y + |y_0|\right)^2}. \tag{3.68}$$

In fact, this clean dynamics is also expected in the nonlinear regime only when there are no resonance-driven terms that could affect the pursued rotational invariance of a normal form transformation (see Eq. (3.62)).

Lost muons also emerge in COSY-based linear simulations. Even though a muon beam with data-driven initial conditions at 4 μs (see Subsec. 3.6.3) and cleaned following conventional scraping (see Subsec. 3.2.1) is tracked down, about 0.2% of the stored muons at $t > 30\,\mu s$ with $r_{max} > r_0$ remain. Figure 3.37 shows a typical sample of these muons and Fig. 3.38 their maximum excursions, which confirm their survival for several microseconds inside the data-taking time range. High-order resonances are irrelevant in the linear regime, and as a consequence linear chromaticities are the only contributors to small tune shifts, given the constrained momentum acceptance of $\delta \sim 0.55\,\%$ (see Fig. 3.39).[6]

[6]In Subsec. 3.4.3, the color coding is shared between phase space, maximum excursion over time, and

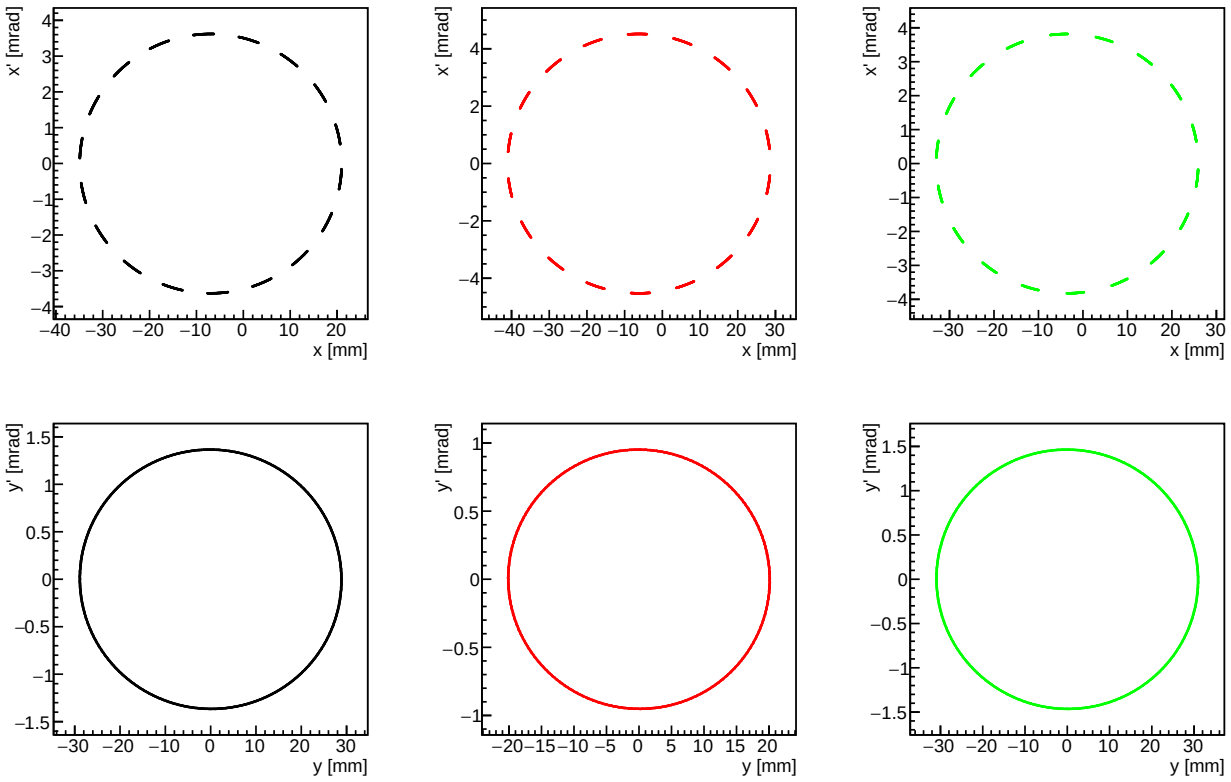

Figure 3.37: Trajectories in phase space of three different muons (distinguished by color) in the linear regime.

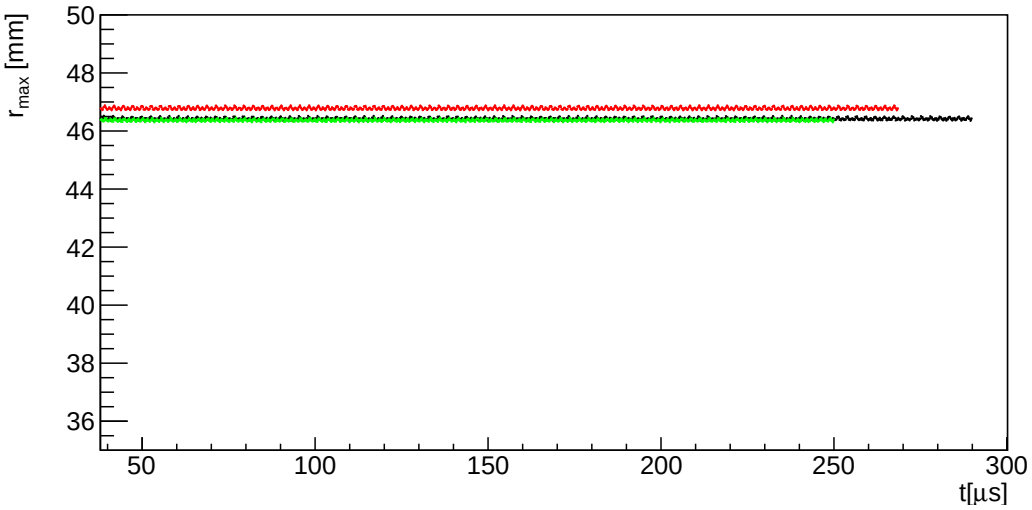

Figure 3.38: Maximum excursions of three lost muons in the linear regime.

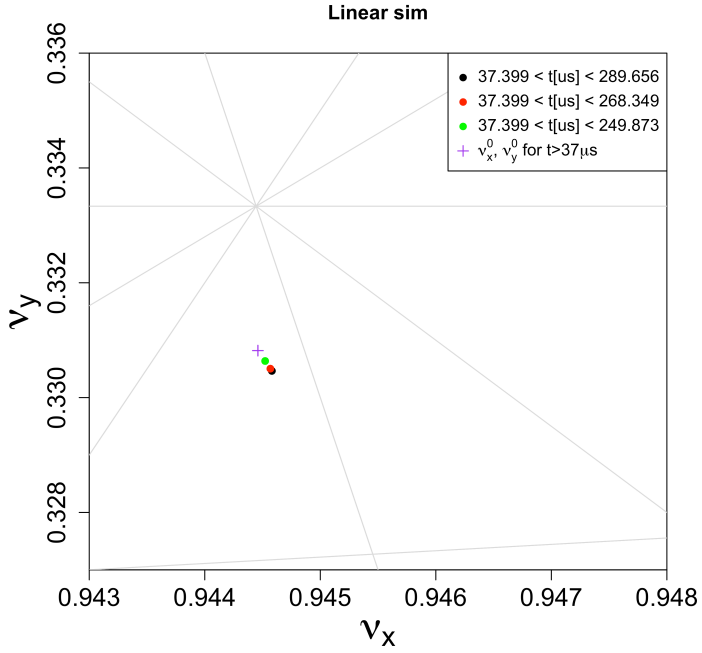

Figure 3.39: Tunes of three lost muons in the linear regime.

Now that lost muons unaffected by nonlinearities are characterized (i.e., it was their fate to be lost from the beginning), the attention is turned to the contrary case for completeness. The same initial muon distribution and scraping scheme are used as in the linear simulations described above. However, the symplectic condition is enforced via a symplectic transformation of the transfer map as described in Ref. 71. In this manner, the Jacobian of the map is equal to one, and consequently the phase space volume is conserved turn by turn, an essential characteristic of Hamiltonian motion.

Figure 3.40 shows phase space in regular coordinates of three muons lost in the nonlinear, symplectic simulations. The radial motion is not influenced by resonance terms, in agreement with the $3\nu_y = 1$ vertical resonance driven by skew sextupole terms of the magnetic field. On the other hand, vertical amplitude modulations manifest and, as a result, maximum excursions evolve over time (see Fig. 3.41). In the linear mechanism, the statistics

tune figures.

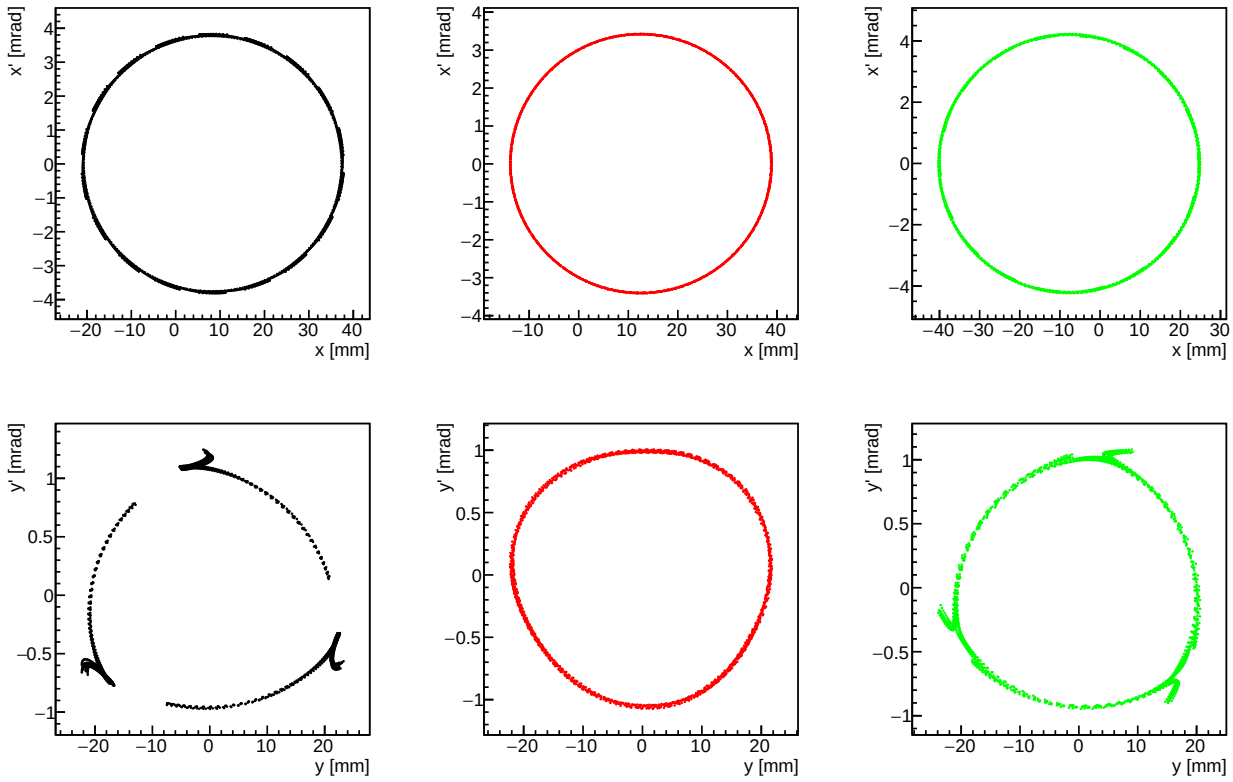

Figure 3.40: Trajectories in phase space of three different muons (distinguished by color) in the nonlinear regime.

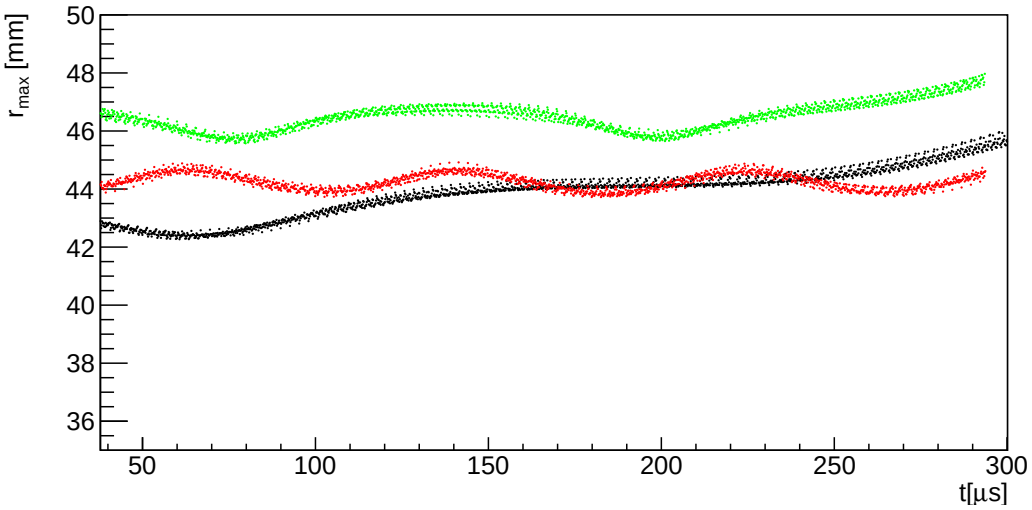

Figure 3.41: Maximum excursions of three lost muons in the nonlinear regime.

involved in the time it takes a muon with $r_{max} > r_0$ is plain. The higher r_{max} is, the faster the muon is lost and loss rates can be derived from Eq. (3.58). On the other hand, muons nonlinearly modulated whose maximum excursions intermittently visit values beyond collimation apertures survive for longer periods, as indicated by linear versus nonlinear muon loss simulation comparisons (see Fig. 3.43).

When the shifted tunes of nonlinearly driven lost muons are extracted as explained in Subsec. 3.4.1, all their coordinates in tune space fall within the vicinity of the $3\nu_y = 1$ resonance as shown in Fig. 3.42; as they move around unstable and stable 3-period fixed points in phase space [12], tunes constantly shift in conjunction with vertical betatron amplitudes in phase space.[7] The period-3 fixed point structures are clearly visible from muon symplectic tracking within the storage region and momentum acceptance, as shown in Fig. 3.44. Vertical betatron amplitudes are modulated as muons move in phase space around the stable and unstable fixed points generated by the $3\nu_y = 1$ nonlinear resonance. Although the motion is stable, modulations interfere with the time it takes for a muon to become lost.

Further studies summarized in Fig. 3.45 were aimed at understanding the multi-dimensional nature of muon loss rates. Using an initial distribution based on straw trackers Run-1a data and conventional scraping, it is concluded that muon loss rates are characterized not only by resonance-driven effects, but by the number of inserted collimators. In the presented results regarding muon loss driving mechanisms, two collimators were inserted (downstream of ESQ stations Q3L and Q4S) as in Run-1 during tracking simulations. For posterior runs, all collimators are inserted, for which case muon loss rates are substantially reduced as suggested by the COSY-based model simulations. However, another factor to account for is the beam injection quality which determines the amount of outermost muons likely to get

[7] Animated examples of lost muon shifting tunes can be found in Ref. 97.

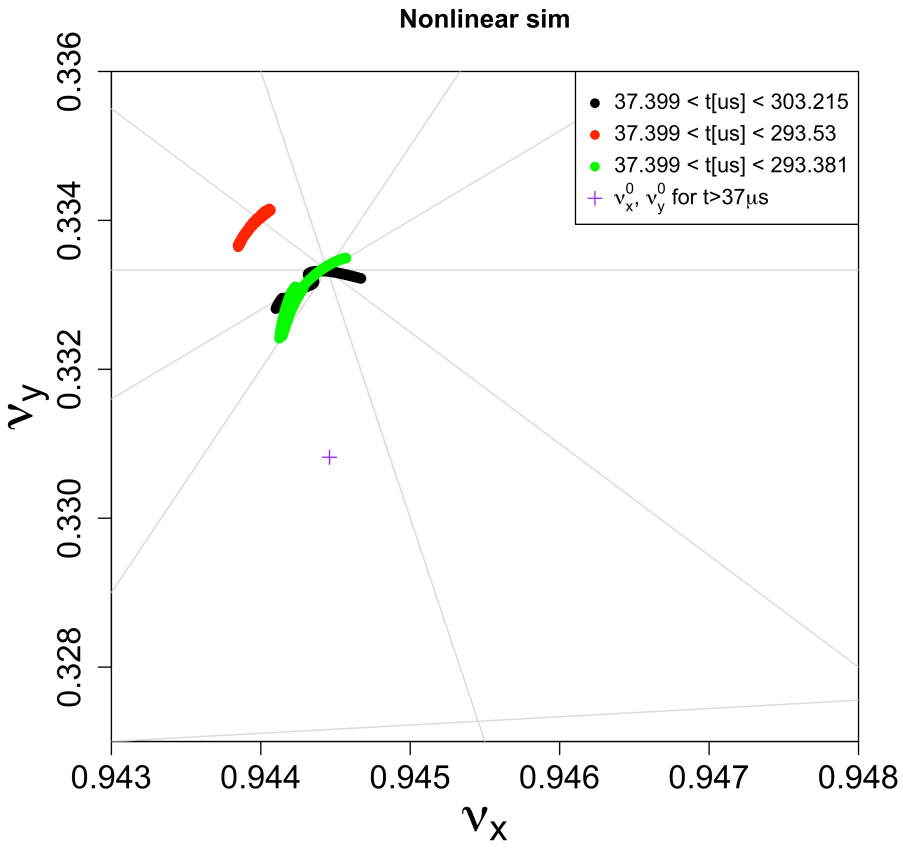

Figure 3.42: Tunes of three muons in the nonlinear regime before getting lost.

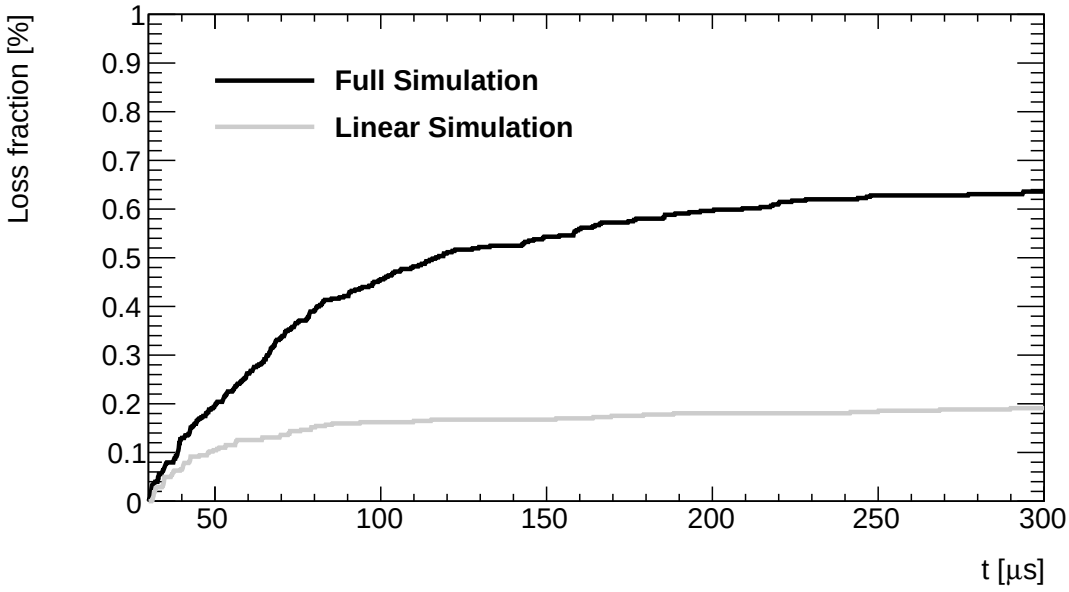

Figure 3.43: Muon loss fractions with nonlinearities (black curve) and without them (gray curve) from symplectic tracking, COSY-based, beam simulations. The ESQ set point was 18.3 kV, two collimators were inserted, and both cases start with the same data-based initial distribution. As observed, muon loss rates are highly affected by nonlinearities of the guide fields.

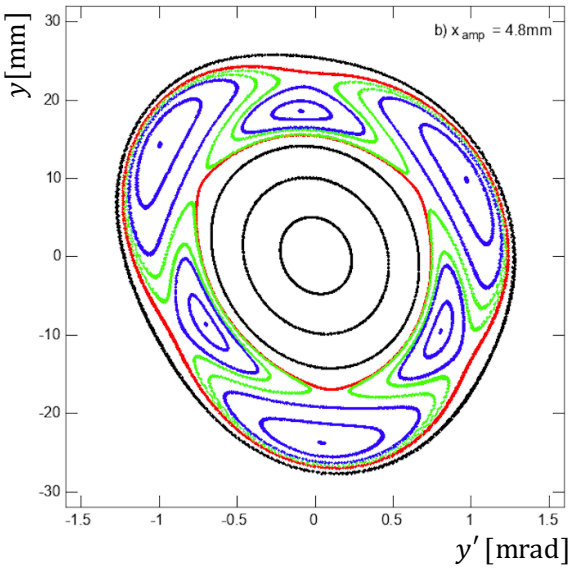

Figure 3.44: Stroboscopic tracking in the vertical phase space illustrating orbit behavior with two period-3 fixed point structures present [12], for ESQ voltage at 18.3 kV. Trajectories in blue and green colors are examples of muons (within the ring admittance and momentum acceptance) with highly modulated vertical amplitudes. Picture author: A. Weisskopf.

lost. In addition, Fig. 3.45 also displays a comparison with and without the effect of the time-evolving ESQ fields during Run-1d (see Sec 3.6), indicating higher a muon loss fraction in the former case as the nominal tune moves toward the $3\nu_y = 1$ resonance and the beam vertical centroid drifts over the data taking period. More important for a reliable analysis of lost muons is the symplectic transformation for tracking; in its absence, an overall emittance growth is observed in simulation results, consequently producing an artificial muon loss fraction increment (see Fig. 3.45).

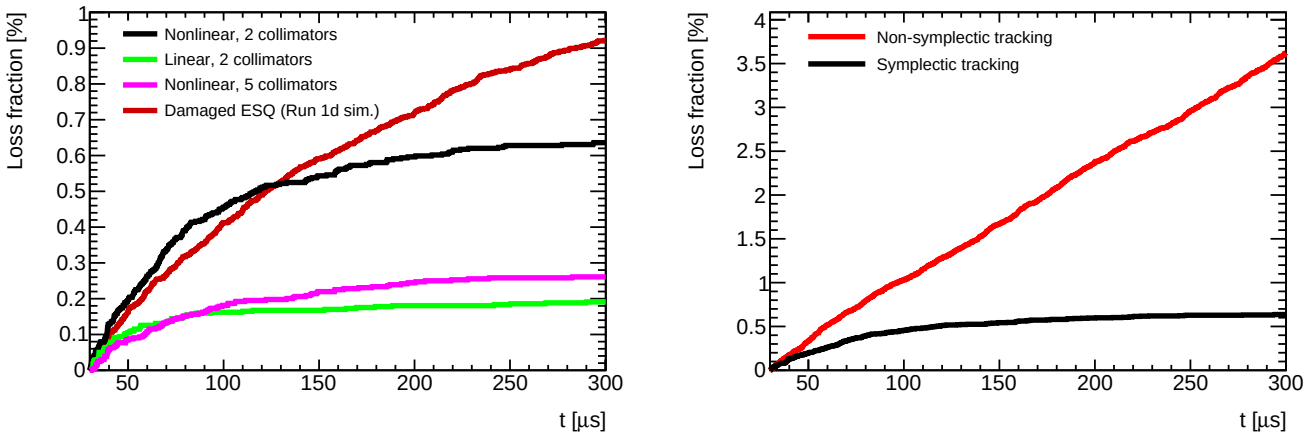

Figure 3.45: Muon loss rates from several tracking simulations (HV=18.3 kV). The effect of damaged resistors, the number of inserted collimators, and the effect from symplectic enforcement during tracking is shown.

3.5 Stored Beam Nominal Characterization

Under regular circumstances, the beam delivery and injection process into the g-2 storage ring at Fermilab, as well as the electric/magnetic lattice inside the ring, specify the temporal and azimuthal behavior of the muon beam. Due to the beam transverse profile being mismatched with the ring optical settings (specially in radial phase space), transverse oscilla-

tions of the beam centroids and widths are common.[8] On the azimuthal side, beam centroids typically follow mm-level closed orbits and beam radial/vertical widths are modulated by the optical lattice (by $\sim 0.4\,\mathrm{mm}$) in an almost four-fold symmetric pattern. By tracking down a realistic beam—whose initial conditions are prepared based on Run-1a beam data (see Subsec. 3.6.3)—with the COSY-based model under nominal settings at HV= 18.3 kV (and magnetic fields as measured around Run-1a), representative samples of the beam over time and azimuth are presented in this section. Several experimental improvements were made after Run-1 concluded, where the radial CBO amplitudes were better controlled and momentum spread became better centered, reducing in this way dispersive effects. However, the main features discussed in this section are always expected to an observational level.

The results presented next serve to characterize the transverse frequencies of the muon beam and validate the implementation of optical lattice functions—as well as a distinction of their limitations—to describe the transverse beam intensity around the azimuth for the g-2 case. These validations are important since the optical lattice functions from the COSY-based model are extensively used for ω_a systematic corrections (i.e., pitch [99], phase-acceptance [16], and Run-1 E-field [100] corrections) and the muon weighting of the magnetic field $\langle B \rangle$ [101].

First, it is useful to specify the boundaries of the stored muon beam. And at the end of the section, the beam initial momentum-time correlation in the g-2 experiment obtained from these studies were used to discover and estimate the largest systematic uncertainty of the E-field correction.

[8] At the time of this dissertation submission, advanced RF techniques to substitute conventional ESQ scraping were being developed by g-2 Collaborators to mitigate beam beating [98].

3.5.1 Beam boundaries

The $r_0 = 45\,\text{mm}$ radius aperture of inserted collimators together with the ring optical lattice define the largest transverse emittance (known as admittance) and momentum acceptance in the storage ring. From these bound parameters, the maximum betatron amplitudes, maximum angles a and b, and limiting momentum can be established along the azimuth. Furthermore, the stored muons fraction is also affected by these quantities as shown in Fig. 3.46.

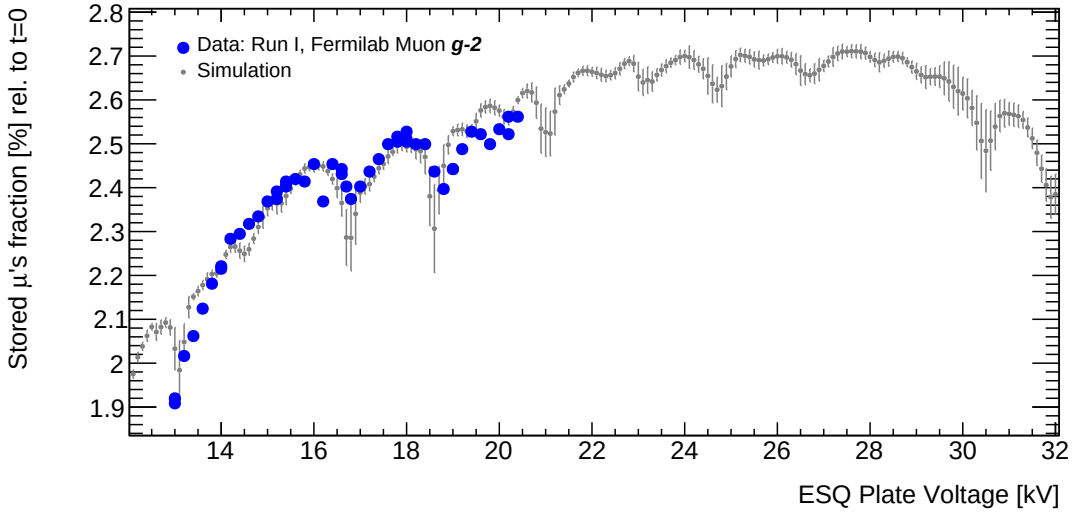

Figure 3.46: Qualitative comparison between stored muon rates from simulations (gray) at $t = 186\ \mu\text{s}$ after beam injection and measured relative positron rates (arbitrary units) from stored muon decays [13]. Error bars correspond to standard errors of the multiple numerical analyses for each ESQ voltage configuration. As the vertical and radial admittances increase and decrease, respectively, proportional to the ESQ voltage, the fraction of stored muons increase, reaching a plateau at 22 kV where the stored fraction starts to become more sensitive to the radial admittance.The low fraction of stored muons is a consequence of the momentum spread being about two times larger than the momentum acceptance, the dispersion mismatch between the end of the M5-line and the storage ring, and the imperfect kicks purposed to inject the beam.

By finding the largest beta functions at collimator locations and using Eq. (3.55), admit-

tances are defined as

$$\varepsilon_{x,y}^{max} = \frac{r_0^2}{\beta_{x,y}^{max}}. \tag{3.69}$$

For Run-1 datasets, their nominal values are shown in Table 3.7. It is worth highlighting the role of the magnetic field in the larger radial admittance.

Table 3.7: Storage ring nominal admittances for Run-1 ESQ set points.

HV [kV]	ε_x^{max}[πmm.mrad]	ε_y^{max}[πmm.mrad]
18.3	268.757	92.8262
20.4	266.946	97.8427

The collimator geometry is circular and not squared, thus admittance values as shown in Table 3.7 would correspond to a beam with very low intensity.

Maximum angles are obtained via

$$a_{max}(\theta) = \sqrt{\varepsilon_x^{max}\gamma_x(\theta)} \quad , \quad b_{max}(\theta) = \sqrt{\varepsilon_y^{max}\gamma_y(\theta)} \tag{3.70}$$

and maximum betatron amplitudes are given by

$$x_{max}(\theta) = \sqrt{\varepsilon_x^{max}\beta_x(\theta)} \quad , \quad y_{max}(\theta) = \sqrt{\varepsilon_y^{max}\beta_y(\theta)} \tag{3.71}$$

For a numerical reference see Table 3.8, which displays the small variations thanks to the weak focusing scheme.

Table 3.8: Maximum value ranges in the storage ring along the azimuth for Run-1 settings.

HV [kV]	x_{max} [mm]	a_{max} [mrad]	y_{max} [mm]	b_{max} [mrad]
18.3	$\{44.46, 45.41\}$	$\{5.91, 6.04\}$	$\{44.27, 45.10\}$	$\{2.06, 2.10\}$
20.4	$\{44.42, 45.57\}$	$\{5.86, 6.01\}$	$\{44.18, 45.12\}$	$\{2.17, 2.21\}$

The momentum acceptance is also directly calculated in the optical view, where the maximum radial dispersion at collimator locations is taken, which yields

$$\delta_{max,min} = \pm \frac{r_0}{D_x^{max}} \approx \pm 0.56\,\%. \tag{3.72}$$

3.5.2 Beam temporal motion

The optical configuration at the end of the M5 beamline is meant to focus the beam horizontally for its passage through the backleg hole in the ring, which houses the 18 mm × 56 mm (horizontal and vertical dimensions, respectively) superconducting inflector that cancels out the magnetic field in its absence. The outcome of this process is a beam whose α, β, and γ functions do not correspond to the optical lattice functions of the ring. Also, the radial dispersion prior to the storage ring entrance is close to zero; thus, stored muons will follow different momentum-dependent radial closed orbits with an overall coherence due to the injection favoring the storage of specific betatron phases. All these features lead to a mismatched beam.

As indicated by Eq. (3.58), the nonzero averaged betatron amplitudes give place to oscillations of the beam centroids and widths over time. Figures 3.47 and 3.48 depict such temporal behavior as seen at one azimuth of the ring from COSY-based simulations. As explained in Subsec. 3.4.1, nonlinear tune shifts and (to a lower extent) the recombination of high- and low-momentum muons yield the de-coherence of the temporal modulations, which are expected to have amplitudes of less than a mili-meter by the end of each fill ($\sim 700\,\mu$s). The beam-ring mismatching is less severe in vertical phase space thanks to the negligible vertical dispersion and more comparable beam-ring optical functions. Fast Fourier

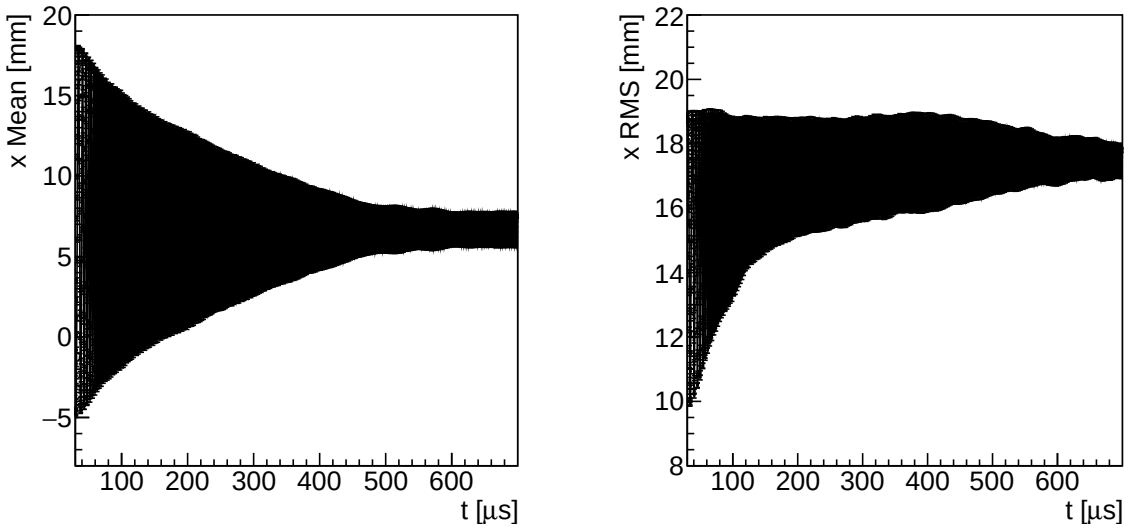

Figure 3.47: Long-term radial beam de-coherence.

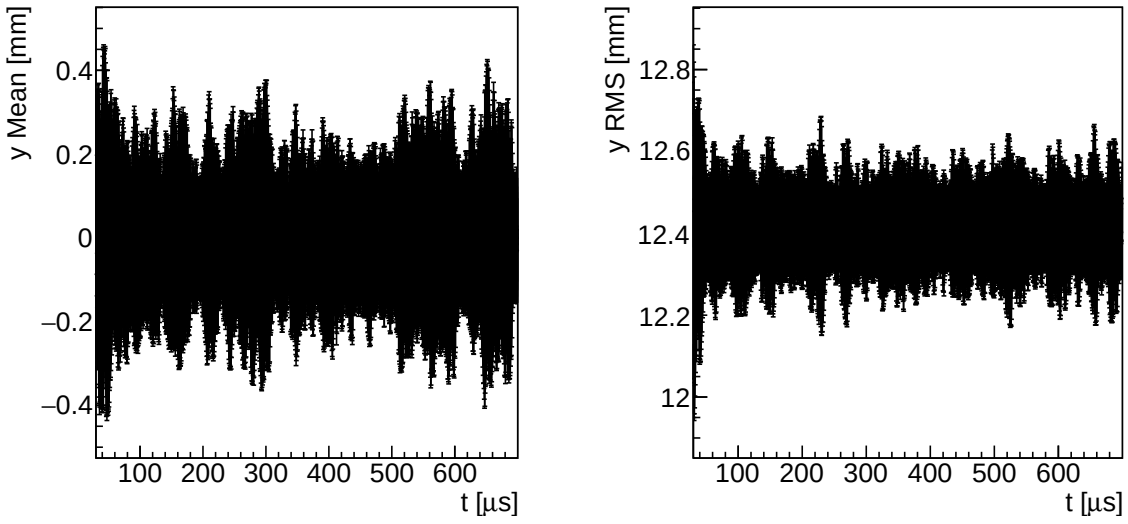

Figure 3.48: Long-term vertical beam temporal modulations.

transforms (FFT), shown in Figs. 3.49 and 3.50, reveal the typical transverse frequencies of the stored beam. Since in this stroboscopic perspective the beam is observed at one

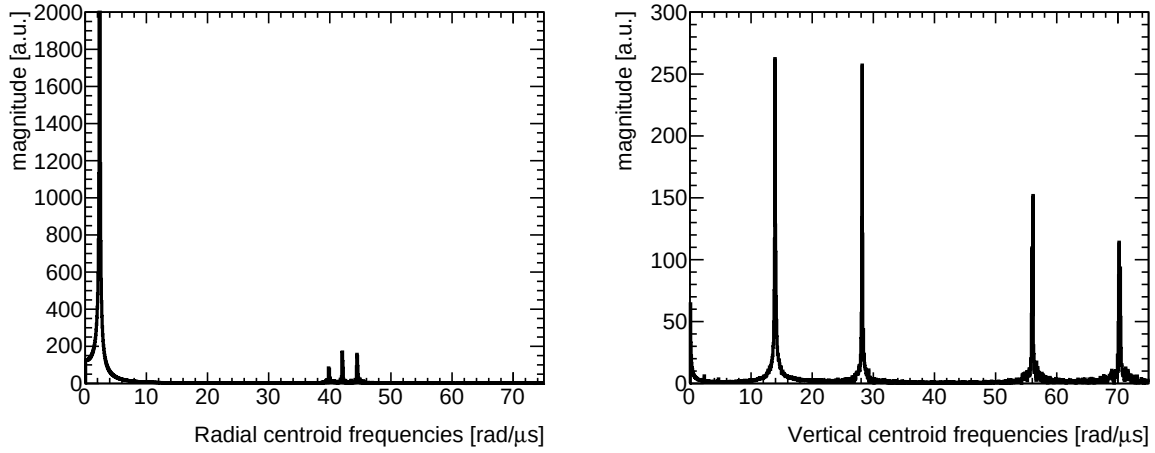

Figure 3.49: Beam frequencies extracted with FFT from centroids motion.

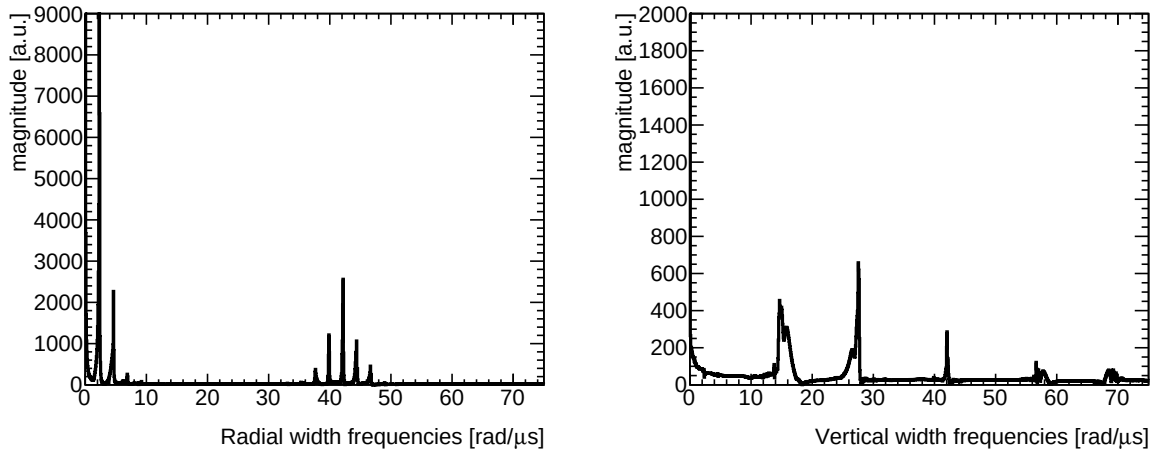

Figure 3.50: Beam frequencies extracted with FFT from widths motion.

location, its frequencies are combinations of cyclotron and radial/vertical frequencies, listed in Table 3.9.

In Sec. 3.3, the concepts of closed orbits and optical lattice functions were elaborated in the context of the g-2 storage ring. In this way, a description of a matched beam is expected to be exact in the linear regime. At this point where nonlinearities and beam mismatch

Table 3.9: Transverse motion frequencies of the g-2 stored beam (HV= 18.3 kV).

Frequency	Expression	[MHz]	[rad/μs]	Period [μs]	T_c revs./period
f_c	$p_0/(2\pi m_\mu \gamma_0 \rho_0)$	6.7050	42.128	0.14914	1.0000
f_x	$f_c \nu_x$	6.3326	39.789	0.15791	1.0588
$f_{\mathrm{CBO},x}$	$f_c\,(1-\nu_x)$	0.37238	2.3397	2.6855	18.006
f_y	$f_c \nu_y$	2.21810	13.937	0.45084	3.0228
$f_{\mathrm{CBO},y}$	$f_c\,(1-\nu_y)$	4.4869	28.192	0.22287	1.4943

are sufficiently quantified, the beam-to-ring relations that emerge in this framework (i.e., Eqs. (3.53) and (3.57)) are tested.

In the temporal dimension, beam centroids and widths at azimuthal locations are tracked from symplectic and nonlinear simulations and the closed orbits and optical lattice functions are calculated with the COSY-based model. Figures 3.51 and 3.52 display results at 157° downstream from the entrance of ESQ station Q1S. An electric field at ESQ station Q1L

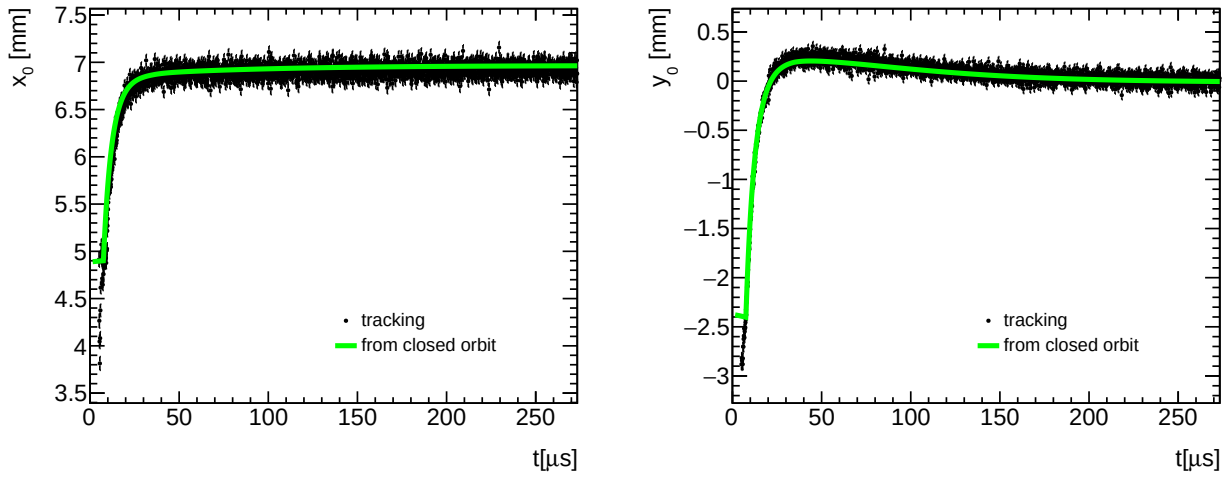

Figure 3.51: Comparison between closed orbit and beam centroid from tracking at 157° downstream from the entrance of Q1S. Tracking data is randomized to remove beam beating from mismatch. The initial distribution and guide fields are prepared for the 60h case as explained in Sec. 3.6.

with the time dependence expected during Run-1a (see Subsec. 3.6.1) is also accounted for in these tracking-vs-lattice comparisons in order to test the framework beyond its nominal conditions. Random time offsets of the size of oscillation periods shown in Table 3.9 are

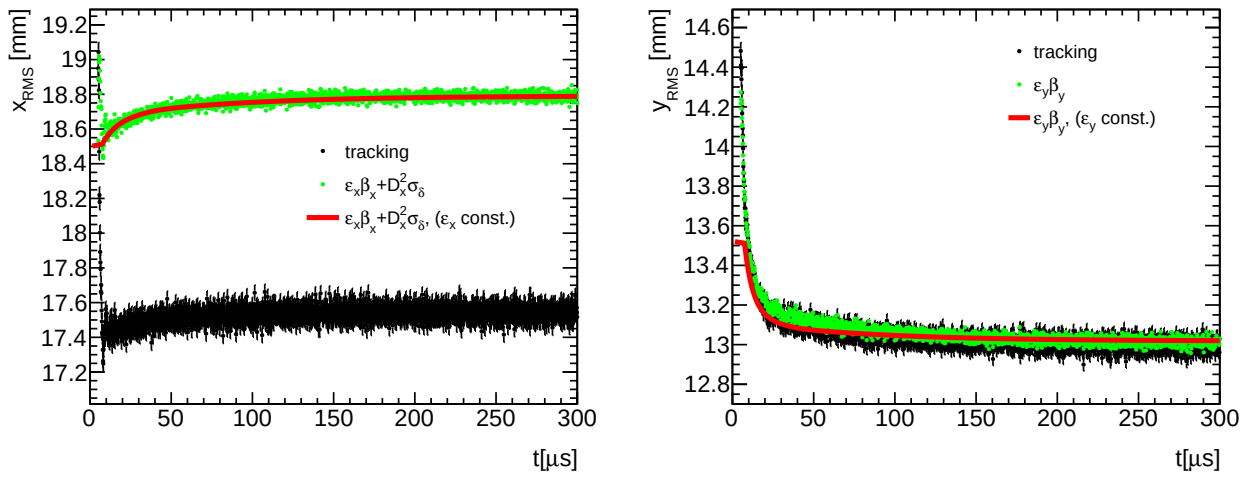

Figure 3.52: Comparison between beam width from optical lattice functions (green and red entries) and beam width from tracking at 157° downstream from the entrance of Q1S. Tracking data is randomized to remove beam beating from mismatch. The initial distribution and guide fields are prepared for the $60h$ case as explained in Sec. 3.6. The red line corresponds to case with constant emittances, which in the vertical case plays a role in describing accurately vertical beam widths.

applied to temporal coordinates from simulation results, in order to wash out frequencies from beam mismatching and directly compare beam drifts over the whole data taking period. Such drifts are the relevant quantity to pay attention since they can potentially bias the ω_a measurement; effects from oscillations driven by beam mismatch in general cancel out.

Beam centroids do follow closed orbits as indicated in Eq. (3.57) and shown in Fig. 3.51; the beam centroid oscillates with the closed orbit as the equilibrium fixed point. Beam widths, on the other hand, require a less straightforward extraction from the lattice side. In the radial case, the momentum spread σ_δ is required to calculate the dispersive effect on the radial width. In addition, emittances are also necessary to be known. Whereas in the experiment these quantities are obtained externally from FR analysis [51] and straw tracker data, at a simulation level are directly obtained. Figure 3.52 show how the vertical width is well described by Eq. (3.53) when the time-evolving vertical emittance is taken into account

(see Fig. 3.53). However, the description of the radial width in the temporal dimension

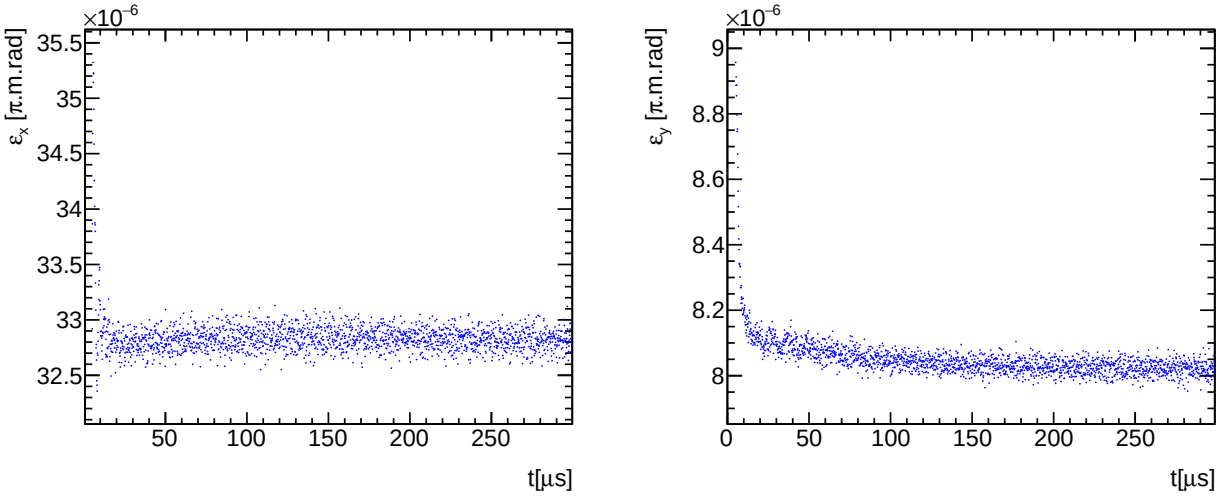

Figure 3.53: Beam emittances from tracking. Due to the smaller vertical admittance, the vertical emittance is more affected by muon loss rates.

from Eq. (3.53) is off by a scale factor of about 1.07. This discrepancy originates from the skewness of the radial (and mismatched) distribution, which deviates from the postulate of having elliptical distributions in phase space (or, equivalently, normal distributions per dimension). Nevertheless, the scale factor is constant and the time evolution is captured by Eq. (3.53). Figures 3.54 and 3.55 show from the simulation side the phase space in both transverse directions, as well as their spatial projections (note skewed radial distribution).

3.5.3 Beam azimuthal modulation

In the muon g-2 experiment the straw tracking detectors precise reconstruction of muon coordinates within their longitudinal acceptances provide reliable transverse muon beam intensity profiles over time. On the other hand, the two tracking detector stations are limited to their narrow sensitivity of about 5°, $\sim 1\,\mathrm{m}$ upstream from their azimuthal locations (see Fig. 1.11). All things considered, the 24 calorimeters around the inner side of the ring could

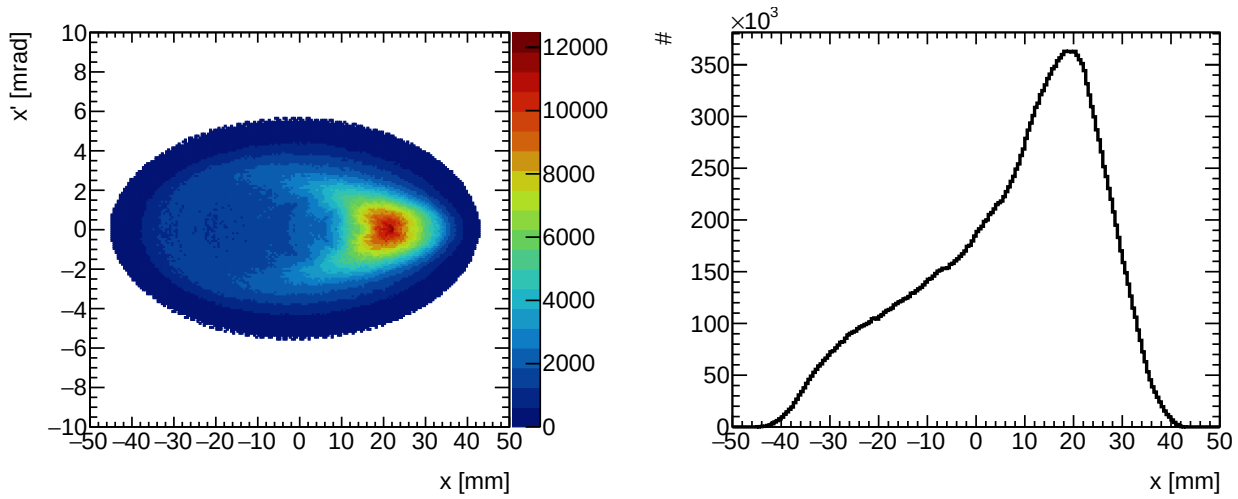

Figure 3.54: Radial phase space at late times of the data taking period (left) and its spatial projection (right) from Run-1 simulation. The pattern closely resembles observations and its characteristic skewness is present in all Run-1 datasets.

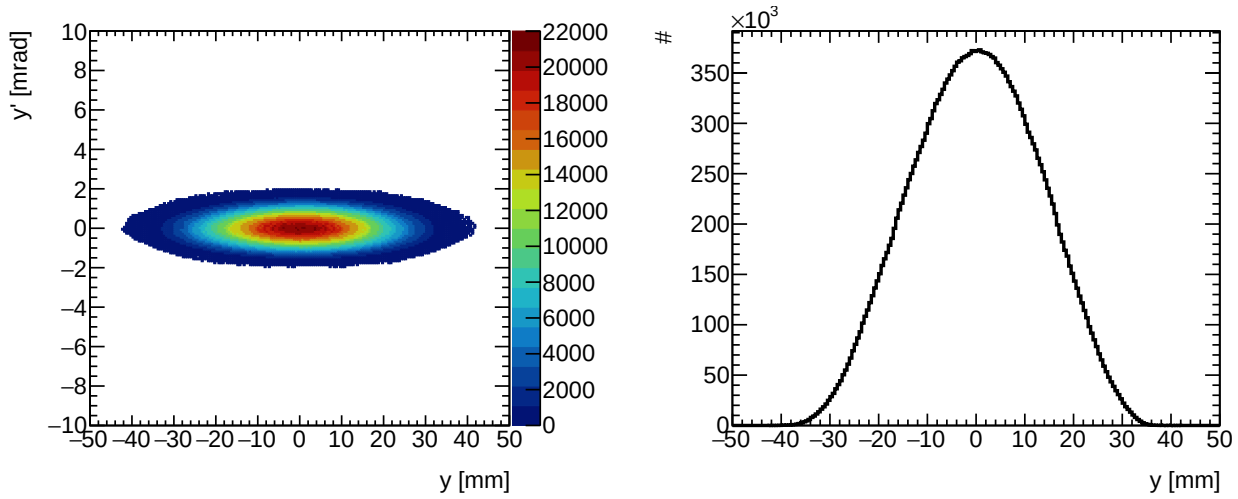

Figure 3.55: Vertical phase space at late times of the data taking period (left) and its spatial projection (right) from Run-1 simulation.

ideally be used to measure the muon beam along the azimuth. However, these detectors were designed to specifically measure positrons energy and arrival time (see Subsec. 1.2.2); a trustworthy reconstruction of the muon beam transverse profile out of detected positrons that hit calorimeter crystals is therefore difficult due to acceptance, resolution, and material effects as positrons travel through the ring instrumentation.

For this purpose, the COSY-based model provides optical lattice functions—verified with reliable tracking simulations—in order to extrapolate straw tracker transverse beam data around the ring. The resulting extrapolation is used to quantify systematic errors from the pitch, electric, and phase acceptance corrections to ω_a. It is also utilized to convolute the muon beam with the magnetic field around the ring for the calculation of $\langle B \rangle$ in Eq. (1.30). Using optical lattice functions is more advantageous than beam tracking simulations since it is not subject to frequencies from beam mismatch nor features of the tracking simulation (e.g., symplecticity and computational time). Once a detailed modeling of the guide fields (under normal or unexpected scenarios as during Run-1) in the storage ring are implemented, optical lattice functions are reproduced on a case-by-case basis. Furthermore, it has been shown that a proper transformation of the measured g-2 beam with all its features is also possible with the optical lattice functions for the purposes of the experiment analysis.

Based on tests with the COSY-based model, the azimuthal behavior of the beam is indeed reproduced by the optical lattice functions in the g-2 case. Since tracker data provides information at two azimuths, an effective radial emittance is calculated via Eq. (3.53), where σ_δ is extracted from FR analysis, the measured radial width is taken and the radial beta and dispersion functions are calculated at tracker locations. In the vertical case, the emittance is simply calculated with vertical width measurements and vertical beta functions from the model. It is necessary to first wash out the beam temporal oscillations with data random-

ization or averaging measurements within time ranges being multiples to CBO frequencies. Figures 3.56 and 3.57 show the good performance of optical functions for the extraction of the beam azimuthal behavior. Even though the radial distribution is not well behaved, the

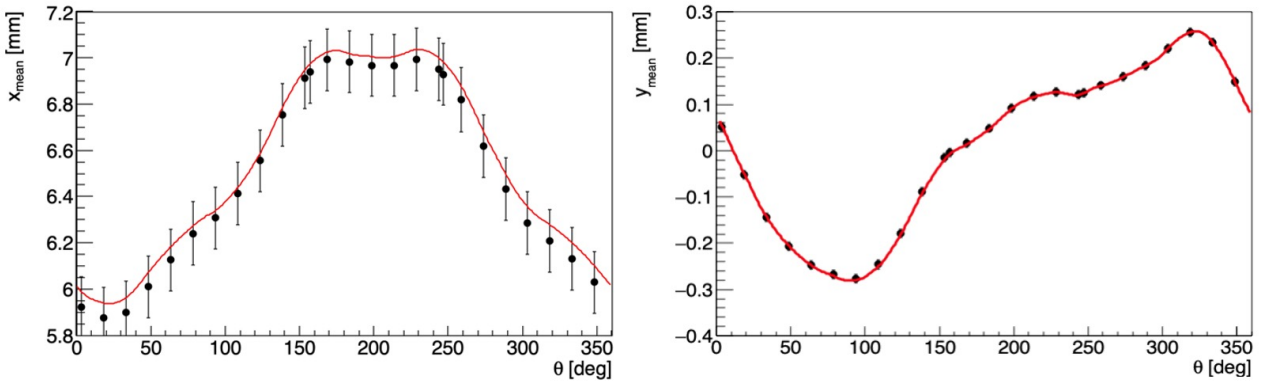

Figure 3.56: Comparison between closed orbits (red curves) and randomized beam centroids from Run-1 tracking simulations.

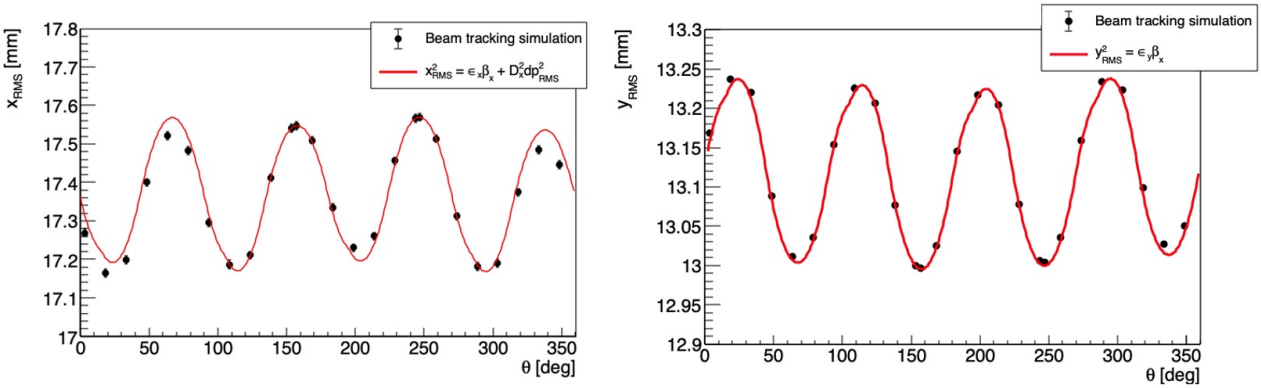

Figure 3.57: Comparison between beam widths from optical lattice functions (red curves) and randomized beam widths from Run-1 tracking simulations.

lattice functions can be safely used within errors of 0.04 mm.

To extrapolate the beam transverse intensity $M(x, y, t; \theta_1) \rightarrow M(x, y, t; \theta_2)$ muon by muon, the following expression is used:

$$\begin{aligned} x(\theta_2) &= \kappa_x(\theta_1, \theta_2)\,(x(\theta_1) - \bar{x}(\theta_1)) + x_0(\theta_2) + D_x(\theta_2)\bar{\delta} \\ y(\theta_2) &= \kappa_y(\theta_1, \theta_2)\,(y(\theta_1) - \bar{y}(\theta_1)) + y_0(\theta_2), \end{aligned} \tag{3.73}$$

where

$$\kappa_x(\theta_1,\theta_2)=\frac{\sqrt{\varepsilon_x\beta_x(\theta_2)+D_x^2(\theta_2)\sigma_\delta}}{\sigma_x(\theta_1)}\quad\text{and}\quad\kappa_y(\theta_1,\theta_2)=\sqrt{\frac{\beta_y(\theta_2)}{\beta_y(\theta_1)}}. \tag{3.74}$$

In this form, the temporal oscillations as measured are captured. Analysis for the phase acceptance correction have proved the validity of these transformations with tracker data as input [102]. For the muon weighting of the magnetic field, since the temporal modulations are not relevant, the entire beam distribution integrated over time is shifted and scaled according to Eq. (3.74); see Sec. 4.5 for more details. Pitch [99] and E-field corrections [100] require a more direct use of the COSY-based optical lattice functions.

3.5.4 Time-momentum correlations

As explained in Subsec. 1.3.3, a momentum-time correlation after beam injection introduces the largest systematic error of the E-field correction. At the time of this dissertation submission, no procedure to measure this correlation in the experiment has been established. With the COSY-based model, the initial distribution at the inflector exit (see Subsec. 3.2.5) is transferred into the storage ring, whose longitudinal profile (Fig. 3.14) and the injection kickers pattern (Fig. 3.10) determine the initial momentum-time correlation. 4 μs after beam injection, the resulting collimated beam is expected to yield a momentum-time distribution as shown in 3.58 under Run-1a kicker settings ($-200, -170, -185$G as maximum strengths). Injection of high-momentum muons ahead of the longitudinal center of the beam is favored; such muons require less outward kick to be stored, and the ringing of the kicker pulse benefits the process. The same pattern occurs for high-momentum muons on the other side of the beam, although to a lower extent. Figure 3.59 reveals the characteristic shape of the beam

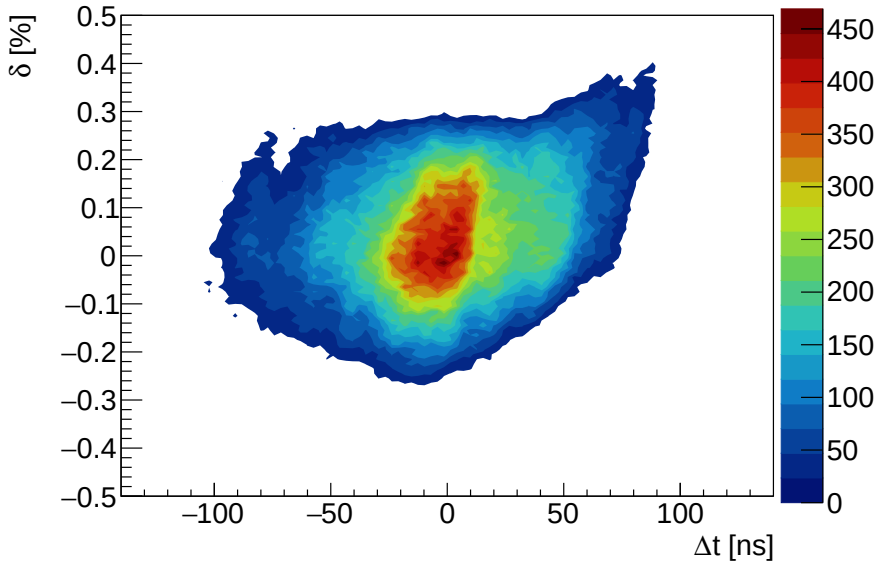

Figure 3.58: Typical Run-1 momentum time beam distribution from Run-1 tracking simulation.

momentum spread from FR analysis, which indicate a proper recreation of the injection process in the COSY-based simulation. Other g-2 collaborators produce similar simulations of the momentum-time distribution [103] and the output is qualitatively equivalent, although the COSY-based exhibits a stronger correlation; collaborative efforts are in process to refine the calculation of the systematic error associated to the momentum-time correlation for g-2 runs posterior to Run-1.

3.6 Run-1 Beam Dynamics

During all the four Run-1 datasets (in chronological order *60h* (1a), *HK* (1b), *9d* (1c), and *EG* (1d)), measurements of the transverse muon beam from the straw tracker detectors revealed unexpected drifts of the beam centroid and width over a fraction of the fill [82] (i.e., $t \lesssim 200\,\mu s$ after beam injection). Furthermore, CBO frequencies of the radial centroid oscillations were also found to evolve during the data taking period, slowly converging to

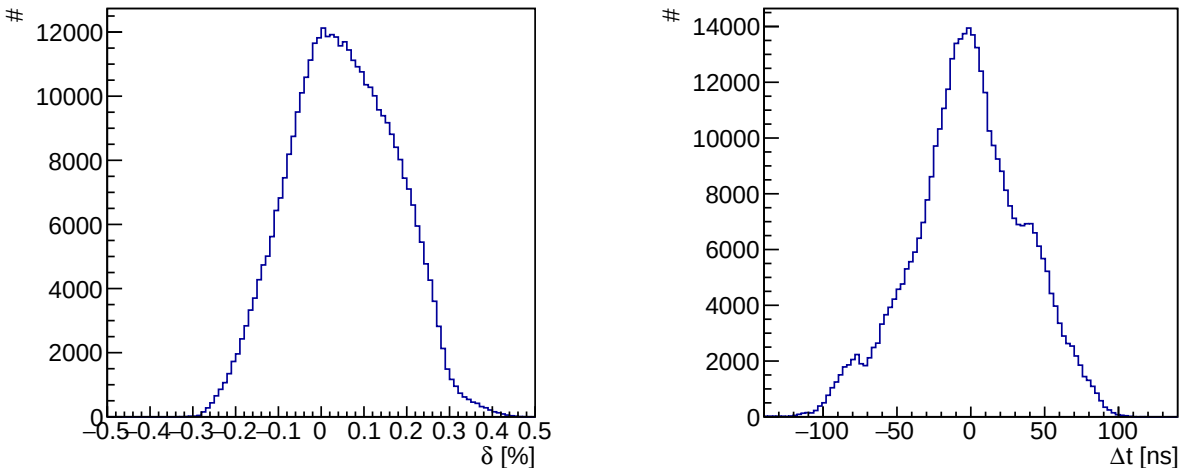

Figure 3.59: Projections of the typical Run-1 momentum time beam distribution from Run-1 tracking simulation.

their nominal values over the course of a fill.

Under nominal conditions the ESQ stabilizes after $t \approx 30\,\mu s$, in which case the guide fields are constant and thus the optical lattice, too. In this normal scenario, CBO frequencies do not change since the stable lattice provides constant betatron tunes (see Table 3.9). Also, closed orbits are expected to be stable and consequently the fixed points around which beam centroids oscillate are indeed fixed. As presented in Subsec. 3.5.2, transverse emittances are sensitive to muon loss rates as experienced during Run-1; therefore, beam widths could drift under a stable optical lattice. All these expectations served to interpret observations and determine the specific behavior of the optical lattice during Run-1.

In particular, CBO frequencies relate to field gradients and centroids result from dipole field steering. Less ambiguously and in the view of 2D multipoles field expansion, normal quadrupole terms strongly relate to the radial CBO frequency via radial tunes and skew dipole terms define long term motion of the vertical beam centroid via vertical closed orbits. Being mindful of such lattice-beam relations, measurements of the radial CBO frequency

and vertical beam centroid over the four Run-1 datasets (see Figs. 3.60 and 3.61) are taken as input for the reconstruction of the unmeasured Run-1 ESQ electric fields.

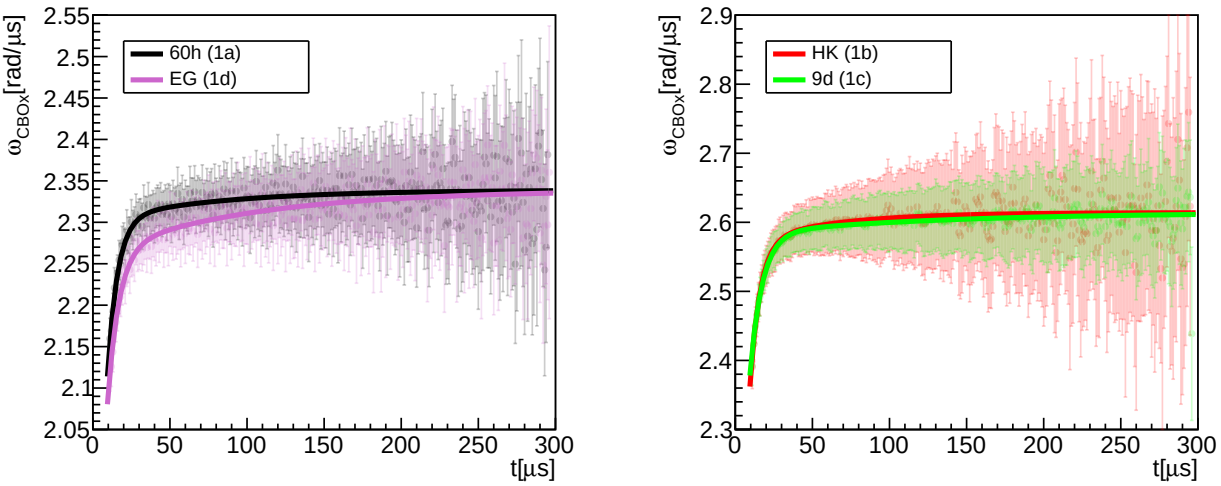

Figure 3.60: Radial CBO frequencies during the four Run-1 datasets from straw tracking detectors data. Semi-transparent markers are obtained from sliding sinusoidal fits (±5 μs) to the recorded radial beam centroid, whereas solid lines result from multi-parameter fits through the entire fill. Both methods are equivalent.

On the other hand, a handful of potted resistors (which connect to ESQ plates as part of the RC circuitry) with HVRs in series were installed during Run-1 for logistical reasons [104] (see Fig. 3.62). Two of them, connected to the top and bottom long plates at ESQ station Q1 ("Q1LT" and "Q1LB"), were measured for several high voltages with a HV probe after Run-1 concluded and found to be damaged. Their HV traces were expected to behave like the nominal ones shown with thin lines in Fig. 3.63. However, measurements displayed longer relaxation times (circular markers in Fig. 3.63). Moreover, the peculiar HV traces from the damaged resistors manifested fluctuations over the course of the probe measurements, providing strong evidence of multimodal stages of the ESQ station Q1L during Run-1 (also reflected from tracker data shown in Figs. 3.60 and 3.61). The faulty behavior of these two resistors (out of all the thirty two installed in the ESQ circuitry) indicated corona discharges

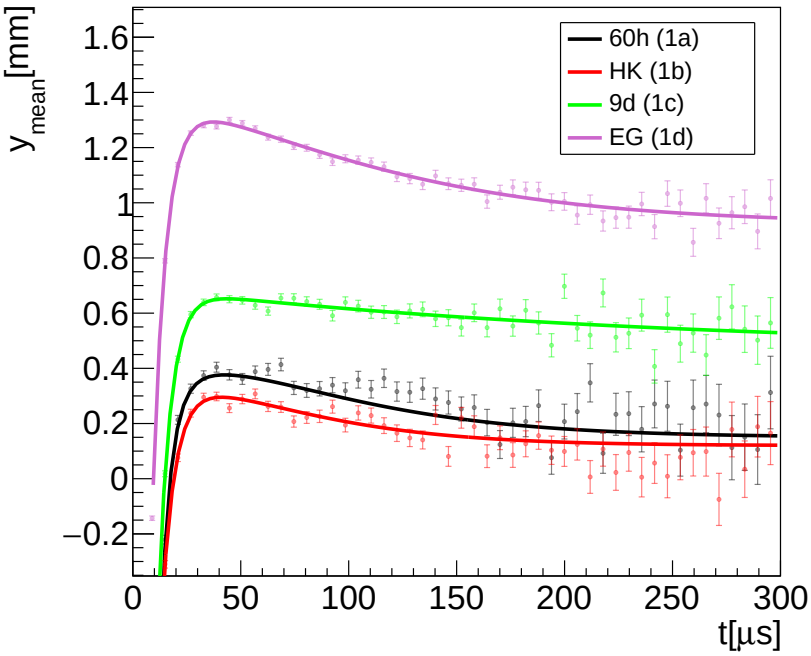

Figure 3.61: Vertical centroid drifts during Run-1 from straw tracking detectors data. Solid lines are fits with double exponential terms and a constant part as the functional form.

Figure 3.62: Single-CADDOCK high-voltage resistor (top) and chain of potted HV resistors (bottom). Two of the latter resistors became damaged during Run-1.

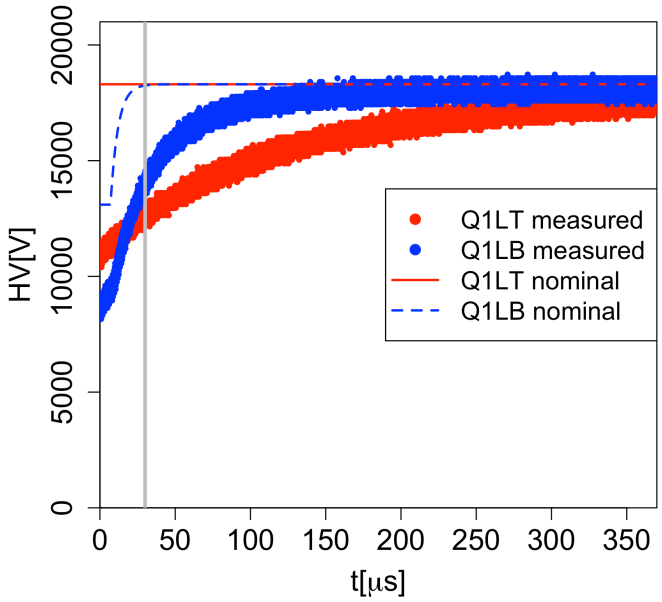

Figure 3.63: HV-traces sample (circle markers) from HV probe measurements in September, 2018, at Q1L plates connected to the damaged resistors. Blue and red lines depict nominal HV traces.

on the resistor surface [105]; resistors outgassed while their temperature raised, leading to the discharge at low voltages. The outgassing was likely more dramatic during the last and longest Run-1 dataset (1d), pushing the ESQ to produce more unusual electric guide fields.

In Subsec. 3.6.1, a method to reverse-engineer the Q1LT- and Q1LB-HV traces per Run-1 dataset is elaborated. From the reconstruction results, derived optical lattice functions are presented in Subsec. 3.6.2.

Subsection 3.6.3 describes a reliable method to reconstruct the beam 6D structure out of experimental data. Lastly, in Sub. 3.6.4 the stored muon beam from tracking simulations is presented, with the reconstructed HV traces and data-based initial beam conditions as input for the COSY-based model.

3.6.1 Reconstruction of the electric guide fields during Run-1

Technique

The electrostatic potential produced at an ESQ station can be represented as a superposition of the four contributions originated by each of its top "T", bottom "B", inner "I", and outer "O" plates. In addition to the potential $V_0(x,y,t)$ expected at ESQ-station Q1L under nominal conditions, an additional contribution $\Delta V_T(x,y,t)$ and $\Delta V_B(x,y,t)$ from the faulty Q1LT and Q1LB plates, respectively, during Run-1 is overlaid as a perturbation under the straight-plates approximation as follows:

$$\begin{aligned} \Delta V(x,y,t) &= \Delta V_T(x,y,t) + \Delta V_B(x,y,t) \\ &= \sum_{k=0}^{\infty}\sum_{l=0}^{\infty} \left(\Delta HV_T(t) g_{k,l} + \Delta HV_B(t) b_{k,l}\right) x^k y^l \end{aligned} \tag{3.75}$$

In Eq. ((3.75)), $\Delta HV_T(t)$ and $\Delta HV_B(t)$ are the extra high voltages "HV" on the top and bottom plates due to the damaged resistors in Run-1 such that the total HV traces are given by

$$HV_T(t) = HV_{0,T}(t) + \Delta HV_T(t) \qquad \text{and} \qquad HV_B(t) = HV_{0,B}(t) + \Delta HV_B(t), \tag{3.76}$$

where HV_0 is the nominal case. The coefficients $g_{k,l}$ and $b_{k,l}$ determine the distribution of $\Delta HV_{T,B}(t)$ among the top/bottom plate multipoles. Since $b_{1,0} = 0$, $b_{1,1} = 0$, and $b_{k,l} = (-1)^{k+l} g_{k,l}$ due to the orientation and 180° rotational symmetry of the top/bottom plates, Eq. ((3.75)) can be rewritten as

$$\Delta V(x,y,t) = \Delta V^s_{dip}(t) y + \Delta V^n_{quad}(t)(x^2 - y^2) + \cdots, \tag{3.77}$$

where

$$\Delta V^{s}_{dip}(t) = \left[\Delta HV_T(t) - \Delta HV_B(t)\right] b_{0,1} \quad , \quad \Delta V^{n}_{quad}(t) = \left[\Delta HV_T(t) + \Delta HV_B(t)\right] b_{2,0}. \tag{3.78}$$

The coefficients $b_{0,1}$ and $b_{2,0}$ are already available [86]. Given the orthogonality of the two equations in Eq. ((3.78)) in terms of ΔHV_T and ΔHV_B, there is a unique set of top and bottom HV traces that yield $\Delta V^{s}_{dip}(t)$ and $\Delta V^{n}_{quad}(t)$. To evaluate these traces, the extra skew dipole $\Delta V^{s}_{dip}(t)$ and normal quadrupole $\Delta V^{n}_{quad}(t)$ terms must be linked to beam dynamic observables measured by the g-2 straw tracking detectors, as shown next.

Implementation

Under the presence of the extra vertical dipole electric potential $\Delta V^{s}_{dip}(t)$ (Eqs. ((3.77)) and ((3.78))), the vertical closed orbit becomes distorted. Therefore, by measuring the distortion of the vertical closed orbit at one azimuthal location of the storage ring (aka vertical fixed points "y_0") over time, $\Delta V^{s}_{dip}(t)$ can be quantified. In fact, the straw trackers have the ability to extract such vertical beam equilibrium positions around specific locations within the ring.

To illustrate the relation between $\Delta V^{s}_{dip}(t)$ and the observable y_0 (equivalent to the non-oscillating vertical mean from tracker data), the former variable can be treated as a dipole steering error [106]:

$$\begin{pmatrix} \mathbf{y} \\ y' \end{pmatrix}_0 = \left(I - M_0^y\right)^{-1} \begin{pmatrix} 0 \\ \Delta\theta_y \end{pmatrix} \quad , \quad \Delta\theta_y \approx -\frac{e\Delta\mathbf{V^s_{dip}}}{E_0}\frac{l}{r_{ref}}. \tag{3.79}$$

It is worth mentioning that the linear vertical transfer map M_0^y has to account for the

gradient error explained next.

The normal quadrupole extra term $\Delta V^n_{quad}(t)$ introduces a distortion to the radial defocusing gradient at Q1L. Consequently, the betatron tunes $\nu_{x,y}$ and beam transversal widths are affected due to the nonzero $\Delta V^n_{quad}(t)$. Trackers can indirectly measure the radial CBO frequency (see Fig. 3.60), ω_{CBO}, which relates to the tunes through the cyclotron frequency, f_C, via $\omega_{CBO} \approx 2\pi f_C(1-\nu_x)$. In a similar fashion, we can elucidate the relation between $\Delta V^n_{quad}(t)$ and the observable ω_{CBO} by treating the action of $\Delta V^n_{quad}(t)$ as a gradient error [74]:

$$\nu_x = 1 - \frac{\omega_{\mathbf{CBO}}}{2\pi f_C} = \frac{1}{2\pi}\left(4\cos^{-1}\left(\frac{Tr(M_0^x)}{2}\right) + \frac{e\Delta\mathbf{V^n_{quad}}}{pv}\frac{\beta_x l}{r^2_{ref}}\right). \tag{3.80}$$

In reality, the action of the extra skew dipole and normal quadrupole terms at Q1L during Run-1 is entangled and magnetic field inhomogeneities already distort closed orbits. Moreover, trackers do not measure the vertical closed orbit at Q1L. Thus, the illustrative but simplistic equations ((3.79)) and ((3.80)) do not suffice to solve for $\Delta HV_{T,B}(t)$ via $\left(\Delta V^n_{quad}(t), \Delta V^s_{dip}(t)\right)$ with (y_0, ω_{CBO}) from tracker data. For this purpose, with the high-fidelity `COSY`-based storage ring model and optimization algorithms supported by `COSY INFINITY` [53, 56], we prepare a more representative set of bijective equations

$$y_0(t) = F_1(\Delta HV_T - \Delta HV_B, \vec{A}; t) \tag{3.81}$$

$$\omega_{CBO}(t) = F_2(\Delta HV_T + \Delta HV_B, \vec{A}; t) \tag{3.82}$$

to determine the Q1LT and Q1LB high-voltage traces (the vector $\vec{A}$ contains all the other nominal parameters of the storage ring independent of the bad resistors behavior). Fig. 3.64

illustrates the optimization process for one set of tracker measurements $(y_0, \omega_{\mathrm{CBO}})$ to obtain the optimal top and bottom HV-trace values at a specific time. In Fig. 3.64, right plot, "f_{obj}" is the sum of objective functions that the optimizer minimizes iteratively:

$$f_{obj,1} = \left(1 - \frac{\nu_x^{sim}(\Delta HV_T, \Delta HV_B)}{\nu_x^{\text{Tracker data}}}\right) \qquad \text{and} \qquad f_{obj,2} = \left(1 - \frac{y_0^{sim}(\Delta HV_T, \Delta HV_B)}{y_0^{\text{Tracker data}}}\right), \tag{3.83}$$

where the superscript "sim" stands for the values from the COSY-based model, dependent on the ΔHV_T and ΔHV_B values input to the model.

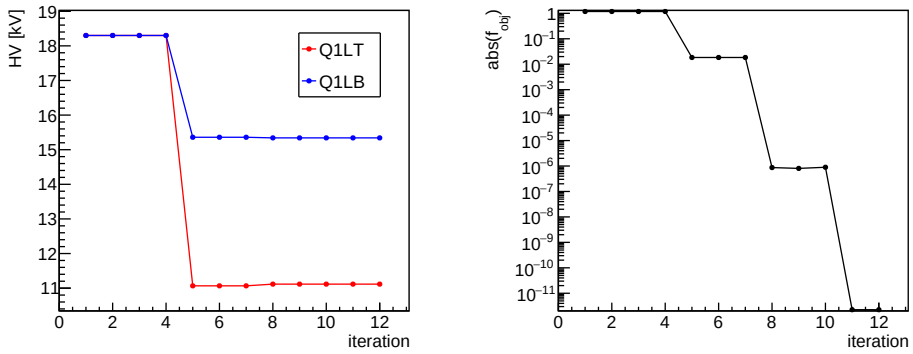

Figure 3.64: High voltage on Q1LT and Q1LB plates (left) and objective function (right) per iteration as the optimization takes place for the Run-1, EndGame dataset, at 40 μs. The optimizer supported by COSY INFINITY (i.e., the generalized least squares Newton method) fits Q1LT/Q1LB HVs such that the COSY-based storage ring model with damaged resistors accounted for reproduces a vertical fixed point (equivalent to the vertical mean) and CBO frequency as measured by tracker station 12.

Reconstruction Results

Fig. 3.65 presents the HV traces from Q1LT and Q1LB during Run-1 datasets as reconstructed with the method described above. For the time window prior to the nominal measurement start time, $t < 30\mu s$, the HV-traces reconstruction fails to output results that resemble the functional forms as directly measured with the probe. The explanation of this mystery is being investigated. To bypass such limitation, the functional form of the

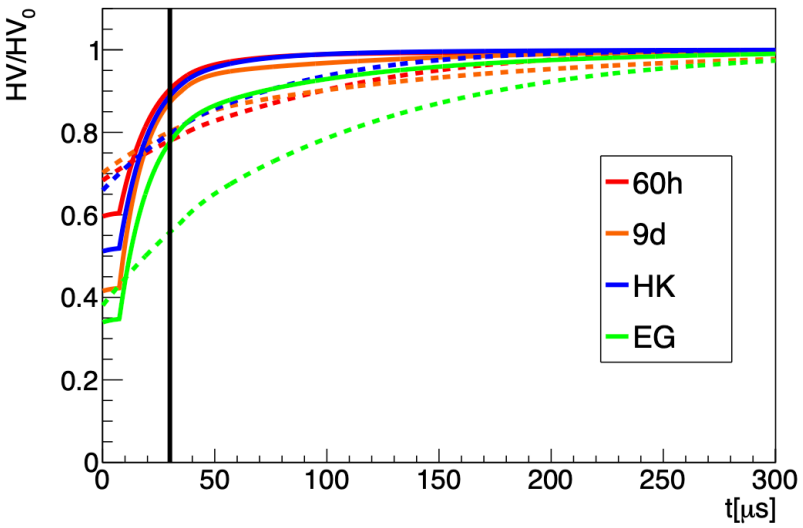

Figure 3.65: Reconstructed HV traces (normalized to their nominal voltage set-points) at Q1L during Run-1 datasets. Dashed and solid lines correspond to Q1LT and Q1LB plates, respectively.

reconstructed HV traces at $t > 30\mu s$ is extended to fill out the gap at $t < 30\mu s$. The implementation of the reconstructed HV traces is validated by comparing beam tracking simulation results with tracker data, i.e., CBO frequencies and vertical centroids over time as shown in Fig. 3.66.

Cross-checks and Uncertainty Estimation

The HV-traces reconstruction raises from the observation of slowly changing beam parameters (CBO frequency and vertical mean) at the azimuthal locations in the ring where trackers take data from. The CBO frequency is a global parameter independent of the ring location, as it is directly related to the betatron tunes, and its direct extraction from radial beam oscillations and functional fits has demonstrated to be reliable. On the other hand, the early-to-late vertical mean drift is more subject to the limited statistics of the available

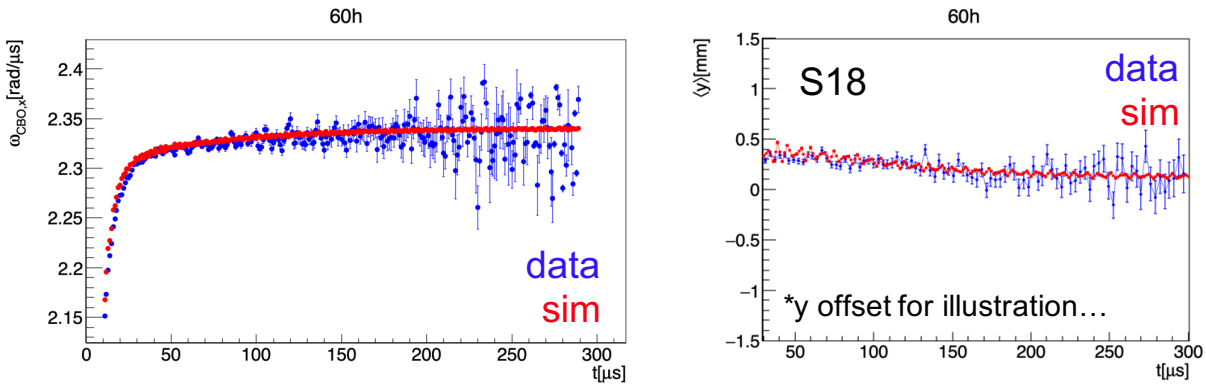

Figure 3.66: Comparisons between tracker data and tracking simulations with the damaged-resistors effect implemented. On the left is the CBO frequency whereas on the right vertical centroids are shown. Similar strong agreements are obtained for the other Run-1 datasets.

data, specially at late times in the fill. To compensate for this aspect, vertical mean drifts as recorded by calorimeters around the ring serve as an extra input to constrain the equilibrium vertical mean after the damaged resistors effect during the fill, this way guaranteeing the overall vertical drifts from tracker data.

Moreover, several aspects from the storage ring modeling that could interfere with the sensitivity of the vertical beam mean and CBO frequency to changes in the guide fields were considered [107], namely:

- Magnetic multipole coefficient errors from Trolley data (not greater than 300 ppb).
- HV reconstruction based on data from tracker station S12 vs. S18.
- Ambiguity of magnetic field reference azimuthal angle.

The largest impact of the listed effects on the reconstructed HV traces came from magnetic coefficient errors and, for instance, their corresponding optical lattice functions led to systematic errors of the phase acceptance correction of about 1 ppb.

The presence of a third damaged resistor at station Q3L was also suspected. However, when a reconstruction of three traces was attempted under these conditions (information

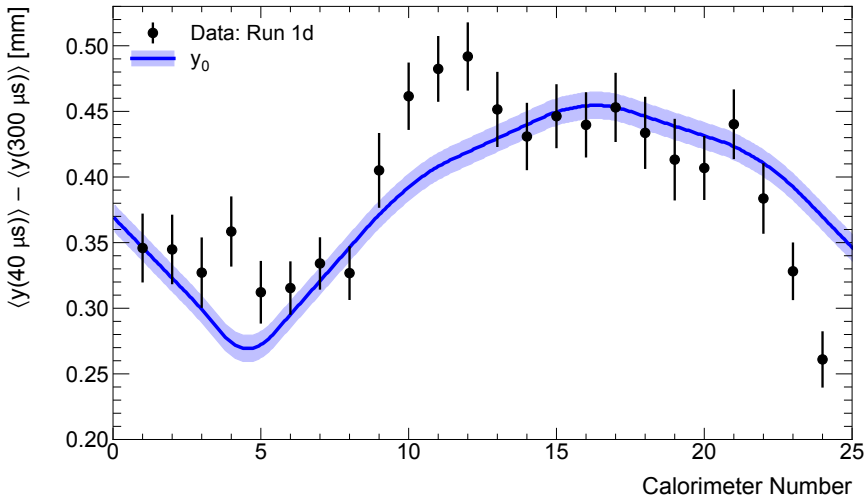

Figure 3.67: Black markers are vertical beam drifts from 40-200 μs from calorimeter data (energy threshold of 1.7 GeV) under material-effect corrections, where double exponential fits were employed. In blue, vertical closed orbit distortion drifts from 40-300 μs using the COSY-based model with the reconstructed HV traces implemented. The blue error band is an estimate of the uncertainty introduced by the vertical dispersion. The simulations are matched to data by associating the closed orbit placed $\sim 22°$ upstream of the calorimeter position.

of the vertical beam at the two tracker stations was accounted for simultaneously, to consider three optimization objective functions), the optimization method did not converge to physical results. In a qualitative level, HV measurements of the third possible plate to have been damaged during Run-1 exhibited a stable behavior after the fit start time [104]. Also, comparisons shown in Fig. 3.67 considering two damaged resistors recreate calorimeter observations, within experimental errors.

3.6.2 Optical lattice functions during Run-1

With the reconstructed HV traces at Q1LT and Q1LB for each Run-1 dataset, the total electric potential at Q1L is defined in the COSY-based model and optical lattice functions prepared (see Subsec. 3.3.2).

Figure 3.68 shows how vertical closed orbits are shifted due to the effect from damaged

resistors. The minimum distortion on the vertical orbit occurs at Q1L, where the steering

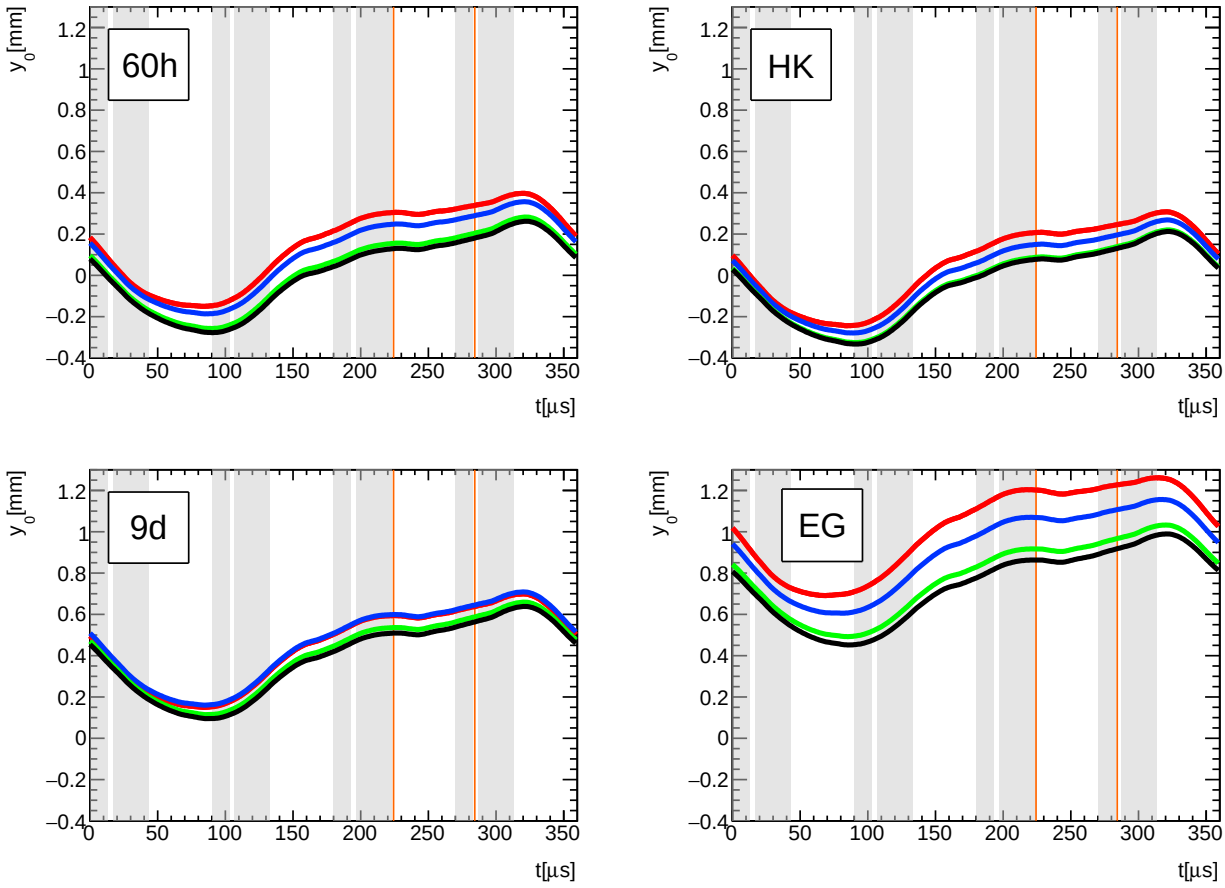

Figure 3.68: Vertical closed orbits at 30 μs (red curves), 100 μs (blue curves), 200μs (green curves), and 300 μs (black curves) during Run-1. Gray shadows depict ESQ stations along the azimuth, where the Q1S upstream edge is at $\theta = 0$. Orange lines indicate collimator locations. Red curves are subject to the effects of the ESQ scraping configuration and the green curves have almost reached the equilibrium values.

error is located. At the opposite side of the ring, the vertical closed orbit suffers its largest drift. A similar pattern arises from the vertical beta functions beating (see Figs. 3.69 and 3.72). The ring is a closed system where extra steering or gradient errors beyond design have global implications on the entire lattice. For instance, while muons cross the mis-powered station Q1L, the lower focusing vertical gradient lets the beam spreads out to a larger amount than the design case, wherein vertical beta functions reflect a proportional

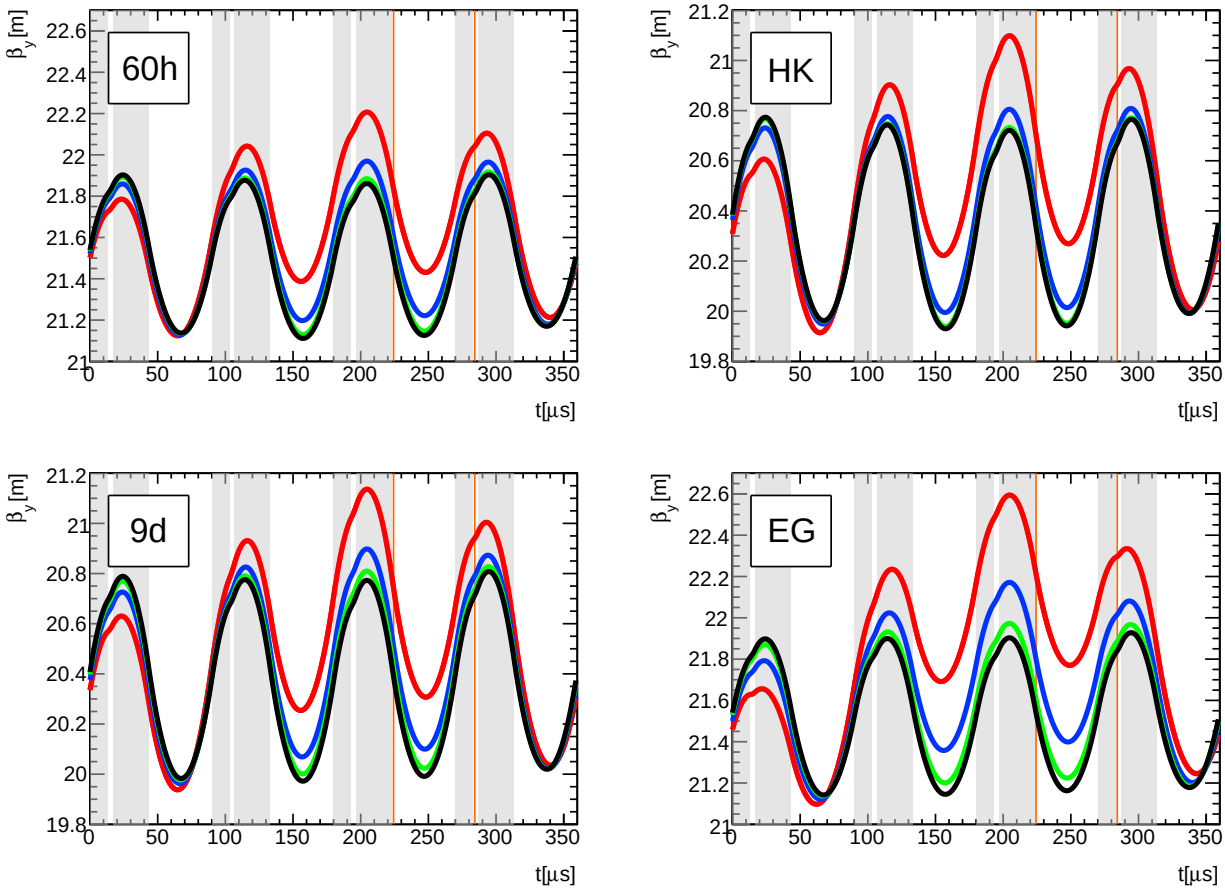

Figure 3.69: Vertical beta functions at 30 μs (red curves), 100 μs (blue curves), 200μs (green curves), and 300 μs (black curves) during Run-1.

azimuthal evolution.

On the radial end, larger radial tunes change the resulting patterns driven by Q1L during Run-1 (see Figs. 3.70 and 3.71). The radial closed orbit is minimally affected by the damaged

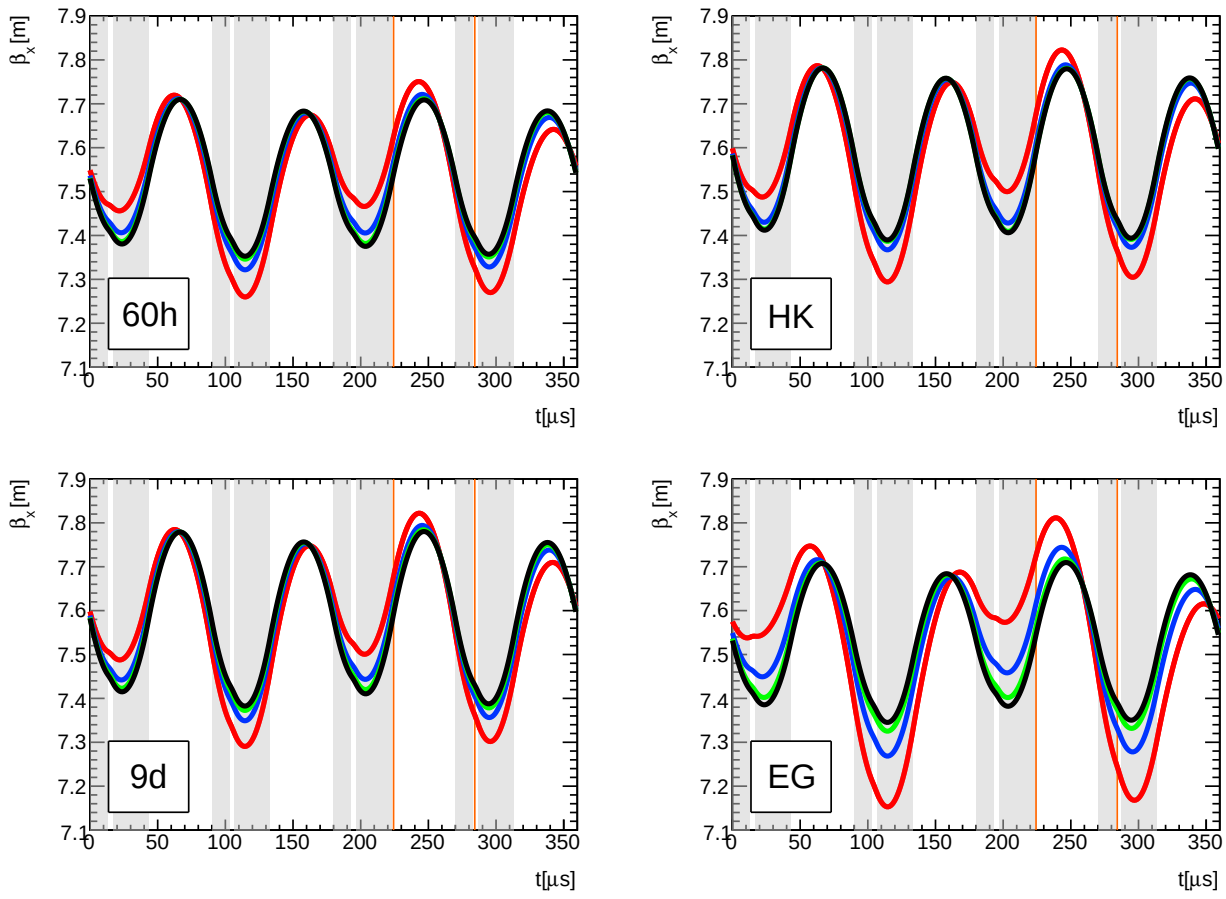

Figure 3.70: Radial beta functions at 30 μs (red curves), 100 μs (blue curves), 200μs (green curves), and 300 μs (black curves) during Run-1.

resistors; the top and bottom plates at Q1L do not introduce normal dipole electric fields.

As the Q1LT and Q1LB plates slowly converge to the nominal HV setting, all optical functions adiabatically converge to a stable state. Figure 3.73 shows the time evolution of the lattice at 210° from the upstream entrance of station Q1S (Run-1 dataset 1d), where the lattice gradients are the largest.

With these dataset-by-dataset periodic functions of the optical lattice, tracker data is

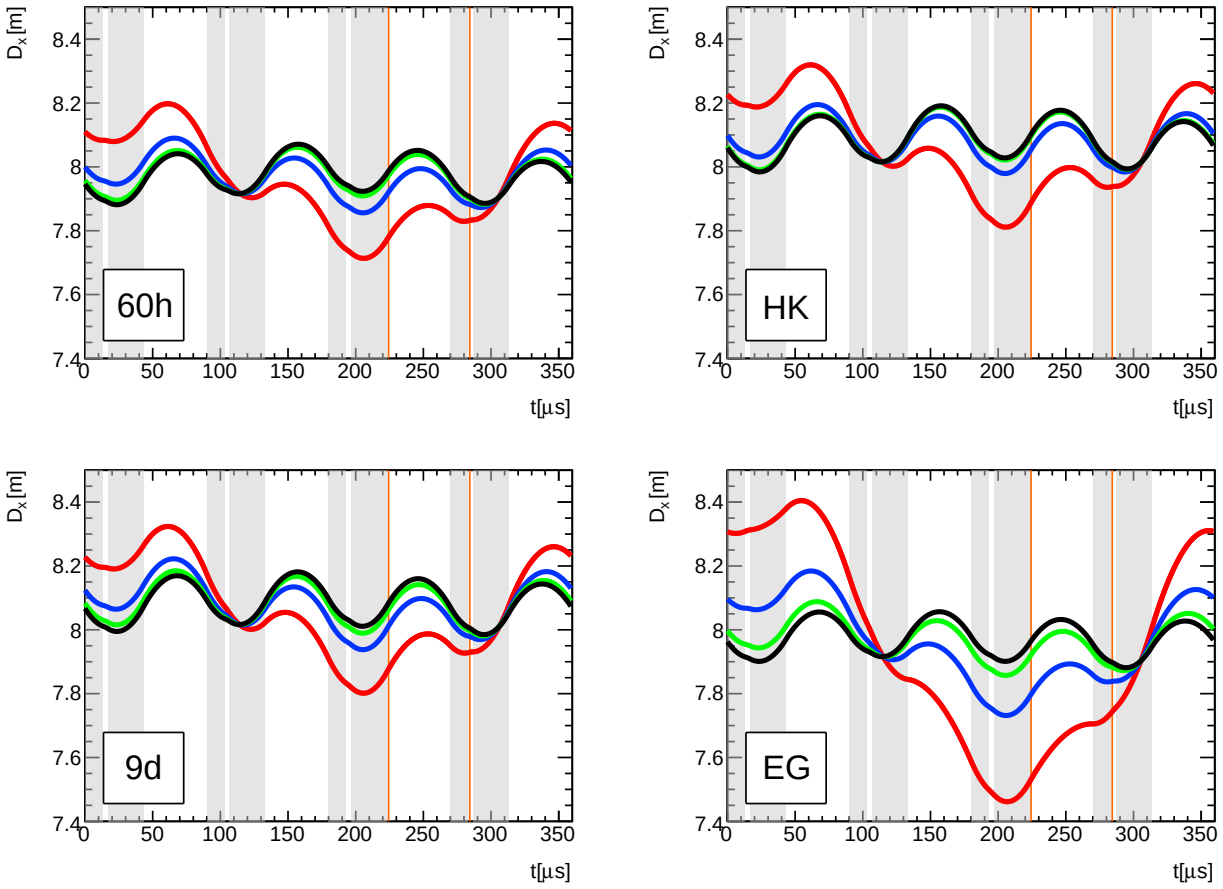

Figure 3.71: Radial dispersion functions at 30 μs (red curves), 100 μs (blue curves), 200μs (green curves), and 300 μs (black curves) during Run-1.

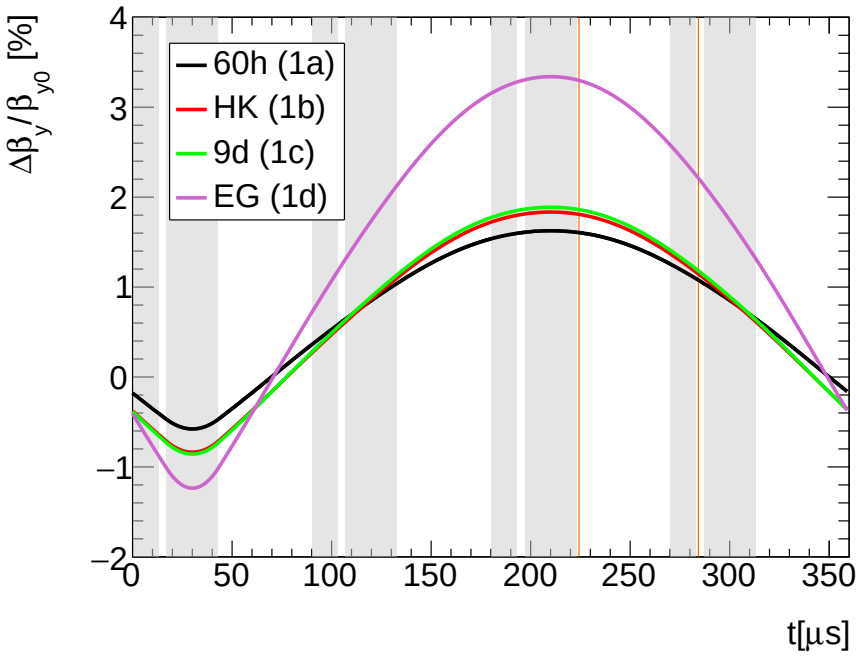

Figure 3.72: Relative vertical beta functions drift from 30 μs to 1000 μs.

extrapolated around the ring (see Subsec. 3.5.3). Figure 3.74 displays the beam centroids and widths based on tracker data (EG), station 12.

3.6.3 Initial beam distributions

The g-2 straw tracking detector system has the beam-diagnosis capability of recording radial x and vertical y muon coordinates to resolutions of $\sigma \approx 4\,\text{mm}$ and time t coordinates with 3.4 ns precision during Run-1 [42].

In the stroboscopic perspective, tracker measurements can be treated as localized in a well-defined azimuthal location as a result of the narrow azimuthal sensitivity ($\approx 4.9°$) and the weakly focusing optics approximation. In this view, the radial motion of the beam is modeled for small time ranges as an ensemble of monochromatic muons oscillating at a common radial CBO frequency ω_{CBO} with different equilibrium positions x_{e}^{i}, betatron

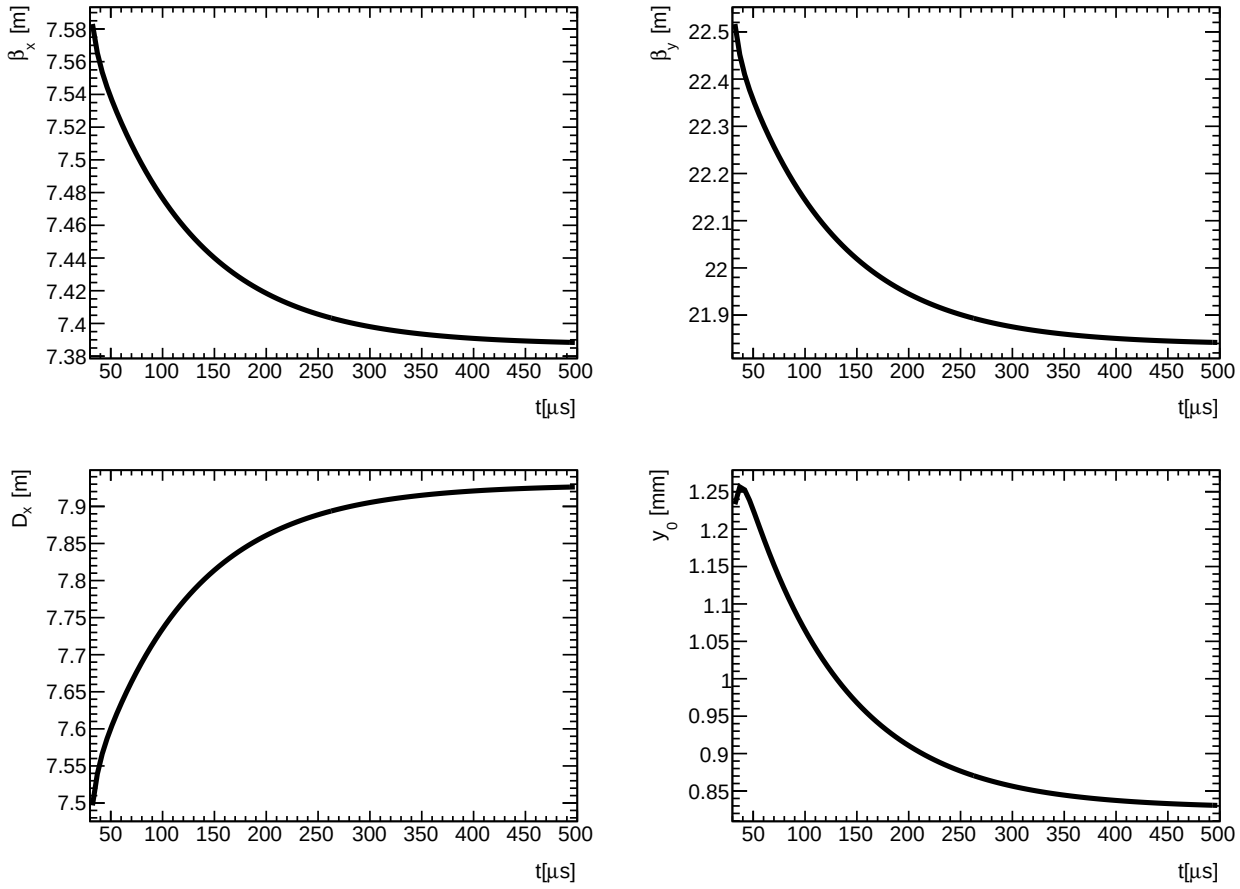

Figure 3.73: β_x, β_y, D_x, and vertical closed orbit at 210° from the upstream entrance of station Q1S for dataset Run-1d.

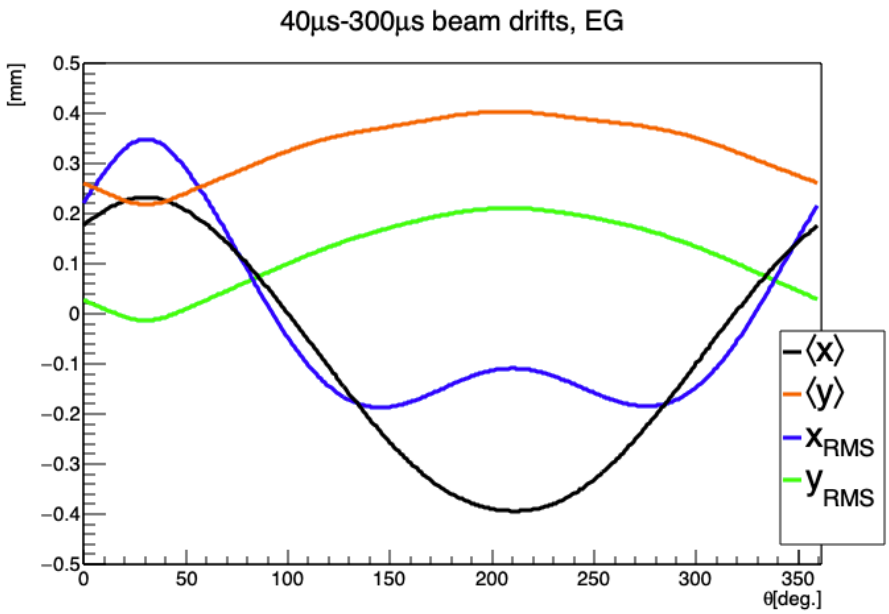

Figure 3.74: Beam drifts anchored to tracker data for the Run-1d dataset.

amplitudes A_j, and phases ϕ_k:

$$x(t) = x_{\mathrm{e}}^{i} + A_j \cos\left(\omega_{\mathrm{CBO}} t + \phi_k\right) \tag{3.84}$$

The measured data-bin intensity N_{mn} at coordinates (x_m, t_n)—see Fig. 3.75—can be expressed as [108]

$$N_{mn} = \sum_{i=1}^{n_i} \sum_{j=1}^{n_j} \sum_{i=k}^{n_k} \beta_{ijkmn} f_{ijk}, \tag{3.85}$$

where f_{ijk} is the relative muon population identified by the set $\{x_{\mathrm{e}}^{i}, A_j, \phi_k\}$ from the beam probability density function (PDF) $f(x_{\mathrm{e}}, A, \phi)$. In Eq. (3.85), the summation upper bounds correspond to the number of values subject to the binning size along each coordinate in f_{ijk} (e.g., $n_i = 45$ for $x_{\mathrm{e}}^{1} = [-45, -43]$ mm, $x_{\mathrm{e}}^{2} = [-43, -41]$ mm, …, $x_{\mathrm{e}}^{45} = [43, 45]$ mm).

On the other hand, the relative number of muons with specific $\left(x_{\mathrm{e}}^{i}, A_j, \phi_k\right)$ coordinates that contribute to the measured intensity N_{mn}, symbolized by β_{ijkmn} in Eq. (3.85) and not to be confused with betatron functions, is equal to the probability of such muons to be found

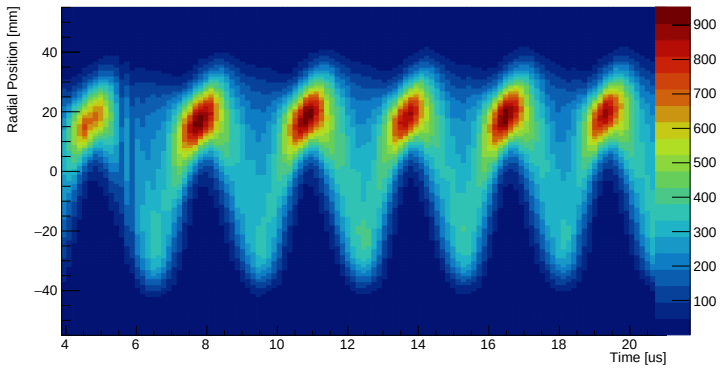

Figure 3.75: Resolution- and acceptance-corrected radial position versus time from tracker data, Station 12. By reconstructing the trajectory of decay positrons detected by the tracking planes, muon decay positions are extrapolated. The coherent oscillations are a consequence of the beam injection process.

at the bin (x_m, t_n):

$$\beta_{ijkmn} = \int_{x_m=r_-}^{r+} \int_{t_m=t_-}^{t+} \frac{\epsilon\left(x_m\right)}{\sqrt{2\pi}\sigma} e^{-\frac{1}{2\sigma^2}\left[x_m - \left(x_{\mathrm{e}}^{i} + x_{off} + A_j \cos(\omega_{\mathrm{CBO}} t_n + \phi_k)\right)\right]^2} dx_m dt_n. \tag{3.86}$$

The radial acceptance $\epsilon(x)$ in Eq. (3.86) [42] accounts for detection effects of the tracker stations. The offset x_{off} is determined based on data and accounts for closed orbit distortions, tracker reconstruction offsets, and tracker misalignments.

With these well-established relations between beam PDFs and $x - t$ tracker data, the optimal f_{ijk} functions can be estimated via non-negative least squares (NNLS) minimization of the following χ^2 expression:

$$\chi^2 = \sum_{m=1}^{n_m} \sum_{n=1}^{n_n} \frac{\left(\sum_{i,j,k} \beta_{ijkmn} f_{ijk} - N_{mn}\right)^2}{\sigma_{N_{mn}}^2}. \tag{3.87}$$

Under constraints inspired by further data analysis, the minimization converges to physical solutions after less than 10,000 iterations. For instance, the FR signal [51] enables to

limit $f(x_e|A,\phi)$, wherein resulting deviations from the original signal can be attributed to differences between calorimeter and tracker detection efficiencies.

Figure 3.76 shows a typical $f(x_e, A, \phi)$ function projected along two dimensions. Correla-

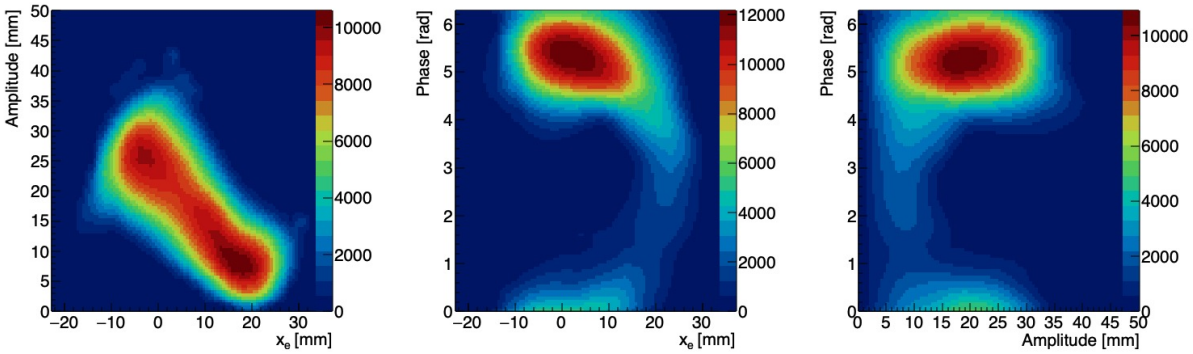

Figure 3.76: Reconstructed beam distribution in the radial direction. On the left plot, the upper limits are determined by the physical apertures of the collimators which bound maximum radial excursions, whereas the maximum kicker strength defines the lower limits.

tions between x_e, A, and ϕ are expected to result from the dynamics caused by the injection, collimation, and circulation of the muon beam in the storage ring [109].

Thanks to the periodicity of the mismatched beam motion over time, a data range of one CBO period is sufficient to reconstruct the beam conditions (and necessary to ignore betatron tune shifts). In order to capture the beam scraping process that took place during Run-1—essential for realistic muon loss rates—the PDFs are calculated from data at around 4 μs after injection while the scraping scheme is at its initial stage.

From the vertical-motion front, the reconstruction follows the same process as for the radial case with a simplification of all vertical oscillations following the same fixed point in the absence of vertical dispersion. Specifically, the vertical distribution of the muon beam is described with vertical betatron functions and constant oscillation offsets.

The initial time profile of the beam is set based on measurements from scintillating detectors. With the COSY-based model, which includes the observed injection-kicker ringing

pattern during Run-1 and a realistic beam distribution at injection (see Subsec. 3.2.5), a correlation between time and momentum offsets is assigned to the initial beam distribution at 4 μs.

Using the linear beam dynamics framework, the initial $\vec{z}_i$ ray coordinate sets are prepared for each muon from the reconstructed PDFs for nonlinear beam tracking simulations with the COSY-based model.

Even though nonlinearities are not considered in the reconstruction of the initial beam conditions, all the de-coherence, betatron amplitude modulation, and tune-dependent shifts originated by the higher-order guide fields are manifested in the nonlinear beam tracking simulations.

This reconstructed method assumes no correlations between the radial and vertical motion, which is in line with tracker data. Sufficiently large skew quadrupole coefficients from the electric and magnetic fields can potentially introduce x-y beam correlations, and a proper modeling of these fields in the simulation give rise to such effects.

3.6.4 The simulated Run-1 beam

The following features developed in this dissertation set the stage for a highly realistic recreation of the stored muon beam during Run-1:

- COSY-based model of the muon g-2 storage ring.
- Reconstructed ESQ fields at station Q1L based on experimental data.
- Realistic initial beam distribution based on experimental data.

By performing symplectic tracking, the beam information is regenerated at arbitrary azimuthal locations. With these distributions—and the optical lattice functions from the

COSY-based model—, beam-dynamics systematic uncertainties in the muon g-2 experiment are assessed to a precision in line with the objectives of the experiment, (see Ch. 4). To validate the results derived from this analysis, experimental data are used to compare results from tracking. Figures 3.77-3.80 show examples.

In Fig. 3.77, the transverse profile of the beam at tracker station 12 is shown during Run-1a, integrated from $30\,\mu s < t < 300\,\mu s$. The characteristic radial structure dictated by correlations between the muon dynamic parameters (momentum-dependent fixed points, betatron phases, and betatron amplitudes) is captured in the simulated beam. The vertical projection, which resembles more closely a normal distribution, is also well represented in the numerical results. Figure 3.78 shows the corresponding projections in Fig.. 3.77 2D

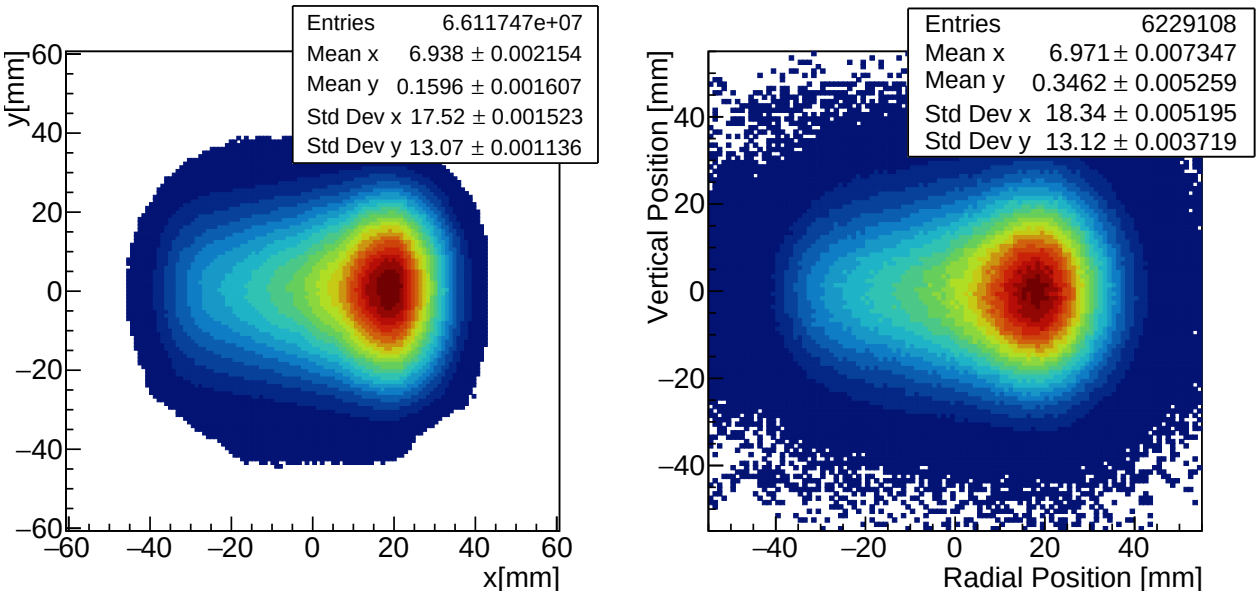

Figure 3.77: Muon beam intensity from simulation (left) and tracker data (right), station 12, during Run-1a from $30\,\mu s < t < 300\,\mu s$.

distributions. Due to either an imperfect simulated scraping process during the first microseconds after beam injection or tracker data resolution, discrepancies smaller than 2 mm are evident in the radial case. Figure 3.79 shows the radial beam motion over time at tracker

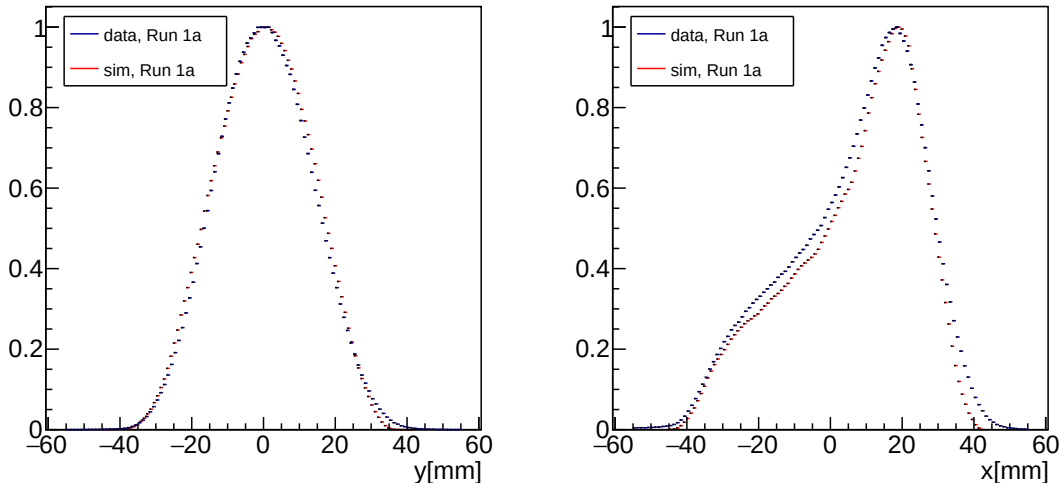

Figure 3.78: Muon beam intensity projections from simulation (left) and tracker data (right), station 12, during Run-1a from 30 μs $< t <$ 300 μs.

station 12 (Run-1a). The measured CBO radial frequency is closely followed in the simulated beam thanks to the implementation of the reconstructed HV traces at ESQ plates Q1LT and Q1LB, which serves as a closure test. CBO radial frequencies are shown in Figure 3.80. The beam centroid drifts from simulations is also reproduced (see Fig. 3.81). The agreement of the momentum spread from simulated Run-1 beams with results from the FR analysis is also strong since the latter was one of the inputs to prepare initial muon beam distributions (see Subsec. 3.6.3). Several efforts within the g-2 were carried out to validate the beam extrapolated as presented in this document with data calorimeter detectors. An example of this collective effort is Fig. 3.67. However, in contrast with the straw tracking detection system and its specialized design to measure the muon beam, the task is daunting since calorimeters measure positron energies and arrival times and not the transverse coordinates of muons where positrons originated in the first place.

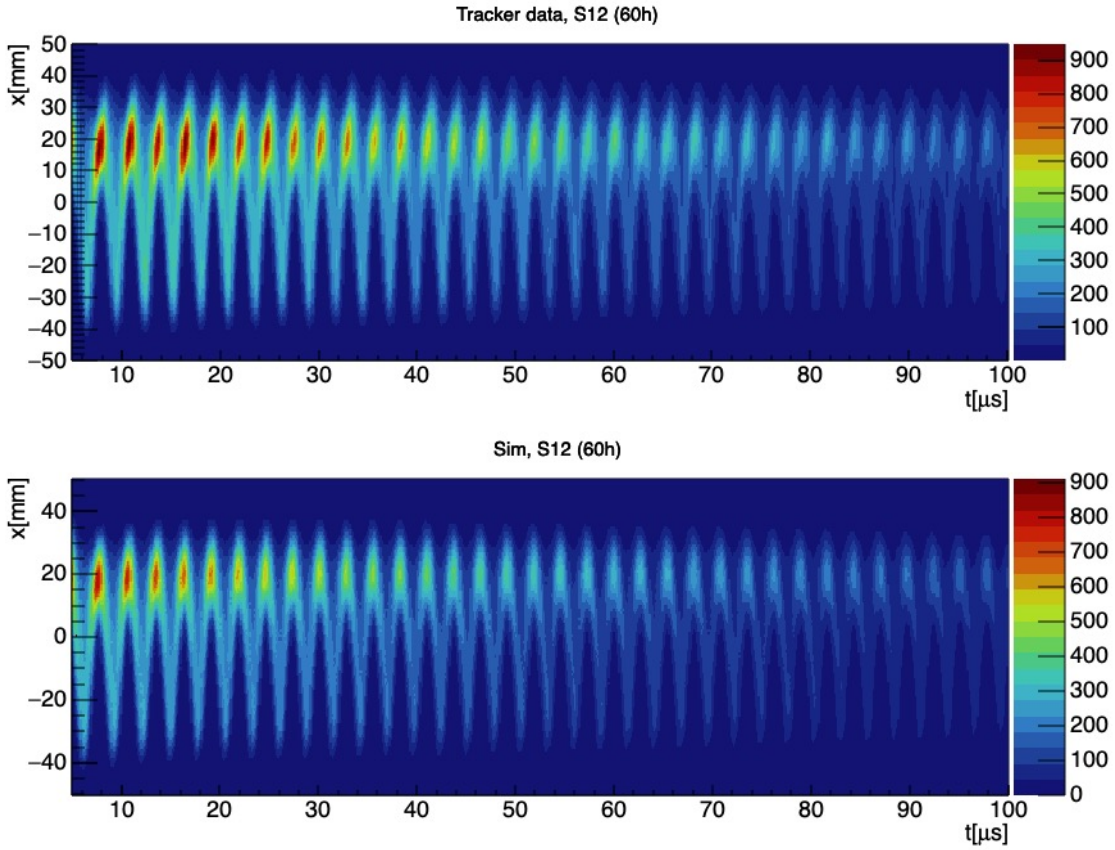

Figure 3.79: Radial beam evolution over time from tracker data (top) and simulated beam (bottom) during Run-1a.

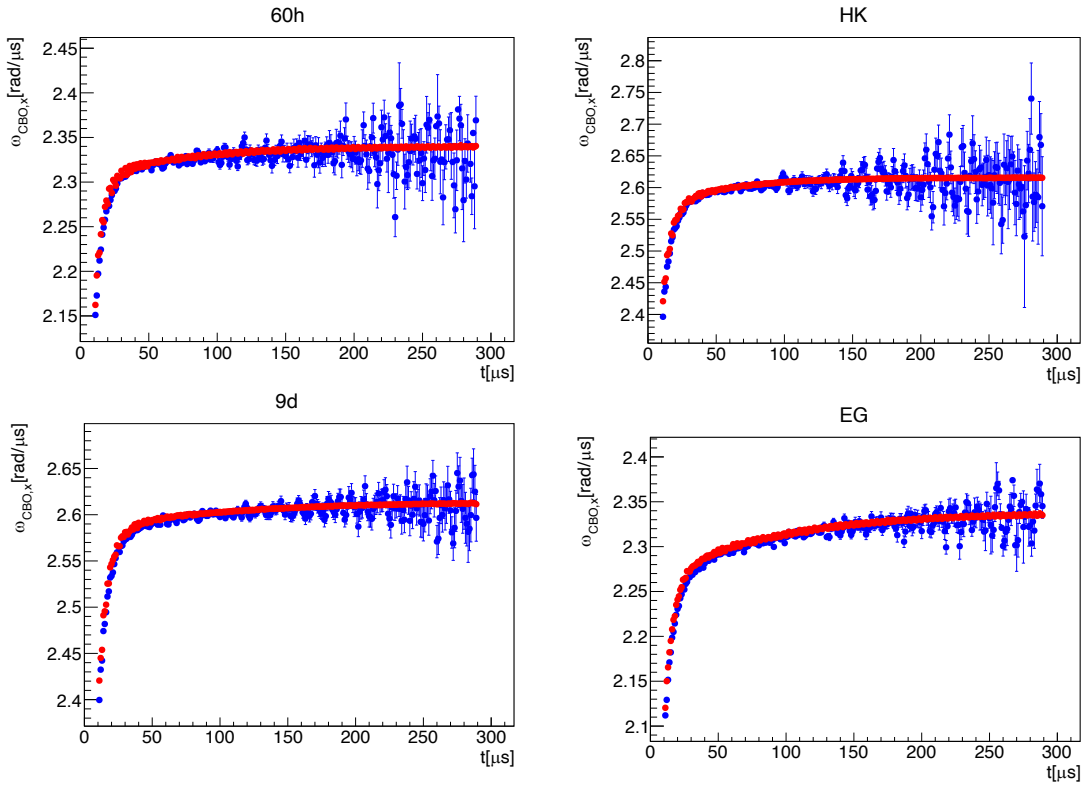

Figure 3.80: Radial CBO frequencies from simulated beam (red) and tracker data (blue) for each Run-1 dataset.

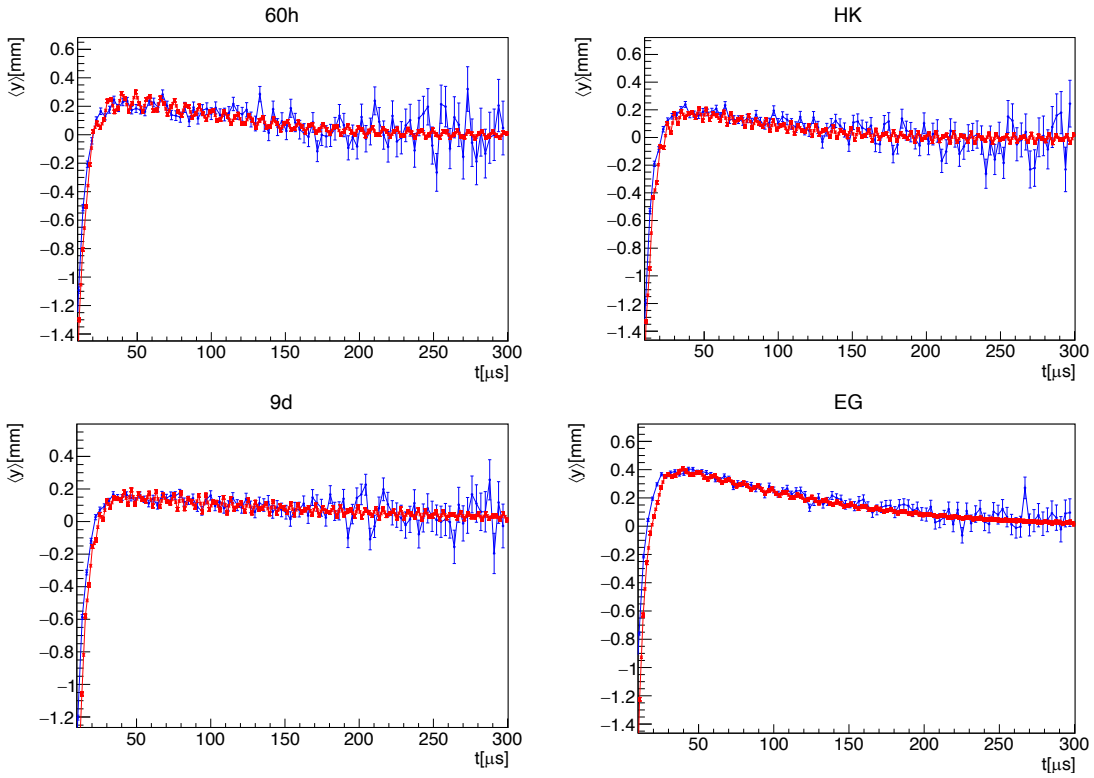

Figure 3.81: Vertical centroid from simulated beam (red) and tracker data (blue), station 12 for each Run-1 dataset. Results from tracker data and simulations are shifted vertically for the intended comparison of gradients. Without the introduced offsetting, data and simulations agree within the straw trackers vertical alignment uncertainty ($\sim 0.6\,\mathrm{mm}$).

3.7 Conclusions

In this chapter, the developed COSY-based model of the muon g-2 storage ring was presented. The model allows for preparations of realistic 10th-order transfer maps used for a detailed characterization of the muon beam stored in the ring via calculations of optical lattice functions and symplectic tracking simulations. The detailed implementation of the electric and magnetic fields based on measurements and modeling allows to capture both the linear and nonlinear behavior of the stored beam.

With the presented linear framework (with nonlinearities permeation in some cases), the optical lattice functions of the ring—including closed orbits—are prepared and tested their validity to describe the beam for the case of the g-2 storage ring. On the other hand, the assessment of nonlinearites permitted to build a detailed description of amplitude- and momentum-dependent tune shifts, as well as their implications on beam de-coherence, betatron resonances, and lost muons due to betatron amplitude modulations.

A nominal characterization of the typical beam injected into the ring was also performed, which is used in the experiment to extrapolate the measured beam transverse intensity to the full azimuthal span. With the modeling of the injection kickers as part of the COSY-based storage ring, the largest systematic uncertainty of the E-field correction is quantified.

The special behavior of the ESQ during Run-1 was reproduced numerically via optical lattice functions and symplectic tracking thanks to the developed method to reconstruct fields at the damaged ESQ station based on experimental data. Furthermore, the elaboration of a method to define initial beam conditions from available data allowed to reproduce with high fidelity the Run-1 beam beyond observations, used for systematic correction studies in the experiment.

Chapter 4

Beam Dynamics Correction Studies

4.1 Introduction

As presented in Sec. 1.3, the dynamical properties of the stored beam from which the anomalous magnetic moment of the muon a_μ is indirectly measured introduces ppb-level systematic corrections to the *measured* anomalous precession frequency ω_a^m [46]. Applications using the beam characterization developed with the COSY-based model of the muon g-2 storage ring (see Ch. 3) aimed at quantifying those corrections and their uncertainties are presented in this chapter.

To initiate the discussion of the aforementioned corrections, it is pertinent to start with the nominal case. In this idealized case of perfect circular motion and the ESQ stations turned off, ω_a is equal to the nominal (g-2) frequency ω_{a0}:

$$\omega_{a0} \equiv -a_\mu \frac{eB_0}{m_\mu}, \tag{4.1}$$

where the magnetic field $\vec{B}_0$ is vertical and constant in magnitude. The four beam-dynamics systematic corrections—necessary to carry ω_{a0} towards the reality of the beam stored in the g-2 storage ring to a ppb-level precision—are symbolized and identified as follows:

- C_{ml}: Muon loss correction.

- C_{pa}: Phase acceptance correction.
- C_e: E-field correction.
- C_p: Pitch correction.

With these systematic corrections properly quantified, the measured frequency ω_a^m is unbiased and the true a_μ calculated:

$$a_\mu = -\frac{m_\mu}{e\langle B\rangle}\omega_{a0} \approx -\frac{m_\mu}{e\langle B\rangle}\omega_a^m \left(1 + C_{ml} + C_{pa} + C_e + C_p\right), \tag{4.2}$$

where $\langle B\rangle$ is the average magnetic field weighted by the muon beam [43]. As shown in Sec. 4.5, the azimuthal characterization of the beam presented in Ch. 3 is utilized to convolute the measured magnetic field with the muon beam around the ring.

C_{ml} and C_{pa} are intrinsic to the experimental technique used in the g-2 experiment, wherein ω_a^m is extracted from fitting the time-dependent detected number of positrons above energy threshold (see Subsec. 1.2.1) with a sinudoidal multi-parameter functional form [37] proportional to

$$\cos\left(\omega_a t + \varphi_0\right). \tag{4.3}$$

As explained in Sec. 1.3, an overall change in the g-2 Phase φ_0 during the data taking period (i.e., $\sim 30\,\mu\text{s} < t < 700\,\mu\text{s}$ after beam injection) is undistinguishable and quietly absorbed by the extracted ω_a^m from the χ^2-minimization fit. When the physical meaning of φ_0 is accounted for, it does become time dependent due to lost muons and momentum-spin correlations; the magnitude of these two beam properties can lead to non-negligible muon loss corrections. In Sec. 4.2, a simulation-driven calculation of the C_{ml} correction during Run-1 with the COSY-based model is presented.

On the detection side, the g-2 phase is in fact an observable derived from positrons that are detected in the experiment [16]. Out of each transverse location, positrons are emitted within a decay cone which, due to finite calorimeter acceptance, most of the cases is not entirely detected. The distribution of detected phases over the decay cone is not uniform since positrons' initial directions are correlated with the spin direction of muons prior to the decay. Therefore, the observed g-2 phase depends on the muon transverse distribution. During Run-1, the muon transverse profile exhibited drifts over the data taking period (see Sec. 3.6). Consequently, the g-2 phase also varied (see Sec. 4.3). This effect introduces the C_{pa} correction. Section 4.3 elaborates on the multiple efforts from the beam-dynamics side that were performed as part of this dissertation to quantify the C_{pa} correction, which became relevant during Run-1 due to the faulty ESQ behavior (posteriorly repaired).

On the other hand, C_e and C_p directly bias the measured precession ω_a^m without the intervention of the g-2 phase. Instead, these corrections encapsulate the first-order effects of vertical motion and momentum spread on the spin dynamics relative to the cyclotron beam motion, for which the expression of the nominal (g-2) frequency ω_{a0} is not sensitive. As shown in Sec. 4.4, the standard expressions of C_e and C_p were tested with the COSY-based model beyond the assumptions on which they were derived for previous versions of the muon g-2 experiment.

4.2 The Muon Loss Correction

4.2.1 Momentum-phase correlations

In real terms, φ_0 in Eq. (1.25) represents the overall angle between the beam spin polarization and its momentum at $t = 0$, i.e., the precession-fit reference time which corresponds to the

moment when the beam is injected into the storage ring:

$$\varphi_0(t) = \frac{1}{N_s(t)} \sum_{i=1}^{N_s(t)} \varphi_{0,i}, \tag{4.4}$$

where $N_s(t)$ is the number of stored muons at time t and $\varphi_{0,i}$ the individual phase of a muon within the stored beam.

For this reason, if there are lost muons (see Subsec. 3.4.3) whose individual phases are correlated with their momenta and, in addition, the stored beam momentum average $\langle\delta\rangle$ is sensitive to muon loss, then a time-dependent phase sufficiently large to bias ω_a^m can potentially emerge (see Eq. (1.29)):

$$\Delta\varphi_0(t) = \frac{d\varphi_0}{d\langle\delta\rangle}\Big|_{t=0} \langle\delta\rangle(t) = m_\delta \langle\delta\rangle(t). \tag{4.5}$$

As explained in Subsec. 2.3.4, due to dispersive effects and the momentum compaction factor in the Delivery Ring, high-momentum muons experience greater integrated magnetic dipole fields along their trajectories. Thus, their spins precess larger angles in the mid-plane in comparison to low-momentum muons (the opposite case). This effect leads to $\varphi_0-\delta$ correlations. From BDS simulations described in Ch. 2 (Fig. 2.17), $m_\gamma = 29.2 \pm 9.4\,\text{mrad}$. In terms of δ as in Eq. (4.5), from $m_\delta \approx \gamma_0\beta_0^2 m_\gamma$ the $\varphi_0-\delta$ linear correlation is

$$m_\delta \approx 8.79 \pm 2.8\,\text{mrad}/(\%\delta). \tag{4.6}$$

Results from external tracking simulations of the Muon Campus (Ref. 110)—in agreement with Eq. (4.6) but with higher statistical power—are used instead for the following simulation-based calculation of C_{ml}. The correlation derived from this work is shown in

Fig. 4.1.

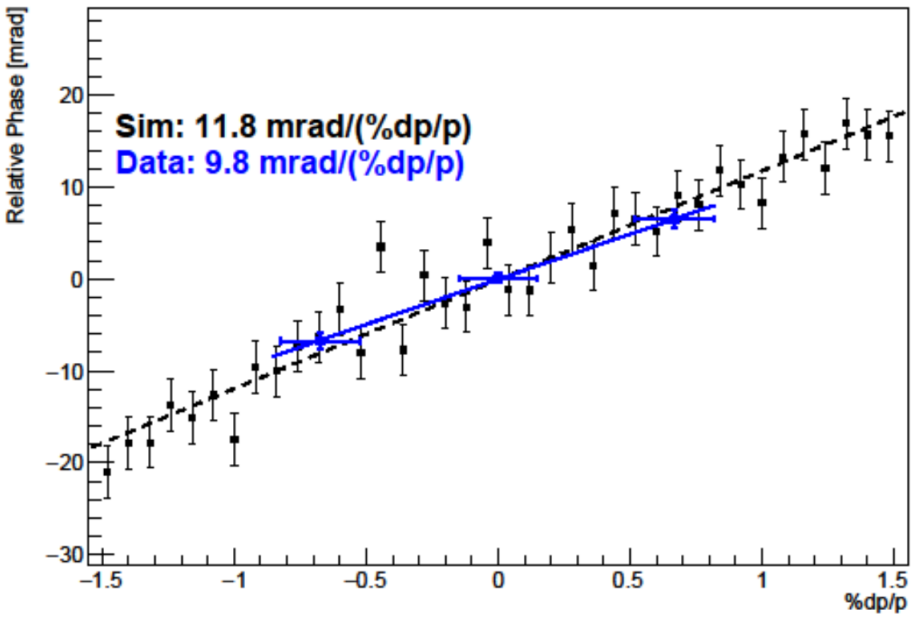

Figure 4.1: Momentum dependence of the initial g-2 phase φ_0. The simulations (black plot markers) are in good agreement with experimental data (blue, preliminary). The experimental data were obtained by studying the behavior of muons with momenta above and below the magic momentum in the storage ring [14].

4.2.2 Momentum spread subject to lost muons

The other ingredient to numerically reproduce the changing phase from muon loss is the evolution of the beam momentum average. For this purpose, the momentum spread from tracking simulations for each of the Run-1 datasets with the COSY-based model (described in Subsec. 3.6.4) is numerically traced as muons get lost during the data-taking period in the simulation.

In general, the momentum compaction in the storage ring yields a longitudinal dilution as shown in Fig. 4.2. Even though the overall momentum spread is diluting in time, as can be observed at any given azimuthal location, this effect does not introduce a slowly-changing momentum profile; for time intervals of the order of a cyclotron period as used in positron

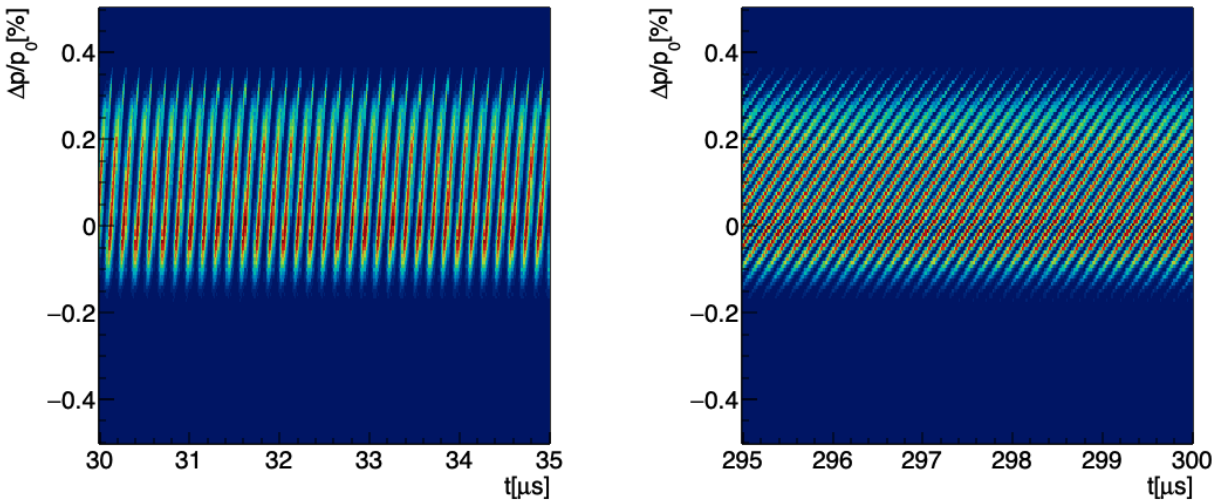

Figure 4.2: Momentum spread over time from Run-1d tracking simulations at early and late times. While the beam spreads in the longitudinal direction, muons with different momenta combine.

signals to extract ω_a, the average momentum does not change.

On the other hand, muon losses cause a lasting momentum dependence when their overall momentum is not the beam's momentum average. Run-1 muon loss rates were low, but large enough to produce a 10 ppb-level systematic error as indicated by dedicated measurements [46] and the beam tracking simulations presented in this section. Figure 4.3 displays muon loss fractions from simulations and data.

Notwithstanding the comparable muon loss fractions between measurements and simulations, differences arise from the magnetic radial field uncertainty implemented in the COSY-based model, a single implementation of the trolley run measurements for all Run-1 datasets, and gain correction uncertainties from the data-taking front.

Several factors influence the relative amount of muon losses. In particular, while the 60h and EG datasets operated at a nominal ESQ set-point of $HV = 18.3\,\mathrm{kV}$ near the $3\nu_y = 1$ resonant condition, the other Run-1 datasets (HK and 9d) operated at $HV = 20.4\,\mathrm{kV}$, farther

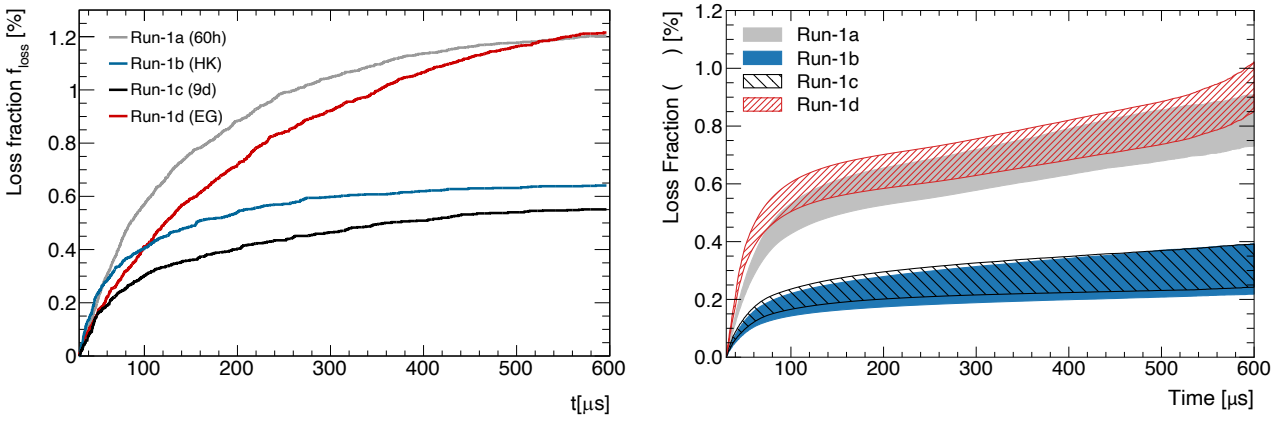

Figure 4.3: Muon loss rates versus time, 30 μs after injection, from symplectic tracking Run-1 simulations (left) and data (right, Ref. 15). The $3\nu_y = 1$ resonance nearby Runs 1a and 1d increases the loss fraction (Sec. 3.4.3). Uncertainty bands on the curves from data accounts for experimental scaling errors in the determination of muon loss rates.

from the nearest resonant conditions of $HV \approx 18.6\,\text{kV}$ and $HV \approx 21\,\text{kV}$ (see Subsec. 3.4.3). For this reason, muon loss rates were lower for HK and 9d datasets. Moreover, the larger the number of inserted collimators, the more likely a muon—either with a modulated betatron amplitude from nonlinearities or not—is to hit a collimator and get lost faster, yielding less lost muons at later times. The initial beam distribution that results from the injection process also determines the population of muons prone to be lost (e.g., outermost muons), thus becoming an important factor on this regard.

Off-momentum muons oscillate around fixed points closer to the limiting collimator apertures due to the radial dispersion functions. This effect favors muon losses, as shown in Fig. 4.4.

4.2.3 The correction C_{ml} from the Run-1 simulated beam

Depending on the betatron amplitude beam distributions and the number of muons with largest momentum offsets, the average momentum of lost muons does modify the overall

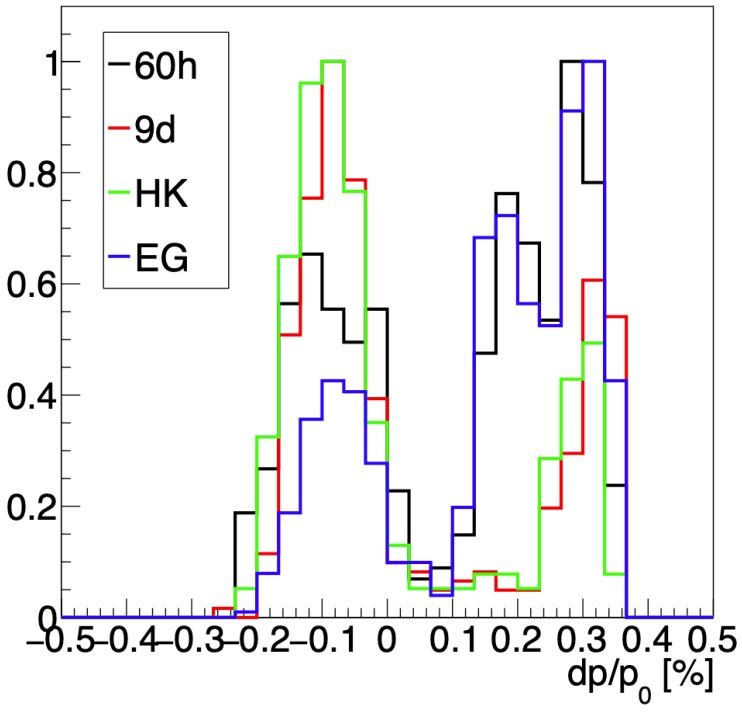

Figure 4.4: Relative momentum offsets of lost muons from Run-1 symplectic tracking simulations ($30\,\mu\text{s} < t < 300\,\mu\text{s}$).

momentum spread of stored muons, as shown in Fig. 4.5. With m_δ and $\langle\delta\rangle(t)$ evaluated, the relative shift of the phase $\Delta\varphi_0(t)$ with respect to the phase at $t = 30\,\mu\text{s}$ is estimated; results are shown in Fig. 4.6.

Monte Carlo simulations to recreate histograms from which ω_a are extracted in the experiment are prepared, where the event generation are obtained from a 5-parameter functional form similar to Eq. (1.25):

$$N(t) = N_0 e^{-\frac{t}{\gamma_0\tau}} \left(1 + A\cos\left(\omega_a t - (\varphi_0 + \Delta\varphi_0(t))\right)\right), \tag{4.7}$$

where N_0, $\gamma_0\tau$, A, $\omega_a = 1.43729\,\text{MHz}$, and φ_0 are constants. The resulting histogram is fitted back with the same generating function, although the phase is a simple parameter with no time dependence. The frequency ω_a' that χ^2-minimizes the fit-vs-MC difference is

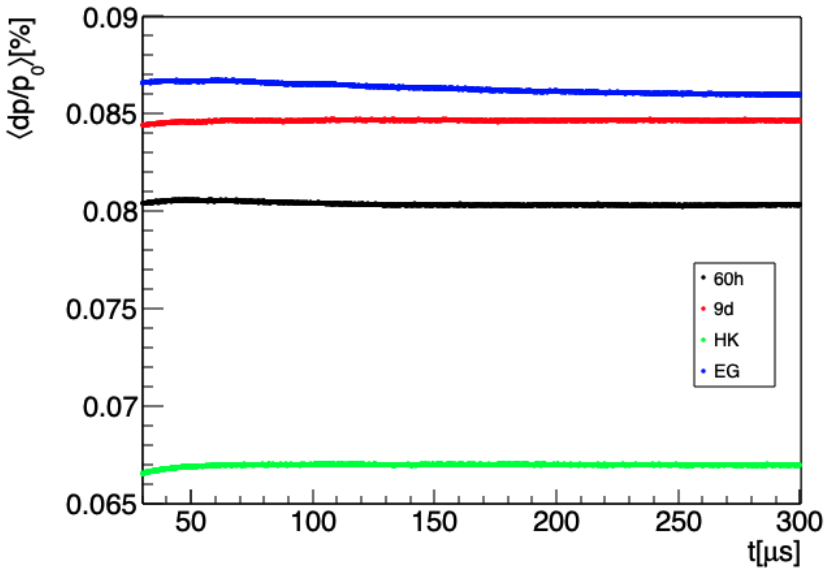

Figure 4.5: Stored beam's average momentum offset, relative to magic momentum, over time from tracking simulations with the COSY-based model.

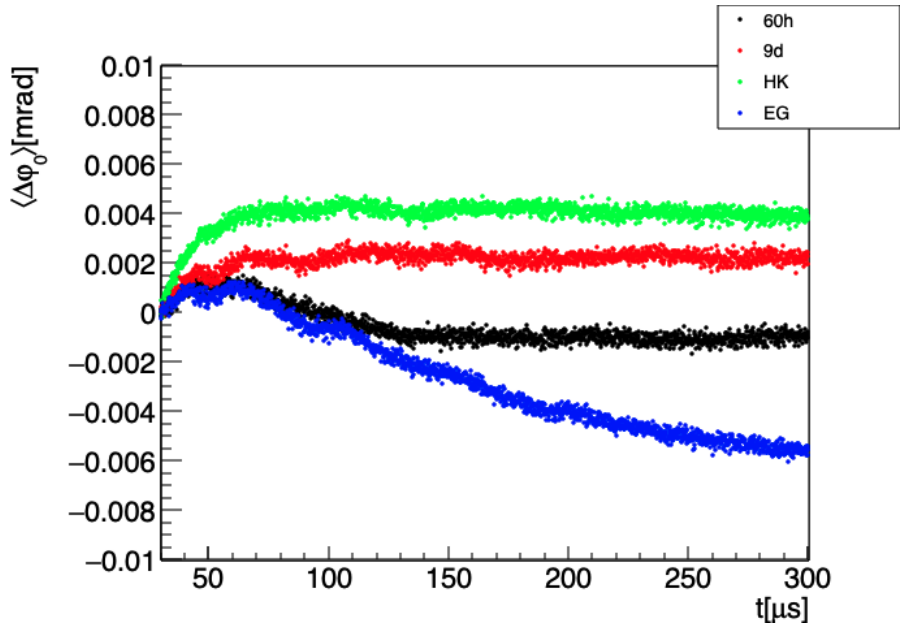

Figure 4.6: g-2 phase time evolution from Run-1 symplectic tracking simulations driven by lost muons. The beam injection scheme and operational set-points lead to different functional forms per Run-1 dataset.

taken to calculate the muon loss systematic correction as [1]

$$C_{ml} = -\frac{\left(\omega_a' - \omega_a\right)}{\omega_a}. \tag{4.8}$$

Results from each of the COSY-based Run-1 tracking simulations are shown in Table 4.1, which are within < 12 ppb away from data-driven results [46].

	C_{ml} [ppb]
Run 1a (60h)	-14.13 ± 4.30
Run 1b (9d)	2.18 ± 2.86
Run 1c (HK)	4.16 ± 4.47
Run 1d (EG)	-24.57 ± 2.47

Table 4.1: ω_a corrections due to muon losses from beam tracking simulations. Errors for each calculation are produced after considering the measured spin-momentum correlation uncertainties and simulation statistical limits.

4.3 The Phase Acceptance Correction

Similar to the muon loss correction C_{ml}, drifts of the g-2 phase φ_0 during the data taking period bias the measured anomalous precession frequency ω_a^m. As explained in the introduction of this chapter, the phase acceptance correction C_{pa} accounts for phase changes from the detection side rather than its physical meaning. From the (V-A) parity violating muon decay $\mu^+ \to e^+\nu_e\bar{\nu}_\mu$, highest-energy positrons are emitted in the muon spin direction with a probability proportional to the angle between these two directions. On the other hand, the positron emitted direction altogether with its initial transverse coordinates in the storage volume determine whether it is detected by a calorimeter or not (see Fig. 4.7, right side, for a

[1] For a convention where the phase is accompanied by a negative sign in the functional form, the C_{ml} sign is reversed, too.

typical calorimeter acceptance map). Therefore, since the g-2 phase carried by a positron is indirectly related by its initial direction thanks to the V-A decay process, positron transverse decay coordinates and g-2 phases are correlated. Phase acceptance maps in transverse $x-y$ planes along the storage region are prepared in the g-2 collaboration with a *Geant4*-based simulation program named *gm2ringsim* [111]. The model includes decay modules as well as all of the active detectors and most of the passive components installed in the storage ring, which allows to recreate with high detail material effects that emitted positrons experience from their initial coordinates to the calorimeter locations. Figure 4.7 shows typical phase and detection acceptance maps prepared with the *gm2ringsim* model by Khaw *et al.* [16].

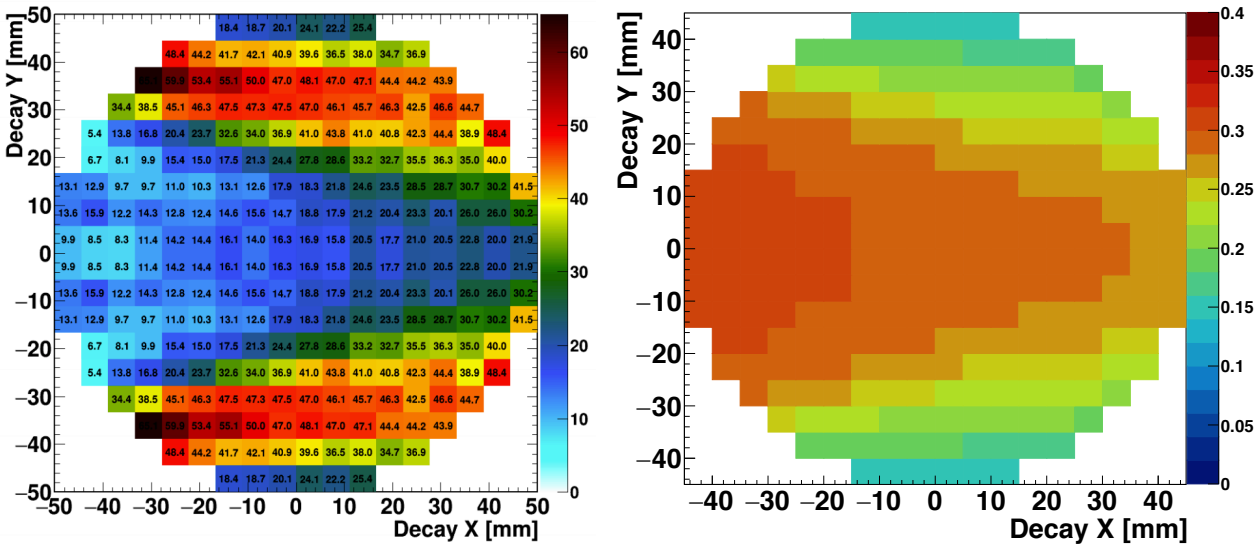

Figure 4.7: Typical detected-phase $\varphi_{0,k}\left(x_i, y_j\right)$ (left) and calorimeter acceptance $\varepsilon_{c,k}\left(x_i, y_j\right)$ (right) maps from *gm2ringsim* [16]. On the phase map, values are relative to a central g-2 phase defined at injection. 1 µrad phase shifts over a muon lifetime in the laboratory frame induce $omega_a^m$ shifts of about 10 ppb.

Under normal conditions, the stored beam—although it may exhibit fast beam and width betatron oscillations due to beam mismatch—is expected to maintain a constant transverse distribution on the time scales of data taking periods (i.e., $30\mu s < t < 700\mu s$) under the effects of a stable optical lattice. If ESQ specifications are met, such scenario is expected [112]

and the overall detected phase remains unchanged over the measurement (i.e, $C_{pa} = 0$). Nevertheless, sufficiently large muon loss rates can potentially induce vertical width beam drifts after the nominal fit start $t = 30\mu$s posterior to injection (see Fig. 3.52). Another potential mechanism that could introduce a changing detected phase owing to beam drifts is amplitude modulations from betatron resonances. However, muon loss studies with the *COSY*-based model (see Subsec. 3.4.3) indicate that stored muons under these modulations exhibit periodic patterns around 3-period fixed points, but do not coherently grow nor decrease to induce slow beam transverse gradients; if they get collimated, their effect potentially adds to the phase-acceptance correction via beam width drifts instead. Regardless of any of these mechanisms, the $g-2$ straw tracking detectors [42] high-resolution measurements encapsulate the information required to quantify beam drifts at their two readout azimuthal locations. This was the case during Run-1, where the unstable optical lattice produced slowly changing beam centroids and widths beyond $t = 30\mu$s (see Sec. 3.6).

A machinery was needed to be developed in order to systematically quantify phase-acceptance corrections during the unusual Run-1 datasets. For this purpose, a multi-disciplinary task force within the $g-2$ collaboration was established [16], wherein the author of this dissertation participated in determining methods to extract C_{pa} from tracker data (Subsec. 4.3.1), distinguish the main mechanisms that drive these corrections (Subsec. 4.3.2), and the extrapolation of phase drifts from tracker data to the entire storage ring (Subsec. 4.3.3).

4.3.1 Extraction of phase drifts

At a given calorimeter $k = \{1, 2, \ldots, 24\}$, positrons emitted at the transverse coordinates $\left(x_i, y_j\right)$ contribute to the total histogram $N_k(t) = N_{0,k} e^{-t/\tau} \left[1 + A_k \cos\left(\omega_a t + \varphi_0^{\text{calo}\,k}(t)\right)\right]$

of detected number of positrons above energy threshold a signal $N_{ijk}(t)$ equal in form [113]:

$$N_{ijk}(t) = M_{T,k}\left(x_i, y_j, t\right) \varepsilon_{c,k}\left(x_i, y_j\right) e^{-t/\tau} \left[1 + A_k(x_i, y_j) \cos\left(\omega_a t + \varphi_{0,k}\left(x_i, y_j\right)\right)\right], \quad (4.9)$$

where $M_{T,k}\left(x_i, y_j, t\right)$ is the relative muon beam intensity at $\left(x_i, y_j\right)$ at calorimeter k readout location, $\varepsilon_{c,k}$ the acceptance that positrons emitted at $\left(x_i, y_j\right)$ will hit calorimeter k and enter the $N_k(t)$ histogram, $A_k(x_i, y_j)$ is the asymmetry amplitude (see Eq. 1.24), and $\varphi_{0,k}\left(x_i, y_j\right)$ the detected position-dependent phase at calorimeter k. In this view and considering

$$N(t) = \sum_{ij} N_{ij}(t), \quad (4.10)$$

the total phase $\varphi_0^{\text{calo}\,k}(t)$ detected by the k^{th} calorimeter is the phasor addition of all the weighted transverse locations [16]:

$$\varphi_0^{\text{calo}\,k}(t) = \arctan \frac{\sum_{ij} M_{T,k}\left(x_i, y_j, t\right) \cdot \varepsilon_{c,k}\left(x_i, y_j\right) \cdot A_k\left(x_i, y_j\right) \cdot \sin\left(\varphi_{0,k}\left(x_i, y_j\right)\right)}{\sum_{ij} M_{T,k}\left(x_i, y_j, t\right) \cdot \varepsilon_{c,k}\left(x_i, y_j\right) \cdot A_k\left(x_i, y_j\right) \cdot \cos\left(\varphi_{0,k}\left(x_i, y_j\right)\right)}. \quad (4.11)$$

Equation 4.11 constitutes the basis to estimate C_{pa} corrections in ω_a^m extracted from the T-Method [37] and is used to calculate detected phases in the following analysis. As observed from this equation, the detected phase develops a time dependence due to beam drifts—accounted for in $M_{T,k}\left(x_i, y_j, t\right)$—which was the case during all Run-1 datasets.

With Eq. 4.11, the phase, acceptance, and asymmetry maps from the *gm2ringsim* Team and, on the other hand, the measured beam intensity M_T at tracker azimuthal readout locations [82], the observed phase at nearby calorimeters (i.e., $k = 13$ and $k = 19$) can be extracted. The next step once $\varphi_0^{\text{calo}\,k}(t)$ is extracted is to determine the resulting shift on ω_a^m

induced by the changing phase. For this end, three different alternatives were analyzed to extract the slow component of the phase derived from Eq. 4.11 (Fig.4.8 shows the detected phase from Eq. 4.11 and its corresponding slow component):

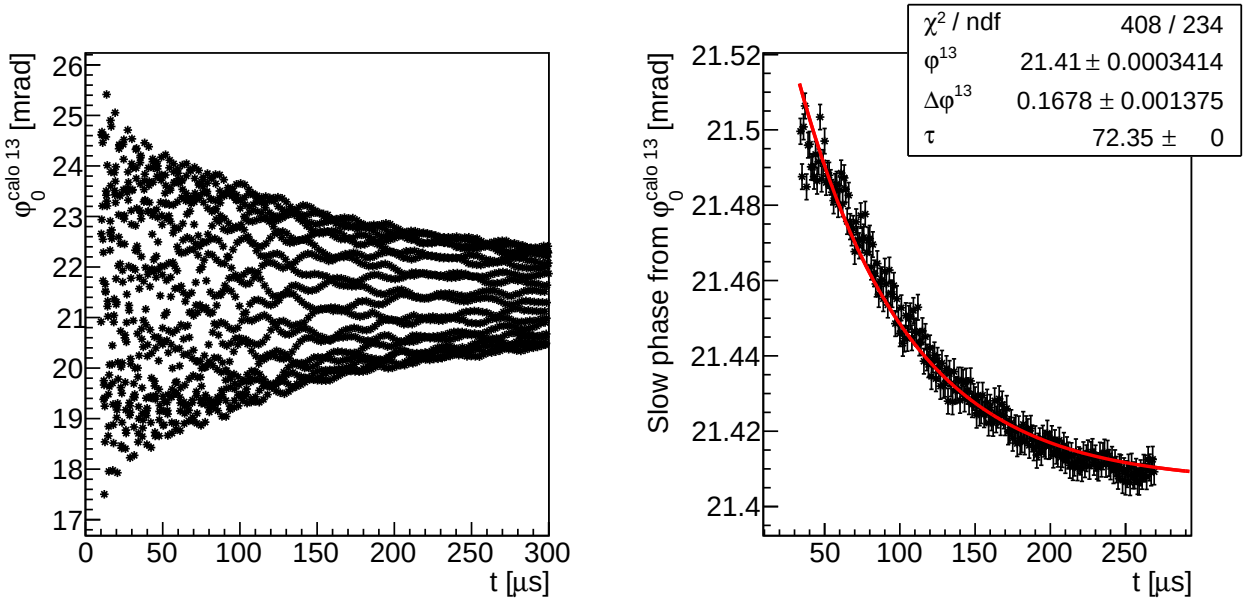

Figure 4.8: On the left side, phase $\varphi_0^{\text{calo }13}(t)$ from *COSY*-based Run-1d simulated beam and *gm2ringsim* maps (T-Method) via Eq. 4.11. On the right, the phase drift extracted with non-randomized, window fits and a single-exponential fit.

- Non-randomized, single fit [113]:

  A functional form with all the oscillatory acceptance-induced components

$$\begin{aligned}\phi(t) = \varphi_0' &+ \Delta\varphi e^{-t/\tau} \\ &+ A_{CBO} e^{-t/\tau_{CBO}} \sin\left(\omega_{CBO}(t)t + \phi_{CBO}\right) \\ &+ A_{2CBO} e^{-2t/\tau_{CBO}} \sin\left(2\omega_{CBO}(t)t + \phi_{2CBO}\right) \\ &+ A_{VW} e^{-t/\tau_{VW}} \sin\left(\omega_{VW}(t)t + \phi_{VW}\right)\end{aligned} \tag{4.12}$$

  is fitted to $\varphi_0^{\text{calo }k}(t)$ and use

$$\varphi_0' + \Delta\varphi e^{-t/\tau} \tag{4.13}$$

from the fit to represent the phase drift. The frequency $\omega_{CBO}(t)$ follows tracker data and

$$\omega_{\mathrm{VW}}(t) = \omega_{\mathrm{c}} - 2\sqrt{2k_{\mathrm{VW}} \cdot \omega_{\mathrm{CBO}}(t) \cdot \omega_c - k_{\mathrm{VW}}^2 \cdot \omega_{\mathrm{CBO}}^2(t)} \tag{4.14}$$

accounts for the aliased "vertical width" frequency $\omega_c - 2\omega_y$ [37]. For more details of the single fit, refer to [113].

- Randomized [114]:

  Produce a beam profile $M_{T,k}(x_i, y_j, t')$ without the frequencies of the beam transverse motion $\omega_i = 2\pi/T_i$ by defining $t' = t + \sum_{i=1} ran_i$, where ran_i is a random number within $\{-T_i, T_i\}$. Use $M_{T,k}(x_i, y_j, t')$ in Eq. 4.11 to obtain the phase drift.

- Non-randomized, window fits [115]:

  Fit $\sim \pm 8\,\mu$s segments of $\varphi_0^{\mathrm{calo}\,k}(t)$ with the functional form

$$\begin{aligned} \phi_i = \varphi_{eq,i} & \\ & + A_{CBO,\tau} \sin\left(\omega_{CBO} t + \varphi_{CBO}\right) \\ & + A_{2CBO,\tau} \sin\left(2\omega_{CBO} t + \varphi_{2CBO}\right) \\ & + A_{VW,\tau_{VW}} \sin\left(\omega_{VW} t + \varphi_{VW}\right) \end{aligned} \tag{4.15}$$

  and use $\varphi_{eq,i}$'s from the fits to define the slow drift.

From Run-1a simulated data with the *COSY*-based model (see Subsec. 3.6.4), it was established that detector acceptance effects damage the randomization procedure to extract phase drifts [115], as shown in Fig. 4.9. Analysis performed by Mott [116] determined the cause of the misleading phase drifts from randomization to be radial decoherence; as the acceptance of the beam is subject to the coherent betatron motion in the radial direction,

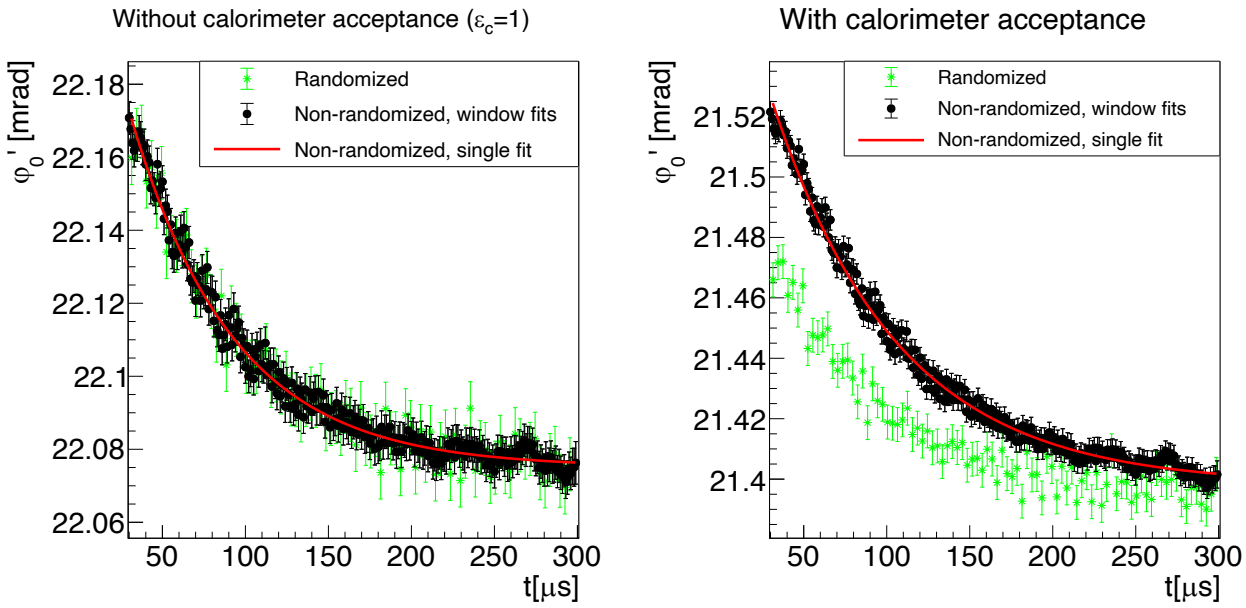

Figure 4.9: Extracted drifting phases from all extraction methods. On the left, all methods agree when detector acceptance is absent. On the right plot, the randomized method does not capture the phase drift from radial CBO decoherence, which emerges under the presence of nonuniform detector acceptance.

the slow decoherence drives a changing coupling of the beam intensity with the observed phase. Since the randomization method deletes the CBO component of the beam motion, ω_a^m shifts introduced by phase drifts from the randomization method are underestimated (see Fig. 4.10). Nevertheless, since coherent betatron oscillations at calorimeters in opposite sides of the ring are out of phase by π radians, their phase drifts due to CBO decoherence mostly cancel out [16]. The C_{pa} correction is induced by the overall detected phases around the twenty four azimuthal locations where calorimeters accept positrons. Therefore, slowly changing detected phases from CBO decoherence tend to cancel out. In the determination of C_{pa} central values for Run-1 datasets, the randomization method was used for this reason and the associated error from the partial cancellation was accounted for as a systematic error [16].

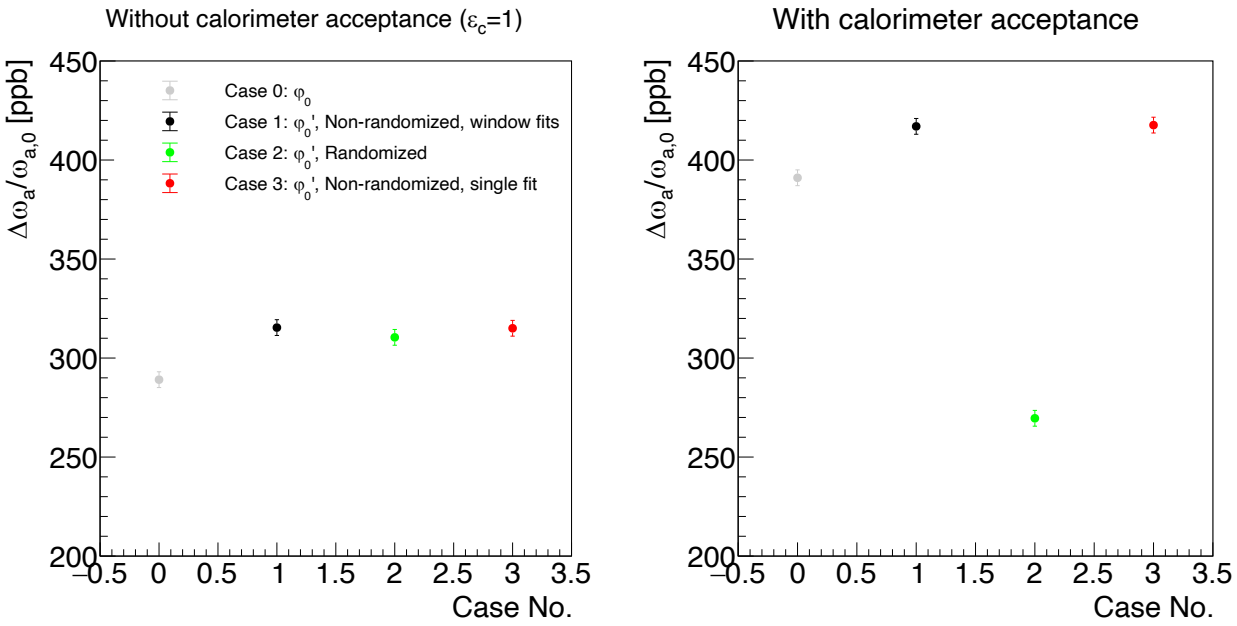

Figure 4.10: ω_a^m shifts due to phase-acceptance corrections mediated by the different phase drift extraction methods, without (left) and with (right) detector acceptance. Monte Carlo $N(t)$ histograms are generated with the drifting phases accounted for to extract the corresponding ω_a^m shifts. In gray, results from the raw phase $\varphi_0^{\text{calo}\,13}(t)$ without drift extraction are shown. The removal of phase drifting from radial CBO decoherence without acceptance is clearly visible in the right plot.

4.3.2 Phase drift driving mechanisms

Detected-phase distributions $\varphi_{0,k}(x_i, y_j)$ exhibit a rather consistent and symmetric pattern in x and y directions for $k = \{1, 2, \ldots, 24\}$ as shown in Fig. 4.7. In the radial direction, the projected phase to second order

$$\varphi_{0,k}(x_i) = \sum_j \varphi_{0,k}(x_i, y_j) \approx a_{x,0} + a_{x,1} x_i \tag{4.16}$$

has an asymmetric linear trend, whereas in the vertical case

$$\varphi_{0,k}(y_j) = \sum_i \varphi_{0,k}(x_i, y_j) \approx a_{y,0} + a_{y,2} y_i^2 \tag{4.17}$$

the detected-phase growth is mostly quadratic around $y = 0$. On the beam transverse distributions side, its representative beam moments during Run-1 are largely dominated by the radial centroid and widths in both transverse directions (see Fig. 4.29). Thus, in the perspective of Eq. 4.11 and recognizing that $|\varphi_{0,k}(x_i, y_j)| \ll 1$, time dependencies of the detected phase are dominated by its coupling with the beam radial centroid and the vertical width. And as discussed in Subsec. 4.3.1, phase drifts also emerge from radial CBO decoherence.

The three dominant mechanisms that produce long-term ($30\mu s < t < 700\mu s$) variations of the detected phase are shown in Table 4.2.

For Run-1 cases, the phase drifts can be represented with the single-exponential functions shown in Table 4.2. The last column lists drift amplitudes by plugging $M_{T,13}$ from the *COSY*-based Run-1a simulated beam (see Subsec. 3.6.4) at $k = 13$, and phase, asymmetry, and acceptance maps from *gm2ringsim*, T-Method [16].

Table 4.2: Main mechanisms of detected-phase drifts. The vertical contribution dominates the phase-acceptance correction during Run-1 at calorimeters $k = 13$ and $k = 19$ near trackers longitudinal acceptance.

Mechanism	Phase drift term	$\Delta\varphi^{13,\cdots}$, Run-1a sim.
Vertical beam drifts	$\varphi^{k,Y} + \Delta\varphi^{k,Y} e^{-t/\tau_{Slow}}$	0.145 mrad
Radial beam drifts	$\varphi^{k,X-Slow} + \Delta\varphi^{k,X-Slow} e^{-t/\tau_{Slow}}$	0.053 mrad
Radial CBO decoherence	$\varphi^{k,X-CBO} + \Delta\varphi^{k,X-CBO} e^{-t/\tau_{CBO}}$	−0.011 mrad

In order to extract drifts for each mechanism individually, the distribution $M_{T,k}$ is manipulated as follows:

- Vertical (Y): Take $M_{T,k}(x_{stable}, y, t)$, where $x_{stable,i}$'s are time-independent (i.e., only vertical slow drifts) and follow the radial beam distribution integrated over 30−300 µs (see Fig. 3.54).

- Slow radial ($X - Slow$): Take $M_{T,k}(x_{slow}, y_{stable}, t)$, where $x_{slow,i}$'s are randomized radial data (i.e., only radial slow drifts). $y_{stable,i}$'s are time-independent and follow a Gaussian distribution with $\bar{y}$ and standard deviation σ_y from data averages between 30−300 µs.

- Radial CBO ($X - CBO$): Take $M_{T,k}(x_{CBO}, y_{stable}, t)$, where $x_{CBO,i}$'s are radial data shifted and scaled to remove mean and RMS drifts (i.e., only X-CBO decoherence).

Figure 4.11 shows the resulting phases with their corresponding drifts on the right side. The decoherence time constant τ_{CBO} is calculated from the radial CBO amplitudes decoherence and τ_{Slow} is taken to be the same for both vertical and slow-radial mechanisms.

When the entire phase drift is directly calculated from the $\varphi_0^{\text{calo}\,k}(t)$ signal without any manipulation of the beam distribution, the drift amplitude is in agreement within $\sim 10\%$

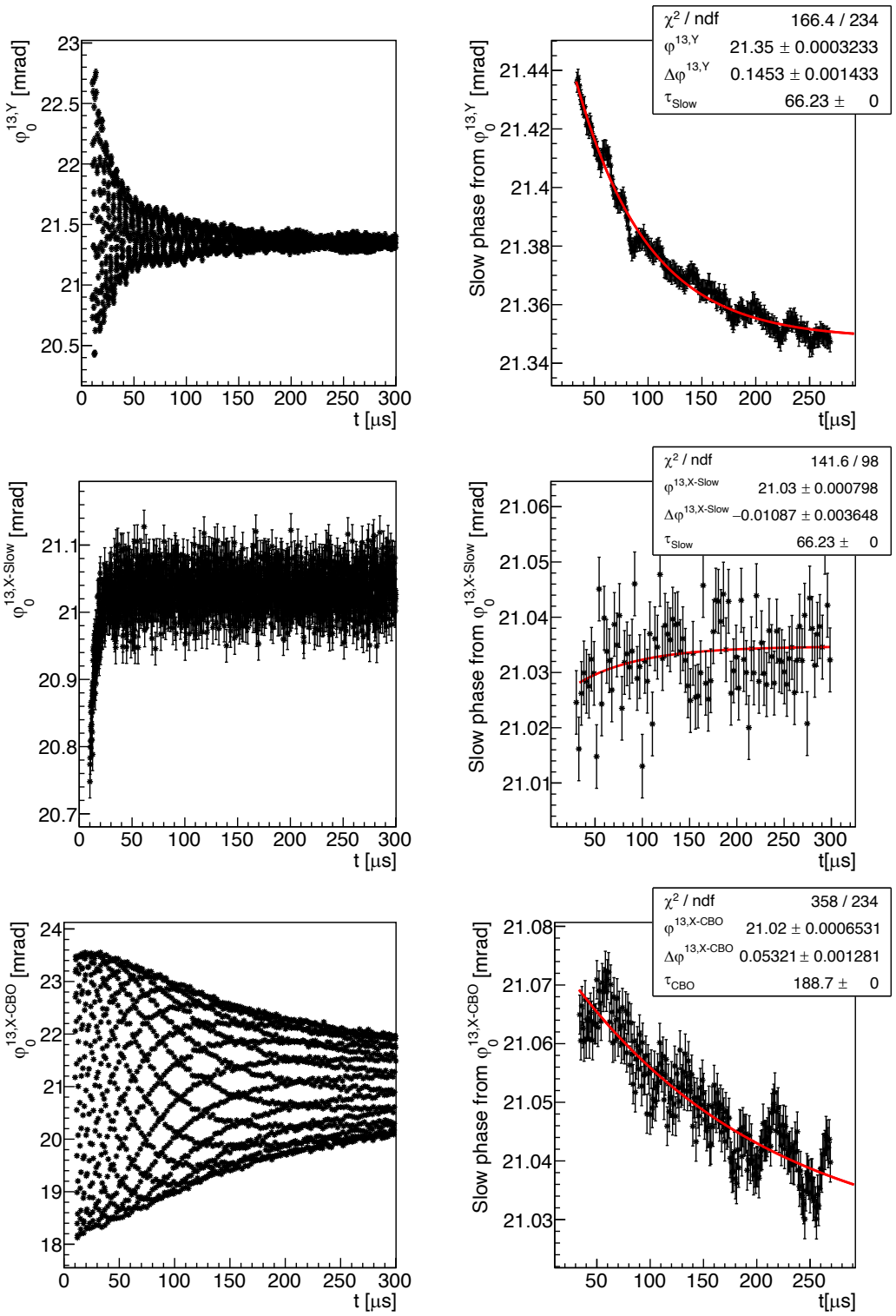

Figure 4.11: Phases $\varphi_0^{\text{calo}\,k}(t)$ (left) and their corresponding phase drifts (on the right) from the non-randomized, window fits method. The two plots on top correspond to a detected phase at calorimeter $k = 13$ from vertical beam drifting. In the middle, phase changes are driven by slow radial beam motion. At the bottom, phase drifting due to radial CBO decoherence. Fits in red are performed to extract drift amplitudes.

with the sum of the contributions from each mechanism [117], i.e.,

$$\Delta\varphi_0^k \approx \Delta\varphi^{k,Y} + \Delta\varphi^{k,X-Slow} + \Delta\varphi^{k,X-CBO}. \tag{4.18}$$

The disagreement is likely due to correlations between $\Delta\varphi^{k,Y}$, $\Delta\varphi^{k,X-Slow}$, and $\Delta\varphi^{k,X-CBO}$.

4.3.3 Azimuthal extrapolation of phase drifts

Since C_{pa} corrects for detected-phase drifts at all the calorimeters and, on the other hand, beam drifts caused by the unstable optical lattice during Run-1 were azimuthally dependent (see Fig. 3.74), phase calculations of $\varphi_0^{\text{calo}\,k}$ near $k = 13$ and $k = 19$ from tracker data is not sufficient. With the detailed knowledge of the main mechanisms that drive detected-phase drifts, it is possible to prepare methods in order to project $\varphi_0^{\text{calo}\,k}$ from tracker data to all calorimeter stations $k = \{1, 2, \ldots, 24\}$. The most precise method found for this end is to transform the time-dependent muon transverse coordinates $\{x(\theta_1, t), y(\theta_1, t)\}$ measured by the straw trackers one by one with the *COSY*-based optical lattice functions. To transform these individual coordinates from the tracker data location θ_1 to the readout azimuthal location of calorimeter k, θ_2, a pair of equations similar to Eqs. 3.73 but with time-dependent lattice functions are used:

$$\begin{aligned} x(\theta_2, t) &= \kappa_x(\theta_1, \theta_2, t)\,(x(\theta_1, t) - \bar{x}(\theta_1, t)) + x_0(\theta_2, t) + D_x(\theta_2, t)\bar{\delta} \\ y(\theta_2, t) &= \kappa_y(\theta_1, \theta_2, t)\,(y(\theta_1, t) - \bar{y}(\theta_1, t)) + y_0(\theta_2, t), \end{aligned} \tag{4.19}$$

where

$$\kappa_x(\theta_1, \theta_2, t) = \frac{\sqrt{\varepsilon_x(t)\beta_x(\theta_2, t) + D_x^2(\theta_2, t)\sigma_\delta}}{\sigma_x(\theta_1)} \quad \text{and} \quad \kappa_y(\theta_1, \theta_2, t) = \sqrt{\frac{\beta_y(\theta_2, t)}{\beta_y(\theta_1, t)}}. \tag{4.20}$$

All the parameters in Eqs. 4.19 and 4.20 are readily available from tracker data and the optical lattice functions for each Run-1 dataset. Shifting factors can be introduced to match offsets between closed orbits and tracker data; these discrepancies are accounted for as systematic errors of the phase-acceptance correction [16]. Also, radial closed orbit drifts can be ignored (see Subsec. 3.6.4) and azimuthal distortions of the vertical closed orbit can be treated as an additional systematic error since the detected-phase does not strongly depend on beam vertical centroid drifts. Once beam transverse profiles $M_{T,k}(x_i, y_j, t)$ are produced in this way, Eq. 4.11 can be utilized to compute the time-dependent phases at each calorimeter station. Validation tests were performed by comparing the resulting ω_a^m shifts following the aforementioned method with detected phases directly computed with $M_{T,k}$ from *COSY*-based tracking simulations [16]. Discrepancies of less than 10 ppb were found between these two approaches, indicating reliance on the reconstructed method via Eqs. 4.19.

Another method to reproduce detected-phase drifts at each calorimeter is to scale drift amplitudes from the main phase-acceptance correction driving mechanisms (see Eq. 4.18) [117]. Although this procedure leads to a less accurate C_{pa} (~ 50 ppb), it provides a path to identify the overall effect of each driving mechanism on the final correction as shown next.

With the *COSY*-based Run-1a simulated beam (see Subsec. 3.6.4) at $k = \{1, 2, \ldots, 24\}$, common phase/asymmetry maps for all calorimeter stations (for comparison purposes), and and per-calorimeter acceptance maps from *gm2ringsim* (T-Method) [16]. $\Delta\varphi^{k,Y}$, $\Delta\varphi^{k,X-Slow}$, and $\Delta\varphi^{k,X-CBO}$ drift amplitudes are calculated at all calorimeter stations as explained in Subsec. 4.3.2; results are shown in Figs. 4.12-4.14.

In the vertical case, even though the induced phase shifts are a consequence of both centroid and width centroid drifts, the drift amplitudes are strongly dominated by vertical

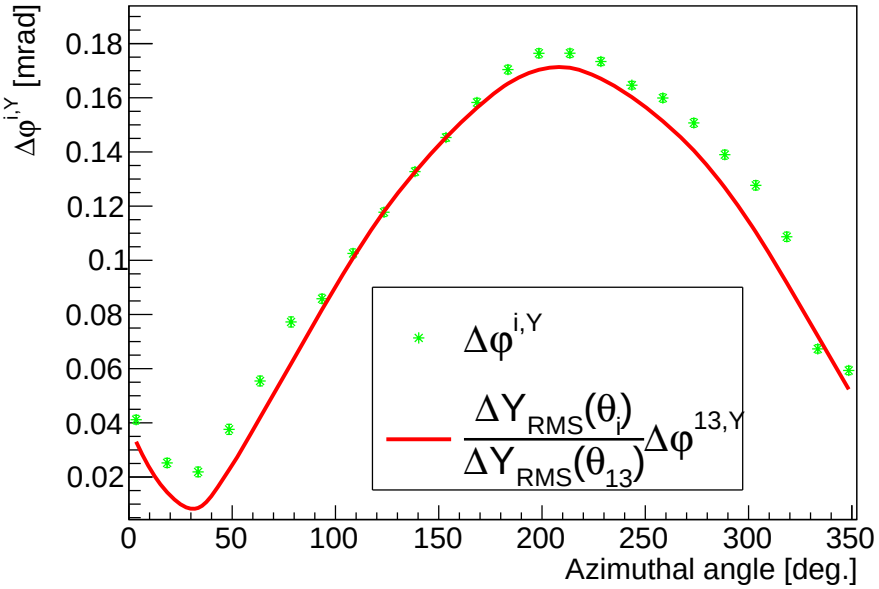

Figure 4.12: Drifting phase amplitudes from single-exponential fits to phase drifts (extracted from non-randomized, sliding window fits) induced by vertical beam motion. In red, scaling of the phase amplitude at calorimeter $k = 3$ with vertical beam width drifts only.

width changes (Fig. 4.12). This feature is evident when a reference drift, in this case at $k = 13$, is scaled according to the relation between vertical width shifts along the azimuth from $t = 30\,\mu$s to $t = 300\,\mu$s and the width changeat $k = 13$ (red line). The scaling factor is prepared either from beam tracking simulations or the squared-rooted ration between vertical beta functions.

In a similar way, induced phase shifts in the *X-Slow* case around the ring are modulated mostly by radial centroid shifts, scaled by the time-evolving radial dispersion function. In spite of radial width changes over time due to unstable radial beta and dispersion functions (see Subsec. 3.6.4), as shown in Fig. 4.13 drifts of the radial centroid is the main source of the phase drifts from this end.

The situation is different in the *X-CBO* case, where differences along the ring azimuth are induced by differences in calorimeter acceptances. By comparing Fig. 4.14 with the

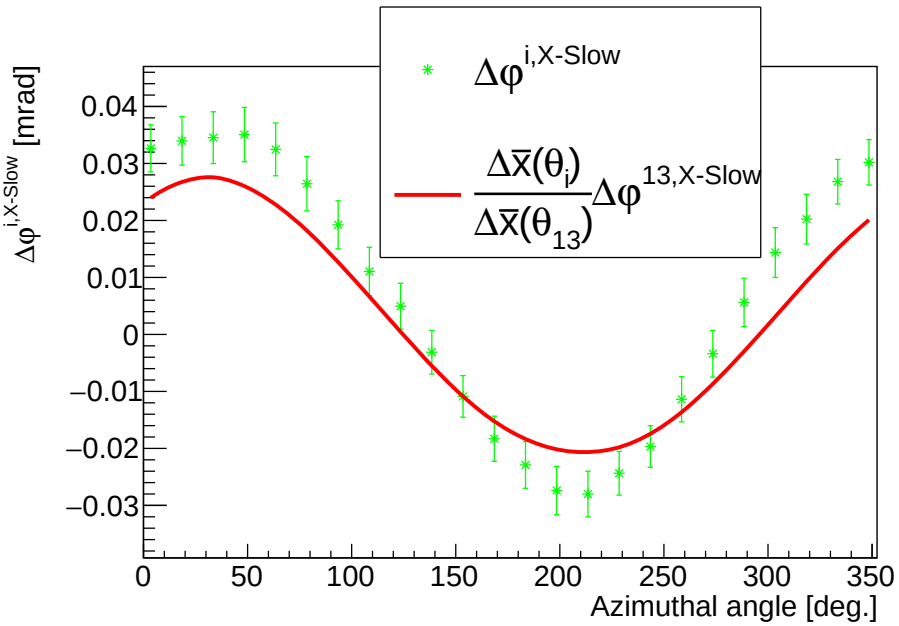

Figure 4.13: Drifting phase amplitudes from single-exponential fits to phase drifts (extracted from non-randomized, sliding window fits) induced by radial slow beam drifts. In red, scaling of the phase amplitude at calorimeter $k = 3$ with radial beam centroid drifts only.

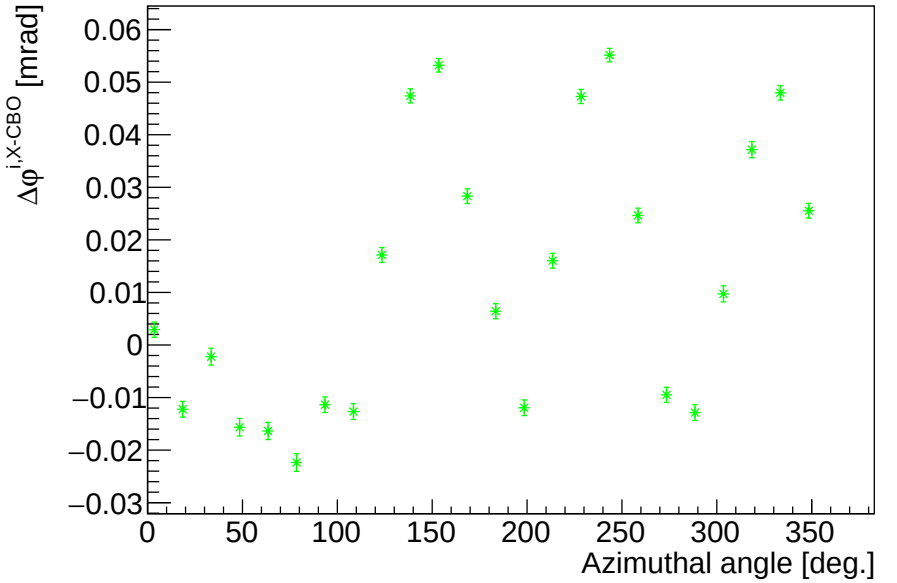

Figure 4.14: Drifting phase amplitudes from single-exponential fits to phase drifts (extracted from non-randomized, sliding window fits) induced by radial CBO decoherence. Variations are largely caused by calorimeter acceptances.

relative total intensity expected to be measured by calorimeters based on the *COSY*-based simulated beam and acceptance maps from *gm2ringsim* (see Fig. 4.15), it is concluded that beam drifts do not interfere considerably with the phase-acceptance correction from radial CBO decoherence. This statement is in agreement with the fact that the decoherence evolves equally along the storage ring.

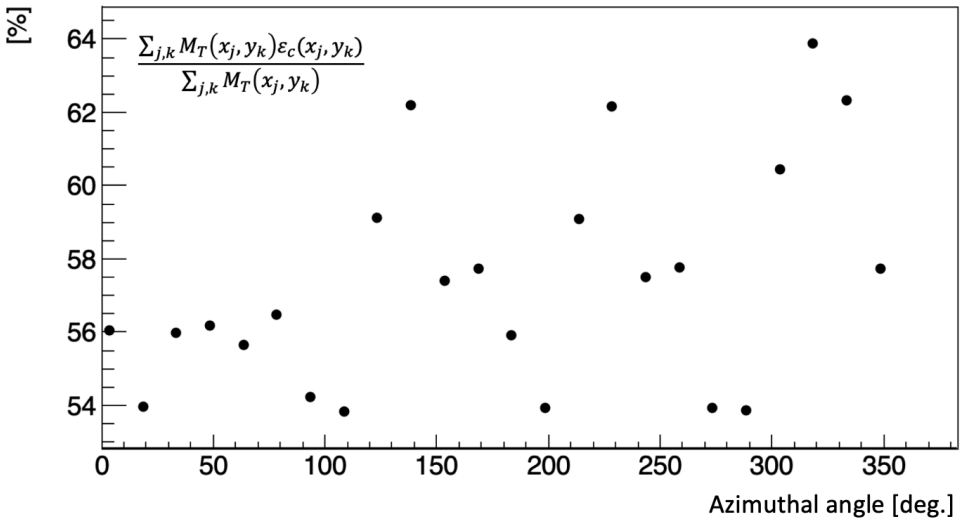

Figure 4.15: Relative total intensities detected by each calorimeter (T-Method) using the *COSY*-based Run-1a simulated beam and *gm2ringsim* acceptance maps.

Figure 4.16 shows the corresponding ω_a^m shifts from each of the phase drifting mechanisms separately and combined. The largest contributor to the phase-acceptance correction—and following the nature of detected-phase maps—is vertical width drifts over the data taking period. The independent contributions roughly combine to produce the total precession shift, and the optical lattice evolution together with the radial CBO decoherence dictate the detected phase behavior over the azimuth.

In reality, detected-phase distributions $\varphi_{0,k}\left(x_i, y_j\right)$ depend on the calorimeter location due to material effects. Figure 4.17 is an example of the ω_a^m shifts derived from tracker data, the *COSY*-based optical lattice functions, and *gm2ringsim* per-calorimeter

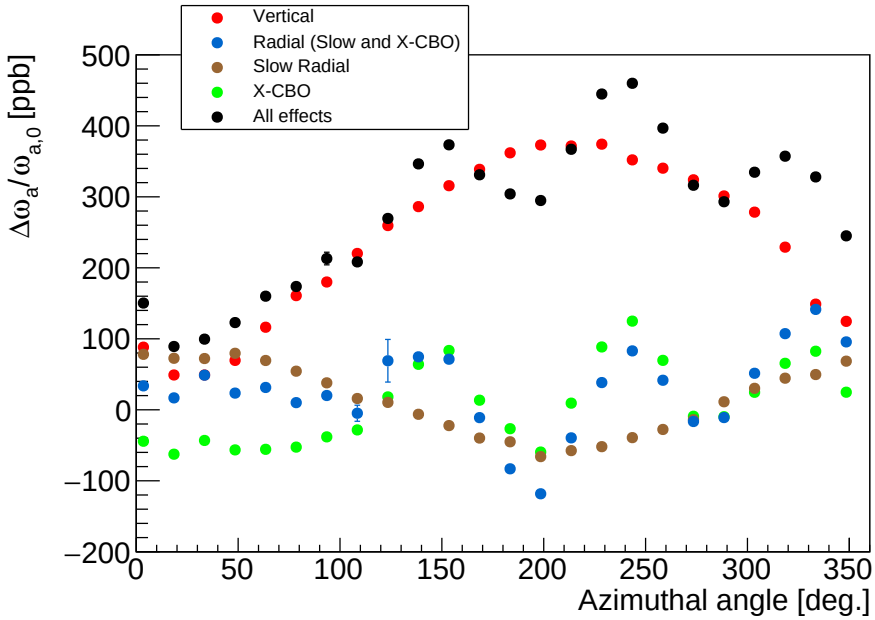

Figure 4.16: Relative ω_a^m shifts induced by each of the drifting phase mechanisms, separated and combined. The largest shifts are produced by beam drifts of the vertical width.

phase/asymmetry/calorimeter maps, where the variations of per-calorimeter maps break the symmetries displayed in Fig. 4.16.

The time-dependent optical lattice during Run-1 was the main driver of non-negligible phase acceptance corrections. Beam drifts during the measurement of ω_a^m were induced by the unstable lattice, and to a lower extent muon loss rates also play a role in the slowly changing vertical beam width. The faulty resistors that affected the ESQ over Run-1 datasets were repaired. Thus, phase acceptance corrections are expected to be significantly smaller during Runs 2 and beyond. The expertise developed during the analysis of the first $g-2$ is planned to be extended for posterior runs to precisely quantify C_{pa} from radial CBO decoherence and beam drifts induced by lost muons.

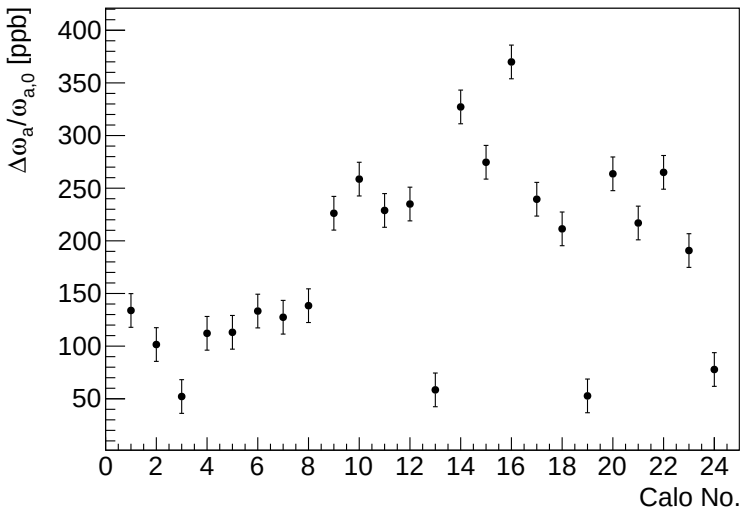

Figure 4.17: ω_a^m shifts induced by phase-acceptance drifts from experimental data (Run-1d) [16]. The Run-1d *COSY*-based optical lattice functions and per-calorimeter maps from *gm2ringsim* (T-Method) are utilized to calculate all the precession corrections from phase drifts extracted with the randomization method. Courtesy of Elia Bottalico.

4.4 The Electric-field and Pitch Corrections

E-field C_e and pitch C_p corrections are introduced in Subsec. 1.3.3:

$$C_e = \frac{n_0\beta_0^2}{1-n_0} 2\left\langle \delta^2 \right\rangle \qquad , \qquad C_p = \frac{n_0}{2\rho_0^2}\left\langle y^2 \right\rangle . \tag{4.21}$$

In principle, these corrections account for the stored muons overall additional rotations of the spin relative to the momentum vector beyond the scope of the (g-2) frequency. Independent hand calculations of C_e and C_p, starting with the work of Farley [49], converge to the expressions shown in Eq. (4.21) for similar conditions characteristic to the g-2 storage ring.

A computationally driven approach to test the standard expressions C_e and C_p is also pertinent and offers advantages when benchmarking them to the ppb-level [118]. In particular, second order effects from the nonlinear ESQ electric field as well as asymmetric momentum spread and discrete ESQ plates can conveniently be accounted for in relation to

the E-field and pitch corrections.

4.4.1 Methodology

With the COSY-based model, spin and orbital tracking of a realistic muon beam in the g-2 storage ring is performed. The method to extract frequencies relative to the nominal (g-2) frequency

$$\Delta\omega_a\left(t'_j\right) = \omega_a\left(t'_j\right) - \omega_{a0} \tag{4.22}$$

is to compute and track muon angles $\varphi_a(t)$ per turn j around the ring. φ_a's are defined as angles between spin and momentum vectors projected on the horizontal midplane.[2] The frequencies $\omega_a\left(t'_j\right)$ are defined turn-by-turn as

$$\omega_a\left(t'_j\right) = \frac{d\varphi_a}{dt} \approx \frac{\Delta\varphi_a}{\Delta t} = \frac{\varphi_a\left(t_{j+1}\right) - \varphi_a\left(t_j\right)}{t_{j+1} - t_j}. \tag{4.23}$$

Unless otherwise specified, a perfectly matched beam of $N_{muons} = 128 \times 10^6$ muons with typical Run-1 experimental distributions (see Fig. 4.18) are tracked $N_{turns} = 100$ turns with the COSY-based model for these studies. Even though the real g-2 beam is mismatched to the optical lattice of the ring, the characteristic oscillations owing to the mismatch introduce equally fast oscillations to the overall spin precession frequency of the beam that cancel out during the data taking period.

The time profile of the simulated beam is shown in Fig. 3.14. To recreate similar conditions of the momentum spread, results from FR analysis for the Run 1d dataset [51] are

[2] In reality, the measured precession frequency in the experiment results from the V-A theory parity violating observable, i.e., the phase between spin and momentum (without projections onto planes). However, the method followed in this work has been proven to recreate the nominal C_e and C_p corrections to ppb-level accuracy and previous analyses have implemented similar methods to high reliability [119].

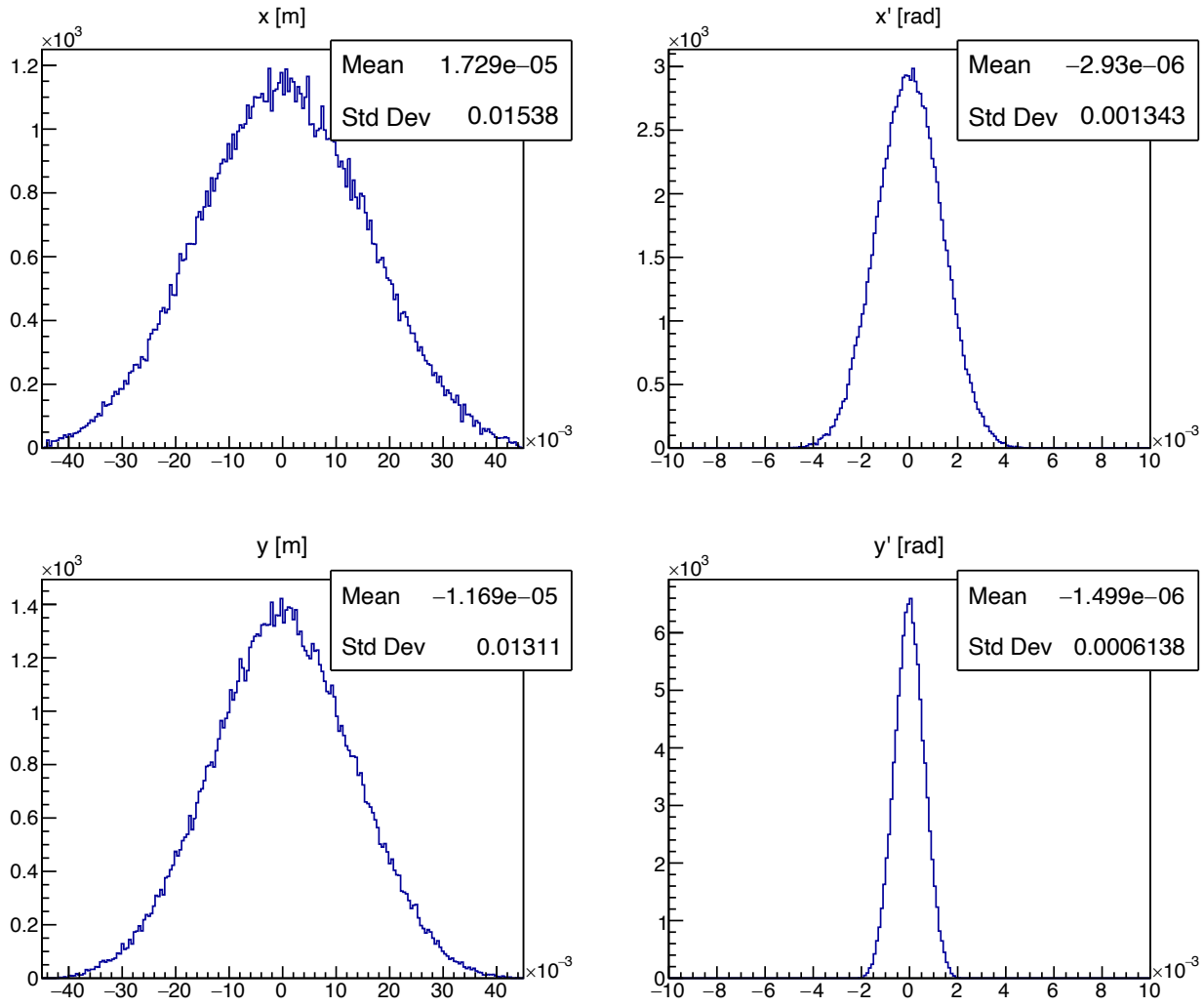

Figure 4.18: $x - x' - y - y'$ beam distributions (matched to the ring optical lattice) used in tracking simulations for $C_{e,p}$ analysis.

implemented in the preparation of the simulated beam (see Fig. 1.13). The spin distribution is taken from BDS numerical results (explained in Ch. 2) at the end of the M5-line (see Fig. 2.11).

The spin and momentum vectors of each muon in the simulation are recorded every turn and individual φ_a's computed. In this way, the overall spin precession frequency (relative to ω_{a0}) of the simulated beam is determined as

$$\left\langle \frac{\Delta\omega_a}{\omega_{a0}} \right\rangle_{\text{sim}} = \frac{1}{N_{\text{turns}}\, N_{\text{muons}}} \sum_{j=1}^{N_{turns}} \sum_{i=1}^{N_{muons}} \left(\frac{\Delta\omega_a\left(t'_j\right)}{\omega_{a0}} \right)_i , \tag{4.24}$$

whereas the associated statistical error of the calculation is defined from the standard error of the mean:

$$\delta\left(\Delta\omega_a/\omega_a\right)^{stat}_{\text{sim}} = \left(\frac{\Delta\omega_a}{\omega_{a0}} \right)_{SE} = \sigma\left(\frac{\Delta\omega_a}{\omega_{a0}} \right) \frac{1}{\sqrt{N_{\text{turns}} N_{\text{muons}}}}. \tag{4.25}$$

With the data analysis framework *ROOT* [120], the quantities above are processed as shown next.

To establish the resolution that can be achieved out of this method, first a muon beam without vertical motion is tracked around a ring with perfectly vertical magnetic field and the ESQ turned off (i.e., HV = 0). Under these conditions, $\Delta\omega_a = 0$ is expected for any muon. Results are shown in Fig. 4.19. The limit (10^{-3} ppb) is comparable to $C{+}{+}$ numbers precision utilized in ROOT. Similar results are obtained for $y = y' = \delta = 0$ and the ESQ turned on, although in this case $\sigma\left(\Delta\omega_a/\omega_{a0}\right) \sim 3$ ppb.

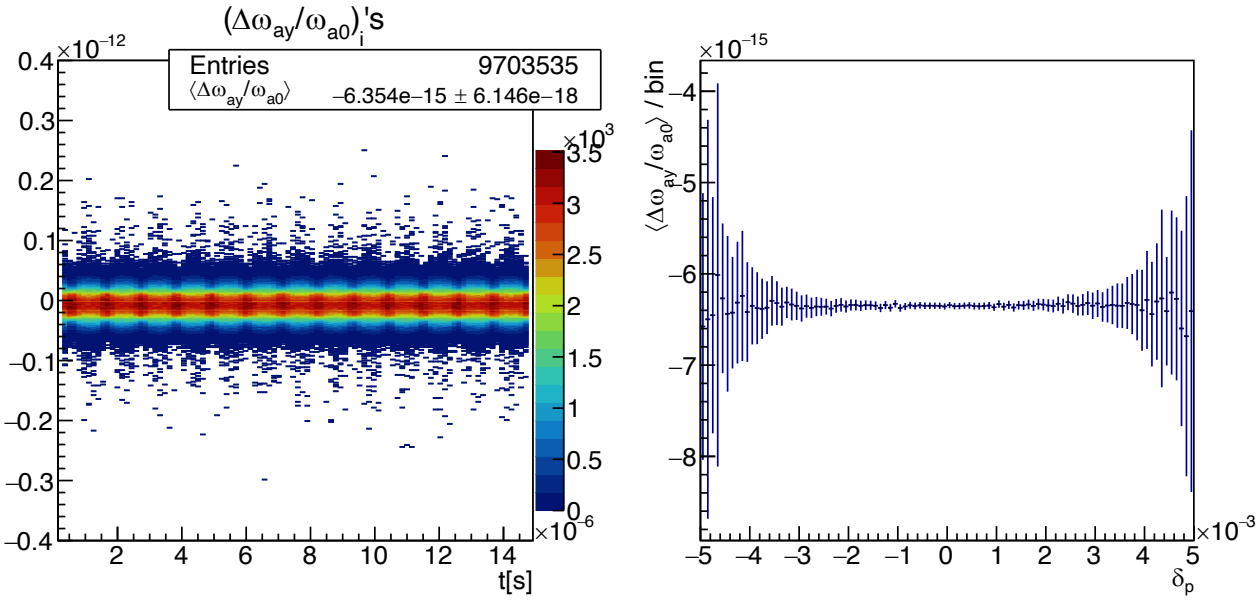

Figure 4.19: $\langle\Delta\omega_a\rangle$ spread versus time (left) and momentum offset (right). Muons are contained in the horizontal midplane and the ESQ is turned off.

4.4.2 Electric field correction C_e

With the resolution of the framework established, more realistic features can be added to simulations with the COSY-based model. To test C_e under the approximations necessary to derive it, a beam without vertical betatron motion, perfectly Gaussian momentum spread is tracked around a ring with perfect vertical magnetic field and ESQ with continuous plates and only quadrupole electric field component (i.e., $a_{k,0} = 0$ for $k > 2$). Figure 4.20 shows results for this scenario. Under these approximations,

$$-|C_e| - \left\langle \frac{\Delta\omega_a}{\omega_{a0}} \right\rangle_{sim} = 0.8 \pm 0.1\,\text{ppb}. \tag{4.26}$$

The small difference is likely caused by the curvature of the plates, since the simulation accounts up to 10th-order terms in the transfer maps. When the momentum spread distri-

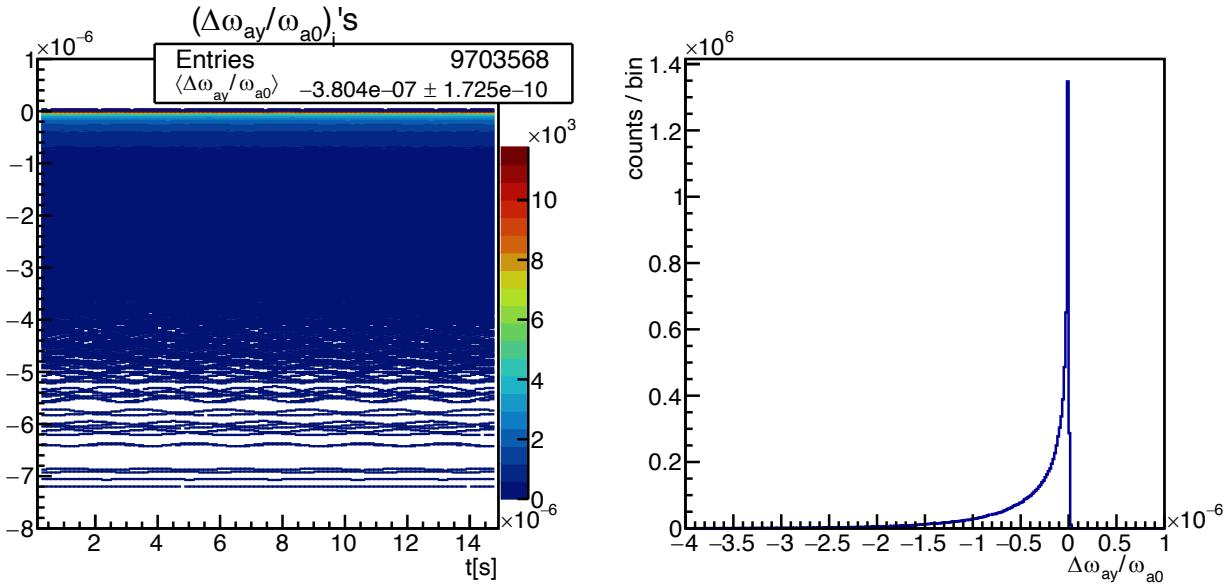

Figure 4.20: $\langle\Delta\omega_a\rangle$ spread distribution (right) and versus time (left). Muons are contained within the horizontal midplane to exclude C_p. The frequencies spread due to the C_e correction is $\sim 537\,\text{ppb}$ as shown in the plot on the right.

bution from FR analysis is used instead:

$$-|C_e| - \left\langle \frac{\Delta\omega_a}{\omega_{a0}} \right\rangle_{sim} = 5.2 \pm 0.1\,\text{ppb}. \tag{4.27}$$

Thus, the isolated effect of an asymmetric Run-1 style δ distribution adds a correction of $\sim 4.4\,\text{ppb}$ to C_e, which introduces higher-order distribution moments (e.g., $\langle\delta^3\rangle$) to the momentum spread such that

$$\begin{aligned}\left\langle \frac{\Delta\omega_a}{\omega_{a0}} \right\rangle &= \left\langle -\frac{e}{m}\left[\left(1-\left(1-\frac{1}{(1+\delta)^2}\right)\right)\frac{\beta_z E_x}{c}\right]\right\rangle \\ &= -|C_e| + \frac{n_0\beta_0^2}{1-n_0}\left(1+2\beta_0^2\right)\left\langle\delta^3\right\rangle + \cdots \\ &\neq -|C_e|\,.\end{aligned} \tag{4.28}$$

In a similar manner, further features of the storage ring—not accounted for in the sensible approximations from which C_e and C_p are derived—are added in the tracking, namely, ESQ

plates discretization, ESQ higher-order multipole terms for all $a_{k,0}$ coefficients, and ESQ fringe fields (see Sec. 3.2.1). Table 4.3 lists all the cases of study, in addition to the beam and ring features implemented until now (i.e., "DIEQ Ring"), and Table 4.4 shows comparisons between C_e and tracking for each of those cases.

Table 4.3: Cases of study for $\langle \Delta\omega_a \rangle$ tracking.

Case label	ESQ Plates discretization	ESQ higher-order multipoles	ESQ Fringe fields
DIEQ Ring			
DIEQ	X		
DIEM	X	X	
DIEM-FR	X	X	X

Table 4.4: C_e versus tracking (no vertical betatron motion).

Case	$-\lvert C_e \rvert - \left\langle \frac{\Delta\omega_a}{\omega_{a0}} \right\rangle_{sim}$ [ppb]
DIEQ Ring	4.4 ± 0.1
DIEQ	-5.5 ± 0.1
DIEM	-9.8 ± 0.1
DIEM-FR	-7.7 ± 0.1

While tracking results indicate an overall ω_a frequency slightly higher than C_e due to an asymmetric momentum spread, the other effect push the discrepancy down up to 7.7 ppb. The disagreements are induced by muons with momentum offsets near the momentum acceptance of the ring, as indicated by δ-binned differentiated results.

4.4.3 Pitch correction C_p

Up to this point, no vertical motion of the beam has been considered in order to analyze C_e only, without the intrusion of C_p. Next, the attention is directed to C_p instead. For this

purpose, a monochromatic beam composed of muons at magic momentum only (i.e., $\delta = 0$) is tracked down. To get closer to the initial ideas that permitted the derivation C_p, muons have initially no radial betatron motion even though a small vertical motion unavoidable emerges from the curvature of the ESQ plates ($E_x(x = 0, y \neq 0) \neq 0$). Nevertheless, since radial and vertical motions are mostly decoupled, the small radial motions do not incorporate errors to the C_p versus tracking comparisons discussed next.

In this scenario—and keeping perfect vertical magnetic field and continuous ESQ plates with a field structure originated only by the $a_{2,0}$ quadrupole coefficient (see Sec. 3.2.1)—results as shown in Fig. 4.21 are obtained. In contrast to the C_e-only studies above where

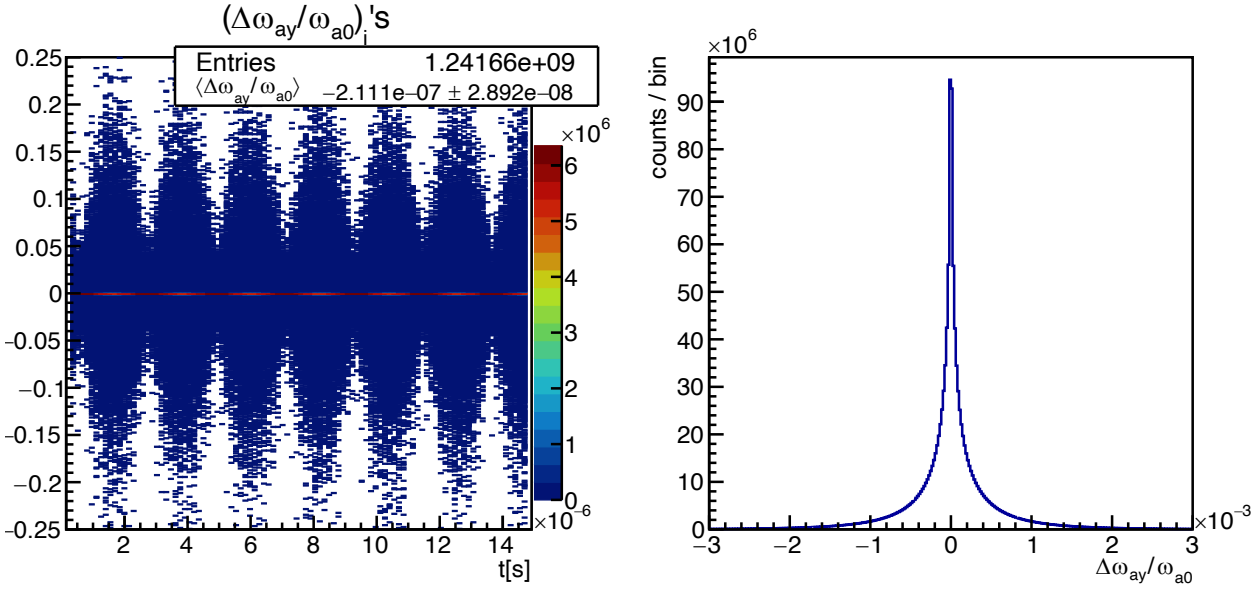

Figure 4.21: $\langle \Delta\omega_a \rangle$ spread distribution (right) and versus time (left). Muons are launched with no radial motion nor momentum offsets, to exclude C_e. The frequencies spread due to the C_p correction is 0.1 % as shown in the plot on the right.

individual $\Delta\omega_a$'s are spread out within a standard deviation of ~ 537 ppb, the C_p-only case exhibits typical spreads of about 0.1 %. As such, the associated statistical error is larger

with $N_{muons} = 128 \times 10^6$ and $N_{turns} = 100$; namely, 8.5 ppb. The comparison yields

$$-\left|C_p\right| - \left\langle \frac{\Delta\omega_a}{\omega_{a0}} \right\rangle_{sim} = -9.1 \pm 8.5\,\text{ppb}. \tag{4.29}$$

One of the main assumptions of C_p is harmonic vertical motion ($y(t) = y_0 \cos\left(\omega_y t + \phi_y\right)$). However, to satisfy Laplace's equation in curvilinear coordinates the vertical electric field that drives the oscillatory vertical motion is not purely linear. Instead, nonlinear components influence the motion as well:

$$E_y(x = 0, y) = -\sum_{l=1}^{\infty} a_{0,l} \frac{y^{l-1}}{(l-1)!}. \tag{4.30}$$

Table 3.1 shows nonzero $a_{0,l}$'s for $l = 0, 2, 4, \ldots$ due to the ESQ stations geometry. Since the tracking simulations encompass such components of the ESQ fields, C_p is not in full agreement with the tracking results (Eq. (4.29)) for which the vertical motion is not fully harmonic.

4.4.4 Electric-field and pitch corrections $C_e + C_p$

In reality, the measured precession frequency of the g-2 stored beam experiences biasing due to both effects that the C_e and C_p attempt to correct. Hitherto, the comparisons between tracking simulation results and these corrections treated independently have yield reassurance on their usage to ~ 10 ppb accuracy. The next step is to track the full beam with betatron amplitudes in both transverse directions and realistic momentum spread, as specified at the beginning of this section. The $\Delta\omega_a$'s spread is dominated by the pitch effect as shown in Fig. 4.22. Table 4.5 lists comparison results for the implemented cases.

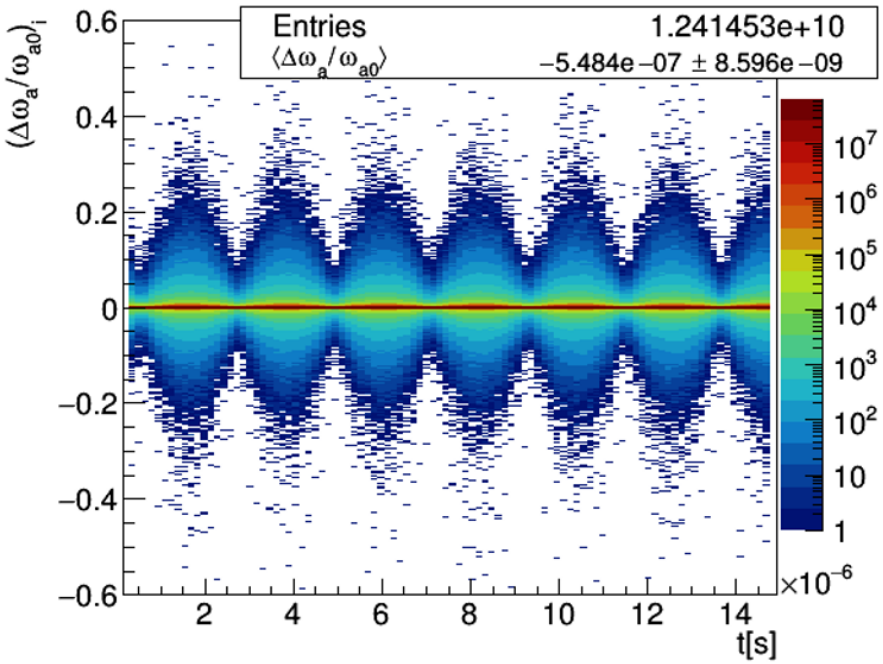

Figure 4.22: $\langle \Delta\omega_a \rangle$ spread distribution versus time of a simulated g-2 beam with Run-1 characteristics (note the logarithmic color scale). The pitch effect dominates the spread.

Table 4.5: $C_e + C_p$ versus tracking (full betatron motion).

Case	$-\left\|C_e + C_p\right\| - \left\langle \frac{\Delta\omega_a}{\omega_{a0}} \right\rangle_{sim}$ [ppb]
DIEQ Ring	-6.4 ± 8.5
DIEQ	-8.7 ± 8.5
DIEM-FR	-10.0 ± 8.5

Due to the circular storage volume, muons with smaller vertical betatron amplitudes y_{max} are allowed to have momentum offsets within the entire momentum acceptance of the ring. On the other hand, the largest y_{max} amplitudes are allowed only for $\delta \to 0$, in which case the E-field correction is minimal. This interrelation is revealed in Fig. 4.23 (left plot); muons near the midplane are more in need of an E-field correction. The beam is normally distributed

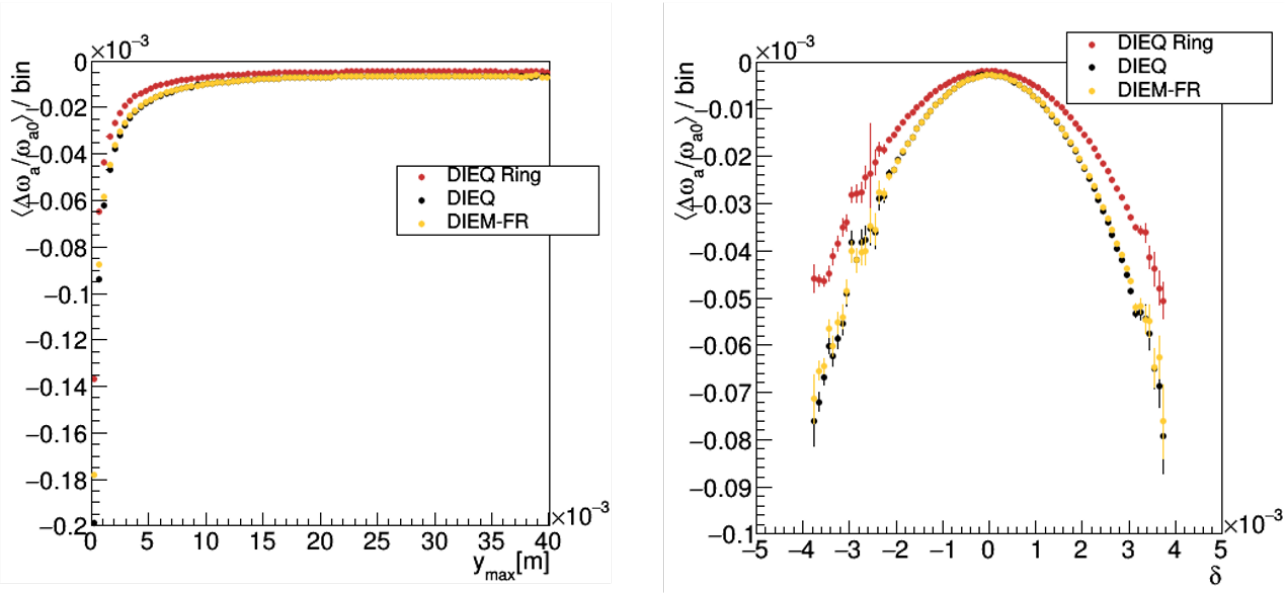

Figure 4.23: $\langle \Delta\omega_a \rangle$ spread binned over vertical betatron amplitudes (left) and momentum offsets (right) for the case of full betatron motion.

in phase space; therefore, the population of muons with small y_{max} amplitudes tends to be small and results in Fig. 4.23 are weighted accordingly to compute the total precession frequency of the beam.

4.4.5 Run-1 considerations

During Run-1, both the field index (Fig. 4.24) and radial dispersion function (Fig. 3.71) drifted during the data taking period. As a consequence, the ESQ electric field and ensemble of momentum-dependent radial closed orbits $x_e = x_0 + D_x\delta$ were slowly varying over time

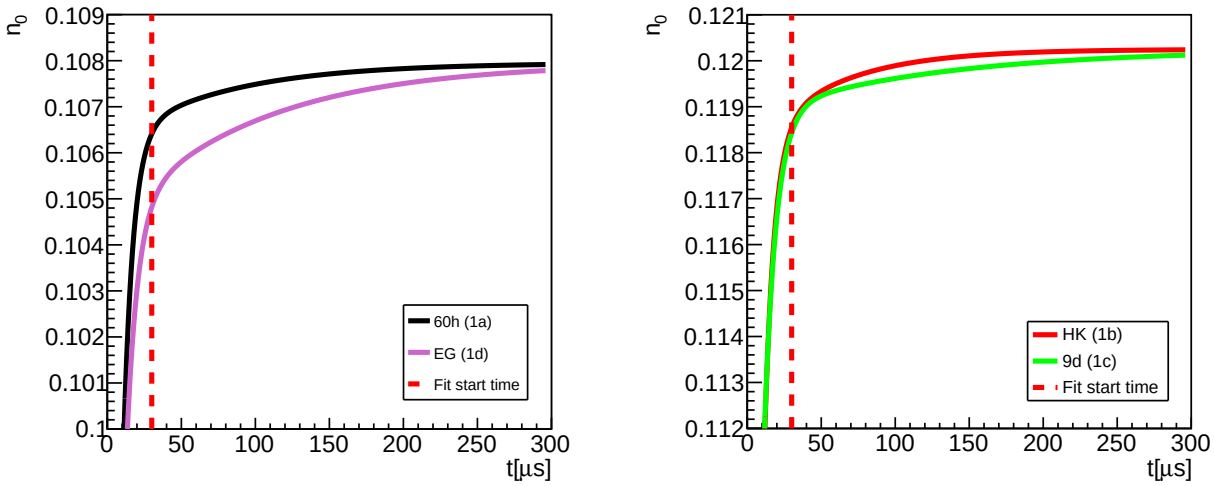

Figure 4.24: Effective field indices over time during Run-1 from straw trackers data ($n_0 = 1 - \left[1 - \omega_{CBO,x}/2\pi f_c\right]^2$).

as well. Moreover, tracking simulations with the COSY-based model indicate a slightly changing momentum spread distribution due to lost muons ($\Delta\bar{\delta}(30\,\mu\text{s} \to 300\,\mu\text{s})/\bar{\delta}(30\,\mu\text{s}) \approx 0.25\%$ and $\Delta\delta_{RMS}(30\,\mu\text{s} \to 300\,\mu\text{s})/\delta_{RMS}(30\,\mu\text{s}) \approx 0.4\%$). The E-field standard correction encompasses such effects as follows [121]:

$$C_e(t) = 2\frac{n_0(t)\beta_0^2}{\rho_0}\left\langle x_e(t)\delta(t)\right\rangle_{N,\varphi} \Rightarrow C_e(t) = 2\frac{n_0(t)\beta_0^2}{\rho_0}\left[\left\langle D_x(t)\right\rangle_\varphi \left\langle \delta(t)^2\right\rangle_N + \left\langle x_0(t)\right\rangle_\varphi \left\langle \delta(t)\right\rangle_N\right], \tag{4.31}$$

where $\langle\rangle_N$ denotes average over the muon bunch and $\langle\rangle_\varphi$ are azimuthal averages along the ring with ESQ occupancy. The momentum-independent closed orbit x_0 was not significantly affected by the changing electric fields, thus its contribution to a changing C_e is negligible. Figure 4.25 shows how the temporary C_e changes due to the dynamic effects of Run-1, relative to the regular calculation of the correction C_{e0} ($\Delta C_e = C_{e0} - C_e(t)$). To estimate the entire effect over each Run-1 dataset due to the time-evolving ω_a from changing electric fields and momentum distribution, results shown in Fig. 4.25 are incorporated into Monte

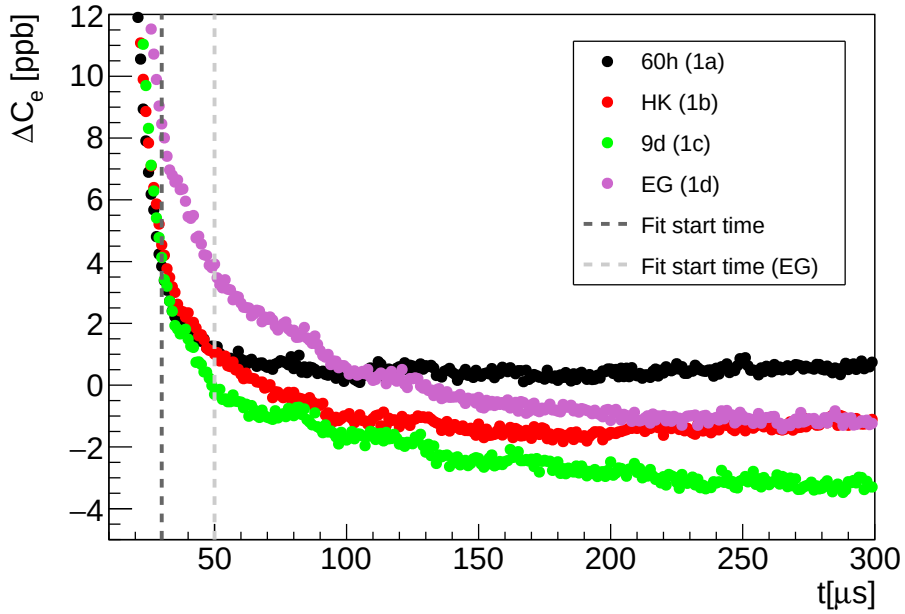

Figure 4.25: Temporal $C_e(t)$ corrections (relative to the time-independent case) during Run-1 under the effects of changing momentum spread and time-dependent ESQ electric fields.

Carlo simulations similar to the method followed in Sec. 4.2 to extract C_{ml} but, instead of a manipulation of φ_0, the spin precession frequency ω_a is directly defined as $\omega_a(t) = \omega_{a0}(1 - C_e(t))$. Table 4.6 lists deviations from time-independent C_e corrections, being all small compared to the main systematic corrections of C_e during Run-1 [46]. The effect of changing vertical beam widths on C_p has also been studied with β_y from the COSY-based model functions [99] and found to be small (~ 1 ppb).

Table 4.6: Deviations to time-independent C_e corrections during Run-1, based on tracking simulations and optical lattice calculations with the COSY-based model of the g-2 storage ring.

	ΔC_e [ppb]
Run 1a (60h)	-0.24 ± 0.013
Run 1b (HK)	-2.76 ± 0.011
Run 1c (9d)	-3.68 ± 0.014
Run 1d (EG)	-2.50 ± 0.012

In conclusion, this analysis has tested the robustness of C_e and C_p and indicates that the asymmetric momentum spread, discrete ESQ plates, nonlinear ESQ fields and its fringe fields introduce a systematic correction of -10.0 ± 8.5 ppb to the standard $C_e + C_p$ formalism used in the experiment.

4.5 The Weighted Magnetic Field $\langle B \rangle$

The driver of the muon beam rotational polarization around its momentum direction is the magnetic field of the g-2 storage ring. Subject to the muon beam spatial distribution during the data taking period, the precession frequency ω_a emerges from the total field $\langle B \rangle$ experienced by the beam. In spite of the high uniformity of the magnetic field in the ring's storage volume (i.e., $|\vec{B}| = B \approx B_y$ to $\mathcal{O}(10\,\text{ppb})$ accuracy [43]), its ppm-level localized variations along the ring azimuth can couple to the azimuthal behavior of the stored beam. At the previous muon g-2 experiment at BNL, the error budget of their a_μ measurement allowed to safely calculate the convoluted field $\langle B \rangle$ without the consideration of the beam azimuthal variations [33]. However, a consideration of such beam variations are required for the muon weighting of the magnetic field to be determined to a precision of 10 ppb or less [47] and in this way achieve the precision goals of the muon g-2 experiment at Fermilab.

For this purpose, a method to perform the muon weighting necessary to obtain $\langle B \rangle$ while accounting for beam azimuthal variations based on straw tracking detectors data [42] and optical lattice functions (see Subsec. 3.6.2) has been developed [101] and is presented in this section. The method, which allows to compute muon-weighted magnetic fields on a run-by-run basis, has been implemented as part of the Run-1 magnetic field analysis. Systematic errors associated to the method (e.g., detection acceptance and alignment) are not studied

in this dissertation, and have been analyzed with detail and documented in Ref. 101.

To benchmark the aforementioned method, a convoluted field $\langle B \rangle_{orig}$ is prepared (see Subsec. 4.5.1) via nonlinear simulations with the magnetic field in the COSY-based model from trolley data, where the beam distribution is tracked at several azimuthal locations of the ring. With these results as reference, the method to reconstruct $\langle B \rangle_{orig}$ out of information of the beam transverse intensity at one azimuthal location (named $\langle B \rangle_{recon}$) presented in Subsec 4.5.2 is validated as shown in Subsec. 4.5.3. Lastly, sensitivity studies to understand the dependence of the muon-weighted field calculation on specific azimuthal variations of the stored beam are discussed.

4.5.1 Convoluted field $\langle B \rangle$ from the simulated beam

Ideally, to capture the coupling between field and beam distortions along the storage ring azimuth in the muon weighting of the magnetic field $B(x, y, \theta)$, the time- and azimuth-dependent muon transverse intensity $M_T(x, y, \theta, t)$ is convoluted with the field throughout the data taking period [43]:

$$\langle B \rangle = \int_{t_0}^{t_f} \int_x \int_y M_T(x, y, \theta, t) B(x, y, \theta) dx dy d\theta dt', \tag{4.32}$$

where θ is the azimuthal angle, x and y the radial and vertical coordinates, t is the time where $t = 0$ coincides with beam injection into the ring, and the beam intensity is normalized:

$$\int_x \int_y M_T(x, y, \theta, t) dx dy = 1. \tag{4.33}$$

However, the azimuthal gradients of the optical lattice functions (including closed orbits) in the weakly focusing ring and the resolution of tracker experimental data are small enough to conveniently consider a discrete summation instead:

$$\langle B \rangle = \frac{1}{N} \sum_{i=1}^{N} \langle B \rangle_i = \frac{1}{N} \sum_{i=1}^{N} \sum_{j}^{N_x} \sum_{k}^{N_y} M_T \left(x_j, y_k, \theta_i \right) B_i \left(x_j, y_k \right), \tag{4.34}$$

where

$$\sum_{j}^{N_x} \sum_{k}^{N_y} M_T \left(x_j, y_k, \theta_i \right) = 1 \tag{4.35}$$

and

- N: Number of azimuthal slices.
- N_x: Number of x bins.
- N_y: Number of y bins.
- $M_T \left(x_j, y_k, \theta_i \right)$: Binned transverse beam profile at θ_i integrated over $30\,\mu\text{s} < t < t_f$.[3]
- $B_i \left(x_j, y_k \right)$: Binned magnetic field map at i-th azimuthal slice, averaged within $\left[\theta_i - \frac{\pi}{N}, \theta_i + \frac{\pi}{N} \right]$.

Although $N = 72$ in practice [101], for the following analysis the number of azimuthal slices is equal to 24, which has been found to be sufficient for incorporating azimuthal dependencies in $\langle B \rangle$.

In order to obtain the $\langle B \rangle_{orig}$ introduced above for the validation of the reconstruction method (see Subsec. 4.5.2 and 4.5.3), Run-1d tracking simulation results for the Run-1a dataset are used. Figure 4.26 shows all the $M_T \left(x_j, y_k, \theta_i \right)$ beam profiles at the 24 locations of

[3] For the purposes of this section, $t_f = 300\,\mu\text{s}$. In the experiment, $t_f \approx 700\,\mu\text{s}$.

interest, centered at the regions of maximum azimuthal sensitivity per calorimeter detector.

Each of the transverse profiles in Fig. 4.26 are convoluted with their corresponding magnetic field slice $B_i\left(x_j, y_k\right)$—shown in Figs. 4.27 and their azimuthal variations in Fig. 3.8—to calculate $\langle B\rangle_{orig}$ as follows from Eq. (4.5.1).

Figure 4.28 shows $\langle B\rangle_i$ at their corresponding θ_i azimuthal locations. The convolution is dominated by the dipole field contribution (compare Fig. 4.28 with c_0 in Fig. 4.30). To identify the main contributions in terms of multipole coefficients, the azimuthally binned muon-weighted field maps are expressed as follows (similar to Eq. (3.8)):

$$\langle B\rangle_i \approx B_0 \left(1 + c_{0,i} + \sum_{n=1}^{4} \left[c_{n,i} I_{n,i} + s_{n,i} J_{n,i}\right]\right), \tag{4.36}$$

where $B_0 = p_0/e\rho_0$ is the ideal field to sustain magic muons at $p_0 \approx 3.094\,\mathrm{GeV/c}$.

$$\begin{aligned} I_{n,i} &= \sum_{j,k} M_T\left(x_j, y_k, \theta_i\right) \left(\frac{r\left(x_j, y_k\right)}{r_0}\right)^n \cos\left[n\phi\left(x_j, y_k\right)\right] \\ J_{n,i} &= \sum_{j,k} M_T\left(x_j, y_k, \theta_i\right) \left(\frac{r\left(x_j, y_k\right)}{r_0}\right)^n \sin\left[n\phi\left(x_j, y_k\right)\right] \end{aligned} \tag{4.37}$$

are the normal, $I_{n,i}$, and skew, $J_{n,i}$, multipole beam projections (see Fig. 4.29). In Eq. (4.37), $r_0 = 4.5\,\mathrm{cm}$ is the normalization radius, $r = \sqrt{x^2 + y^2}$ the transverse radius relative to the reference orbit, and ϕ the polar angle such that $x = r\cos\phi$ and $y = r\sin\phi$. The normal, $c_{n,i}$, and skew, $s_{n,i}$, magnetic multipole terms in Eq. (4.36) at each of the $B_i(x_j, y_j)$ maps are shown in Fig. 4.30.

The contribution of each $n \geq 1$ magnetic multipole to the muon-weighted field is strongly

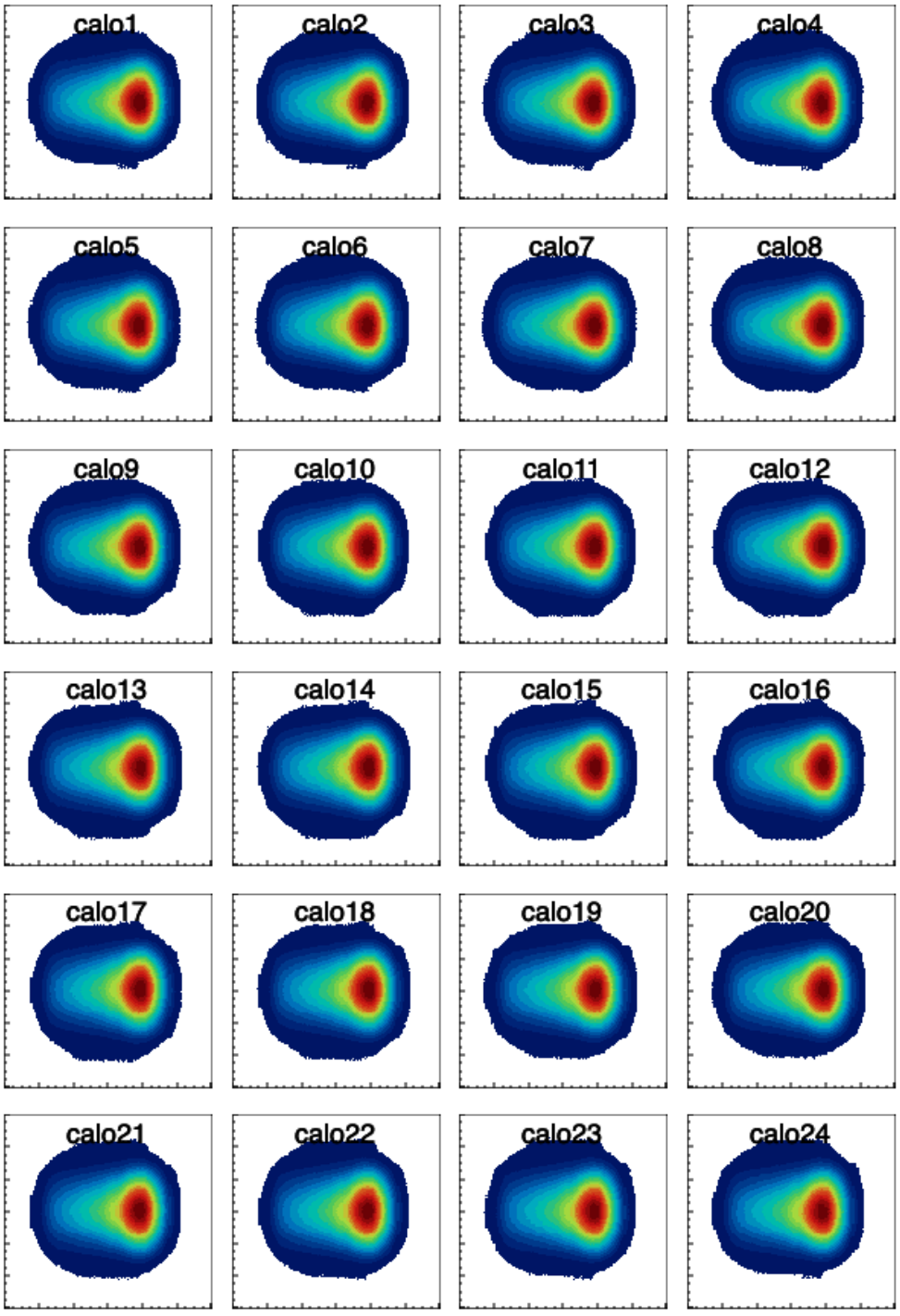

Figure 4.26: Run-1a simulated beam transverse profiles $M_T^{orig}(x_j, y_k, \theta_i)$, integrated over $30\,\mu s < t < 300\,\mu s$. The 24 azimuthal locations coincide with the regions of maximum calorimeter detection acceptance. Horizontal and vertical axes correspond to $-60\,mm < x < 60\,mm$ and $-60\,mm < y < 60\,mm$. Refer to Fig. 4.36 for the color legend.

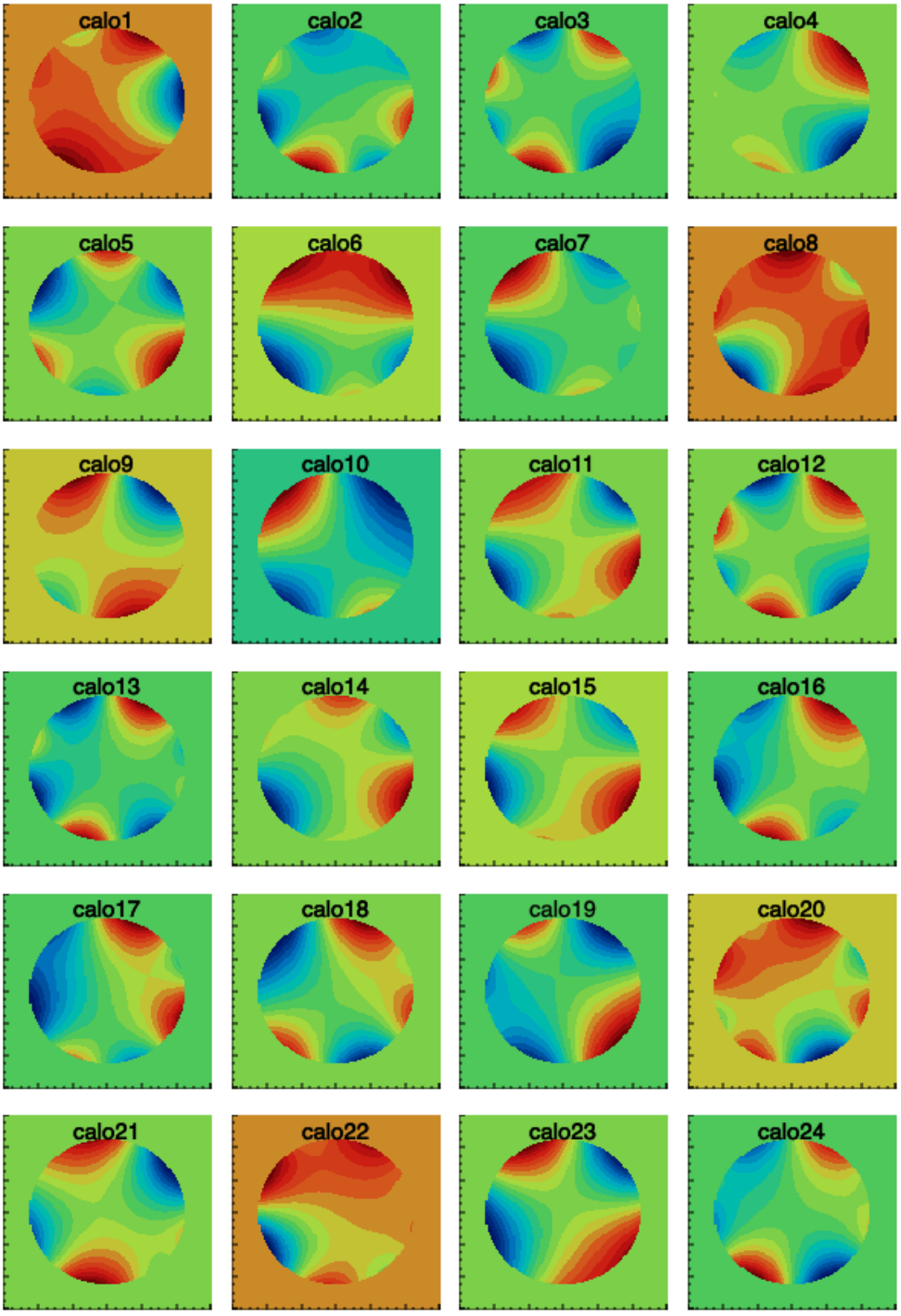

Figure 4.27: Magnetic field maps $B_i\left(x_j, y_k\right)$ from trolley run number 3956 (close to Run-1a data period). The azimuthal locations of each map correspond to the beam profile azimuths arrangement in Fig. 4.26. Field intensities are shown for $\sqrt{x^2+y^2} < 45\,\text{mm}$, where the horizontal and vertical axes are x and y, respectively. Each color represents a particular magnetic field magnitude to illustrate polar uniformities.

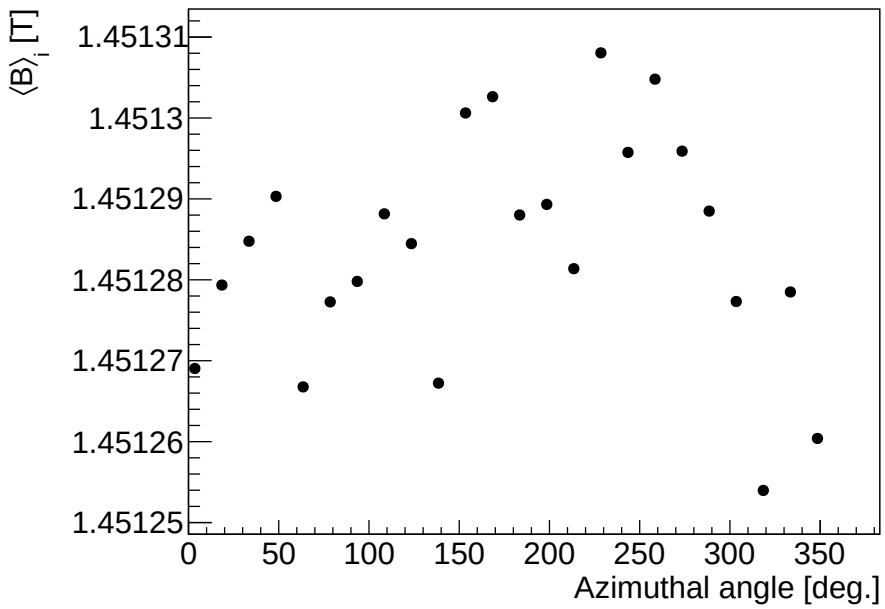

Figure 4.28: $\langle B \rangle_i$ magnetic fields (trolley run 3956) convoluted with the Run-1a simulated beam at 24 azimuthal locations.

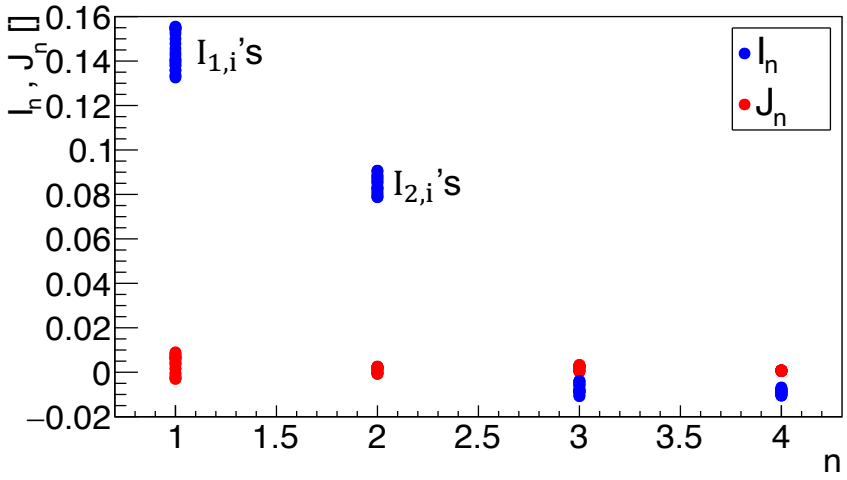

Figure 4.29: Multipole beam projections $\{I_{n,i}, J_{n,i}\}$ versus order n from the Run-1a simulated beam (Similar projections are observed in the other $Run{-}1$ datasets). Projections of the same order and different azimuthal locations group together in the plot.

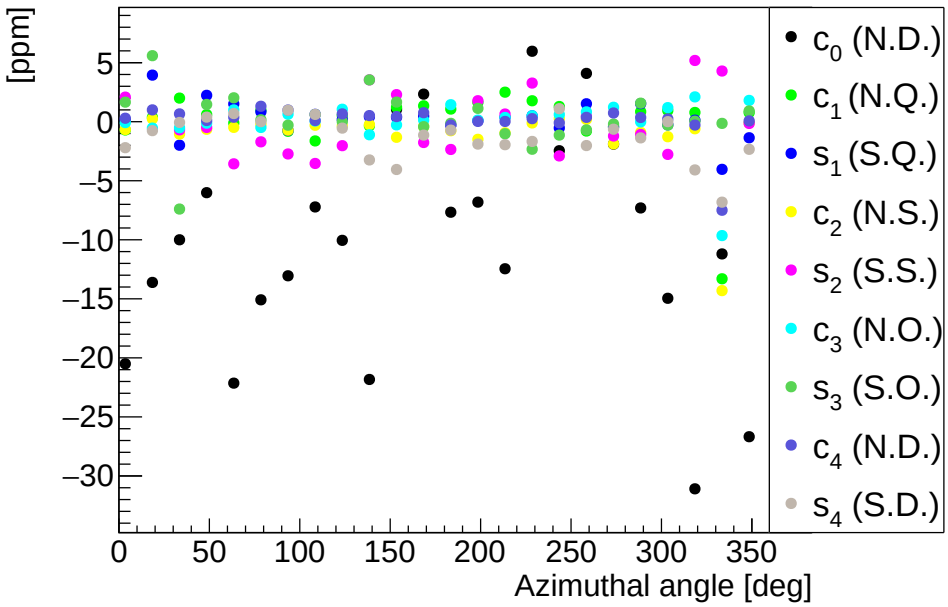

Figure 4.30: Magnetic field multipoles averaged out every 15° (trolley run 3956). Refer to Eq. (4.36).

dictated by the $\{I_{n,i}, J_{n,i}\}$ multipole beam projections:

$$\langle B \rangle = \frac{1}{N}\sum_{i=1}^{N}\langle B \rangle_i = B_0\left(1 + \langle c_0 \rangle\right) + B_0 \sum_{n=1}^{4}\left(\langle c_n I_n \rangle + \langle s_n J_n \rangle\right). \tag{4.38}$$

In Fig. 4.31, the convoluted beam projection contributions $\{\langle c_n I_n \rangle, \langle s_n J_n \rangle\}$ are shown. Due to the overall radial off-centering of the beam caused by the nonzero average of its momentum spread, the normal quadrupole beam projection plays an important role in the muon-weighting of the field. Similarly, the beam widths couple with the magnetic normal sextupole term via its normal sextupole projection. The vertical closed orbit is expected to be within 1 mm from the horizontal midplane during the data taking period due to inhomogeneities in the skew dipole term of the magnetic field; therefore, skew quadrupole beam projections weakly interfere with the convolution. Uncertainties from tracker and ESQ misalignments are the main sources of systematic error in the muon weighting during Run-1

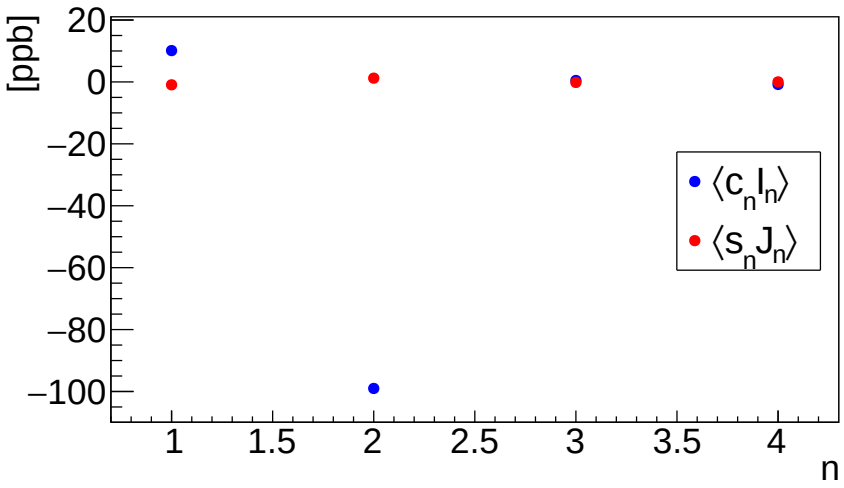

Figure 4.31: Convoluted beam projection contributions $\{\langle c_n I_n\rangle, \langle s_n J_n\rangle\}$ versus order n from the Run-1a simulated beam and magnetic field based on trolley run 3956.

($\sim 13\,\text{ppb}$ and $\sim 5\,\text{ppb}$, respectively) [43, 101]. Lastly, even though the radial and vertical motion are highly decoupled, small correlations driven by the skew quadrupole component of the fields introduce a small contribution to $\langle B\rangle$. Higher-order beam projections of the typical g-2 stored beam are not relevant for the convolution (see Fig. 4.31). The aforementioned features are observed in Fig. 4.32.

With the relevant beam projections identified (i.e., centroids and widths) for the muon-weighted magnetic field in the storage ring, a method to calculate $\langle B\rangle$ based on tracker data at one azimuthal location and lattice functions is developed and presented next.

4.5.2 Method to define $\langle B\rangle$ from experimental data

In the experiment, transverse beam profiles $M_T\,(x, y, \theta_{Tr})$ are available at the two azimuthal regions where straw tracking detectors are located (see Fig. 1.11). FR analysis reconstructs momentum spread distributions [51] and lattice functions are calculated from the COSY-based model (see Subsec. 3.3.2) based on magnetic field measurements [43]. With these

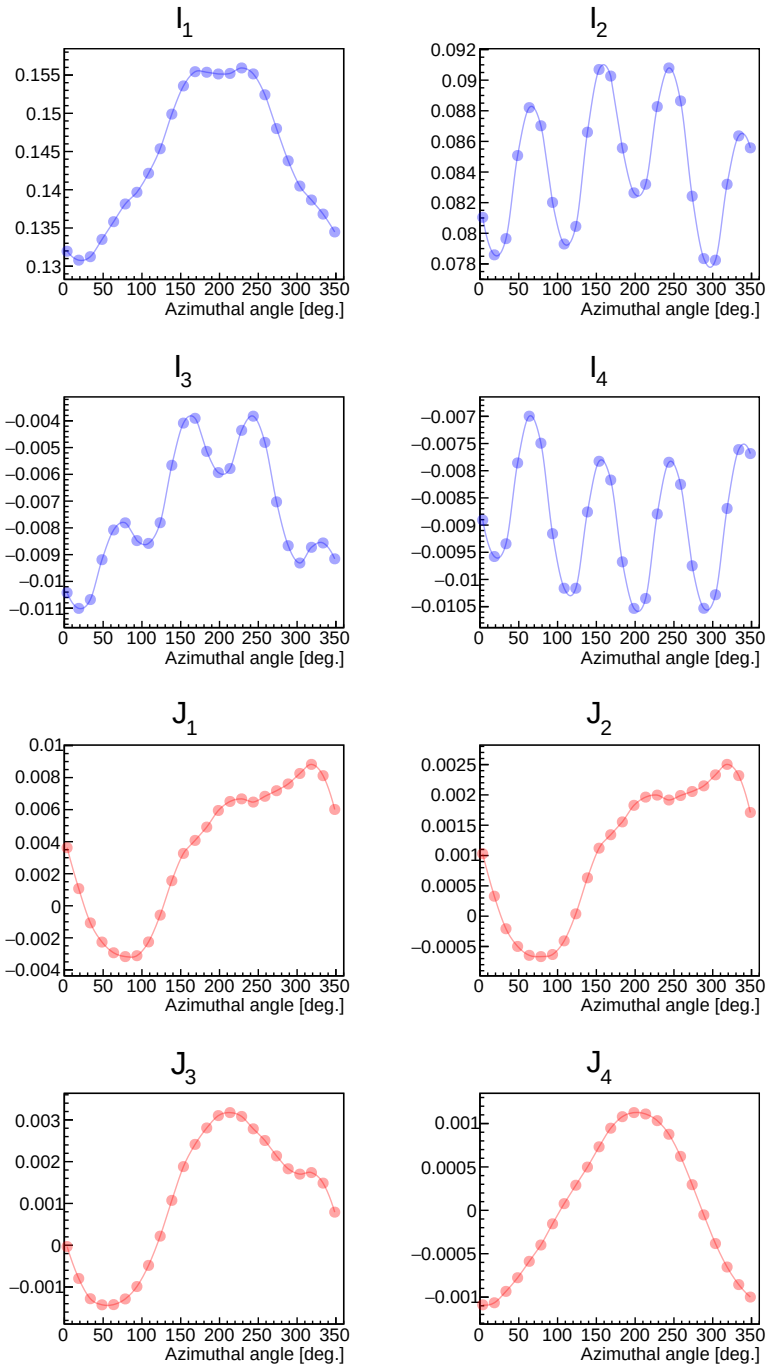

Figure 4.32: Multipole beam projections $\{I_{n,i}, J_{n,i}\}$ versus azimuthal angle from the Run-1a simulated beam.

available ingredients, beam profiles $M_T(x, y, \theta_i)$ can be reconstructed by "shifting" and "scaling" $M_T(x, y, \theta_{Tr})$ at any azimuthal location θ_i [122] as illustrated in Fig. 4.33.

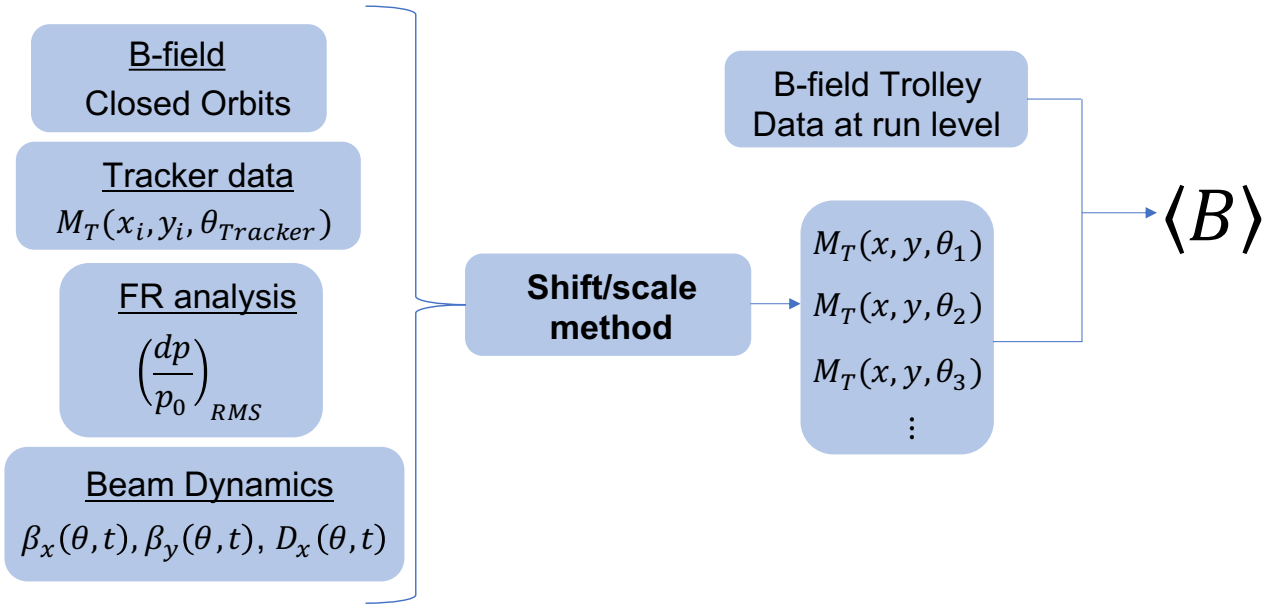

Figure 4.33: Flow chart of the method to reconstruct $\langle B \rangle$ from experimental data and the optical lattice. With this input, beam transverse profiles $M_T(x, y, \theta_i)$ are prepared at a run level in the experiment.

First, $M_T(x, y, \theta_{Tr})$ is shifted in proportion to the radial and vertical closed orbits:

$$\begin{aligned} \Delta_x &= x_0(\theta_i) - x_0(\theta_{Tr}) \text{ in } x \text{ and} \\ \Delta_y &= y_0(\theta_i) - y_0(\theta_{Tr}) \text{ in } y \end{aligned} \tag{4.39}$$

The resulting profile $M_T(x + \Delta_x, y + \Delta_y, \theta_{Tr})$ is scaled by

$$\begin{aligned} s_x = \frac{x_{RMS}(\theta_i)}{x_{RMS}(\theta_{Tr})} &= \sqrt{\frac{a_x \beta_x(\theta_i) + b D_x^2(\theta_i)}{a_x \beta_x(\theta_{Tr}) + b D_x^2(\theta_{Tr})}} \text{ in } x \text{ and} \\ s_x = \frac{y_{RMS}(\theta_i)}{y_{RMS}(\theta_{Tr})} &= \sqrt{\frac{\beta_y(\theta_i)}{\beta_y(\theta_{Tr})}} \text{ in } y \end{aligned} \tag{4.40}$$

where $a_{x,y} = \epsilon_{x,y}^{Tr}$ are defined from $M_T\left(x, y, \theta_{Tr}\right)$ via

$$x_{RMS}^2\left(\theta_{Tr}\right) \approx \epsilon_x^{Tr}\beta_x\left(\theta_{Tr}\right) + bD_x^2(\theta_{Tr}) \quad , \quad y_{RMS}^2\left(\theta_{Tr}\right) \approx \epsilon_y^{Tr}\beta_y\left(\theta_{Tr}\right) \tag{4.41}$$

and $b = \delta_{RMS}^2$ is taken from an external analysis (e.g., FR analysis [51]). In this way, $M_T\left(x, y, \theta_i\right)$ is reconstructed:

$$M_T^{reco}\left(x, y, \theta_i\right) = M_T\left(s_x\left(x + \Delta_x\right), s_y\left(y + \Delta_y\right), \theta_{Tr}\right). \tag{4.42}$$

Figure 4.34 shows the resulting beam profiles where $M_T\left(x, y, \theta_{Tr}\right)$ prepared from the Run-1d COSY-based simulation and the optical lattice functions are prepared with the corresponding field settings in the COSY-based model (see Subsec. 3.6.2). Although lattice functions slowly changed over time during Run-1, only their values at $t = 94\,\mu\text{s}$ (the mean time of the data taking period, accounting for muon decays) were used. The validity of this method, practical at a run level for the muon-weighted convolution of the magnetic field, is discussed next.

4.5.3 Method validation

A perfect reconstruction of the beam profiles is achieved with the "shift/scale" method if

$$M_T^{reco}\left(x, y, \theta_i\right) = M_T^{orig}\left(x, y, \theta_i\right), \tag{4.43}$$

where M_T^{orig} are the original intensity profiles from tracking simulation results (see Subsec. 4.5.1). Figure 4.35 shows a comparison of centroids and widths, which are the essential beam moments for the magnetic field convolution. Disagreements between reconstructed and original distributions in the vertical direction are below 0.02 mm, whereas in the radial

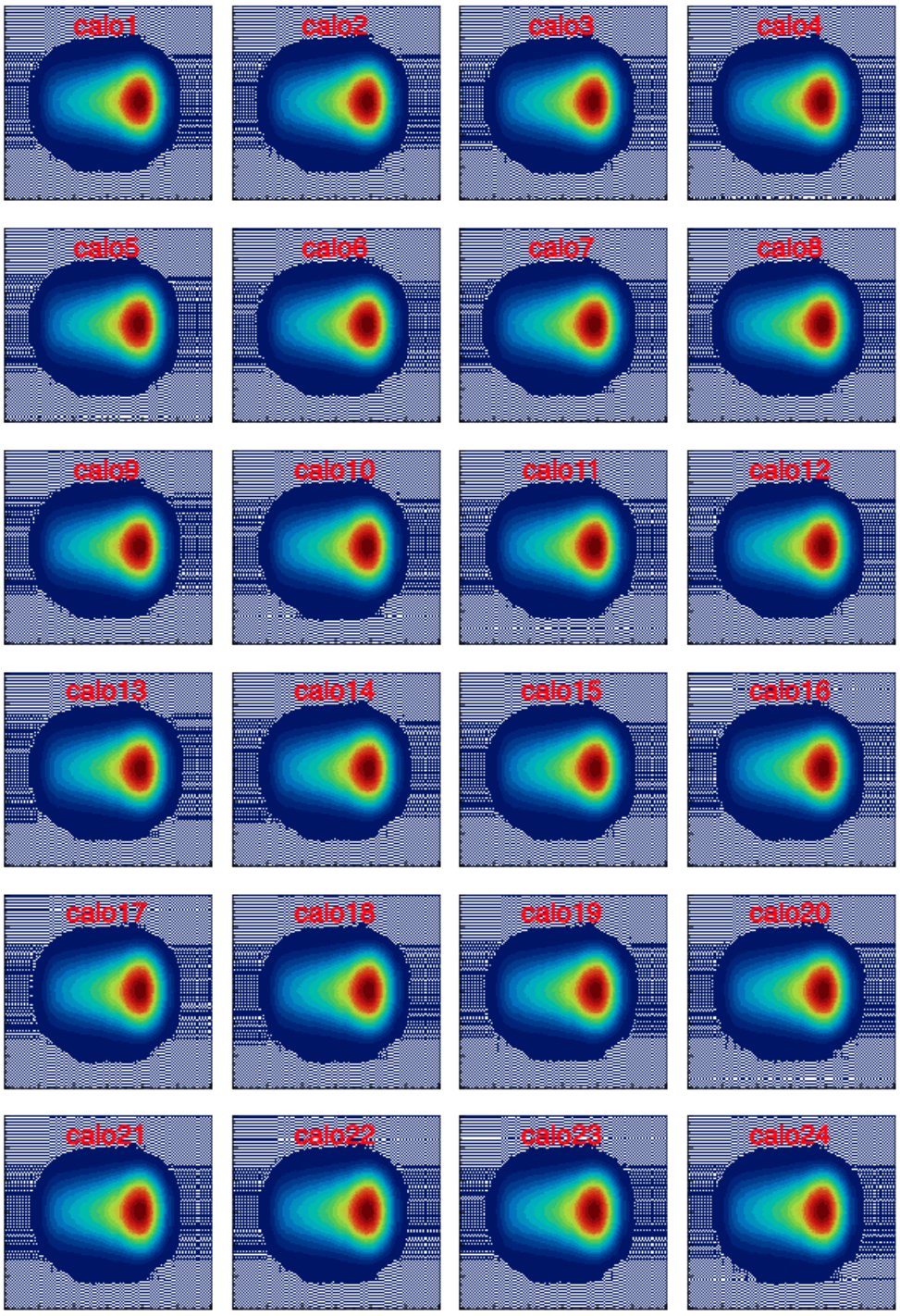

Figure 4.34: Run-1a reconstructed beam transverse profiles $M_T^{reco}(x_j, y_k, \theta_i)$, integrated over $30\,\mu s < t < 300\,\mu s$. The 24 azimuthal locations coincide with the regions of maximum calorimeter detection acceptance. Horizontal and vertical axes correspond to $-60\,mm < x < 60\,mm$ and $-60\,mm < y < 60\,mm$. Refer to Fig. 4.36 for the color legend.

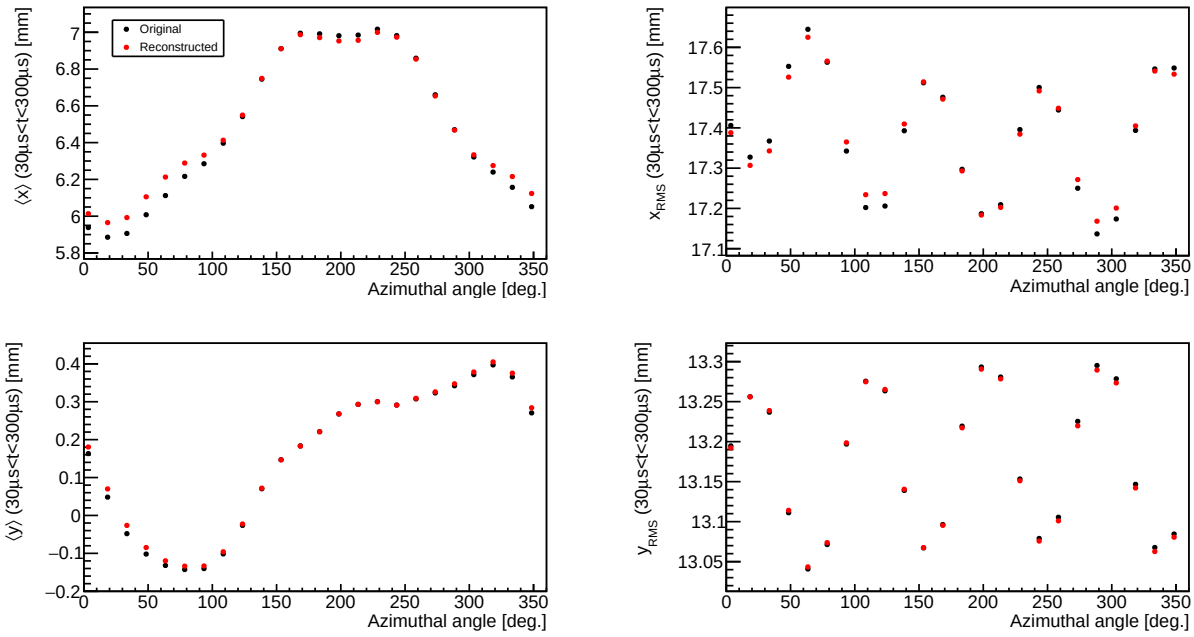

Figure 4.35: Time-integrated beam centroids and widths over the azimuthal angle. Red markers correspond to reconstructed beam profiles $M_T^{reco}(x, y, \theta_i)$, whereas entries from the simulated beam profiles $M_T^{orig}(x, y, \theta_i)$ are shown in black.

case the more evident discrepancies are intrinsic to the method; for the analysis of Run 2 and beyond, an upgraded method to reconstruct beam profiles for the field convolution is under development, which would follow more closely Eq. (3.73). Figure 4.36 displays azimuthally averaged beam profiles from the simulated (original) and reconstructed beam. Differences between the two cases are better observed in Fig. 4.37, owing to not transforming properly the higher-order beam moments with the reconstruction method.

Notwithstanding the differences between reconstructed and original profiles, the resulting muon-weighted field $\langle B \rangle_{reco}$ reliably reproduces the original case $\langle B \rangle_{orig}$ throughout the azimuth, as shown in Fig. 4.38. The larger variations at 335° and 25° are caused by the less uniform magnetic fields at the inflector and magnet leads, respectively. In spite of these two

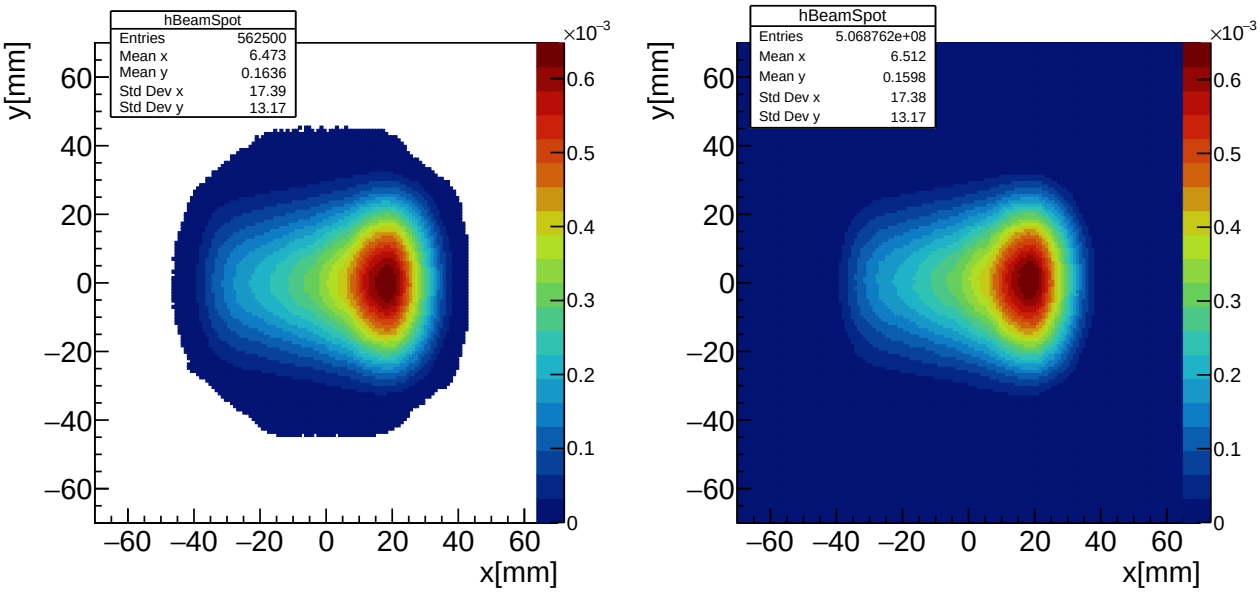

Figure 4.36: Reconstructed $M_T^{reco}(x,y)$ (left) and original $M_T^{orig}(x,y)$ (right) beam transverse profiles azimuthally averaged and integrated in time ($30\,\mu s < t < 300\,\mu s$).

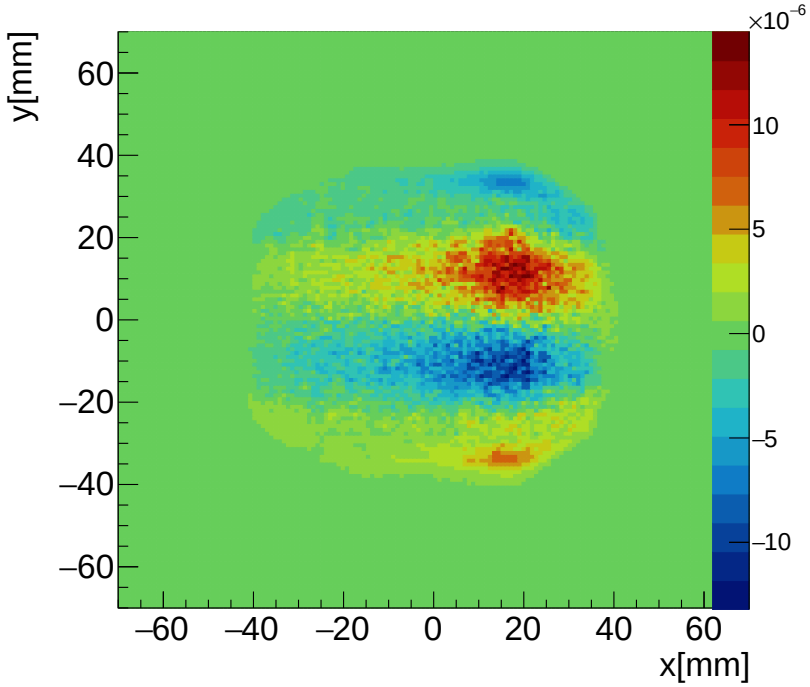

Figure 4.37: Difference between reconstructed $M_T^{reco}(x,y)$ (left) and original $M_T^{orig}(x,y)$ (right) beam transverse profiles azimuthally averaged and integrated in time ($30\,\mu s < t < 300\,\mu s$). Higher-order beam moments unaccounted-for in the method to reconstruct profiles M_T^{reco} introduce discrepancies with the reference case M_T^{orig}.

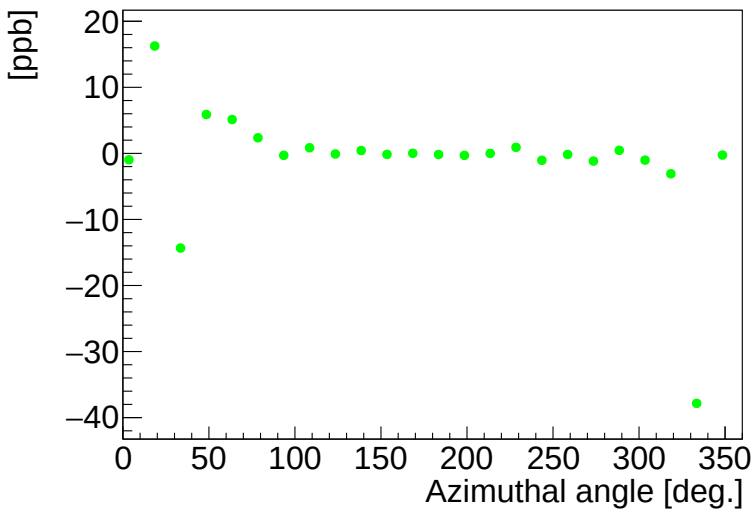

Figure 4.38: Relative differences between roconstructed and original muon-weighted fields $\big(\langle B\rangle_{i,reco} - \langle B\rangle_{i,orig}\big)/\langle B\rangle_{i,orig}$ over the azimuthal angle. Largest discrepancies emerge at azimuthal regions where the field is less uniform (i.e., at 335° and 25° around the inflector and magnet leads, respectively).

regions, the reconstructed weighted field resembles the real case to high accuracy:

$$\frac{\langle B\rangle_{reco} - \langle B\rangle_{orig}}{\langle B\rangle_{orig}} = -1.2\text{ppb} \tag{4.44}$$

An assessment of the differences from the perspective of convoluted beam projection distributions and multipole beam projections over the azimuth is shown in Figs. 4.39 and 4.40, respectively. With all the convoluted projections below 1 ppb and the lower order beam moments satisfactorily transformed, the method is validated for its use with experimental data as part of the field analysis. Since the simulated beam accounts for nonlinearities from both the electric and magnetic fields in the storage ring, it is also concluded that their effect on the beam distribution around the ring for the magnetic field convolution is negligible.

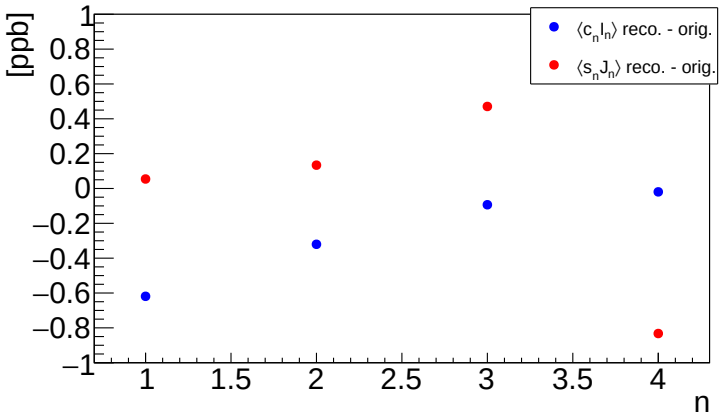

Figure 4.39: Differences between reconstructed and reference convoluted beam projection contributions.

4.5.4 Sensitivity of $\langle B \rangle$ to azimuthal beam variations

The versatility of the method allows to perform sensitivity studies of the azimuthal beam behavior on the reconstructed field $\langle B \rangle_{reco}$. Centroid variations from closed orbit distortions and width modulations from dispersion and beta functions characteristic to the ring's optical lattice have different consequences on the convolution as shown in Table 4.7.

Table 4.7: Sensitivity studies of the convoluted field to azimuthal beam variations.

Case	Shift/scale factors	$\frac{\langle B \rangle_{reco} - \langle B \rangle_{orig}}{\langle B \rangle_{orig}}$ [ppb]
Full shifting/scaling	–	-1.2
No radial centroid shifting	$\Delta_x = 0$	-13.1
No vertical centroid shifting	$\Delta_y = 0$	-0.6
No radial width scaling	$s_x = 1$	-1.8
No vertical width scaling	$s_y = 1$	-1.7
No shifting/scaling	$\Delta_x = \Delta_y = 0$, $s_x = s_y = 1$	-13.6 ppb

It is found that although the beam width (and vertical centroid) azimuthal dependence can be ignored while maintaining the reconstructed muon-weighted field to $\mathcal{O}(2\,\text{ppb})$ accuracy, the behavior of the radial centroid along the ring must be accounted for in order to satisfy the precision goals of the muon g-2 experiment. Unless the beam is better centered

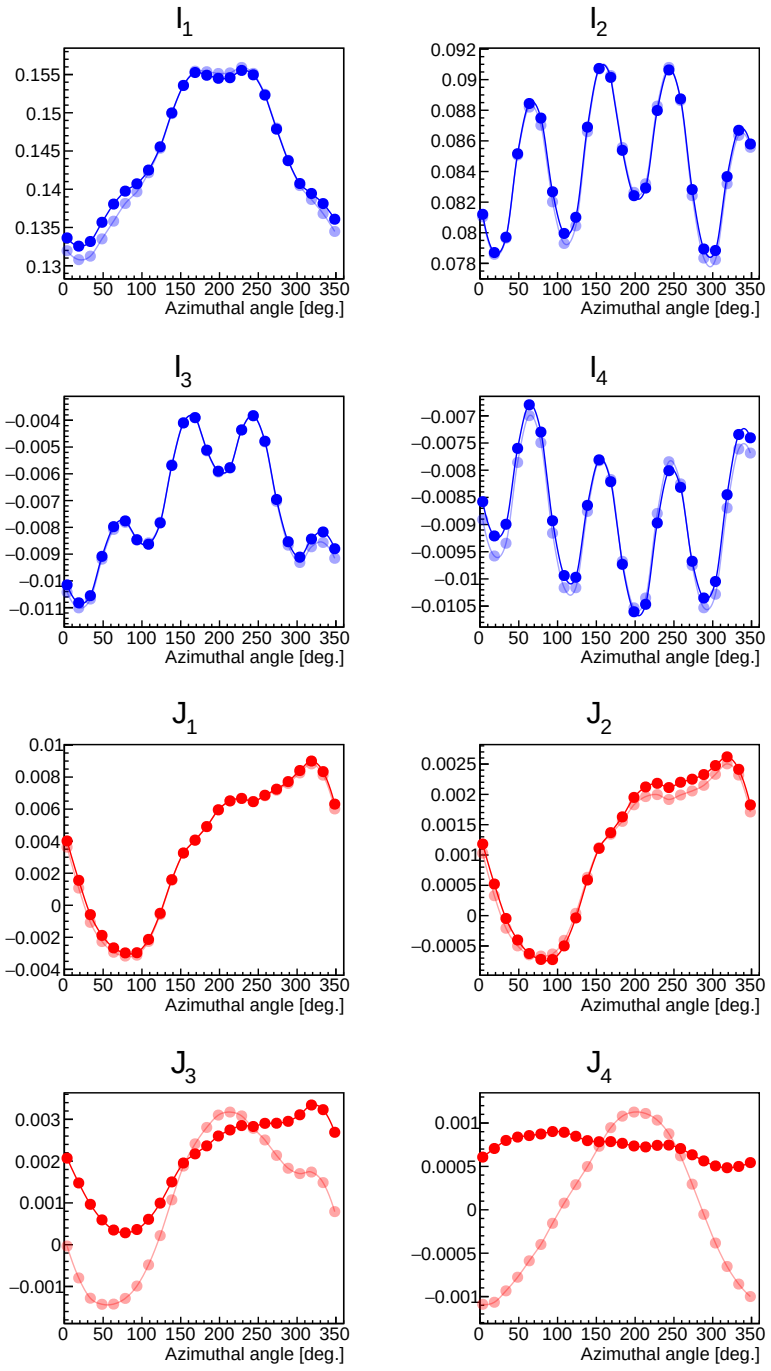

Figure 4.40: Multipole beam projections $\{I_{n,i}, J_{n,i}\}$ versus azimuthal angle from the Run-1a simulated beam (semi-transparent colors) and reconstructed profiles (solid colors). The small contributions from the skew octupole and decapole projections are not well transformed in the reconstruction method.

in the radial direction and radial closed orbits from the normal dipole inhomogeneities of the magnetic field are under control, the coupling between the normal quadrupole beam and magnetic field projections must be considered for an accurate calculation of $\langle B \rangle$.

For sensitivity studies specific to Run-1, the time evolution of the optical lattice was ignored in the reconstruction method to quantify their effect on the convolution, and was estimated to introduce an error of $\sim 1.4\,\text{ppb}$. Time variations of $\langle B \rangle$ due to beam drifts bias the measured anomalous precession frequency and, together with the lattice functions from the COSY-based model, were estimated (outside the work of this dissertation) to be negligible ($< 2\,\text{ppb}$) [101].

4.6 Conclusions

The beam characterization developed with the COSY-based model of the storage ring and documented in Ch. 3 was directly applied to quantify systematic corrections and their uncertainties driven by beam dynamics effects in the muon g-2 experiment.

The computational derivations of the Run-1 muon loss corrections via symplectic tracking agreed with data-driven results to within 12 ppb, indicating reliance in the experimental technique required to derive C_{ml} from observations. The understanding of betatron resonances, tune shifts, and the data-driven implementation of magnetic fields and the ESQ behavior during Run-1 set the stage to reach confidence in the symplectic tracking results.

Methods to extract phase acceptance corrections from detected-phase drifts, identification of the main driving mechanisms of C_{pa}, and accurate procedures to calculate this correction based on the beam behavior along the entire storage ring were developed and tested for their further use with experimental data. With the time-dependent optical lattice reconstructed

from tracker data, beam drifts around the ring azimuth are well understood and recreated for the determination of the phase acceptance correction during Run-1 datasets.

The standard corrections used in the muon g-2 experiment to define the E-field and pitch corrections were tested under effects not directly accounted for in their derivation, such as nonlinear ESQ electric fields, fringe fields, and segmented ESQ plates. A systematic correction of -10 ± 8.5 ppb from these effects was quantified in relation to the standard C_e and C_p corrections. Specific to Run-1 conditions in the storage ring, the effect of the unstable optical lattice on C_e was established to be negligible compared to the other systematic corrections of this correction.

And lastly, the optical lattice framework permitted to develop a method that accounts for the azimuthal behavior of the beam to calculate on a run-by-run basis the muon-weighted magnetic field, which is important for the determination of a_μ from measurements. Tests with the simulated Run-1a beam from the COSY-based model validates the method. Also, it was determined that for typical Run-1 beam distributions and magnetic fields, the dominant coupling that necessitates to be accounted for in the muon-weighted convolution of the magnetic field along the azimuth emerges from the radial centroid, which contributes to the total convolution about 12 ppb relative to the main value. Minimizing field inhomogeneities of the magnetic normal dipole term and centering the beam closer to the magic momentum is expected to alleviate the dependence of the field convolution on the radial beam centroid.

Chapter 5

Conclusions

The objective of this dissertation was to develop a detailed characterization of the beam dynamics in the Muon g-2 Experiment at Fermilab (E989), toward constraining effects intrinsic to the beam motion on the final measurement of the experiment. To that end, several methods and data-driven computational models were produced to analyze the evolution of the beam along the Muon Campus and, with more depth, inside the g-2 storage ring.

Chapter 1 covered the theoretical and experimental efforts aimed at resolving the value of the anomalous magnetic moment a_μ to unprecedented precision. In relation to the experimental technique of E989, the beam dynamics requirements that are necessary to achieve the experimental goals were presented, and the work described in the subsequent chapters of this document aimed at addressing them to contribute with the high-precision experimental determination of a_μ. At the time of this dissertation, the discrepancy between a_μ from theory and experiment had a significance of 4.2σ. However, both the muon g-2 experiment at Fermilab and the theory initiative still plan to keep refining their values in order to either declare physics beyond the Standard Model or to further validate the fundamental knowledge provided by this model.

In Chapter 2, the modeling of the beam delivery system (BDS) as part of this dissertation was presented. Results derived from this analysis served to validate the other models of the Muon Campus within the g-2 collaboration. Numerical studies of the muon beam polariza-

tion from pions decay were performed, as well as an analysis of the impact of nonlinearities of the guide fields along the BDS on the muon population downstream from the pion production target. In particular, the studied effects of nonlinearities on the g-2 phase—important for beam dynamics corrections on the measured anomalous precession frequency ω_a^m—suggest further investigation of the momentum-phase correlation in relation to the fringe fields of the multiple rectangular magnets inside the Delivery Ring.

In Chapter 3, the COSY-based model together with complementary methods to characterize the beam dynamics in the muon g-2 storage ring were presented. These tools were developed on experimental data, optimization techniques and the DA framework within COSY INFINITY. Linear and nonlinear beam dynamics were accounted for in order to recreate all the conditions that the stored muon beam experiences while ω_a^m is measured. The model provided understanding of the optimal guide field ring configurations during data taking. With a detailed implementation of the electric and magnetic fields in the model, nonlinear effects such as betatron tune shifts and resonances were characterized, which allowed for the detailed beam dynamics systematic corrections and uncertainties on a_μ presented in Ch. 4. Available beam diagnostics from the straw tracking detectors and high-voltage scans of the ESQ system permitted to benchmark results from the COSY-based model via symplectic tracking simulations. Of particular importance, the reconstruction of the unstable ESQ guide fields during Run-1 and a detailed description of the optical lattice set the stage for quantifying the beam behavior along the storage ring azimuth under these special circumstances and, in this way, determining ω_a^m corrections to the ppb level. In addition, the particular time-momentum correlations of the stored muon beam owing to the injection process were recreated with the model, which allowed to discover it as part of a collective effort in the g-2 collaboration. The work presented in Ch. 3 took place during the commis-

sioning and first data collection period (Run-1) of E989, although it is expected to continue being utilized for the data analysis of the experiment (i.e., Run-2 to Run-5).

Direct applications to quantify corrections (and their systematic uncertainties) of ω_a^m and the convoluted magnetic field—derived from the work presented in Chapter 3—are elaborated in Chapter 4. Muon loss corrections C_{ml} during Run-1 were recreated from symplectic tracking simulations with the COSY-based model, with results comparable to the data-driven quantifications ($< 12\,\text{ppb}$). Even though muon loss corrections are expected to be negligible for Run-2 and beyond thanks to improved beam injection, the replacement of the Run-1 damaged resistors, more collimators inserted, temperature control, and a ESQ set point further from betatron resonances, detailed simulations of muon loss rates would contribute to diagnose the storage ring conditions during data taking.

With the detailed description of the beam around the ring from Chapter 3, a detailed study of the phase acceptance correction C_{pa} during Run-1 was performed. Methods to extract this correction, as well as the understanding of the mechanisms that induce C_{pa} due to the beam motion around the storage ring were developed. Similar to the C_{ml} correction, the phase acceptance correction is expected to be considerably smaller during Runs 2-5 thanks to a stable ESQ system, although the precision goals of E989 would demand to evaluate this correction and its associated systematic uncertainties for all the runs.

In relation to the E-field (C_e) and pitch (C_p) corrections, the applicability for their usage in E989 was tested under several realistic scenarios characteristic of the g-2 beam storage ring (i.e., asymmetric momentum spread, segmented ESQ stations, and ESQ nonlinear fields). A small correction originated by those specific features was found to be small ($-10 \pm 8.5\,\text{ppb}$). The time-evolving ESQ electric fields during the Run-1 ω_a^m measurement was found to not affect the E-field correction in a significant way. As a next step, the effect of nonlinearities

(e.g., betatron amplitude modulations) and closed orbit distortions from magnetic field inhomogeneities on the E-field and pitch corrections could be analyzed with the COSY-based model, which could become relevant due to the proximity of the operational ESQ set point to the resonant condition $3\nu_y = 1$ during Runs 2-5.

And lastly, a method to implementation optical lattice functions for weighting the magnetic field in the storage ring with the stored muon beam was discussed. Validations with tracking simulations indicated reliance for its further used with experimental data. Sensitivity studies determined that, due to the specific transverse beam profile in E899 measured by the straw tracking detectors, azimuthal dependencies of the beam radial centroid are essential to be accounted for in the field convolution in order to estimate it with ppb precision. Based on this work, it can be concluded that further improvements of the beam injection process (which is the case for Run-2 and beyond) would be less dependent on the beam azimuthal behavior.

BIBLIOGRAPHY

BIBLIOGRAPHY

[1] P. J. Mohr, D. B. Newell, and B. N. Taylor, "CODATA recommended values of the fundamental physical constants: 2014," *Rev. Mod. Phys.* **88** no. 3, (2016) 35009.

[2] J. Abdallah, D. collaboration, *et al.*, "Study of tau-pair production in photon-photon collisions at LEP and limits on the anomalous electromagnetic moments of the tau lepton," *arXiv preprint hep-ex/0406010* (2004) .

[3] J. Schwinger, "On quantum-electrodynamics and the magnetic moment of the electron," *Physical Review* **73** no. 4, (1948) 416.

[4] **Muon** $g-2$ Collaboration, "Measurement of the Positive Muon Anomalous Magnetic Moment to 0.46 ppm," *Phys. Rev. Lett.* **126** (2021) 141801.

[5] T. Aoyama, N. Asmussen, M. Benayoun, *et al.*, "The anomalous magnetic moment of the muon in the Standard Model," *Physics Reports* **887** (2020) 1–166.

[6] R. Osofsky, *Magnetic Field Determination for Run 1 of the Fermilab Muon g-2 Experiment*. PhD thesis, University of Washington, 2019.

[7] J. Mott, "Field convolution workshop: tracker perspective." E989 Document 21555, 2020.

[8] J. D. Crnkovic, "Muon Campus beam bunch cycle diagram." E989 Document 21527, 2020.

[9] D. Stratakis, B. Drendel, J. P. Morgan, M. J. Syphers, and N. S. Froemming, "Commissioning and first results of the Fermilab Muon Campus," *Physical Review Accelerators and Beams* **22** no. 1, (2019) 011001.

[10] D. Stratakis, "Application of passive wedge absorbers for improving the performance of precision-science experiments," *Physical Review Accelerators and Beams* **22** no. 5, (2019) 053501.

[11] S. Ganguly, "Muon Losses - an Overview." E989 Document 12912, 2018.

[12] D. A. Tarazona *et al.*, "Lost-Muon Studies." E989 Note 265, 2021.

[13] J. Crnkovic, "Relative Decay Positron Storage for 02/10/18 Fine Quad Scan." E989 Document 11454, 2018.

[14] H. P. Binney, "Measurement of the phase-momentum correlation lost muon systematic error." E989 Note 248, 2019.

[15] H. P. Binney. Private communication.

[16] K. Khaw *et al.*, "Phase Acceptance Correction Analysis Report." E989 Note 262, 2021.

[17] B. L. Roberts, "The history of the muon (g-2) experiments," `arXiv:1811.06974 [hep-ex]`.

[18] A. Zangwill, *Modern Electrodynamics*. Cambridge University Press, 2012.

[19] P. A. M. Dirac, "The quantum theory of the electron," *Proceedings of the Royal Society of London. Series A, Containing Papers of a Mathematical and Physical Character* **117** no. 778, (1928) 610–624.

[20] W. Gerlach and O. Stern, "Das magnetische moment des silberatoms," *Zeitschrift für Physik* **9** no. 1, (1922) 353–355.

[21] A. H. Compton, "The magnetic electron," *Journal of the Franklin Institute* **192** no. 2, (1921) 145–155.

[22] G. E. Uhlenbeck and S. Goudsmit, "Ersetzung der Hypothese vom unmechanischen Zwang durch eine Forderung bezüglich des inneren Verhaltens jedes einzelnen Elektrons," *Die Naturwissenschaften* **13** no. 47, (1925) 953–954.

[23] J. P. Miller, E. d. Rafael, and B. L. Roberts, "Muon (g-2): experiment and theory," *Reports on Progress in Physics* **70** no. 5, (2007) 795–881.

[24] J. Schwinger, "Quantum electrodynamics. III. The electromagnetic properties of the electron—radiative corrections to scattering," *Physical Review* **76** no. 6, (1949) 790.

[25] T. Aoyama, M. Hayakawa, T. Kinoshita, and M. Nio, "Tenth-order QED contribution to the electron g-2 and an improved value of the fine structure constant," *Physical Review Letters* **109** no. 11, (2012) 111807.

[26] F. Jegerlehner and A. Nyffeler, "The muon g-2," *Physics Reports* **477** no. 1-3, (2009) 1–110.

[27] C. Gnendiger, D. Stöckinger, and H. Stöckinger-Kim, "The electroweak contributions to $(g-2)_\mu$ after the Higgs-boson mass measurement," *Physical Review D* **88** no. 5, (2013) 053005.

[28] A. Keshavarzi, D. Nomura, and T. Teubner, "Muon $g-2$ and $\alpha(M_Z^2)$: a new data-based analysis," *Physical Review D* **97** no. 11, (2018) 114025.

[29] A. Kurz, T. Liu, P. Marquard, and M. Steinhauser, "Hadronic contribution to the muon anomalous magnetic moment to next-to-next-to-leading order," *Physics Letters B* **734** (2014) 144–147.

[30] J. Prades, E. De Rafael, and A. Vainshtein, "The hadronic light-by-light scattering contribution to the muon and electron anomalous magnetic moments," in *Lepton Dipole Moments*, pp. 303–317. 2010.

[31] A. Nyffeler, "Precision of a data-driven estimate of hadronic light-by-light scattering in the muon g-2: Pseudoscalar-pole contribution," *Physical Review D* **94** no. 5, (2016) 053006.

[32] T.-D. Lee and C.-N. Yang, "Question of parity conservation in weak interactions," *Physical Review* **104** no. 1, (1956) 254.

[33] G. W. Bennett, B. Bousquet, H. Brown, G. Bunce, R. Carey, P. Cushman, G. Danby, P. Debevec, M. Deile, H. Deng, *et al.*, "Final report of the E821 muon anomalous magnetic moment measurement at BNL," *Physical Review D* **73** no. 7, (2006) 072003.

[34] S. Borsanyi, Z. Fodor, J. Guenther, C. Hoelbling, S. Katz, L. Lellouch, T. Lippert, K. Miura, L. Parato, K. Szabo, *et al.*, "Leading hadronic contribution to the muon magnetic moment from lattice QCD," *arXiv e-prints* (2020) arXiv–2002.

[35] J. Grange, V. Guarino, P. Winter, *et al.*, "Muon (g-2) Technical Design Report," `arXiv:1501.06858 [physics.ins-det]`.

[36] E. J. Konopinski, "The Experimental Clarification of the Laws of beta-Radioactivity," *Annual Review of Nuclear Science* **9** no. 1, (1959) 99–158.

[37] **Muon** $g-2$ Collaboration, "Measurement of the anomalous precession frequency of the muon in the Fermilab Muon $g-2$ Experiment," *Phys. Rev. D* **103** (2021) 072002.

[38] K. Khaw, M. Bartolini, H. Binney, R. Bjorkquist, A. Chapelain, A. Driutti, C. Ferrari, A. Fienberg, A. Fioretti, C. Gabbanini, *et al.*, "Performance of the Muon g-2 calorimeter and readout systems measured with test beam data," *Nuclear Instruments and Methods in Physics Research Section A: Accelerators, Spectrometers, Detectors and Associated Equipment* **945** (2019) 162558.

[39] H. P. Binney *et al.*, "T0 update." E989 Document 10162, 2018.

[40] P. Kammel *et al.*, "Inflector Beam Monitor System." E989 Document 2692, 2015.

[41] A. Chapelain, "Beam dynamics from Fiber Harps." E989 Document 10884, 2018.

[42] S. Charity, *Beam profile measurements using the straw tracking detectors at the Fermilab muon g-2 experiment, and a study of their sensitivity to a muon electric dipole moment*. PhD thesis, University of Liverpool, 2018.

[43] **Muon** $g-2$ Collaboration, "Magnetic-field measurement and analysis for the Muon $g-2$ Experiment at Fermilab," *Phys. Rev. A* **103** (2021) 042208.

[44] M. W. Smith, *Developing the Precision Magnetic Field for the E989 Muon g-2 Experiment*. PhD thesis, University of Washington, 2017.

[45] D. Flay, "Magnetic Field Calibration Analysis for Run 1." E989 Note 191, 2020.

[46] **Muon** $g-2$ Collaboration, "Beam dynamics corrections to the Run-1 measurement of the muon anomalous magnetic moment at Fermilab," `arXiv:2104.03240 [physics.acc-ph]`.

[47] J. Grange, "Shift in ω_p due to couplings between longitudinal and transverse magnetic field inhomogeneities (distortion of the closed orbit)." E989 Note 57, 2019.

[48] V. Bargmann, L. Michel, and V. Telegdi, "Precession of the polarization of particles moving in a homogeneous electromagnetic field," *Physical Review Letters* **2** no. 10, (1959) 435.

[49] F. J. M. Farley, "Pitch correction in (g-2) experiments," *Physics Letters B* **42** no. 1, (1972) 66–68.

[50] K. Makino, E. Valetov, and M. Berz, "Detailed Linear Optics and Tunes of the g-2 Ring." E989 Note 104, 2017.

[51] T. Barrett *et al.*, "Run 1 Fast Rotation Analysis with the Fourier Method." E989 Note 245, 2020.

[52] D. Tarazona, M. Berz, K. Makino, D. Stratakis, and M. Syphers, "Dynamical simulations of the Muon Campus at Fermilab," *International Journal of Modern Physics A* **34** no. 36, (2019) 1942033.

[53] K. Makino and M. Berz, "Cosy infinity version 9," *Nuclear Instruments and Methods in Physics Research Section A: Accelerators, Spectrometers, Detectors and Associated Equipment* **558** no. 1, (2006) 346–350.

[54] D. Stratakis, M. E. Convery, C. Johnstone, J. Johnstone, J. P. Morgan, D. Still, J. D. Crnkovic, V. Tishchenko, W. M. Morse, and M. J. Syphers, "Accelerator performance analysis of the Fermilab Muon Campus," *Physical Review Accelerators and Beams* **20** no. 11, (2017) 111003.

[55] H. Wiedemann, *Particle accelerator physics*. Springer Nature, 2015.

[56] M. Berz and K. Makino, "COSY INFINITY 10.0 beam physics manual," *MSU Report MSUHEP* (2017) .

[57] N. S. Froemming, *Optimization of Muon Injection and Storage in the Fermilab g-2 Experiment: From Simulation to Reality*. PhD thesis, University of Washington, 2018.

[58] N. Mokhov, "Recent MARS15 developments: nuclide inventory, DPA and gas production," *arXiv preprint arXiv:1202.2383* (2012) .

[59] V. Tishchenko, "MARS simulations of pion production and capture." E989 Document 1569, 2014.

[60] A. Chapelain, "Cornell fast rotation Fourier method." E989 Note 206, 2019.

[61] F. Combley and E. Picasso, "The muon (g-2) precession experiments: Past, present and future," *Physics Reports* **14** no. 1, (1974) 1–58.

[62] D. Tarazona, M. Berz, R. Hipple, K. Makino, and M. Syphers, "Muon Beam Tracking and Spin-Orbit Correlations for Precision g-2 Measurements," tech. rep., Fermi National Accelerator Lab. (FNAL), Batavia, IL (United States), 2016.

[63] J. Crnkovic, W. Morse, V. Tishchenko, and D. Stratakis, "Spin Correlations study for the new g-2 Experiment at Fermilab," in *Proc. 7th Int. Particle Accelerator Conf.(IPAC?16), Busan, Korea*, pp. 1301–1303. 2016.

[64] D. Tarazona, M. Berz, and K. Makino, "Muon loss rates from betatron resonances at the Muon g-2 Storage Ring at Fermilab," *International Journal of Modern Physics A* **34** no. 36, (2019) 1942008.

[65] B. Erdélyi and M. Berz, "Optimal symplectic approximation of Hamiltonian flows," *Physical Review Letters* **87** no. 11, (2001) 114302.

[66] E. Valetov, M. Berz, and K. Makino, "Computation of the main and fringe fields for the electrostatic quadrupoles of the Muon g-2 storage ring," *International Journal of Modern Physics A* **34** no. 36, (2019) 1942041.

[67] M. Berz, *Modern map methods in particle beam physics*. Academic Press, 1999.

[68] K. Makino, "The COSY 8th order Runge-Kutta integrator," *Neutrino Factory/Muon Collider Notes MUC-NOTE-COOLTHEORY-0238, Fermi National Accelerator Laboratory* (2002) .

[69] Y. K. Semertzidis, G. Bennett, E. Efstathiadis, F. Krienen, R. Larsen, Y. Lee, W. M. Morse, Y. Orlov, C. S. Ozben, B. L. Roberts, *et al.*, "The brookhaven muon (g-2) storage ring high voltage quadrupoles," *Nuclear Instruments and Methods in Physics Research Section A: Accelerators, Spectrometers, Detectors and Associated Equipment* **503** no. 3, (2003) 458–484.

[70] J. D. Crnkovic *et al.*, "Quad Capacitances and HV Resistors." E989 Note 92, 2016.

[71] M. Berz, K. Makino, and W. Wan, *An introduction to beam physics*. CRC press, 2014.

[72] M. Berz *et al.*, "Quad Voltage / Quad Voltage = Oomph: A Quantitative Oomph Theory." E989 Note 149, 2018.

[73] J. Grange, "Introduction to two-dimensional magnetic field multipoles." E989 Note 77, 2016.

[74] D. A. Edwards and M. J. Syphers, *An introduction to the physics of high energy accelerators*. John Wiley & Sons, 2008.

[75] A. Mikhailichenko and D. Rubin, "Latest Results on Fast Kicker for g-2 E-989 Experiment at Fermilab," in *8th Int. Particle Accelerator Conf. (IPAC'17), Copenhagen, Denmark, 14â 19 May, 2017*, pp. 4616–4618, JACOW, Geneva, Switzerland. 2017.

[76] C. Stoughton, "Current Measurement into Kicker 1." E989 Document 11571, 2018.

[77] Data developed by S. Chang and distributed by O. Kim.

[78] T. Chupp, "Collimator effects on magnetic field." E989 Document 24661, 2021.

[79] M. Korostelev, I. Bailey, A. Herrod, D. Stratakis, V. Tishchenko, A. Wolski, *et al.*, "Update on Bmad Simulations From Target to Storage Ring for the New Muon g-2 Experiment at Fermilab," in *Proc. of International Particle Accelerator Conference (IPAC?17), Copenhagen, Denmark*, no. 8, pp. 791–794. 2017.

[80] D. Rubin, "Phase Space at Inflector Exit." E989 Document 11703, 2018.

[81] D. Rubin, "Investigating Dependencies and Systematics with BMAD." E989 Document 24751, 2021.

[82] J. Mott, "Beam Measurements: Run 1." E989 Document 22002, 2020.

[83] E. D. Courant and H. S. Snyder, "Theory of the alternating-gradient synchrotron," *Annals of Physics* **3** no. 1, (1958) 1–48.

[84] Y. Orlov, C. S. Ozben, and Y. K. Semertzidis, "Muon revolution frequency distribution from a partial-time Fourier transform of the g-2 signal in the muon g-2 experiment," *Nuclear Instruments and Methods in Physics Research Section A: Accelerators, Spectrometers, Detectors and Associated Equipment* **482** no. 3, (2002) 767–775.

[85] M. J. Syphers, "Closed Orbit Distortions from Quad Alignment." E989 Document 13414, 2018.

[86] E. Valetov and M. Berz, "Main Field of the Muon g-2 Collaboration Quadrupole in the Case of Mispowered Plates." E989 Note 100, 2016.

[87] A. Weisskopf, D. Tarazona, and M. Berz, "Computation and consequences of high order amplitude-and parameter-dependent tune shifts in storage rings for high precision measurements," *International Journal of Modern Physics A* **34** no. 36, (2019) 1942011.

[88] M. J. Syphers, "Nonlinear Detuning." E989 Note 142, 2018.

[89] H. Nguyen, "Detuning and CBO Frequency Shift during Spill." E989 Document 12506, 2018.

[90] J. Mott, "Randomisation in Phase Acceptance Analysis." E989 Document 24128, 2021.

[91] F. J. M. Farley, "Some calculations on resonance excitation in the g-2 ring." E821 Note 106, 1992.

[92] S. Ganguly, "The $3Q_y = 1$ resonance for differnet time scans." E989 Document 11796, 2018.

[93] M. J. Syphers, "Some Calculations and Comments." E989 Document 11424, 2018.

[94] D. A. Tarazona *et al.*, "$3Q_y = 1$ and collimation studies with COSY." E989 Document 12416, 2018.

[95] M. Kargiantoulakis, "Alignment survey results for the Electrostatic Quadrupole System of the Muon g-2 Experiment." E989 Note 177, 2019.

[96] M. J. Syphers, "Long-Term Muon Loss Rates and an Estimate of ω_a Systematic Uncertainty." E989 Note 226, 2020.

[97] D. A. Tarazona *et al.*, "Nonlinear+Linear lost muons." E989 Document 23624, 2020.

[98] O. Kim *et al.*, "Qualitative estimation of the RF CBO reduction." E989 Note 260, 2021.

[99] T. Barrett and J. Mott, "Measurement of the Pitch Correction for Run 1." E989 Note 252, 2020.

[100] D. A. Tarazona *et al.*, "Effect of bad resistors on E-field correction." E989 Document 22107, 2020.

[101] B. MacCoy *et al.*, "Muon B-field Weighting Report for Bloch Team." E989 Document 24447, 2021.

[102] E. Bottalico, J. Mott, and D. A. Tarazona, "Phase Acceptance - Procedure Checks." E989 Document 24504, 2020.

[103] R. Fatemi, "Simulation Contributions to the Run 1 Beam Dynamics Systematics." E989 Document 24754, 2021.

[104] J. D. Crnkovic, "High voltage pulse models for the bad resistors." E989 Note 187, 2019.

[105] W. Morse, "Whence the End-Game Damaged Quad Resistors." E989 Document 18127, 2019.

[106] M. J. Syphers, "Beam Dynamics Primer – II." E989 Document 14145, 2018.

[107] D. A. Tarazona, "β_y systematic-error studies." E989 Document 23915, 2020.

[108] D. A. Tarazona, J. Mott, *et al.*, "Extracting COSY input from data." E989 Document 22660, 2020.

[109] D. Rubin, "Injection Dependencies." E989 Document 10563, 2018.

[110] E. V. Valetov, "Toward the Frontiers of Particle Physics With the Muon g-2 Experiment," tech. rep., Fermi National Accelerator Lab.(FNAL), Batavia, IL (United States), 2020.

[111] T. Arvanitis and A. Lyon, "artG4: A Generic Framework for Geant4 Simulations," in *Journal of Physics: Conference Series*, vol. 513, p. 022023, IOP Publishing. 2014.

[112] Y. Orlov, "Changes of Muon Betatron Amplitudes During Their Lifetime as a Possible Source of a Small g-2 Error." E821 Note 440, 2003.

[113] V. Tishchenko, "P-A updates." E989 Document 20285, 2020.

[114] E. Bottalico *et al.*, "Effect on R due to variable phase from tracker data." E989 Note 233, 2020.

[115] D. A. Tarazona *et al.*, "PA-related ω_a shifts from simulated data." E989 Document 24092, 2020.

[116] J. Mott, "Phase acceptance: what we think we know." E989 Document 24231, 2020.

[117] D. A. Tarazona *et al.*, "PA corrections from simulated data. And 1st-level approach." E989 Document 24459, 2020.

[118] D. A. Tarazona *et al.*, "E-field/Pitch corrections from $\langle\omega_a\rangle$ tracking simulations." E989 Document 18088, 2019.

[119] E. M. Metodiev *et al.*, "Analytical Benchmarks for Precision Particle Tracking in Electric and Magnetic Rings," *Nucl. Instrum. Meth. A* **797** (2015) 311–318.

[120] R. Brun and F. Rademakers, "ROOT—an object oriented data analysis framework," *Nuclear Instruments and Methods in Physics Research Section A: Accelerators, Spectrometers, Detectors and Associated Equipment* **389** no. 1-2, (1997) 81–86.

[121] D. A. Tarazona *et al.*, "Effect of bad resistors on E-field correction." E989 Document 22107, 2020.

[122] D. A. Tarazona *et al.*, "Combining B and the azimuthally changing beam." E989 Document 24188, 2020.